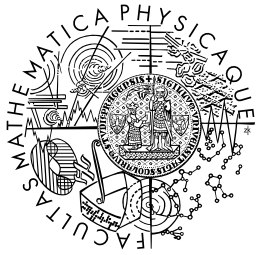

FACULTY
OF MATHEMATICS
AND PHYSICS
Charles University

DOCTORAL THESIS

Pavel Háček

Plasma diagnostics using neutral lithium beam on the COMPASS tokamak

Department of Surface and Plasma Science

Supervisor of the doctoral thesis: RNDr. Jan Stöckel, CSc.

Study programme: Physics

Specialization: 4F2 Physics of Plasma and Ionized Media

Prague 2018

I would like to thank to my dear wife, my family and my friends for their love, support and encouragement. I would also like to thank to my colleagues on COMPASS tokamak, who created a warm, friendly and enthusiastic team and motivated me in my work. They were the reason I did not give up during the dark long times when I doubted that the diagnostic of lithium beam will ever work.

Namely, I would like to thank to Miklos Berta, my consultant and friend, without whom this work would have never been done. For all their help and support, I would like to thank to Jan Stockel, Vladimir Weinzettl, Jaroslav Krbec, Martin Hron, Jiri Adamek, Matej Tomes, Karel Kovarik and our team of COMPASS pilots.

"Bratří, já nemám za to, že jsem již u cíle; jen to mohu říci: zapomínaje na to, co je za mnou, upřen k tomu, co je přede mnou, běžím k cíli, abych získal nebeskou cenu."

I declare that I carried out this doctoral thesis independently, and only with the cited sources, literature and other professional sources.

I understand that my work relates to the rights and obligations under the Act No. 121/2000 Coll., the Copyright Act, as amended, in particular the fact that the Charles University in Prague has the right to conclude a license agreement on the use of this work as a school work pursuant to Section 60 paragraph 1 of the Copyright Act.

In ..... date ..... signature of the author

Název práce: Diagnostika plazmatu využívající neutrální lithiový svazek na tokamaku COMPASS

Autor: ing. Pavel Háček

Katedra: Katedra fyziky povrchů a plazmatu

Vedoucí disertační práce: RnDr. Jan Stöckel, Csc. Ústav Fyziky Plazmatu, Akademie Věd České Republiky, v.v.i.

Abstrakt: Tato disertační práce prezentuje diagnostiku neutrálního lithiového svazku na tokamaku COMPASS v Praze. V technické části je popsán systém pro vstřikování urychleného lithiového svazku do tokamaku COMPASS a detekční systémy pro emisní spektroskopii na svazku. Fyzikální část popisuje analýzu naměřených spektroskopických dat zejména se zaměřením na hustotní fluktuace v okrajovém plazmatu. Je prezentována detailní analýza turbulentních struktur v neudržené části plazmatu a výzkum nestabilit typu ELM během módu plazmatu s vysokým udržením energie. Práce také představuje vývoj a měření nové unikátní diagnostiky - sondy atomového svazku - využívající detekce ionizované části svazku k měření okrajového profilu proudové hustoty plazmatu.

Klíčová slova: tokamak, diagnostický svazek, emisní spektroskopie na svazku, sonda atomového svazku

Title: Plasma diagnostics using neutral lithium beam on the COMPASS tokamak

Author: ing. Pavel Háček

Department: Department of Surface and Plasma Science

Supervisor: RnDr. Jan Stöckel, Csc. Institute of Plasma Physics of the Czech Academy of Sciences

Abstract: The doctoral thesis presents the diagnostic neutral lithium beam on the COMPASS tokamak in Prague. The technical part describes the system for injection of accelerated lithium beam into the COMPASS tokamak and the respective detection systems for beam emission spectroscopy. The physical part describes the analysis of measured spectroscopic data, with particular emphasis on density fluctuations in the edge plasma. Detailed analysis of turbulent structures outside of the confined plasma region is presented, as well as investigations of the ELM instabilities during high confinement mode plasma operation. The thesis also presents the development and proof-of-concept measurements of a new and unique diagnostic method - atomic beam probe. The method uses detection of the ionized part of the beam for current density profile measurements in the plasma edge.

Keywords: tokamak, diagnostic beam, beam emission spectroscopy, atomic beam probe

Contents

1. Introduction

This thesis summarizes part of my work during the doctoral studies at the Charles University in Prague. The work was done at the Tokamak department of the Institute of Plasma Physics of the Czech Academy of Sciences in Prague. At the time of the start of my studies in 2009, the reinstalled tokamak COMPASS just started its operation with several basic plasma diagnostics. One of the major challenges for the growing COMPASS team was to develop and build a new set of diagnostics to support the planned scientific exploitation of COMPASS. I became the person responsible for the development, commissioning and operation of the neutral lithium beam system and related diagnostics of beam emission spectroscopy and atomic beam probe on COMPASS.

Hungarian scientific group from the Wigner Institute in Budapest had experience of building and running a lithium beam diagnostic on the TEXTOR tokamak and Wendelstein 7-AS stellarator. Therefore a collaboration was established and the group designed and manufactured the beam system for COMPASS, including the optical detection systems for beam emission spectroscopy, a test atomic beam probe detector and the respective data acquisition systems. The main parts of the beam hardware were brought to Prague in early 2011 and I assisted in its assembly. My main work then became the integration of the system to tokamak COMPASS environment, its commissioning and operation. This work was done for the most part by the lithium beam group on COMPASS, comprising of 2 - 3 people. Beam commissioning proved to be a difficult and complex task. It took almost 3 additional years before a reliable beam operation in plasma was established (end of 2013). The work of the lithium beam group then relied on routine measurements in the COMPASS discharges and continual diagnostic improvements. My independent work consisted of analyses of the spectroscopic data and the development of a novel diagnostic method using the diagnostic beam - atomic beam probe.

1.1 Goals and thesis overview

The main goal of the work was to build and operate the neutral lithium beam on COMPASS. The individual goals may be specified as follows:

1. Commissioning of the beam emission spectroscopy diagnostic (Li-BES) using the neutral lithium beam on COMPASS

2. Routine measurement of plasma density profiles by the Li-BES diagnostic

3. Evaluation of the Li-BES data with regard to the COMPASS scientific goals - physics of the high confinement mode and turbulent transport in the edge plasma and scrape-off layer (SOL) regions

4. Development and proof of concept of the novel atomic beam probe diagnostic using the neutral lithium beam

The thesis is divided into seven chapters and following appendices:

- **Chapter 1** is the *Introduction*.
- **Chapter 2** - *COMPASS tokamak* - contains a brief introduction of the COMPASS tokamak and its parameters and overview of the available diagnostics.
- **Chapter 3** - *Diagnostic neutral lithium beam on COMPASS* - describes the principle of the lithium beam injection and its main individual components on COMPASS, the lithium emitter and ion optics, beam neutralizer and the Farady cup for beam inspection.
- **Chapter 4** - *Beam emission spectroscopy* - gives a detailed description of the collisional-radiative model for the beam-plasma interaction. It outlines the possibility of density profile reconstruction from the measured spectroscopic data and describes the reconstruction method used on COMPASS. It presents two installed independent observation systems - CCD camera and avalanche photo-diode detector - and their capabilities. It describes the features of the COMPASS visible spectrum around the observed Li line and its consequences for the design of used interference filters and finally, comparisons of the measured density profiles with other COMPASS diagnostics are provided.
- **Chapter 5** - *BES measurements in COMPASS plasmas* - is one of the two most important chapters of the thesis. Firstly, the measurement methods and the quality of the data are discussed. My own analyses of the Li-BES data are then presented - general evaluation of the edge and SOL density fluctuations, detailed analysis of the blob structures in the SOL, calculation of poloidal rotation velocity of the plasma and observations of the fast density profile changes in high confinement mode plasma.
- **Chapter 6** - *Atomic beam probe* - is the second pivotal chapter of the thesis. It presents in detail the development process of the new concept of atomic beam probe diagnostic using the lithium beam on COMPASS, which consisted mostly of my own independent work. Theoretical idea of the diagnostic supported by modelling is described, as well as detector design development, production of the final detector solution and first measurements in COMPASS H-mode plasma.
- **Chapter 7** - are the *Conclusions*
- **Appendices** - contain *References*, *List of Figures*, *List of Tables*, *List of Abbreviations* and *Attached Publications*. Three publications are attached: article [A1] describing the avalanche photo-diode system for Li-BES and its first measurements on COMPASS, article [A2] about development and first measurements with the atomic beam probe diagnostic and article [A3] describing the density reconstruction method from Li-BES data and presenting reconstructed profiles with 2 μs temporal resolution.

2. COMPASS tokamak

2.1 Brief history

The COMPASS tokamak (COMPact ASSembly) is a small to medium-sized device which was developed in the 1980s in the Culham Science Centre, United Kingdom. The first plasma breakdown was achieved in 1989 in a vacuum vessel with circular cross section. In 1992, the tokamak was upgraded with a D-shaped vacuum vessel and renamed as COMPASS-D. It was able to achieve high plasma confinement mode - the reference scenario of the ITER tokamak - and studied it extensively. In 1999, a spherical tokamak MAST was put into operation in Culham. Simultaneous operation of the two tokamaks proved to be unsustainable and COMPASS-D operation was terminated in 2001. The tokamak was offered to the Institute of Plasma Physics (IPP) of the Czech Academy of Sciences in Autumn 2004 and it decided to accept the offer in 2005. The process of reinstallation officially started in July, 2006 [1]. In December 2008, the first plasma discharge was achieved and 29th November 2012, the reinstalled COMPASS tokamak again reached H-mode operation [2].

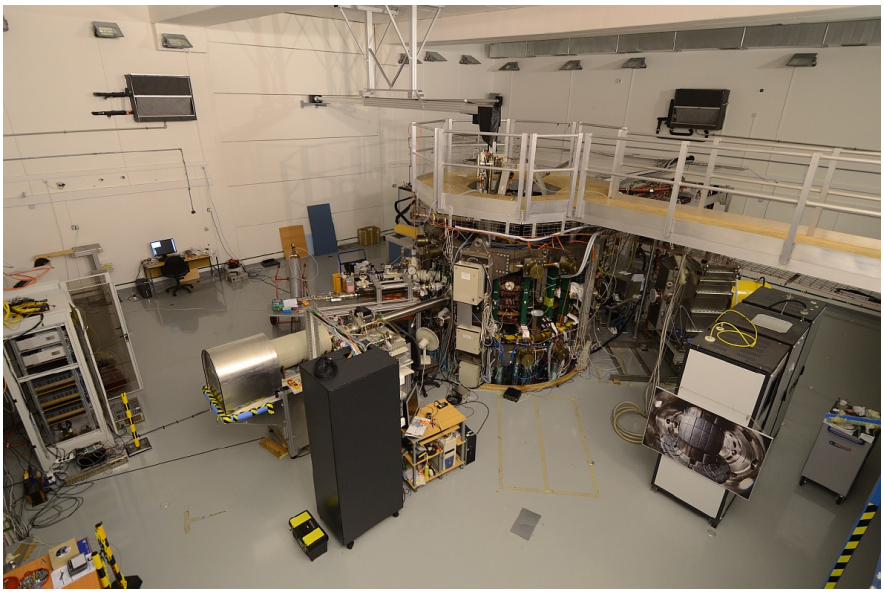

Figure 2.1: Photograph of the reinstalled COMPASS tokamak, surrounding diagnostics and auxiliary systems taken in 2015.

The rebuilt COMPASS tokamak replaced older CASTOR (Czech Academy of Sciences TORus) and allowed the IPP group to perform fusion research on a considerably higher level with focus on ITER–relevant physics and technology. The reinstallation process involved extensive development of new tokamak systems. Most importantly (1) power supply systems [3], (2) data acquisition system [4], (3) Fast feedback system for vertical plasma stabilization [5], (4) Neutral beam injection system (NBI) for additional plasma heating [6] and (4) new set of plasma diagnostics [7]. Figure 2.1 shows a photograph of the COMPASS tokamak in Prague taken in June 2015.

2.2 Parameters and research topics

COMPASS tokamak plasmas have ITER-like shape (with 1 : 10 ratio of sizes in the linear scale) which, together with the H-mode operation, make it a suitable device to study many plasma physics phenomena relevant to ITER, most notably in the edge plasma region. Presently, there are only two other European devices with ITER-like plasmas capable of achieving H-mode: the ASDEX Upgrade tokamak in Garching, Germany and the Joint European Torus (JET) in Culham, United Kingdom. In Figure 2.2a, the plasma shapes of these tokamaks are scaled for comparison together with ITER. Scale of GOLEM, former CASTOR tokamak operated by IPP Prague, is also added. Figure 2.2b shows a photograph of the COMPASS vacuum vessel.

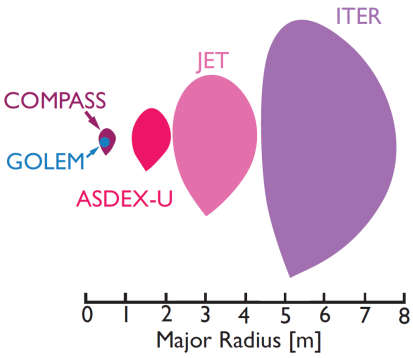

(a)

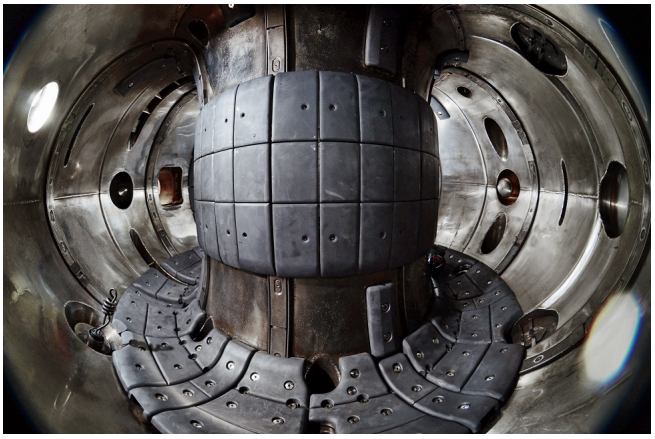

(b)

Figure 2.2: (a) Comparison of plasma shapes from European tokamaks with ITER-relevant cross-sections. Taken from [8]. (b) Inside photograph of the COMPASS vacuum vessel.

Main parameters of the COMPASS tokamak are summarized in Table 2.1. The major radius is 56 cm and minor radius $\sim$ 20 cm. The D-shaped vac-

Table 2.1: COMPASS tokamak parameters

Major radius R	56 cm
Minor radius a	$18 - 23$ cm
Max. plasma current I_p	350 kA
Toroidal magnetic field B_t	$0.9 - 2.1$ T
Pulse length	~ 0.5 s
Vacuum pressure	$1 \cdot 10^{-6}$ Pa
Elongation	≤ 1.8
Plasma shape	circular, elliptic, SND, SNT
NBI heating power P_{NBI}	$2 \cdot 400$ kW
Vessel material	Inconel 625
divertor material	graphite

uum vessel consists of 8 welded octants made of 3 mm thick Inconel 625 - a

non-magnetic, corrosion and oxidation resistant nickel-based alloy. There are 69 ports allowing a good diagnostic coverage of the plasma. 16 toroidal field coils with 4 windings each are used to create toroidal magnetic field with a low ripple. The maximum achievable toroidal magnetic field is 2.1 T on the magnetic axis, while for the standard operation, 1.15 T field is used. Maximum plasma current is ~ 350 kA and standard discharge duration is ~ 0.5 s with 300 ms long stable current flat-top phase. Maximal achieved plasma discharge duration was ~ 1 s. Ohmic plasma heating power is ≤ 500 kW, which is sufficient to reach H-mode phase. However, two neutral beam injectors (NBI) with 400 kW can be used for additional plasma heating allowing investigation of plasmas well above the L-H threshold. Tokamak coil systems are also capable of creating different plasma shapes (circular, elliptic or D-shaped with single-null divertor configuration) providing a good operational flexibility.

The main scientific research topics of the COMPASS tokamak team are:

1. H-mode physics - study of pedestal, L-H transition, edge localized mode and its suppression
2. Turbulent plasma transport in the edge and scrape-off layer (SOL) region
3. Plasma-wall interaction
4. Study of runaway electrons and plasma disruptions
5. Development of advanced diagnostic methods
6. Integrated modelling and code development

2.3 Overview of COMPASS diagnostics

To achieve its scientific goals, COMPASS is equipped with an extensive set of plasma diagnostics with high temporal and spatial resolution focused mainly on the edge and SOL plasma region. Most of the diagnostics were developed by the COMPASS team after tokamak reinstallation. Comprehensive review of COMPASS tokamak diagnostics was given by Weinzettl in [7, 9]. Overview picture of the diagnostic systems can be seen in Figure 2.3. In the following paragraphs, a brief introduction of the COMPASS diagnostics is provided. It has to be noted that the diagnostic categorization as provided below is ambiguous and individual diagnostic systems may belong to multiple categories.

2.3.1 Magnetic diagnostics

Magnetic diagnostics are the basic tokamak diagnostics. There are various magnetic field sources in tokamaks: plasma current, currents in the vacuum vessel generated by induced voltages and currents generated by the power supplies in the coil systems. These currents give birth to tokamak poloidal and toroidal magnetic fields. Measurement of these fields can provide information on plasma current density, total plasma current, loop voltage, plasma position, plasma

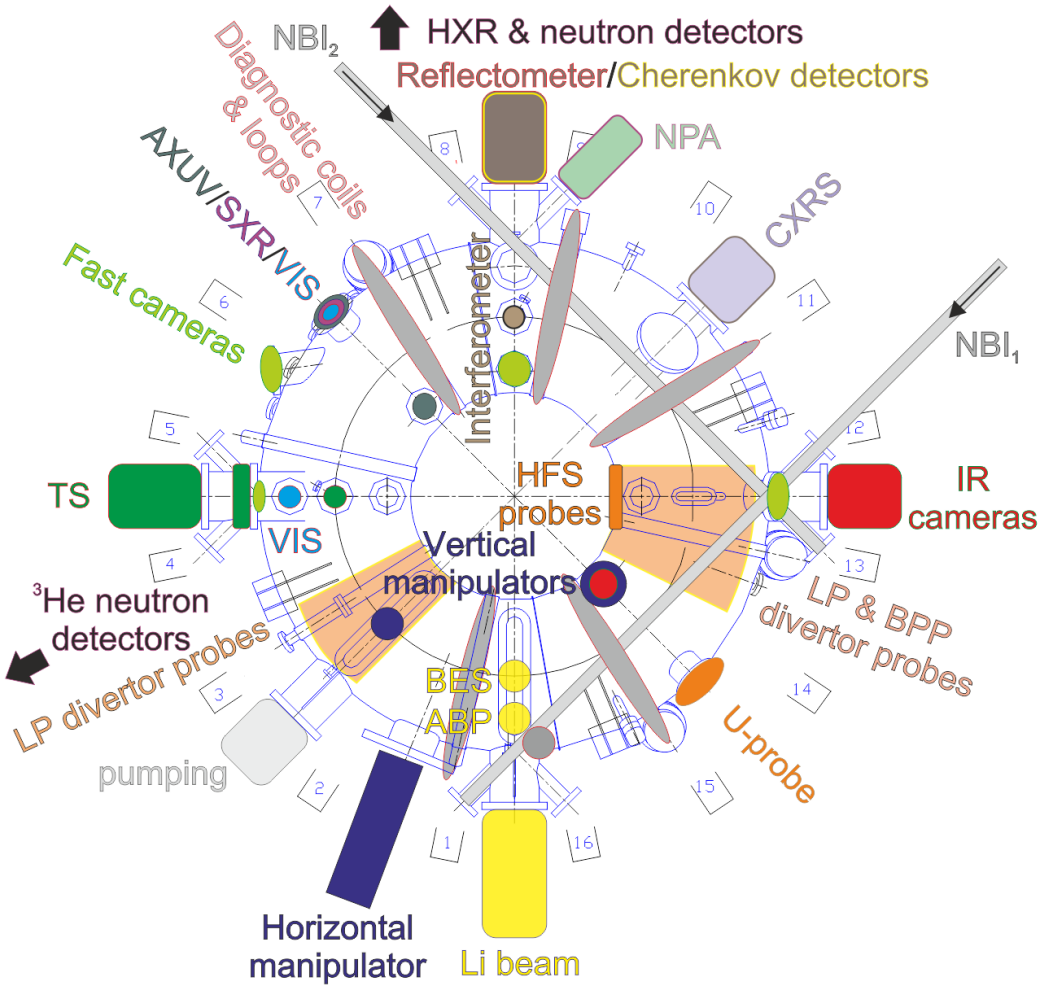

Figure 2.3: Overview of COMPASS diagnostics.

shape, plasma conductivity, total energy content and allows numerical reconstruction of magnetic surfaces geometry in the plasma. The COMPASS tokamak is equipped by more then 400 magnetic diagnostic coils covering the vacuum vessel in both the poloidal and toroidal directions [10].

2.3.2 Microwave diagnostics

Propagation of the microwave electromagnetic radiation through plasma can be used to determine physical properties of the plasma electrons. Tokamak is equipped with both active (interferometer, reflectometer) microwave diagnostics, transmitting a probing electromagnetic wave through the plasma, and passive (radiometer) diagnostics, detecting waves generated by the plasma itself. The principle of interferometer is to observe phase difference between a wave traveling through plasma and a reference wave. The phase shift of the waves is proportional to a line-averaged electron density along the optical path of the wave. Reflectometer [11] makes use of the fact that at a certain limit electron density, electromagnetic waves of a given frequency are reflected. By sweeping the frequency of the emitted waves and measuring the time delay of their reflection, it

is possible to reconstruct radial electron density profile. COMPASS radiometer [12] measures the radiation generated by gyration of the plasma electrons along the magnetic field lines. Frequency of the radiation is proportional to the local magnetic field strength and its power is proportional to electron temperature. Absolutely calibrated radiometric measurement can be used (with the knowledge of toroidal magnetic field) to reconstruct electron temperature profile.

2.3.3 Spectroscopic diagnostics

A large number of spectroscopic diagnostics on COMPASS measure the radiation coming from plasma, investigating infrared, visible, ultraviolet, soft X-ray and hard X-ray spectral regions. Again, active and passive spectroscopic diagnostics can be discerned. Thomson scattering [13] is an active spectroscopic method using a probing laser beam to measure the plasma electron properties. Scattering of laser radiation on plasma electrons leads to its spectral broadening due to the Doppler effect. Measurement of the spectral width of scattered laser light allows to determine local electron temperature, while the signal intensity is proportional to electron density.

There is a wide range of passive spectroscopic diagnostics. Two fast color cameras [14] provide a view of the vacuum vessel in visible spectrum, visualizing plasma wall interaction and accumulation of impurities. Fast infra-red camera [15] serves for observations of surface temperature of the in-vessel components and estimation of the incident heat flux. An integrated spectroscopic system with multi-channel view for visible, soft X-ray ($0.5 - 20$ keV) and bolometric (7 eV $- 6$ keV) measurements allows tomographic reconstruction of the plasma radiation in the respective spectral regions [7, 16]. Poloidal rotation of plasma can be determined by spectral measurement of the Doppler shift of carbon line CIII [17].

2.3.4 Beam-based and particle diagnostics

COMPASS tokamak has two neutral heating beams (using hydrogen/deuterium) and neutral diagnostic lithium beam [18] which is the subject of this thesis. Charge exchange recombination spectroscopy (CXRS), uses one of the heating beams to derive impurity ion temperature and toroidal plasma rotation profiles from spectral observation of the Doppler shift and Doppler broadening of impurity spectral lines (He, C, B). The neutral lithium beam is used by two diagnostic methods - beam emission spectroscopy for plasma density profile reconstructions, and atomic beam probe, detecting the beam ions to provide edge current density measurements. Neutral particle analyzer belongs into the category of particle diagnostics, detecting fast neutral atoms (H,D) leaving the plasma and using energy analyzer to gain their energy distribution.

2.3.5 Probe diagnostics

Probes employ a relatively simple diagnostic concept of inserting one or more electrodes directly into the plasma. Two most commonly used probes on COMPASS are the basic Langmuir probes and ball-pen probes [19]. From the current-voltage

characteristic, Langmuir probes can measure electron temperature, electron density, floating potential and electron energy distribution function. Ball-pen probes have a conical collector hidden in an insulating shielding tube, equalizing the electron and ion saturation currents. Its measured floating potential therefore equals directly the plasma potential. Combined measurement of Langmuir and ball-pen probes allow fast electron temperature measurements in the microsecond timescale [20]. To avoid destruction of the probes by strong heat fluxes of the plasma, they are either positioned well outside the confined plasma region or use a special manipulator to insert them into the plasma only for a very short period in the order of 100 ms. COMPASS tokamak is equipped with an extensive number of probes, installed either in the bottom divertor tokamak region [21, 22] or using vertical and horizontal fast reciprocating manipulator [23].

3. Diagnostic neutral lithium beam on COMPASS

During my doctoral study, I was the responsible person of the diagnostic group, which commissioned and started operating the lithium beam system on COMPASS in collaboration with the Wigner Institute, Budapest. This system has several unique technical features which distinguish it from other similar devices. Most notably, the detected photon flux by the avalanche photo-diode detector for beam emission spectroscopy (BES) (see Chapters 4, 5) is high as the detection optics system is located near to the plasma. Therefore, the signal to noise ratios are among the highest compared to other machines and allow unparalleled temporal resolution of the reconstructed density profiles of up to 2 μs. Secondly, for purposes of atomic beam probe (ABP) measurements (see Chapter 6), the beam is designed as a high energy (up to 120 keV) beam, although for standard beam emission spectroscopy purposes, it is operated on lower energies. Also, the possibility of reducing the beam diameter to few mm in order to improve the spatial resolution of both BES and ABP diagnostics was successfully demonstrated (in Section 6.7). COMPASS lithium beam system and its commissioning was described in the attached article [A1] and also in [7, 18, 24].

3.1 Introduction

With the rapid development of detector technologies and improvement of their spatial and temporal resolution, non-perturbative tokamak plasma diagnostics have become increasingly attractive. One of the widely used diagnostic methods is a neutral diagnostic beam injecting a low power (few hundred W) collimated beam of neutral light atoms into the plasma. Beam-plasma interaction is then studied by various detection means and local plasma parameters along the beam path can be determined.

The following plasma diagnostic methods are used by means of neutral diagnostic beams:

1. Beam emission spectroscopy
2. Charge exchange recombination spectroscopy
3. Zeeman splitting or Motional Stark effect (MSE) observations

BES is the primary diagnostic method of most of the operating fusion devices. It is based on spectroscopic measurement of the characteristic emission lines of the particular beam species. With detailed knowledge of the collisional-radiative processes of the plasma-beam interaction, it allows reconstruction of the plasma electron density (and in some cases temperature) profile.

CXRS is a diagnostic method (usually applied on heating beams) which determines the physical properties of impurity ions. Impurities such as carbon are usually present in tokamak plasmas and contribute to the complex plasma

physics processes. The impurity ions are visualized by the probing neutral beam via charge exchange reaction, when electron is transferred from the beam atom into an excited state of the impurity ion. This process is followed by a radiative de-excitation measured by the CXRS system. Spectroscopic analysis of the line intensity, Doppler shift and Doppler broadening can yield information about ion density and temperature profiles and also about the plasma rotation [25].

Zeeman splitting is the quantum physics phenomenon of spectral lines splitting in the presence of a magnetic field. Fine-tuned spectroscopic observations of a beam emission line can provide information about the strength and pitch of the magnetic field lines along the beam path and ultimately (separating the known toroidal field), the profile of poloidal magnetic field (= profile of plasma current density). MSE diagnostic method makes use of a similar phenomenon of spectral lines splitting in the presence of electric field. It is based on the fact that as the beam moves through the tokamak magnetic field, the beam atoms experience in its reference frame an electric field $\mathbf{E} = \mathbf{v} \times \mathbf{B}$. It is therefore an analogous method for the measurement of poloidal magnetic field profile [26].

Lithium is one of the most frequently used beam species as it features several major advantages: 1) the technology of Li ion extraction by thermionic emission from certain ceramic materials is long established, 2) the atomic physics of the interaction of Li with plasma particles is a well documented field and 3) Li is not standardly present in the plasma and therefore it is generally easier to distinguish between the measured beam-plasma interaction and plasma background. Lithium beam systems are used most notably on tokamaks ASDEX-U [27], JET [28], DIII-D [29], JT-60U [30], KSTAR [31] and EAST [32].

Lithium beam system on COMPASS was built primarily for the BES diagnostic purpose. Its main goal is detailed measurement of the electron density profile and its fluctuations in the plasma edge region. Secondary purpose of the beam system is the investigation and development of a new diagnostic method - atomic beam probe. This proposed method relies on detection of the ionized fraction of the beam. The trajectory of the beam ions is determined by the local magnetic field and ion detection can theoretically yield information about fast perturbations of the poloidal magnetic field (= plasma current density) in the plasma edge.

3.2 COMPASS Li-beam overview

Overview picture of the lithium beam system installed on COMPASS can be seen in Figure 3.1. In the vacuum system of the beam, lithium ions Li^+ are extracted from the ion source ("emitter") by thermionic emission. A set of carefully designed electrodes ("ion optics") is used to focus the ion beam and accelerate it towards the tokamak vessel entrance port. The ion beam then passes between 2 pairs of deflection plates, horizontal and vertical. By applying voltage on the plates, they can be used to correct spatial alignment of the beam and also for beam sweeping/chopping measurement technique (described in detail in Section 5.2). Next, the ion beam passes through the neutralization chamber, where a heated container produces sodium vapor. Lithium ions are partially neutralized by charge exchange reaction with sodium atoms without any significant energy

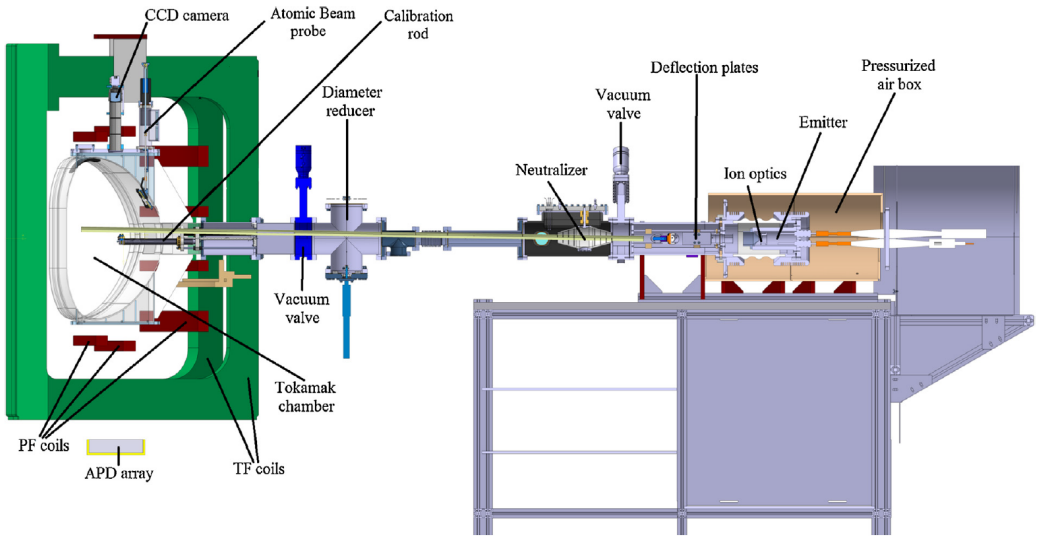

Figure 3.1: Scaled model of diagnostic lithium beam system on the COMPASS tokamak with description of its main parts as well as BES and ABP detection systems. Taken from [18].

and momentum loss. Neutralization is crucial for the beam in order to reach the vacuum vessel through the strong tokamak magnetic field. Remaining Li^+ ions are deflected by the magnetic field, while the neutral part of the beam continues and is injected radially into the plasma. Before the beam entrance to the tokamak vessel, a special set of diaphragms can be used to limit the beam diameter (see Section 6.4).

In plasma, lithium atoms are excited and ionized by collisions with plasma electrons and ions. The excited states decay by the emission of a photon of characteristic wavelength. The most intense is the 2p-2s transition ($\lambda_{Li} = 670.8$ nm). Radial profile of the lithium emission is then observed by 2 independent BES detection systems - an array of avalanche photo-diodes and a CCD camera. The correct part of the detected spectrum around the λ_{Li} line is chosen by an appropriate interference filter placed in the optical path of BES systems. The ionized part of the beam ions is deflected by the tokamak magnetic fields and follows a curved trajectory. For carefully calculated beam energy, beam ions generated in the edge plasma region can reach the current-sensitive atomic beam probe detector.

3.3 Li-beam system components

Emitter and ion optics

The source of lithium ions is a solid-state emitter made of β-eucryptite ($Li_2O + Al_2O_3 + 2SiO_2$), which is manufactured in the Wigner institute. The emitter design is an upgrade of alkali emitters made by Heatwave company, and is tailored for more reliable operation in lithium diagnostic beams. The emitter works on a principle of thermionic emission from a heated anode. The ceramic material of the emitter is filled into a porous molybdenum cup and heated by a SiC heater

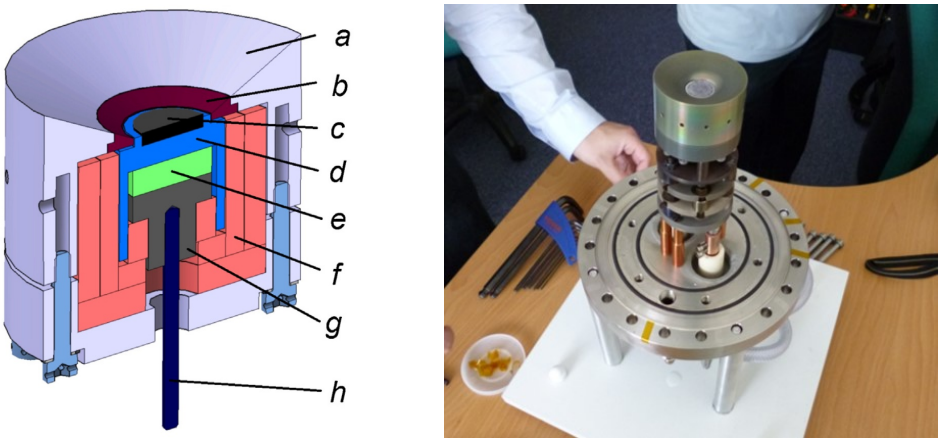

Figure 3.2: (left) Schematic picture of emitter with described parts: (a) Pierce electrode, (b) Nb filling, (c) ion source, (d) Mo house, (e) SiC disc heater, (f) Al heat shields, (g) CFC current conductor, (h) W current conductor. Taken from [18]. (right) Photo of emitter structure mounted on a vacuum flange.

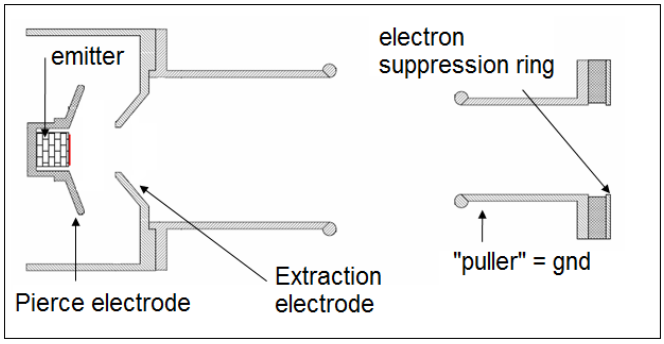

Figure 3.3: Schematic picture of the ion optics, consisting of Pierce electrode, extraction electrode, puller and the electron suppression ring.

disc. The emitter and its heater along with aluminum heat shields are embedded in a compact structure with a Pierce electrode [18] (see Figure 3.2). The mechanism of the ion conduction is electrolysis in the emitter material. The emitter is constantly heated using $\sim 60 - 70$ A of alternating current and reaches surface temperatures of $\sim 1300°$ C. At this temperature, the lithium ions can diffuse with relatively high velocity inside the ceramic. However, the heated emitter does not emit ions on its own, only if an extraction electric field is applied at the same time. Because the emitter is not a perfect conductor, the electric field can enter into the ion source. As soon as the Li-ion emission starts, negative charges stay behind inside the emitter and it is assumed that they are carried by O^{2-} ions [33].

The ion optics consists of a set of four electrodes (see schematic Figure 3.3). Their goal is to create an electric field which extracts the lithium ions from the source and focuses them into a collimated beam. There are two high voltage power supplies: 120 kV/10 mA and 120 kV/0.25 mA. The first one is connected

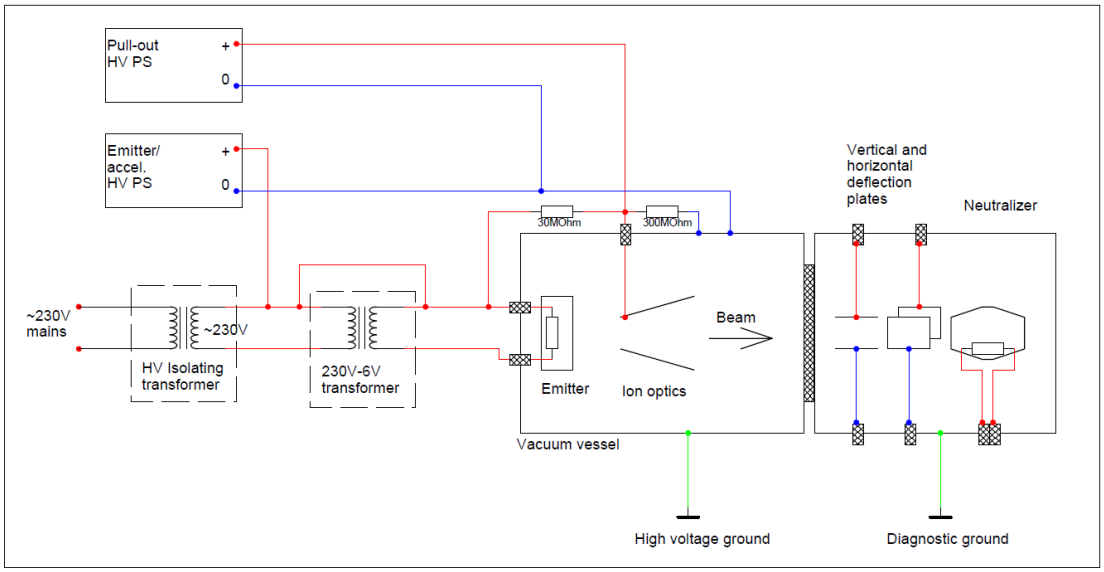

Figure 3.4: Electrical scheme of the lithium beam system.

to an isolation transformer and then to a second transformer which produces the necessary current for emitter heating (see Figure 3.4). The heating current is controlled by a thyristor unit. This line is connected to the emitter and the Pierce electrode. The second power supply unit is connected directly to the extraction electrode [18]. Voltage applied to the Pierce electrode defines the beam energy. Somewhat smaller voltage is applied to the extraction electrode. Voltage difference between the two electrodes create the necessary extraction electric field to pull out Li^+ ions, while their ratio define the beam focus. For example, the presently used values for a well focused 60 keV lithium beam (~ 2 cm diameter in the tokamak vessel) are 60/51 kV. The third component of the ion optic is the "puller" electrode, which is connected to the high voltage ground. Last component is the "electron suppression ring", which is negatively biased to -500 V. Its role is to prevent acceleration of electrons towards the emitter.

The current extracted from emitter depends on the extraction voltage. The theoretical dependence is given by Child-Langmuir law as:

$$I = \frac{4\epsilon_0}{9} S \sqrt{\frac{2q}{m}} \frac{U^{3/2}}{d^2} \propto U^{3/2} \tag{3.1}$$

where ϵ_0 is the vacuum permittivity, S is the emitter surface, q is the elementary charge, m is the Li^+ mass, U is the extraction voltage and d is the distance between the electrodes. Current–voltage characteristics of the emitter for different emitter heating are plotted in Figure 3.5. A temperature dependent saturation of the emission current, typically observed also on other devices, can be seen. To prevent emitter damage, it is necessary to keep the heating current below 70 A and therefore the achievable extracted currents for different beam energies are in the range of $\sim 1 - 4$ mA.

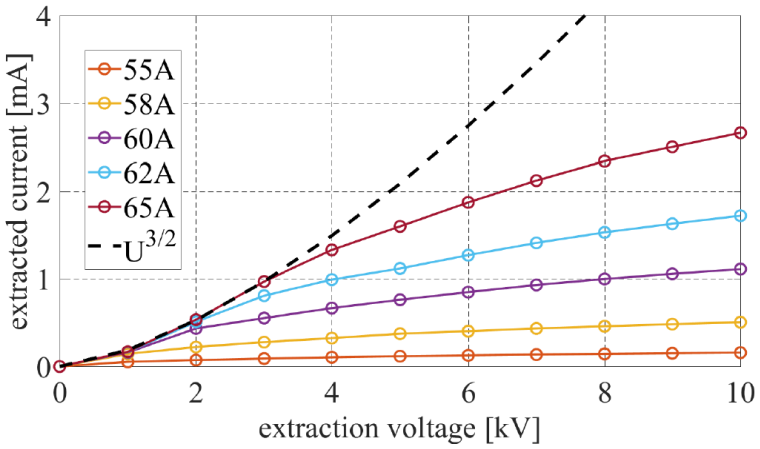

Figure 3.5: Dependence of the extracted ion current from the emitter on the extraction voltage. Curves for different level of emitter heating are shown along with the theoretical prediction by Child-Langmuir law.

Neutralizer

The function of neutralizer is to create a localized region of target atoms A^0 with which the beam ions undergo charge exchange (CX) collisions ($Li^- + A^0 \rightarrow Li^0 + A^-$) neutralizing a significant fraction of the beam. At first approximation, the ratio R of neutralized beam atoms after passing through the neutralizer is given as:

$$R = 1 - e^{(-n\,l\,\sigma_{cx})} \tag{3.2}$$

where l is the path length in the neutralizer, n is the density of target atoms and σ_{cx} is the cross section for charge exchange collisions between the beam ions and the target medium. In reality, this equation is further modified by a minor effect of beam re-ionization. σ_{cx} is the largest for resonant or near-resonant charge-exchange, therefore lithium beam prefers use of another alkali metal as the target medium [34]. Lithium and sodium are both good candidates in terms of their low vapor pressure at room temperature and their relatively easy handling. In the work by McCormick [34], optimal vapor pressures for CX in the neutralizer were estimated for Li and Na target gas along with the necessary operating temperature of the alkali metal container. They were found to be: $P_{Li} = 1.07 \cdot 10^{-2}$ Torr at $T = 790$ K and $P_{Na} = 9 \cdot 10^{-3}$ Torr at $T = 562$ K. This indicates the clear disadvantage of operation with Li in the neutralizer cell, as significantly higher temperature has to be reached, increasing the risks of mechanical failure. From this reason, COMPASS neutralizer chamber employs sodium as the target gas, as is also common on other devices. In Figure 3.6a, one can see the equilibrium vapor pressure for Li and Na plotted against the heating temperature of the reservoir and Figure 3.6b shows the neutralization efficiency of $20-70$ keV lithium beam in the sodium neutralizer cell experimentally determined by [35]. The expected neutralization efficiency values for this range of beam energies are $68\%-95\%$ with a decreasing tendency towards higher beam energies. COMPASS lithium beam uses a newly designed recirculating neutralizer, which allows better handling of sodium used for charge exchange reaction with the

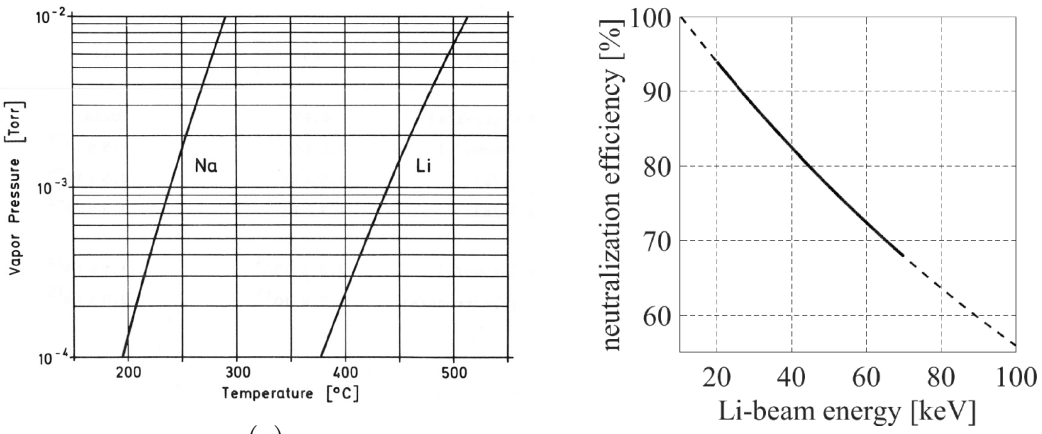

(a) (b)

Figure 3.6: Dependence of the equilibrium pressure of Li and Na on temperature of the reservoir. Taken from [34]. (b) Neutralization efficiency of the lithium beam in sodium neutralizer against beam energy.

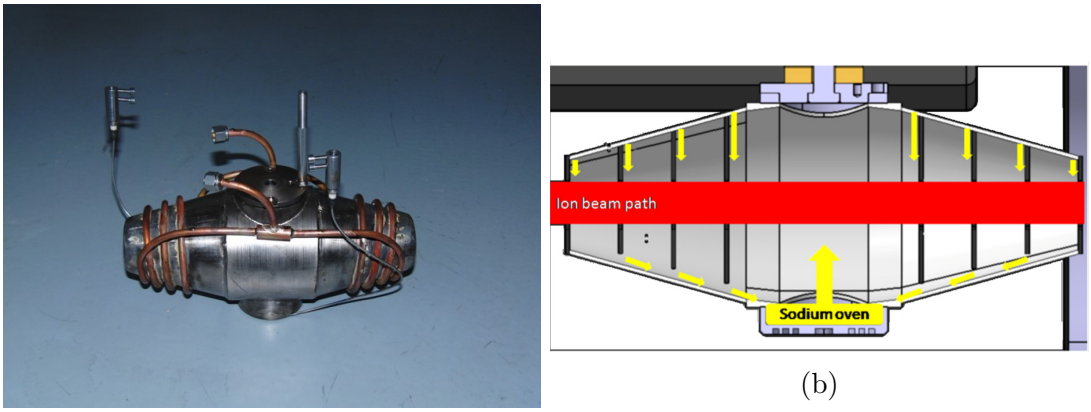

(a) (b)

Figure 3.7: (a) Photo of the COMPASS neutralizer chamber. (b) Schematic view of the neutralizer chamber with depicted beam path and sodium flow. Taken from [18].

beam ions. Usual solution on other lithium beam devices is to keep sodium inside a reservoir closed by a plug which is removed for a short period during the plasma discharge to let the sodium vapor into the beamline. This way, the sodium reservoir has to be refilled on a frequent basis and the surrounding vacuum components suffer from sodium deposition. The new COMPASS design uses double-cone shaped neutralizer chamber with 2.5 cm circular holes for the passing beam at both sides (see Figure 3.7). On its bottom, there is an open sodium container heated to 300° C during the measurement. The edges of the neutralizer are actively cooled by tubes with flowing air to a preset temperature of usually 120° C. This way, the sodium vapors condense on the cooler edge parts of the neutralizer and sodium flows back to the heated pool. The loss of sodium at both ends is minimized.

Faraday cup

At the end of the COMPASS lithium beam flight tube, near the entrance to the tokamak vessel, a Faraday cup (FC) is installed. It can be moved to the beamline in order to measure important beam properties. Faraday cup is basically a metal conductive cup designed to catch charged particles in vacuum and measure the incident current. In our system, Faraday cup is designed as a cubic stainless steel case ("FC house") with a front circular hole for the impacting beam. Inside FC house is an isolated titanium plate which is hit by the entering beam and the incident current on the plate is measured. FC house is biased either positively or negatively to ±500 V in order to either suppress or pull out secondary electrons generated by the impacting beam particles (see the experimental scheme in Figure 3.8.

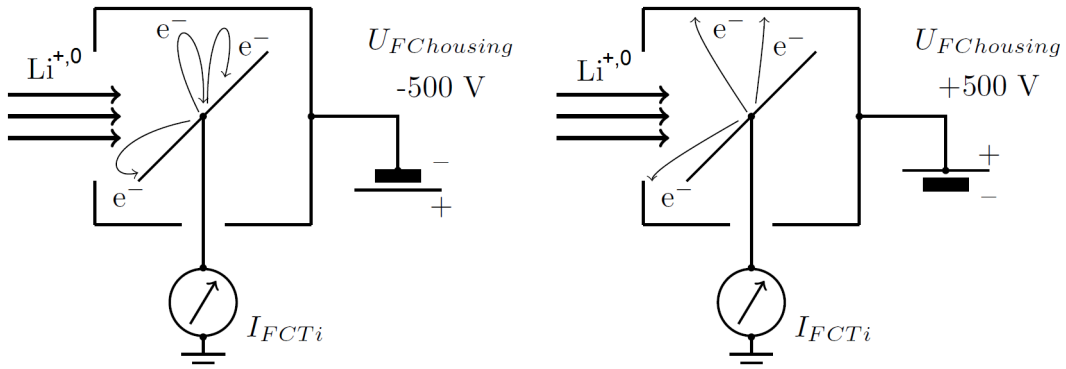

(a) (b)

Figure 3.8: Schematic view of the Faraday cup measurement. (a) FC house is biased to −500 V - electron suppression mode, (b) FC house is biased to +500 V - electron pull-out mode. Taken from [8].

FC can be used to determine 1) the fraction of the extracted beam current (measured by the main HV power supply) which enters the tokamak, 2) beam neutralization efficiency and 3) vertical and horizontal beam profile (in combination with the deflection plates). In the electron suppression mode, FC directly measures the current I_{Li^+} of the ion part of the beam. In the electron pull-out mode, it measures the sum of Li-ion current and secondary electron current induced by the impact of beam particles:

$$I_{-500} = I_{Li^+} \tag{3.3}$$

$$I_{+500} = I_{Li^+} + (I_{Li^+} + I_{Li^0}) \cdot \eta_e \tag{3.4}$$

where I_{-500} is the current measured by FC in the suppression mode, I_{+500} is the current measured in the pull-out mode, I_{Li^0} is the equivalent current of the neutral beam part and η_e is the electron yield per Li particle impact (same yield is assumed for Li^+ and Li^0). The electron yield can be estimated when measuring without beam neutralization simply as:

$$\eta_e = \frac{I_{+500}}{I_{-500}} - 1 \quad ; \quad I_{Li^0} = 0 \tag{3.5}$$

Observed electron yield for standardly used 60 keV beam is ~ 5. With this knowledge it is immediately possible to calculate the equivalent current of the neutral beam part and thus the neutralization efficiency η_n:

$$I_{Li^0} = \frac{I_{+500} - I_{-500}}{\eta_e} - I_{-500} \tag{3.6}$$

$$\eta_n = \frac{I_{Li^0}}{I_{Li^0} + I_{-500}} \tag{3.7}$$

As was already stated above, while sweeping voltage on the deflection plates (horizontal and vertical), it is possible to measure 2D beam profile by the Faraday cup. Example of a horizontal beam profile measurement is shown in Figure 3.9. The second image shows the beam profile in spatial coordinates, recalculated from the deflection geometry.

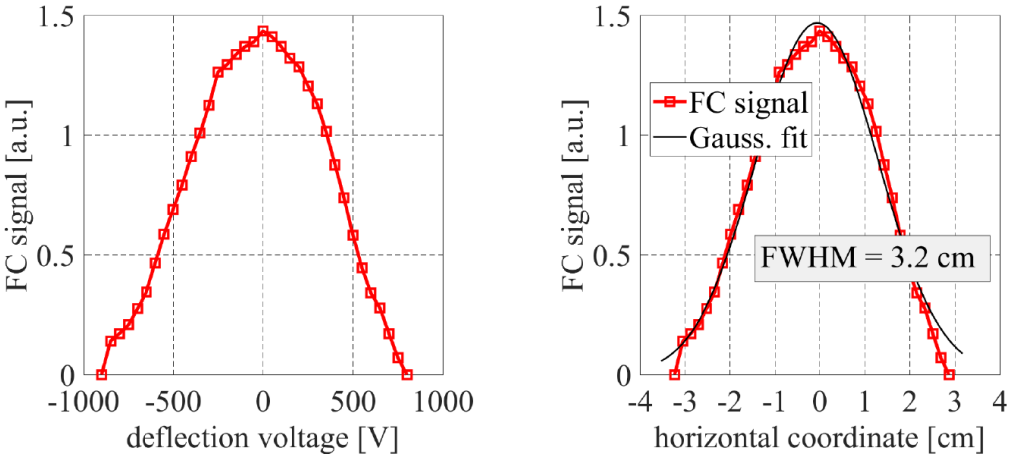

(a) (b)

Figure 3.9: (a) Beam profile measured in the Faraday cup by sweeping of the horizontal deflection plates. (b) Recalculated beam profile to the spatial coordinates. Gaussian fit allows to specify the beam diameter as the full width at half maximum (FWHM = 3.2 cm).

3.4 Vacuum handling

Lithium beam system on COMPASS is a vacuum chamber connected to the tokamak vessel. It employs one rotary pump for forevacuum pumping (with limit pressure 10^{-2} Pa) and three turbomolecular pumps keeping a high vacuum level of $\sim 10^{-6}$ Pa. The schematic drawing of vacuum components can be found in Figure 3.10. There are basically two beam areas separated by a gate valve - the emitter part and the neutralizer part. The reason for the separation is protection of the emitter from sodium contamination. During standby beam operation between the tokamak discharges, both the emitter and neutralizer parts (as well as the tokamak vessel) are kept vacuum-separated. In a time window starting ~ 2 minutes before a plasma discharge, the sodium reservoir inside the neutralizer is

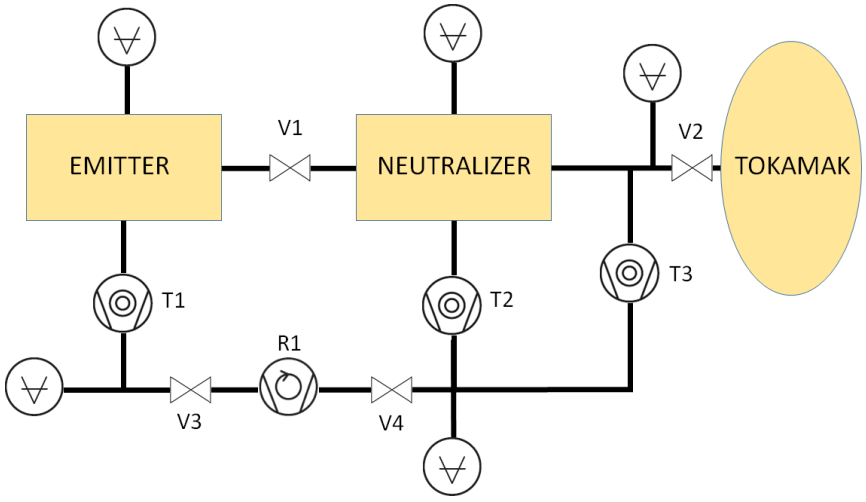

Figure 3.10: Schematic view of the vacuum system with described vacuum elements: turbopumps T1-T3, rotary pump R1, valves V1-4 and vacuum gauges.

heated from a standby value of 180° C, featuring relatively low level of sodium pressure, to 300° C. At that temperature, the sodium pressure reaches $\sim 10^{-1}$ Pa inside the neutralizer and the pressure in the vacuum chamber surrounding the neutralizer rises to $\sim 10^{-3}$ Pa. Both valves separating the neutralizer part from emitter and tokamak are opened for the beam injection only in a short time period of -1 to $+3$ s with respect to the start of plasma discharge. Vacuum handling, emitter and neutralizer heating and switching of the high voltage power supplies during the plasma discharges was fully automated and ensures safe and reliable beam operation.

4. Beam emission spectroscopy

This chapter describes in detail the diagnostic method of beam emission spectroscopy and its application on COMPASS using the lithium beam system. As the responsible person of the lithium beam group on COMPASS, I participated on the diagnostic development and commissioning work in collaboration with the Wigner Institute, Budapest. Part of the described work is in the attached articles [A1, A3] and also in [18, 36].

4.1 Introduction

Beam emission spectroscopy is an active spectroscopic method used to diagnose tokamak plasmas. It is based on neutral beam injection and measurement of line radiation coming from the transitions between atomic levels of the beam species. Neutral beams commonly used on tokamak and stellarator devices around the world vary in terms of beam species, energy and power. Beam emission spectroscopy is done on

1. high-power (hundreds of kW to MW) heating neutral beams (H or D) with energies $50 - 100$ keV [31, 37, 38, 39],

2. low-power (hundreds of W) accelerated diagnostic beams (He, Li, or higher alkali metals) with energies $20 - 100$ keV [27, 28, 30, 31, 32, 40]

3. diagnostic thermal beams (He) [41].

The advantage of BES on heating beams is their greater penetration depth while the disadvantage is reduced spatial resolution due to greater beam diameters and the necessity of carefully designed optical path with angled lines of sight in order to distinguish the Doppler shifted beam emission from a strong background plasma radiation. On the other hand, diagnostic beams have the advantage of well localized position (smaller diameters in the order of $\sim$ cm) and they usually employ beam species not naturally present in the plasma. This makes the separation of plasma background radiation easier. Collisional cross sections of alkali beam atoms with plasma particles are also only weakly dependent on the plasma temperature, therefore reconstruction of density profile is easier. The downside of diagnostic neutral beams is their limited penetration depth in the plasma, reducing the BES applicability only to the edge plasma region. Second downside is the necessity to build a very complex beam system only for a standalone diagnostic purpose. On COMPASS, we built and commissioned accelerated neutral lithium beam with achievable energy range of ≤ 120 keV and standard diameter ≤ 2.5 cm (depending on the beam focus). Let's now explain in greater detail the BES diagnostic on the example of COMPASS system.

On COMPASS, lithium beam is injected radially into the plasma. Injected lithium atoms are excited and ionized due to collisions with protons (deuterons) and electrons (and marginally with neutrals and impurities) in the tokamak plasma. The ionized part of beam atoms is deflected by the magnetic field and removed from the beam and therefore the beam is attenuated along its path and

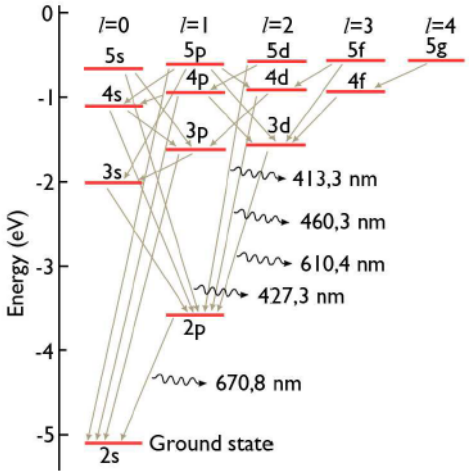

Figure 4.1: Grotrian diagram of Li I emission lines between energy levels with principal quantum number $n \leq 5$. Taken from [8].

has a certain penetration depth depending on the plasma parameters. BES detection systems measure the radial profile of intensity of the most bright Li I line of 670.8 nm corresponding to the atomic transition from the first excited level to the basic level $1s^2 2p - 1s^2 2s$. The beam is mono-energetic and it is not in thermal equilibrium with the plasma. The interaction of Li atoms with the plasma can be described by the collisional-radiative model [8, 42] (more in Section 4.2), where the relative occupation of the excited electron states (see Figure 4.1) and the ionization rate is calculated using known tabulated values [43, 44, 45, 46, 47] of the cross sections and transition probabilities for all considered reactions. These cross sections depend on the plasma density and temperature. However, in the case of lithium atoms, the temperature dependence is weak. On COMPASS, the numerical reconstruction of plasma density from the occupation of 2p excitation level is done according to a technique described by Schweinzer [48] and implemented by Krbec [A3], [8]. I will cover the method in Section 4.3.

There are two independent optical detection systems for observation of the lithium emission on COMPASS. The slow branch of the observation is the CCD camera (see Section 4.4) with focusing optics and the fast branch comprises of an array of 18 avalanche photo-diode (APD) detectors also with its own optical system (see Section 4.5). The central line-of-sight of both branches is kept perpendicular to the beam path to minimize the Doppler shift of detected photons. This is important for designing of a proper interference filter to measure the lithium line. As a result of the optical design, interference filters at 670.8 nm central wavelength and 1 nm FWHM are used (more in Section 4.6) [18].

4.2 Collisional radiative model

Before describing the atomic physics of the beam-plasma interaction, let us define some basic terms. Cross section σ is a physical quantity which describes the likelihood of a collision of two (or more) particles. It can be conceived as an

effective area of the colliding particles, its units are in m^2 and it is generally dependent on the relative velocity of the particles. Rate coefficient of a particle traveling through a target with particle density n is defined as the number of collisions per unit time per unit density. For a lithium beam atom, the rate coefficient at which it undergoes collisions with certain plasma particles is:

$$\langle \sigma v \rangle = \int \sigma(|\mathbf{v_b} - \mathbf{v}|) \cdot |\mathbf{v_b} - \mathbf{v}| f(\mathbf{v}) d\mathbf{v} \tag{4.1}$$

where σ is the cross section of the particular collision, $\mathbf{v_b}$ is the beam velocity and $f(\mathbf{v})$ is the probability density function of plasma particles.

The intensity of emitted light for individual electron transition channels of the lithium atom depends on electron populations on corresponding energetic levels. A change of electron population density of the state i can be described by the following equation [42]:

$$\begin{aligned} \frac{\partial}{\partial t} N_i = & \sum_{j,j\neq i} \langle \sigma_{e,ji} v \rangle n_e N_j - \sum_{j,j\neq i} \langle \sigma_{e,ij} v \rangle n_e N_i + \sum_{j,j\neq i} \langle \sigma_{p,ji} v \rangle n_{ion} N_j \\ & - \sum_{j,j\neq i} \langle \sigma_{p,ij} v \rangle n_{ion} N_i + \sum_{j,j>i} A_{ji} N_j - \sum_{j,j<i} A_{ij} N_i \\ & - \langle \sigma_{e\rightarrow ion,i} v \rangle n_e N_i - \langle \sigma_{p\rightarrow ion,i} v \rangle n_{ion} N_i - \langle \sigma_{cx,i} v \rangle n_{ion} N_i \end{aligned} \tag{4.2}$$

where n_e, n_{ion} are the densities of electrons and ions, N_i, N_j are the electron population densities of states i and j, $\langle \sigma_{e,ij} v \rangle$, $\langle \sigma_{p,ij} v \rangle$ are the rate coefficients for electron, resp. ion impact excitation from state i to j, A_{ij} is the transition probability (Einstein coefficient) of spontaneous emission from state i to j, $\langle \sigma_{e\rightarrow ion,i} v \rangle$, $\langle \sigma_{p\rightarrow ion,i} v \rangle$ are the rate coefficients for electron, resp. ion impact ionization and $\langle \sigma_{cx,i} v \rangle$ is the rate coefficient for charge exchange. As the beam is injected radially into the plasma and the contribution of individual terms in the Equation 4.2 depend on the profiles of plasma electron and ion density and temperature along the beam path, it is more appropriate to rewrite the equation for the spatial derivative (using beam path coordinate z) of the electron population density of the state i as:

$$\frac{\partial}{\partial t} N_i = \frac{\partial}{\partial z} \frac{\partial z}{\partial t} N_i = v_b \frac{\partial}{\partial z} N_i \tag{4.3}$$

where v_b is the beam velocity. To solve the outlined system of equations, it is necessary to limit the number of considered lithium atomic levels. Schweinzer [48] found that the electron population of Li energetic states with principal quantum number $n \geq 4$ is small and can be neglected.

Cross sections of the collisional processes in Equation 4.2 can be found in [43, 44, 45] and the Einstein coefficients of spontaneous lithium de-excitation are given in [47]. In Figure 4.2, one can see the tabulated cross sections for Li excitation and ionization by electron and proton impact for the relevant Li energetic levels.

For $40 - 60$ keV lithium beam standardly injected for BES purposes on COMPASS, beam atoms are much faster than the plasma ions and, apart from the very cold plasma near the walls, also much slower than the plasma electrons. To quantify: lithium velocity for the given beam energies $v_b(40 - 60 \text{ keV}) =$

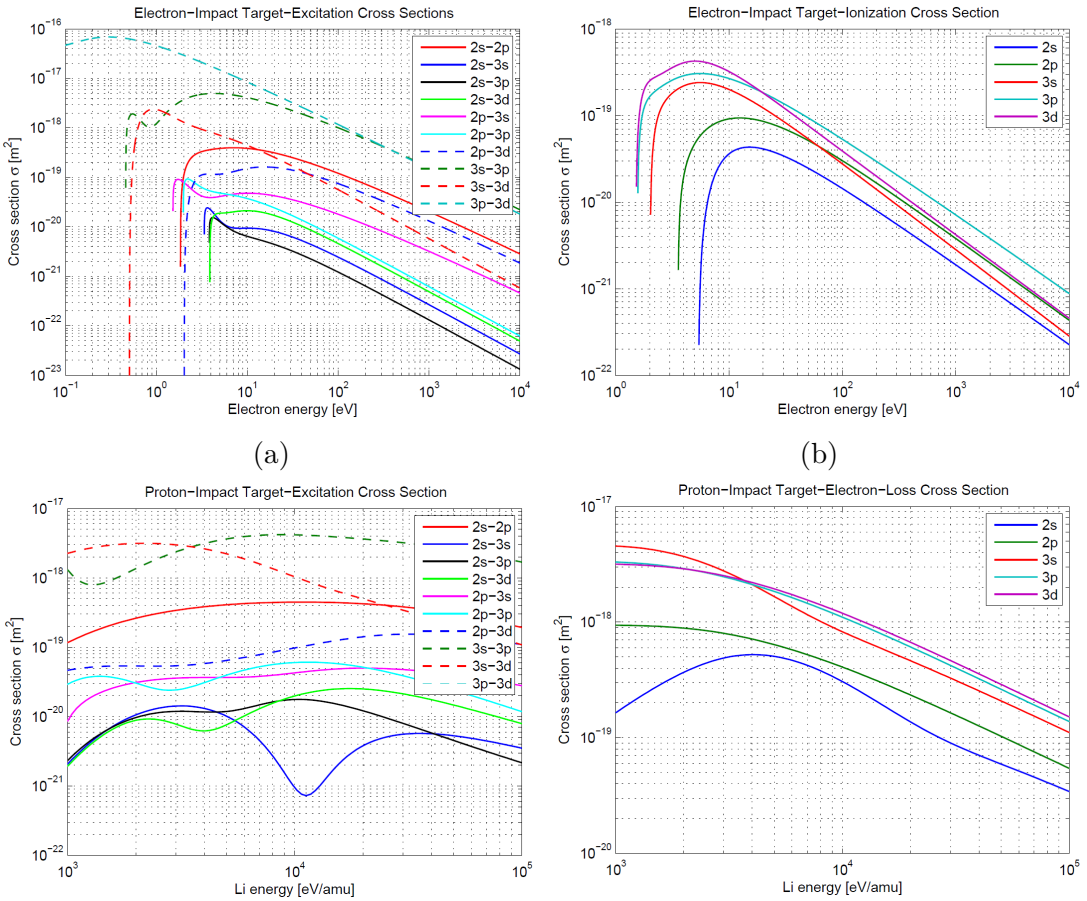

Figure 4.2: Cross section for (a) Li excitation by electron impact, (b) Li ionization by electron impact, (c) Li excitation by proton impact and (d) Li electron loss by proton impact (combining collisional ionization and charge exchange) given for the relevant energetic levels of lithium. Taken from [8].

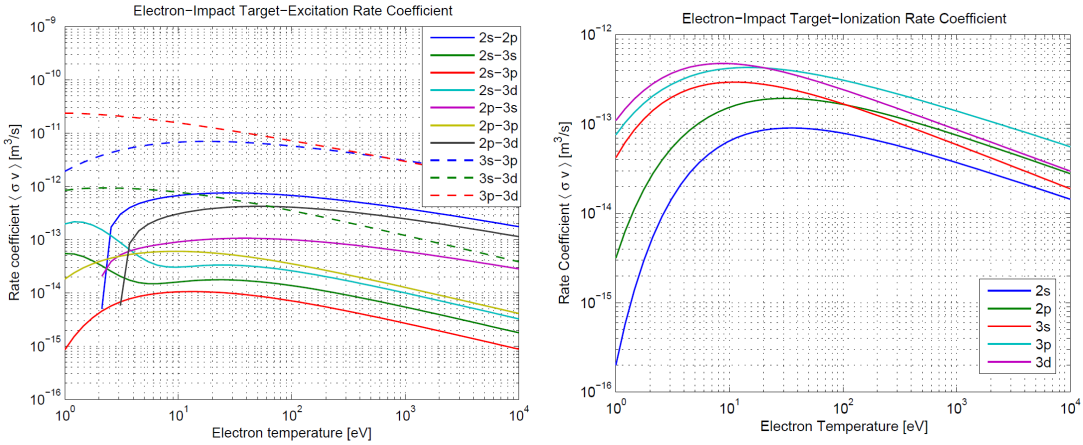

(a) (b)

Figure 4.3: Reaction rates for lithium excitation and ionization by electron impact calculated from Equation 4.4. Taken from [8].

$1.05 - 1.29 \cdot 10^6$ m/s, thermal ion velocity in the edge plasma region of COMPASS is approx. $v_i(T_i < 150 \text{ eV}) < 1.7 \cdot 10^5$ m/s and thermal electron velocity is approx. $v_e(50 - 300 \text{ eV}) = 4.2 - 10.3 \cdot 10^6$ m/s. From this reason, the relations for relative velocities in the rate coefficient calculations for collisions with protons and electrons are usually simplified as [A3]:

$$\langle \sigma_p(v)v \rangle \approx \sigma_p(v_b)v_b \quad ; \quad \langle \sigma_e(v)v \rangle \approx \int \sigma_e(\mathbf{v_e})\mathbf{v_e} f(\mathbf{v_e}) d\mathbf{v_e} \tag{4.4}$$

where $f(\mathbf{v_e})$ is the Maxwellian electron velocity distribution:

$$f(\mathbf{v_e}) = \left(\frac{m_e}{2\pi k_B T_e} \right)^{3/2} \exp\left(- \frac{m_e \mathbf{v_e}^2}{2 k_B T_e} \right) \tag{4.5}$$

where m_e is the electron mass, k_B is the Boltzmann constant and T_e is the electron temperature. Rate coefficients for the lithium collisions with electrons calculated from the tabulated cross sections using the Equations 4.4 and 4.5 are given in Figure 4.3. With use of Equations 4.2, 4.3 and 4.4, the final set of ordinary differential equations used in the plasma density reconstruction process is:

$$\begin{aligned} \frac{\partial}{\partial z} N_i = & \sum_{j,j\neq i} \frac{\langle \sigma_{e,ji} v \rangle}{v_b} n_e N_j - \sum_{j,j\neq i} \frac{\langle \sigma_{e,ij} v \rangle}{v_b} n_e N_i + \sum_{j,j\neq i} \sigma_{p,ji} n_p N_j \\ & - \sum_{j,j\neq i} \sigma_{p,ij} n_p N_i + \sum_{j,j>i} \frac{A_{ji}}{v_b} N_j - \sum_{j,j<i} \frac{A_{ij}}{v_b} N_i \\ & - \frac{\langle \sigma_{e\rightarrow ion,i} v \rangle}{v_b} n_e N_i - \sigma_{pEL,i} n_p N_i \end{aligned} \tag{4.6}$$

where $\sigma_{pEL,i}$ denotes the tabulated cross sections for proton impact electron loss. Number of equations is limited to 5 for Li 2s, 2p, 3s, 3p and 3d levels and only collisions with plasma electrons and protons are taken into account. Reaction rates of collisional de-excitation processes, which are not included in the atomic data tables, are determined from the principle of detailed balance.

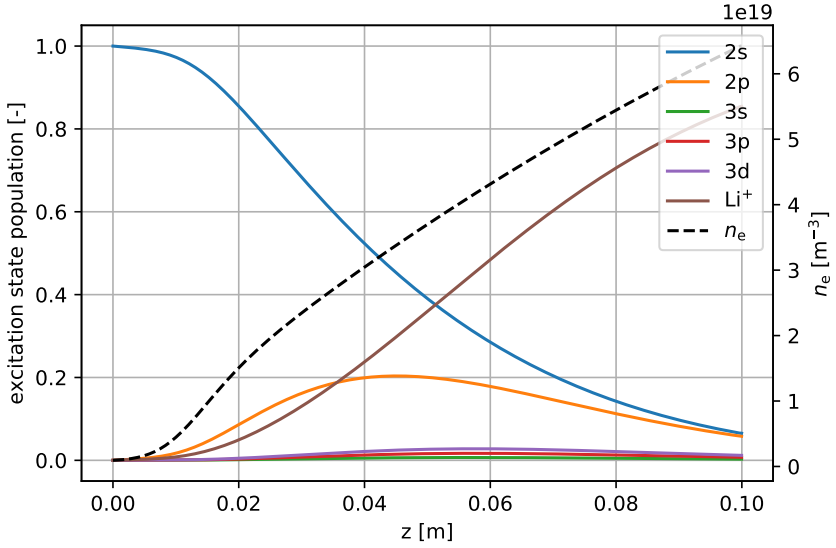

Figure 4.4: Simulated electron populations of the energetic states of 60 keV Li beam atoms along its path for prescribed electron density and temperature profiles (using Equation 4.6, resp. 4.7). The ionized part of the beam is also shown. Temperature profile (not shown) was parabolic with 800 eV central temperature.

4.3 Reconstruction of electron density profile

Density reconstruction method used on the COMPASS tokamak [A3], [8] is based on the algorithm first proposed and used by Schweinzer [48] on the TEXTOR tokamak. The advantage of the method is that it can provide absolutely calibrated density profiles from relative measurements of the beam light intensity. To introduce the method, let's first rewrite the initial set of 5 differential equations for the electron populations (Equation 4.6) of Li atoms in a simple form:

$$\frac{dN_i(z)}{dz} = \sum_j \Big(n_e(z) a_{ij}[T_e(z)] + b_{ij}\Big) N_j(z) \tag{4.7}$$

$$N_i(z=0) = \delta_{ij} \tag{4.8}$$

where the rate coefficients $a_{ij}, i \neq j$ cover collisional excitation and de-excitation processes from state j to state i, a_{ii} cover all collisional excitation, de-excitation and ionization processes which attenuate the state i and b_{ij} similarly describes the spontaneous emission processes. It is assumed that plasma is without impurities and thus $n_e = n_p$. For given profiles of electron density and temperature, it is immediately possible to calculate the respective electron populations of Li atoms along the beam path by integrating the given set of equations. For illustration, the relative populations of energy states calculated for 60 keV lithium beam and prescribed electron density and temperature profiles are shown in Figure 4.4. It can be clearly seen that the populations of higher states are very small compared to the first excited level. It can be also seen that for given density profile, the beam is practically fully ionized on 10 cm of its path inside the plasma.

However, the density reconstruction requires solving of the inverse problem - to get $n_e(z)$ from the Equation 4.7 only with the knowledge of $N_2(z)$. By

integrating the second equation for $dN_2(z)/dz$ and rearranging its terms, one may write [48]:

$$n_e(z+h) \approx \frac{\alpha(Li_{2p}(z+h) - Li_{2p}(z)) - \alpha b_{22} \int_z^{z+h} Li_{2p}(s)ds + \sum_j hb_{2j}N_j(z)}{\alpha \int_z^{z+h} a_{22}(s)Li_{2p}(s)ds + \sum_j \int_z^{z+h} a_{2j}(s)dsN_j(z)} \tag{4.9}$$

$$\alpha Li_{2p}(z) = N_2(z) \tag{4.10}$$

where $Li_{2p}(z)$ is the measured lithium emission profile, α is a calibration constant characterizing both the optical path and the detection system which relates the real and the measured beam emission, and h is the integration step. By a stepwise integration of Equation 4.7 and simultaneous solving of Equation 4.9, one may get the electron density profile $n_e(z)$ as well as electron populations of the individual states along the beam path.

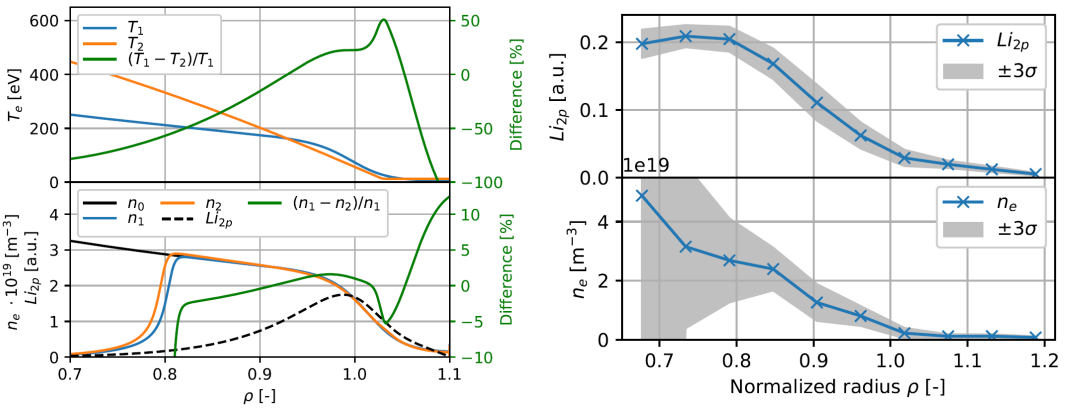

(a) (b)

Figure 4.5: (a) Simulation of the sensitivity of reconstructed density on electron temperature. (b) Lithium light profile measured by the Li-BES APD system in COMPASS discharge #13691 (top) and corresponding reconstructed density profile with depicted reconstruction error (bottom). Taken from [A3].

However, the above described method is applicable only if the denominator in the Equation 4.9 does not cross zero. This usually happens at some point z_s after which the denominator changes sign. This singularity can be explained as the point, at which the beam is so strongly attenuated that the collisional depopulation rate for Li(2p) state cancels out its previously prevailing population rate mainly by collisional excitation from the ground state. At this point, the net depopulation of the Li(2p) state is caused by spontaneous radiative de-excitation and it is not sensitive any more to the local density [48]. This singularity can however help to determine the optimal calibration constant α by setting a requirement that both the numerator and the denominator in Equation 4.9 have to change sign at the same value of z in order to keep the density positive and therefore physically reasonable. The calibration constant α can be determined by an iterative process.

It is necessary to note two important points. 1) as was already stated before, the dependence of the measured light signal on plasma electron temperature is

weak. This can be seen in Figure 4.3a, where the relevant curves describing dependence of Li excitation rates by electron impact on electron temperature are flat for a wide range of temperatures. In [A3], a simulation of the sensitivity of density reconstruction on electron temperature was done. Its result can be seen in Figure 4.5a. Firstly, using prescribed density profile n_0 and temperature profile T_1, the light profile Li_{2p} was calculated from the collisional radiative model. The density was then reconstructed again using different temperature profiles T_1 and T_2. It can be seen that the relative difference of reconstructed densities is ≈ 10 times smaller than the relative difference of temperatures. The temperature profile usually used for density reconstructions by Li-BES is taken from the Thomson scattering measurement. 2) The error of the reconstructed density profile propagates and increases along the beam path. At some point behind the maximum of light profile, where the sensitivity of lithium emission to density significantly decreases, the error is too large and the reconstruction has to be ended. An example is given in Figure 4.5b. It shows the light profile from 60 keV Li-beam measured by the avalanche photo-diode system in COMPASS discharge #13691 at time $t = 1009$ ms and corresponding density reconstruction with the depicted growing errorbars.

4.4 CCD camera

We are using conventional CCD camera (PCO PixelFly) which is placed on the top oval port of the vacuum vessel (see the CATIA model of CCD placement and the optical path in Figure 4.6a). It has spatial resolution 640×480 px and temporal resolution 20 ms at full frame. The temporal resolution can be doubled by pixel binning at the expense of spatial resolution and amount of detected light. The main purpose of the CCD camera is its use for determination and shot-to-shot correction of the beam alignment with respect to the radial axis and determination of the beam focus. It can be used for density reconstruction, but if the avalanche photo-diode measurement is (standardly) available, then the APD data are used for reconstruction instead, as the APDs are more sensitive and have better temporal resolution.

The CCD optics introduce significant barrel distortion. Figure 4.6b shows CCD camera image of a regular grid taken in laboratory. It can be seen that the image magnification decreases with the distance from the optical axis resulting in a barrel distorted image [18]. The images can be corrected using fish-eye distortion nonlinear model described in [49]. In this model, the radial distortion function r_d is given by:

$$r_d = \frac{1}{\omega} \arctan(2r_u \cdot \tan \frac{\omega}{2}) \tag{4.11}$$

where parameter ω is the ideal fish-eye lens field of view and r_u is distance from optical axis on the corrected image. The straightened radial coordinate r_u can be obtained by inversion of the equation 4.11:

$$r_u = \frac{\tan r_d\omega}{2 \tan \frac{\omega}{2}} \tag{4.12}$$

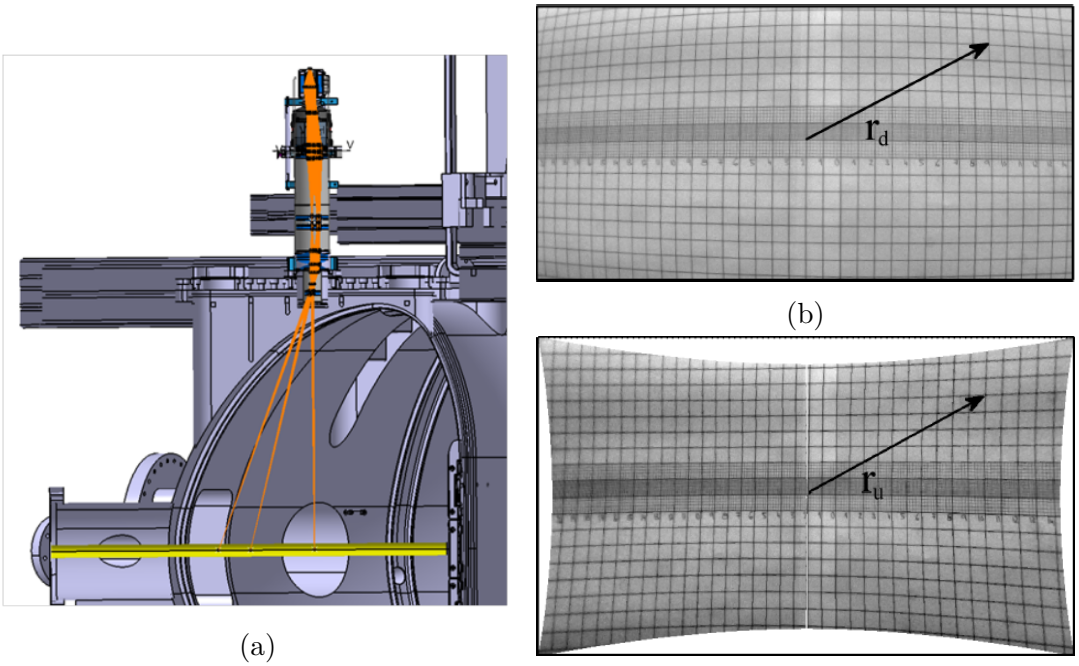

(a) (b) (c)

Figure 4.6: (a) CATIA drawing of the CCD observation system. (b) Image of a regular grid taken by COMPASS CCD camera showing the barrel optical distortion. (c) processed straightened image. Taken from [18].

The fish-eye corrected image can be found by adjusting the field-of-view parameter ω until the image grid becomes equidistant [18] (see Figure 4.6c).

In Figure 4.7, one can see the CCD images from COMPASS discharge #6484. 30 keV Li-beam was injected into the circular plasma discharge with moderate line-averaged plasma density $n_e = 3.5 \cdot 10^{19}$ m^{-3} and plasma current of $I_p = 130$ kA. It shows typical captured CCD frames with exposition time 44 ms at full frame resolution with the beam in plasma (a) and beam chopped out of plasma (b). Images (c) and (d) then depict the image processing – background image correction (c) and consequent correction for optical barrel distortion (d). The latter image can then be used to calculate the radial beam light emission profile by integration across the beam diameter.

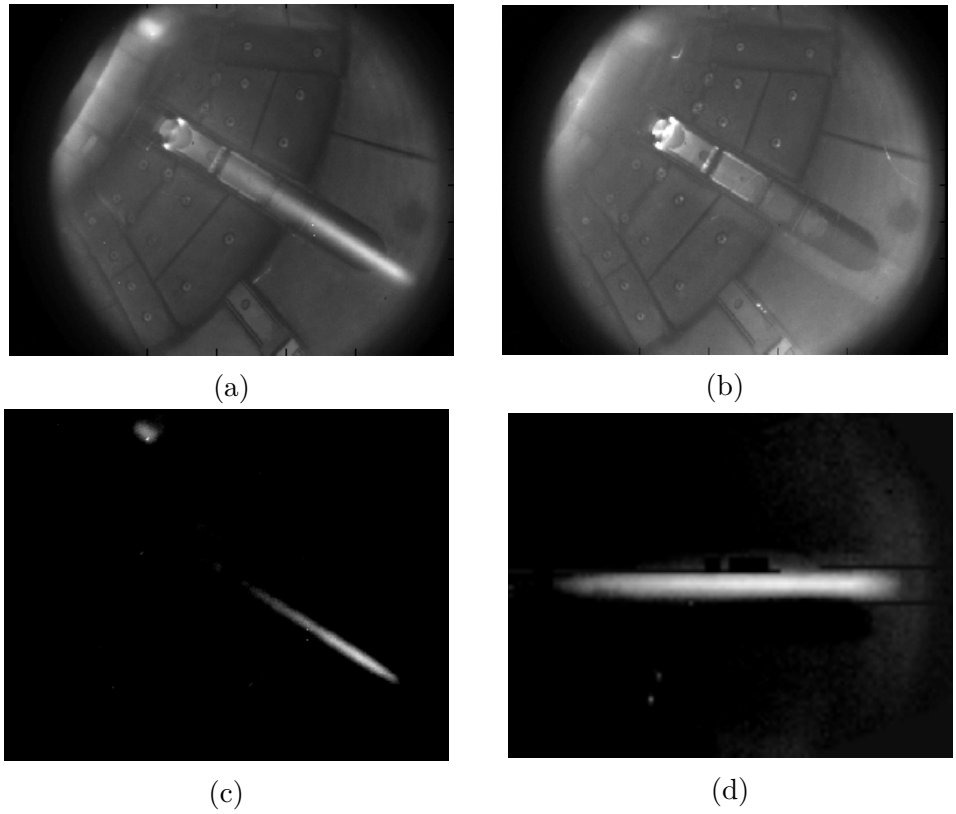

Figure 4.7: CCD camera frames for discharge #6484: (a) beam in plasma, (b) plasma background, (c) background subtracted beam and (d) fish-eye corrected frame. Taken from [18].

4.5 Avalanche photo-diode detector

The fast observation branch for detection of the lithium beam emission on COMPASS comprises of compact APD camera unit (APDCAM) containing the optics, interference filter and an array of 18 APDs with integrated amplifiers. It is installed on the bottom vertical port of the vacuum vessel of the COMPASS tokamak [A1] (see Figure 4.8).

4.5.1 Optics

In Figure 4.8, you can see the optical elements which guide the light to individual photo-diodes. The first optical lens is $\sim$ 40 cm below midplane, behind the bottom vertical oval port window. It leads the light through the interference filter, which was designed in a way to take into account the combined effect of Doppler shift and varying angle of incidence (more in Section 4.6). The second focusing element is a pair of plano-convex lenses projecting 1 : 1 image of the beam on to the array of 18 cylindrical field lenses. These are used to lead the light from the image plane ($\approx 10 \times 50$ mm radial-toroidal area corresponding to one channel) to the individual sensors (5×5 mm) [A1].

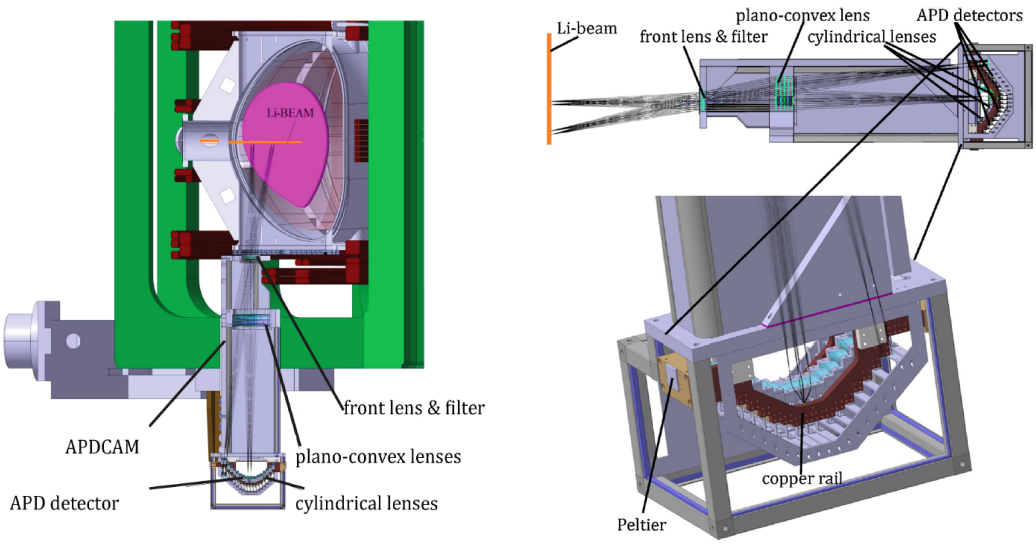

Figure 4.8: CATIA model of the installed APD camera system on COMPASS with described optical path. Taken from [18].

4.5.2 APD detector system

The APDs have been chosen due to their superior performance in terms of the signal to noise ratio (SNR) in the wide region of incident photon flux $5{\cdot}10^8 - 5{\cdot}10^{10}$ photons per second compared to other possibilities like photomultiplier tubes (PMT) and photoconductive photo-diodes (PPD) [A1], [50] (see Figure 4.9). The compact assembly and size of the system is made specifically for the COMPASS tokamak in order to place the collection optics and the detection system as near to the plasma as possible and thus maximize the photon flux on the APDs. Estimation of the incident photon flux from the measured signals is in the range of $(1-5)\cdot 10^{10}$ photons/s, which surpasses similar experiments on other devices. The minimum level of detectable plasma fluctuations is limited by the statistical photon noise, which is given by Poisson distribution as $\delta n_e/n_e \approx 1/N^{1/2}$ where N is the number of photons detected during the integration period. For an incident light of $5\cdot 10^{10}$ photons/s, the photon noise level is ~ 0.6 % at 2 MHz bandwidth and so the sensitivity of the system to low level density fluctuations is high [A1].

The avalanche photo-diodes used on COMPASS are silicon solid state detectors with 5×5 mm effective photosensitive area made by Hamamatsu (type $S8664-55$). They are sensitive to wavelengths in the range of $320-1000$ nm, have high quantum efficiency (85 % at 650 nm) and intrinsic gain up to 100 for used reverse biasing voltage in the range of $350-450$ V. APDs do not require cryogenic cooling, but in order to ensure the same sensitivity of the individual sensors, their temperature needs to be stabilized. For this reason, they are mounted on a common copper rail. A possibility of their cooling by two Peltier elements was prepared, but ultimately found unnecessary. Each detector has its own special low noise operational amplifier developed in Wigner RCP and operated with 1 MHz bandwidth. The data acquisition system uses a 32-channel, 2 MHz analogue-to-digital converter (ADC) with 14 bit resolution [A1], [50].

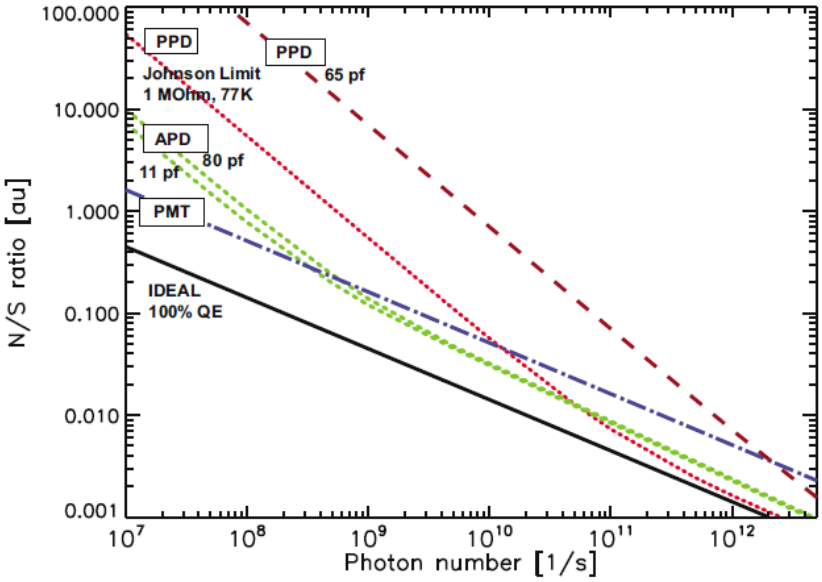

Figure 4.9: Comparison of the noise to signal ratios of different detectors as a function of incident light level at 1 MHz bandwidth. Taken from [50].

4.5.3 Spatial calibration of APD channels

A special calibration rod was used to calibrate the radial positions of individual APD channels with respect to the tokamak vessel. It was mounted upon a flange, which was firmly attached to the beam entrance port. A sprocket was used to move the rod radially, its one full revolution being equal to 1.5 mm. As a light source, a red LED was used and attached to a fixed position on the rod. The LED head was cut to reduce the spot size to ~ 1 mm. The measurement was done in the range of $245 - 343$ revolutions which corresponded to radial positions $R = 788.68 - 641.68$ mm in steps of 1 full revolution $= 1.5$ mm. The detected signal intensity profile for each APD channel is shown in Figure 4.10a. One can see, that the LED light intensity was not stable in time, giving us oscillating signals for each channel.

From the measured data, the following method was used to estimate the calibration constant: Let's denote $r_{a,i}$ the i-th value of position of channel a where i represents one of the n measurements for channel a. And $\omega_{a,i}$ the i-th value of signal intensity of channel a. Then the arithmetic mean value of position of the channel a will be calculated as a weighted sum:

$$r_a = \frac{\sum_{i=1}^{n} r_{a,i}\omega_{a,i}}{\sum_{i=1}^{n} \omega_{a,i}} \tag{4.13}$$

Positions of the APD channels with estimated error are shown in Figure 4.10b together with a linear fit. The fit was done using weighted least squares. Maximum error of the fit is 1.3 mm, giving us the uncertainty of the calibration. The values are tabulated in Table 4.1.

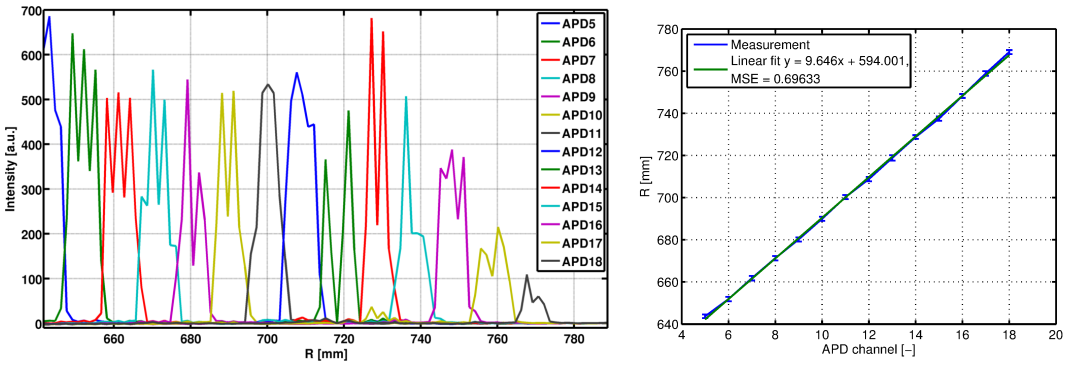

(a) (b)

Figure 4.10: (a) Measured spatial APD signal intensity for each APD channel. (b) Calculated radial center-positions for each APD channel together with a linear fit.

Table 4.1: Tabulated radial positions of individual APD channels.

APD channel	Radial position R [mm]	APD channel	Radial position R [mm]
1	603.6	10	690.5
2	613.3	11	700.1
3	622.9	12	709.7
4	632.6	13	719.4
5	642.2	14	729.0
6	651.9	15	738.7
7	661.5	16	748.3
8	671.2	17	758.0
9	680.8	18	767.6

4.6 Interference filter

Interference filter is an optical filtering element which transmits chosen parts of the frequency spectrum and reflects others. In the case of Li-BES on COMPASS, bandpass interference filters are placed in the optical paths of both APD and CCD detection systems to transmit a narrow spectral region around the Li I (2p-2s) line of 670.8 nm and to suppress all other wavelengths. Used filters are Fabry-Perot type filters made by Andover with multiple dielectric reflective layers which feature a bandpass region with Lorentzian shaped edges (see Figure 4.11a of a filter used for the APD system).

The design of optics for Li-BES detection had to be tightly linked to the filter design. This is due to the fact that lines of sight (LOS) of different detector channels observing different radial positions along the beam path have different angles with respect to the filter. The COMPASS APD and CCD observation geometry is illustrated in Figure 4.11b. The angles between the beam axis and LOS of individual APD channels differ in a range $77.2-89.7°$. The effect of angled lines of sight is twofold: 1) Due to the beam velocity and LOS angle, emitted Li line wavelength is affected by the Doppler shift and 2) the central wavelength

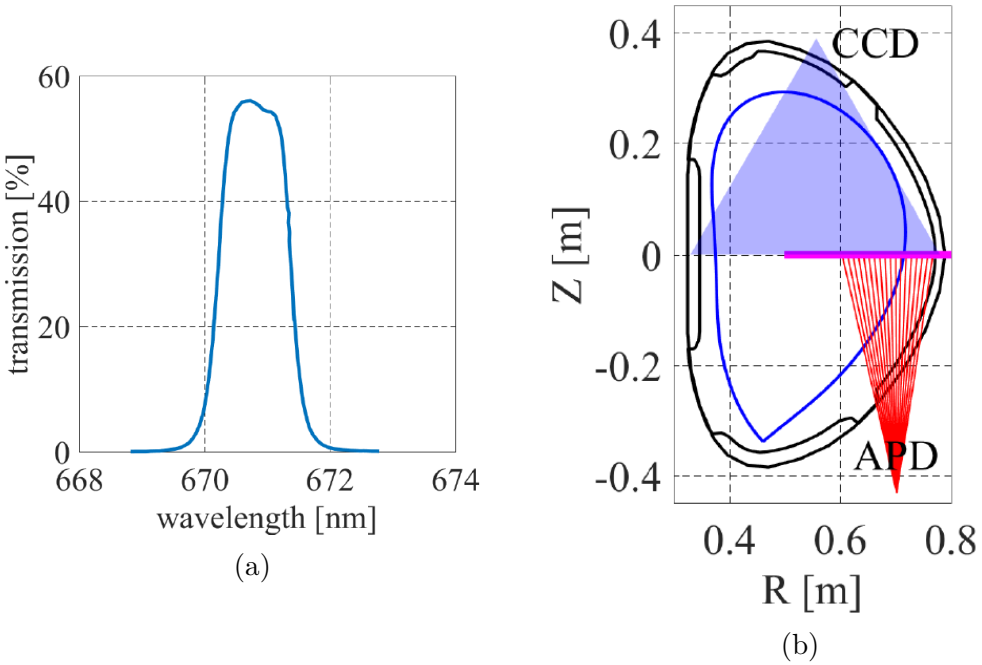

Figure 4.11: (a) Transmission of the bandpass interference filter in the optical path of the APD system. (b) Geometry of the APD and CCD observation systems.

of the bandpass interference filter is blue-shifted towards shorter wavelengths for incident light under a non-normal angle. The respective equations for these effects are:

$$\Delta\lambda = \lambda \cdot \frac{v_b \cos\alpha}{c} \tag{4.14}$$

$$\lambda_\theta = \lambda_0 \cdot \sqrt{1 - \frac{\sin^2\theta}{n^2}} \tag{4.15}$$

The first equation describes the Doppler shift $\Delta\lambda$ of the Li light, where λ is the wavelength of a wave emitted by Li atom, v_b is the beam velocity, c is the velocity of the wave and α is the angle between the LOS and the beam axis. The wave emitted by the Li-beam atoms at different radial positions will have different Doppler shifted wavelengths, the shift being towards longer wavelengths for inner APD channels (beam moving away of the APD optics) and towards shorter wavelengths for the more outer channels. The second equation describes the shifted position λ_θ of the central filter wavelength λ_0 for incident light with angle θ to the filter normal. Coefficient n denotes the effective index of refraction of the filter which is 2.05 in the case of COMPASS filters.

In the designing phase of the COMPASS APD optics, the use of a bandpass filter with 10 nm full width at half maximum (FWHM) with a central wavelength of 670.8 nm was anticipated to ensure transmission of lithium light emitted from the relevant radial positions of the APD observation while suppressing the plasma background - most notably the strong lines of H_α (λ = 656.3 nm) and CII (λ = 658 nm), the most intensive lines in the visible light spectrum at tokamak

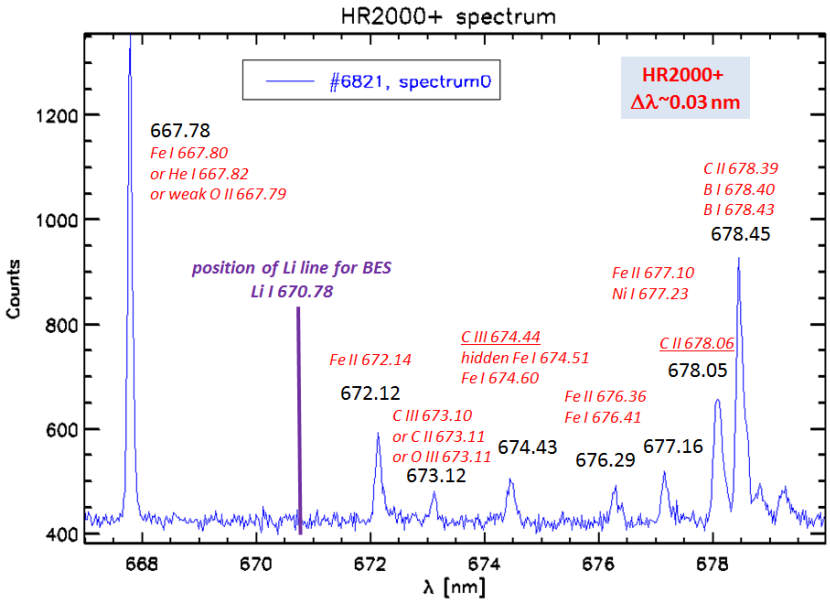

Figure 4.12: Spectrum of the COMPASS tokamak plasma around the Li emission line measured in discharge #6821 by HR2000+ spectrometer.

COMPASS. However, during initial measurements with the system on COMPASS, it turned out that the background suppression was not sufficient as the background level measured by the APD channels could be as high as the beam signal itself. This would seriously impact the possibility of the diagnostic to measure fast plasma density fluctuations - one of its main goals. The spectrum of COMPASS plasma around the Li line of interest was therefore investigated in detail using COMPASS spectrometer HR2000+ with spectral coverage $630 - 680$ nm. It was found that several impurity lines are near to the Li line (see Figure 4.12). Especially a strong, probably He I line at 667.8 nm could be transmitted by the filter. From this reason, it was decided to use narrower ~ 1 nm FWHM filter (see Figure 4.11a) at the expense of transmission of the more inner APD channels due to shift of central filter wavelength for angled lines of sight (see Figure 4.13). This could be justified by the fact that apart from very low density COMPASS plasmas, Li-beam is usually strongly ionized on the first 10 cm of its path, rendering more inner APD channels useless. Figure 4.13a shows both the Doppler shifted Li emission and the position of central filter wavelength for the individual APD channels. The difference between those two curves and the filter shape yield in a transmission curve for the APD channels depicted in Figure 4.13b, which needs to be used for APD signal calibration after each measurement. However, the real calibration curve is also affected by the state of the optics, especially the cleanness of the port window, which deteriorates in tokamak conditions, and also by small sensitivity differences of the individual APD detectors. It is therefore calculated after each measurement from the almost uniform beam light emission in the residual gas after plasma discharge.

For the CCD camera, 2 nm FWHM interference filter is used and enables almost full transmission of Li-beam light for the whole observation area. The background plasma radiation is not suppressed as well as in the case of APD

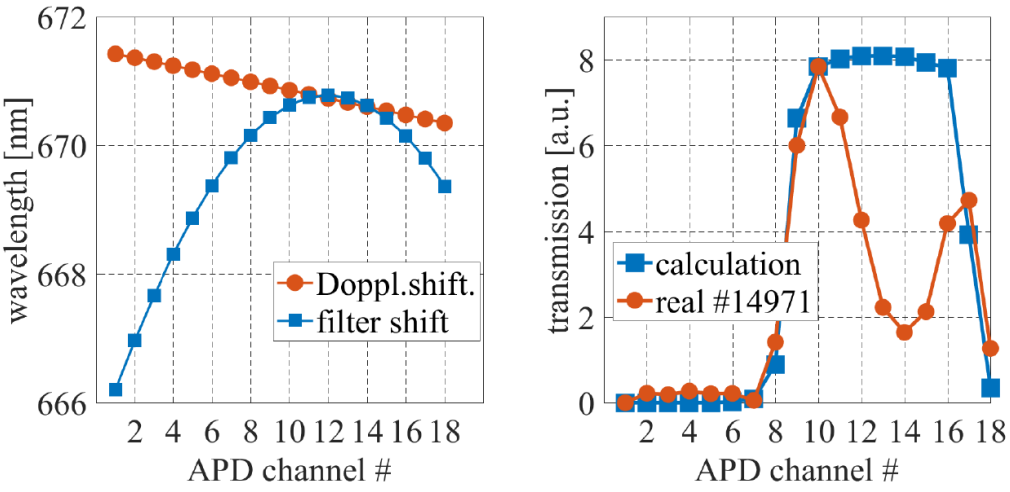

(a) (b)

Figure 4.13: (a) Calculated Doppler-shifted wavelengths of the Li line 670.8 nm (red) and shifted central filter wavelength positions (blue) for individual APD channels. (b) Transmission curve of the interference filter for individual APD channels (blue) and real calibration of the measured APD signal for COMPASS discharge #14971.

detector array, but it is sufficient for the purpose of the CCD measurement.

4.7 Comparison of Li-BES density profiles with other COMPASS diagnostics

On COMPASS, there are several diagnostics observing the edge and SOL plasma regions with different temporal and spatial resolutions, which can measure plasma density and complement the spectroscopic measurements by the lithium beam:

- *Microwave interferometer* - Two probing electromagnetic waves with frequencies 138.9 and 139.6 GHz ($\lambda \approx 2.15$ mm, critical density $n_{crit} = 2.4 \cdot 10^{20}$ m^{-3}) are used for density measurements. They propagate along the same vertical chord at $R = 560$ mm. The phase shift between a wave propagating through plasma and a reference wave is proportional to the plasma density integrated along the wave path in plasma. In the case of COMPASS, the phase shift between two waves propagating through plasma with slightly different frequencies is used, as it is necessary to keep the measured phase-shift small to avoid fringe jumps. This way, the whole range of COMPASS densities can be measured. Temporal resolution of the diagnostic is 20 μs and its real-time measurement is used for plasma density feedback control [9, 51]. As the measurement is line-integrated, it provides only a basic reference for comparisons with other density diagnostics.

- *Microwave reflectometer* - Microwave reflectometry uses a range of frequencies for which the plasma is reflective (tens of GHz). The limit frequency

for wave reflection is directly dependent on local electron density and so the density profile can be measured by fast frequency sweeping of the emitted waves. COMPASS system presently consists of O-mode transmitters and receivers for K ($18 - 26.5$ GHz), K_a ($26.5 - 40$ GHz) and a part of V ($40 - 53$ GHz) spectral bands. It allows to measure density profiles in the range of $0.4 - 3 \cdot 10^{19}$ m^{-3}. One full frequency sweep takes 6 μs and it is followed by 1.5 μs recovery time. To reduce the level of noise, 4 consecutive sweeps are usually averaged, thus providing electron density profiles with a temporal resolution of 30 μs and spatial resolution < 1 cm [9, 11].

- *Thomson scattering* - Four Nd:YAG laser beams are injected vertically into the vacuum vessel. The lasers feature 1064 nm wavelength, about 1.5 J output energy, 30 Hz repetition rate and the Q-switched laser pulse width is about 7 ns [13]. Laser light scattered on plasma electrons is detected by two separate optical systems for core and edge plasma region. Measurement of the spectral broadening of the scattered light is used to determine electron temperature profile, while the measured signal intensity provides electron density profile. The spatial resolution of the diagnostic is $9 - 12$ mm in the core and $3.6 - 3.8$ mm in the edge region. Combined use of four lasers provides temporal resolution of ~ 8.3 ms for equidistant laser timing.

- *Reciprocating probes* - Using fast reciprocating manipulators, probe measurements across the whole SOL and small part of the edge plasma region are possible. On COMPASS, there are two manipulators - vertical and horizontal - allowing fast insertion of an interchangeable probe head in the time frame of few 100 ms. The probe head then measures profile of the chosen plasma parameters on its way in and out of the plasma. Several probe heads were developed on COMPASS for different measurement purposes. Probe head suitable for fast electron temperature and density measurements consists of 3 ball-pen probes and 2 Langmuir probes [52]. Simultaneous measurement of the plasma potential by ball-pen probe and floating potential by a Langmuir probe provides electron temperature with 1 μs temporal resolution. Using the second Langmuir probe in the ion saturation mode, one can also calculate electron density.

Comparing the Li-BES diagnostic to other plasma density diagnostics on COMPASS, all have their advantages and disadvantages. Microwave reflectometer is the closest to Li-BES in the measurement parameters - it features similar temporal and spatial resolutions, while presently covering a narrower region of low plasma densities, mostly in SOL. Reciprocating probes provide a very well spatially resolved measurement in the submillimeter region. However, it can provide only 2 density profiles per the whole discharge and cover practically only the SOL region. Thomson scattering delivers measurement of plasma density with excellent spatial resolution, especially in the edge plasma region. Its temporal resolution is however limited by the repetition rate of used lasers.

In Figure 4.14, comparison of density profiles measured in COMPASS discharges by the above mentioned diagnostics is provided. Figure 4.14a is from diverted L-mode COMPASS discharge #10759 with plasma current $I_p = 200$ kA and line-averaged density $n_e = 4 \cdot 10^{19}$ m^{-3} (as measured by the interferometer).

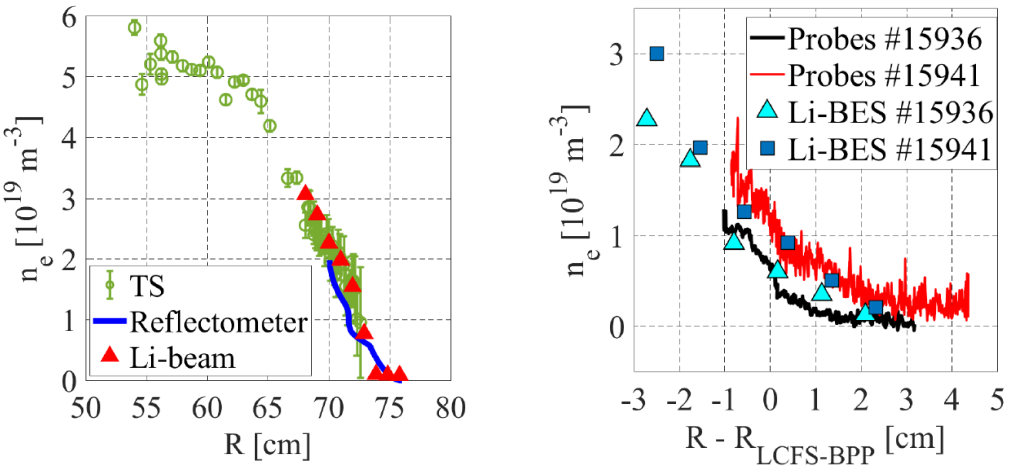

Figure 4.14: Comparison of measured density profiles by different COMPASS diagnostics. (a) Density profiles measured in COMPASS discharge #10759 at time $t = 1014$ ms by Thomson scattering, reflectometer and Li-BES systems. (b) Density profiles measured by Li-BES and reciprocating probes in the flat-top phase of discharges #15936 and #15941.

40 keV lithium beam was injected into the plasma. It was chopped for background correction with a period of 4 μs. The figure shows density profile measured by the Thomson scattering diagnostic at time $t = 1114$ ms and Li-BES and reflectometer density profiles averaged over the same time window of 30 μs around the time of Thomson measurement. Figure 4.14b shows comparison of density profile measured by Li-BES and horizontal reciprocating manipulator in COMPASS discharges #15936 and #15941. Both discharges were diverted L-mode discharges with plasma current $I_p = 160$ kA. Discharge #15936 had line-averaged density $n_e = 4 \cdot 10^{19}$ m^{-3} and discharge #15941 featured high line-averaged density of $n_e = 8 \cdot 10^{19}$ m^{-3}. The provided spatial coordinate is the relative distance from separatrix, which was measured by ball-pen probe as the place of maximum plasma potential. The reciprocation occurred at time window $t = 1070 - 1230$ ms during the long stable plasma flat-top phase. Li-BES density profile is averaged over this time window.

Generally, our observations show that the measured density profiles are very well comparable, both in the edge and in the SOL region. Thomson scattering data need to be mapped on the radial coordinate using the EFIT magnetic reconstruction. Therefore, sometimes a shift of the measured density profile in the order of < 1 cm appears with respect to the other diagnostics due to the systematic error of EFIT.

5. BES measurements in COMPASS plasmas

Li-BES diagnostic is a tool for measuring plasma density and density fluctuations in the scrape-off layer (SOL) and edge plasma region. The main goals of the Li-BES diagnostic on COMPASS are:

1. fast reconstruction of the edge plasma density profiles (with temporal resolution up to 2 μs and spatial resolution 1 cm). This is the default option - Lithium beam is operated routinely in COMPASS discharges to provide density profiles.

2. Measurement of the character of density fluctuations in the edge plasma and SOL regions in different plasma regimes.

In this chapter, I describe in detail the various possibilities of the diagnostic and I present my own analyses and observations of the measured raw Li-BES data or of the data reconstructed by the algorithm implemented in [A3]. Part of the observations was published in [A1] and also in [9, 53]

5.1 Motivation

5.1.1 Edge localized modes

In 1982 on the ASDEX tokamak, an advanced plasma confinement regime, so called high confinement mode or H-mode, was discovered [54]. This regime features enhanced plasma pressure profile (see Figure 5.1a), steep gradients of the edge plasma density and temperature which form an edge transport barrier, reduced turbulence and increased energy confinement time. The H-mode is considered as the operational regime of ITER and also future tokamak power plants. However, frequently, the H-mode is unstable and suffers from quasi-periodic crashes of the edge transport barrier. This phenomenon is called the Edge Localized Mode (ELM) instability [55, 56, 57]. During the short time of the ELM crash (from $\sim$ hundreds of μs to 10 ms), part of the plasma particles, carrying up to $\sim 10\,\%$ of the total plasma energy [58], is ejected out of the plasma column. Associated strong heat fluxes can cause severe damage to the device [59] and disallow its operation. Therefore, a strong effort is being made in the fusion community to understand the underlying physical processes and find ways to mitigate or suppress the instability [60, 61, 62].

It is believed that the sheared flows at the plasma edge play a crucial role in the suppression of the turbulent fluctuations and trigger the L-H transition process. These flows are connected to the negative radial electric field which gets even more negative during the L-H transition, increasing the poloidal rotation velocity of the plasma and its shear at the edge [63, 64, 65]. The widely accepted concept of ELM's formation during the H-mode is the magnetohydrodynamic (MHD) model of peeling-ballooning instability [66].

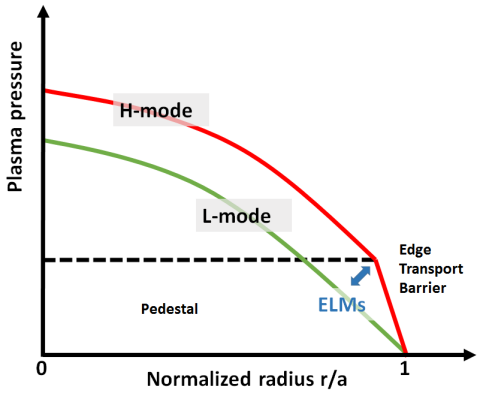

(a)

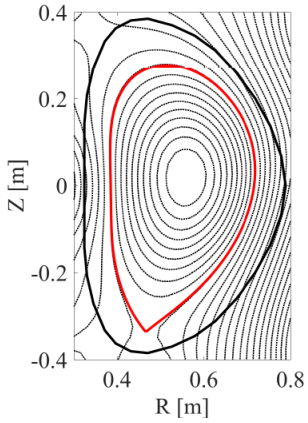

(b)

Figure 5.1: (a) Scheme of plasma pressure profile during L and H-mode regime in a tokamak. (b) Topology of the magnetic field surfaces in a poloidal cut of the COMPASS tokamak in discharge #14069 and time $t = 1150$ ms. Reconstructed by the EFIT code. Last closed flux surface is highlighted by a red line.

The COMPASS tokamak is a suitable device to study the H-mode, as it has demonstrated the ability to achieve H-mode operation over a wide range of plasma parameters, both with ohmic and NBI-assisted plasma heating [2] (see Figure 5.2 showing plasma current and H_α emission from COMPASS H-mode discharge #17283). The analysis of the density evolution and fluctuations during H-mode is one of the primary goals of Li-BES diagnostic.

5.1.2 Edge and SOL plasma turbulence

The Li-BES diagnostic measures in the plasma region around the last closed flux surface (LCFS). In the narrow region of several cm around LCFS (see Figure 5.1b), essentially important transport phenomena occur which determine the particle and energy confinement times and the strength of the plasma-wall interaction. Apart from the important physics of the L-H transition and H-mode, this region is rich in different stable and unstable modes like drift waves (DW) [67], neoclassical tearing modes (NTMs) [68], Zonal flows (ZF) and geodesic acoustic modes (GAMs) [69, 70] etc. The unstable modes can lead to coherent structure formation through nonlinear mode couplings. The size and the dynamics of these structures is governed by local and global plasma parameters, underlying sheared flows and the interaction with plasma facing materials (divertor, limiter). A comprehensive review of the edge turbulence in tokamaks can be found for example in the work of Scott [71].

The tokamak plasma region inside of LCFS is usually referred to as the confined plasma region, while the plasma region outside of LCFS, which features open magnetic field lines, is called the scrape-off layer. In COMPASS plasmas, the radial position of LCFS on midplane, where the beam is injected, is usually around $R \approx 70-73$ cm, while the plasma center is at $R \approx 56$ cm. Due to the beam ionization and also the transmittance of the interference filter (more in Section 4.6), only APD channels $8-17$ are useful, giving us usually $6-7$ measurement

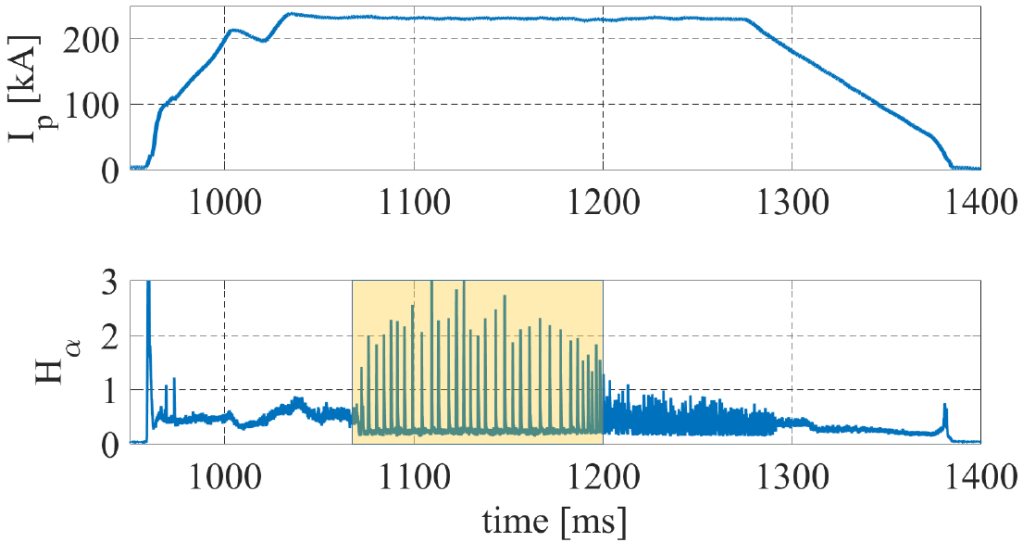

Figure 5.2: (a) Plasma current and (b) H_α radiation in H-mode COMPASS discharge #17283. H_α signal is a good indicator of the H-mode regime. It features a characteristic drop in intensity during the L-H transition and the plasma wall interaction during the ELM crash is visualized by large emission peaks. On figure (b), the temporal range of the H-mode phase is highlighted by an orange rectangle.

channels in the edge plasma and $3-4$ channels in SOL. With its moderate spatial resolution and very good temporal resolution, Li-BES is a suitable diagnostic to measure spatio-temporal characteristics of the edge/SOL turbulence and can help to clarify the underlying physics processes.

5.2 Modes of beam operation

Using a pair of deflection plates (see also Section 3.3) in the beam line before the neutralization chamber, the beam ions can be deflected by applied electric field. If the electric field is large enough (usually 2 kV over 5 cm distance between the plates is used), the beam is deflected completely from the plasma and hits the wall of the guiding flight tube. This technique is called the 'beam chopping'. If smaller electric field is applied, the beam position in plasma is deflected (swept) by a few cm. Chopping the beam allows the correction of signals for the background, while deflection (done in poloidal direction) allows quasi 2D-measurements at 2 poloidal beam positions [72]. The achievable switching frequencies of the sweeping/deflection system are presently up to 250 kHz. The poloidal resolution of the deflection technique is limited by the $\sim 2-2.5$ cm beam diameter.

There are basically 2 ways to analyze density fluctuations measured by Li-BES:

1) The first is to analyze fast density profiles reconstructed from the measured light profiles. This approach requires correction of the APD channel signals for background and therefore use of beam chopping technique. This reduces tempo-

ral resolution of the signals due to the chopping frequency to 2 μs at best, but often the signal quality is not good enough and there is a need of additional time averaging before the reconstruction can take place. Therefore, theoretically, this method allows observation of density fluctuations with frequencies up to 250 kHz, but more usually up to several tens of kHz, which can be at the limit for observation of certain phenomena (i.e. geodesic acoustic modes with characteristic frequency ~ 30 kHz on COMPASS).

2) The second possibility is to analyze density fluctuations directly from the raw lithium light emission signals. This is applied when the beam is not chopped or when it is swept between 2 poloidal positions. Then the sampling of the APD measurement of 0.5 μs defines the observable frequency range as up to 1 MHz. The detected light intensity is in the first approximation taken as proportional to the local electron density. However, this approach needs careful considerations. Firstly, the signal to background ratio should be sufficiently high, otherwise the measurement is not local anymore due to the contribution of plasma background integrated along the line of sight of the APD channels. Secondly, the actual radial resolution of the light signals strongly depends on the nonlocal nature of the lithium light emission due to the finite lifetime of the excited Li(2p) states. The upper limit for the radial smearing effect can be quantified as:

$$\Delta r = \sqrt{\frac{2E_{\mathrm{b}}\tau_{\mathrm{life}}^2}{m}} \tag{5.1}$$

where E_{b} is the beam energy, τ_{life} is the lifetime of the excited Li(2p) atomic state and m is the mass of Li atom. For standardly used beam energy of 60 keV, using the tabulated value of $\tau_{\mathrm{life}} = 27.1$ ns [47] for spontaneous de-excitation of Li(2p) state, the equation 5.1 yields $\Delta r \approx 35$ mm. It is important to understand that this is a theoretical maximum of the radial smearing of lithium light signals. In reality, it is reduced significantly by the mechanism of collisional de-excitation depending on the local plasma density [27, 73].

5.3 Quality of Li-BES signals

The quality of the measured signals is described by the ratio of lithium light signal to plasma background and also by the signal-to-noise ratio of the light signal. As was stated in previous Section 5.2, the predominance of the beam light signal over background is essential for fluctuation analysis of the lithium light signals. The main noise sources of the avalanche photo-diode measurement on COMPASS are the photon noise and the amplifier noise. On Figure 5.3b, one can see the result of calculation of the signal-to-noise ratio for COMPASS discharge #14971 and APD channel 11. The typical APD signal of few hundred mV shown on Figure 5.3a features signal to background ratio of $\sim 15:1$ and signal-to-noise ratio of $\sim 60:1$. These achieved parameters are comparable to the very best world BES diagnostics and allow analyses of a wide range of physics phenomena (see Figure 5.4).

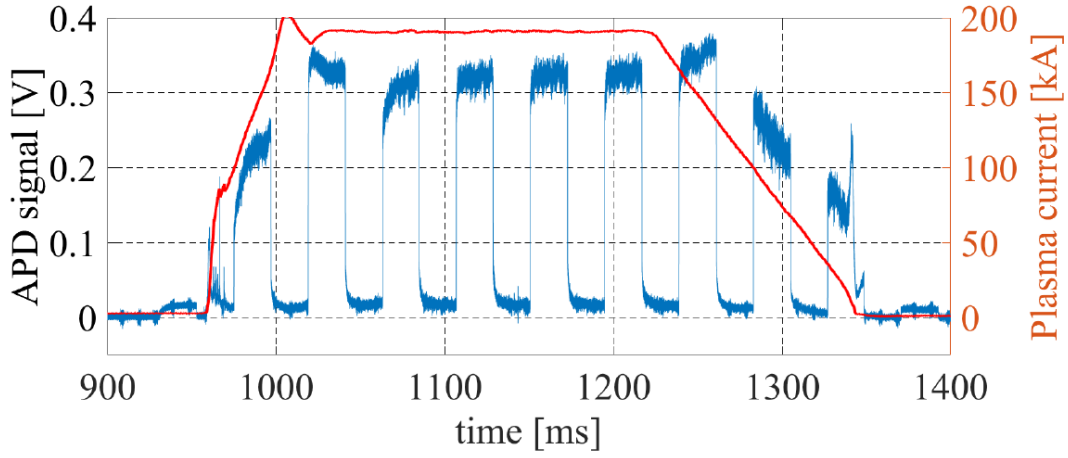

(a)

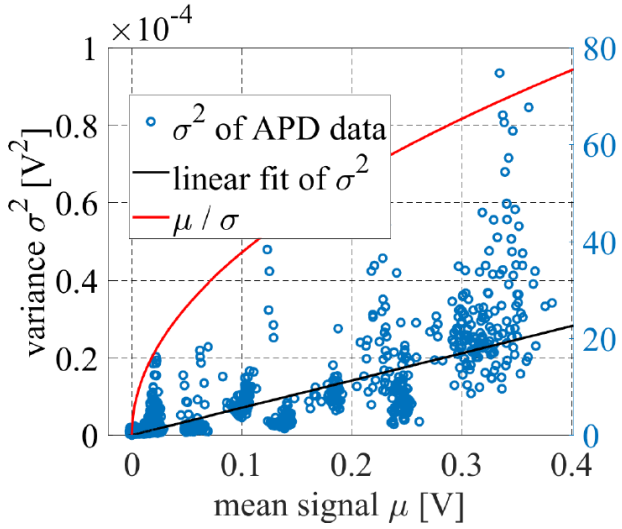

(b)

Figure 5.3: (a) Signal of avalanche photo-diode channel 11 in L-mode COMPASS discharge #14971 with 60 keV lithium beam chopped with a period of 44 ms. (b) Signal-to-noise ratio calculated from APD channels for the discharge #14971 as the ratio of the mean and standard deviation calculated over 500 μs time windows.

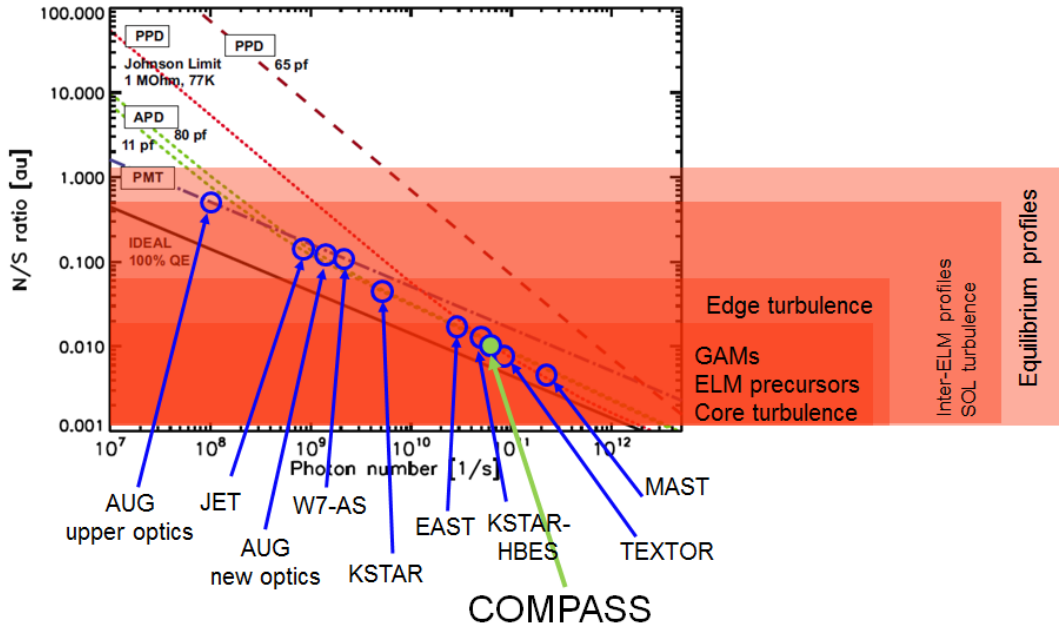

Figure 5.4: Comparison of different detector types - APD, photomultiplier tube, photoconductive photodiode - in terms of the relation between the noise-to-signal ratio and the incident photon flux (taken from [50]). Positions of the COMPASS APD system and other world BES diagnostics are shown [27, 28, 32, 38, 74]. Also, the possible physics areas of interest which can be investigated with given signal-to-noise ratios are outlined.

5.4 Edge plasma and SOL fluctuations

This section presents analyses of the density fluctuation measurements by Li-BES APD system on COMPASS. Part of the observations were published in [A1].

5.4.1 General fluctuation properties

The density (and temperature) fluctuations show clearly different character in the confined plasma region and the scrape-off layer. This difference is a well-known behavior in tokamak (and stellarator) physics. In the confined plasma region, the measurements on various devices [75, 76, 77] have shown turbulent structures with correlation lengths of a few cm both in radial and poloidal direction, lifetimes in the few μs range and fluctuation amplitudes not exceeding few percent of the average density level. In the region near the last closed flux surface, the turbulence quickly changes and the relative fluctuation level rises. Turbulent plasma filamentary structures, referred to as blobs, are born there and propagate to the SOL [78]. These blob structures are elongated along the magnetic field lines and have distinctly higher density and temperature than the surrounding SOL background. The structure of the SOL turbulence was studied extensively and similar properties were found on different devices, namely relative fluctuation amplitudes of several tens of %, correlation lengths of cm scales both radially and poloidally and tens of μs long lifetimes [77].

These general properties of density fluctuations in the edge and SOL region were observed also by the COMPASS Li-BES system. Figure 5.5a shows light signal of two APD channels radially separated by 5 cm, during a stable phase of COMPASS discharge #16090.

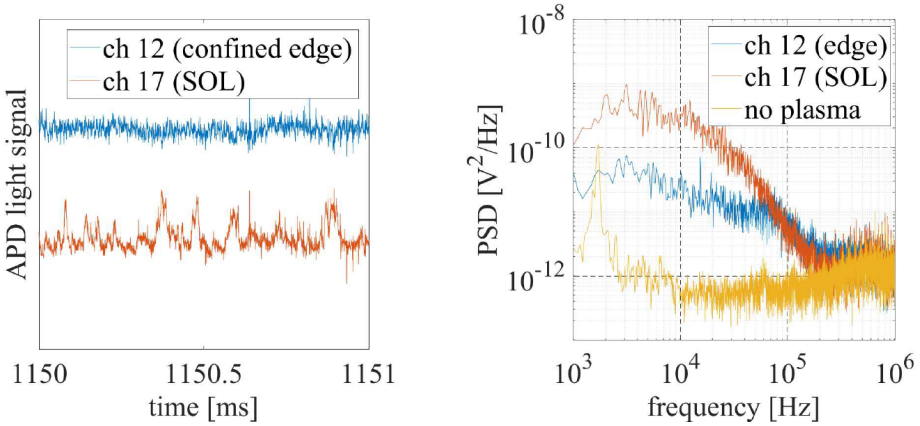

Figure 5.5: Comparison of light fluctuations measured by two (SOL and edge) APD channels during COMPASS discharge #16090. (a) shows 1 ms time window of the raw signals with clear difference in the fluctuation character and (b) shows the respective frequency spectra of the signals along with a reference spectrum of the electronic noise.

The upper (blue) signal from the confined plasma has a a higher amplitude, but shows relatively small-scale fluctuation level compared to the signal (red)

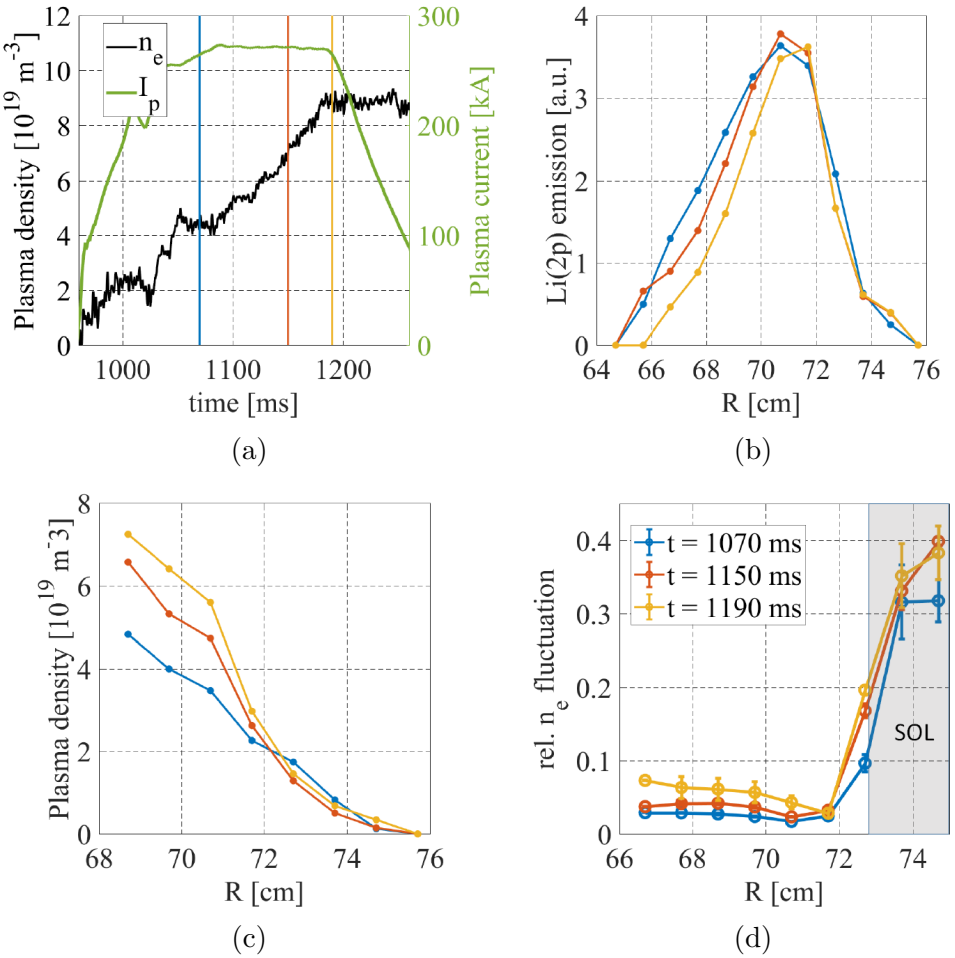

Figure 5.6: (a) Plasma density and plasma current evolution during COMPASS discharge #12230. Three times used at different plasma density levels for the fluctuation analysis are depicted. (b) Measured APD light profiles during the chosen times. (c) Density profiles reconstructed from the APD light profiles. (d) Relative fluctuation amplitude profiles.

from SOL region. The observed SOL fluctuations show the presence of large intermittent events - blobs, which dominate this region. Figure 5.5b shows the power spectral density (PSD) of these 2 APD channels during the plasma discharge and also a signal without plasma for reference. PSD is a measure of how power of a signal is distributed over frequencies:

$$S_{xx}(\omega) = \lim_{T\to\infty} \mathbf{E}\left[|\hat{x}(\omega)|^2\right] \tag{5.2}$$

$$\hat{x}(\omega) = \frac{1}{\sqrt{T}} \int_0^T x(t) e^{-i\omega t} dt \tag{5.3}$$

where $S_{xx}(\omega)$ is the PSD function, $\hat{x}(\omega)$ is the finite Fourier transform of signal $x(t)$ and $\mathbf{E}$ is the expected value operator. The turbulent spectrum of the SOL plasma shows considerable increase in spectral power in the frequency range from a few kHz up to $70 - 80$ kHz.

Figure 5.6 shows an observation of relative fluctuation amplitude profiles measured by the APD channels during COMPASS discharge #12230 with a plasma

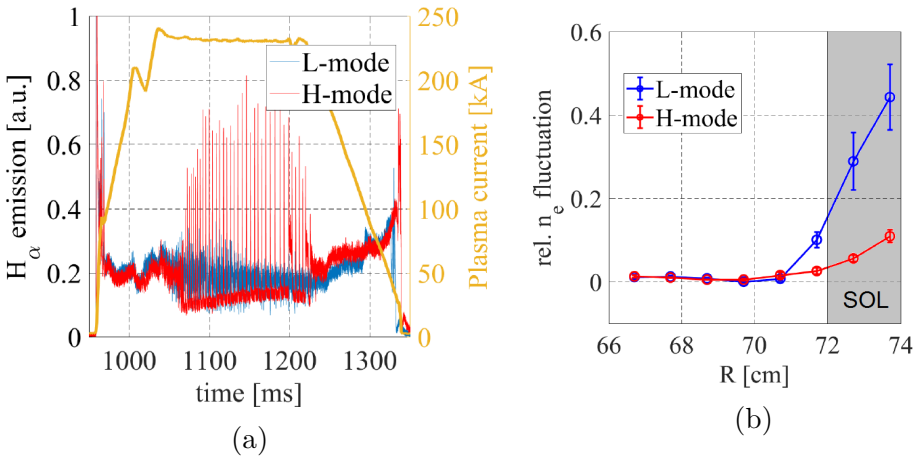

Figure 5.7: (a) Plasma current and H_α signals for L-mode discharge #13419 and H-mode discharge #13424. (b) Relative fluctuation amplitude profiles calculated from the measured APD light signals in both discharges. Time windows for the calculation were chosen to be in the inter-ELM region.

density ramp-up. Three 1 ms time windows at different plasma densities were chosen to determine the relative fluctuation amplitudes defined as the ratio of standard deviation and mean of the signal. In the confined plasma region, relative fluctuation amplitudes are in the few % range while they grow fast near the LCFS and reach $30-40\%$ in the SOL. Higher plasma density levels seems to have a slight effect in the increase of the relative fluctuation amplitudes. Similar behavior in the COMPASS SOL region was also observed by probe diagnostics [79].

Figure 5.7 shows comparison of the relative fluctuation amplitude profiles measured by the APD system in L-mode (#13419) and H-mode (#13424) discharge. Both discharges were identical in terms of global plasma parameters. In the discharge #14324, transition to H-mode was induced by additional heating of the core plasma by NBI injection. In the H-mode discharge, APD data were evaluated in an inter-ELM time window. It can be seen that relative fluctuation amplitudes in the SOL region are strongly suppressed in the H-mode phase. It is the effect of reduced size of the blobs, probably due to enhanced poloidal velocity shear in the H-mode, which can de-correlate larger-scale turbulent structures [69].

On Figure 5.8, one can see the calculated radial profile of skewness from the measured APD light signal in L-mode discharge #16090. It is interesting to observe that the symmetry of the amplitude distribution function changes its sign when crossing the separatrix. The sign of skewness divides plasma into the part of the edge region, where the turbulent structures are born (negative sign) and SOL (positive sign), to where they propagate. Similar behavior was also observed by probes [79, 80].

5.4.2 SOL turbulence analysis

As was already partly described in Section 5.4.1, the transport of particles and heat in SOL plasma is caused by radial motion of blobs. Single point measure-

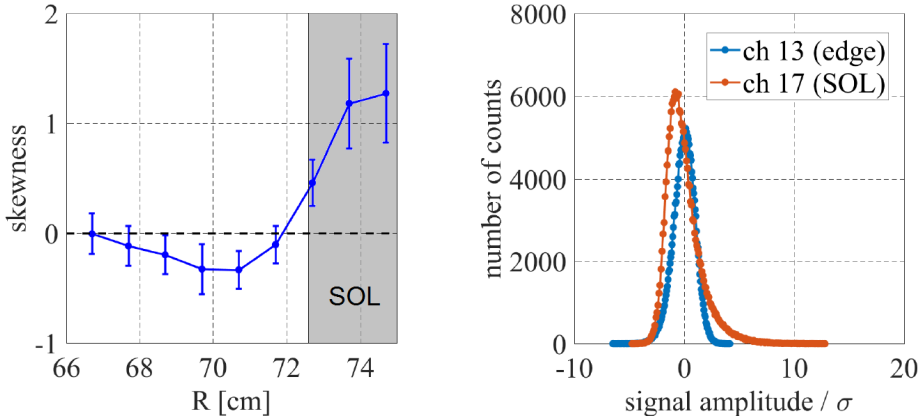

(a) (b)

Figure 5.8: (a) Profile of skewness of the measured APD light signals calculated in a time window $t = 1100 - 1200$ ms of COMPASS discharge #16090. (b) Comparison of differently skewed amplitude distributions of the APD signals for channel 13 in the confined plasma edge and channel 17 in SOL.

ments in SOL are dominated by large amplitude bursts with asymmetric shape with faster rise time and slower decay time and the amplitude probability density function is positively skewed. In [81], Garcia presented a stochastic model to describe the fluctuations of SOL plasma observed by a single point measurement, which was later adjusted by Theodorsen [82] according to probe measurements on the TCV tokamak. The model represents the measurement as a random sequence of bursts:

$$\Phi(t) = \sum_k A_k \psi(t - t_k) \tag{5.4}$$

where A_k is the burst amplitude, t_k is arrival time of k-th burst event and $\psi(t)$ is a fixed burst waveform. It assumes that the bursts arrive according to a Poisson process, which leads to the fact that the waiting times between the individual bursts are exponentially distributed with rate $\frac{1}{\tau_w}$:

$$P_\tau(\tau) = \frac{1}{\tau_w} e^{-\frac{\tau}{\tau_w}} \tag{5.5}$$

The signal amplitudes also follow the exponential distribution. Calculating the cumulants of the probability density function of the signals yields formulas for its skewness and flatness that show a parabolic relation, which is a feature characteristic of systems that are dominated by intermittent fluctuations. The bursts are assumed to have a double exponential waveform:

$$\psi(t) = \begin{cases} \exp(t/\tau_r) & \text{for } t < 0, \\ \exp(-t/\tau_f) & \text{for } t \geq 0, \end{cases} \tag{5.6}$$

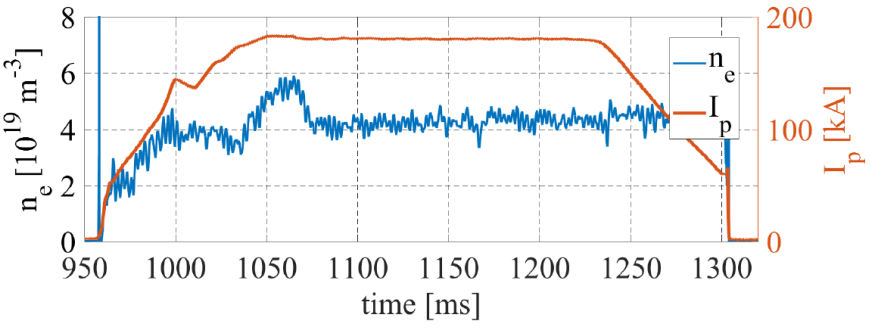

(a)

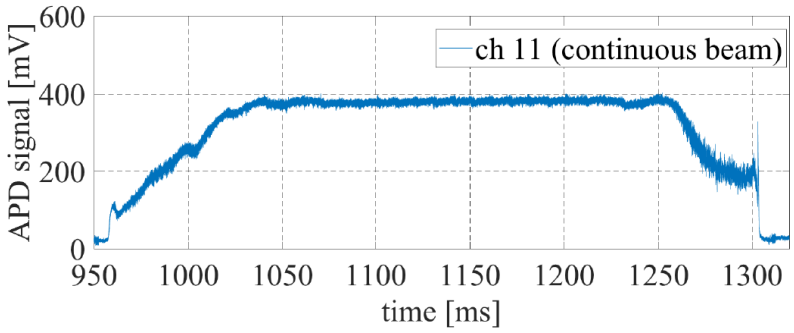

(b)

Figure 5.9: (a) Plasma current and plasma density evolution during COMPASS discharge #16090. (b) APD light signal measured by channel 11 in the edge plasma during the discharge. 60 keV continuous beam was injected into the plasma.

where τ_r and τ_f are the rise time and the fall time and the burst duration is $\tau_d = \tau_r + \tau_f$. The probability density function of a measured variable Φ (in our case density) then follows a Gamma distribution [82]:

$$\langle\Phi\rangle P_\Phi(\Phi) = \frac{\gamma}{\Gamma(\gamma)}\left(\frac{\gamma\Phi}{\langle\Phi\rangle}\right)^{\gamma-1}\exp\left(\frac{\gamma\Phi}{\langle\Phi\rangle}\right) \tag{5.7}$$

where the shape parameter $\gamma = \tau_d/\tau_w$, Γ is the Gamma function and angular brackets denote an average of a random variable over all its values.

The aim of the following SOL analysis was to experimentally verify the Garcia model by Li-BES measurements on COMPASS and to investigate the blob parameters. For this purpose, APD light signal measured by a SOL APD channel 17 in COMPASS discharge #16090 was studied. The signal was filtered by a 1 kHz high-pass Butterworth filter to select the turbulent part of the frequency spectrum. The discharge featured stable long flat-top phase with line averaged density $4 \cdot 10^{19}$ m^{-3} and 180 kA plasma current (see Figure 5.9). 60 keV lithium beam was injected continually without chopping. The APD signal was searched for blobs in a long time window of $t = 1100 - 1200$ ms by a threshold method (see Figure 5.10).

The threshold method is the most frequently used method in the literature for blob detection. It is based on a predetermined arbitrary threshold, which

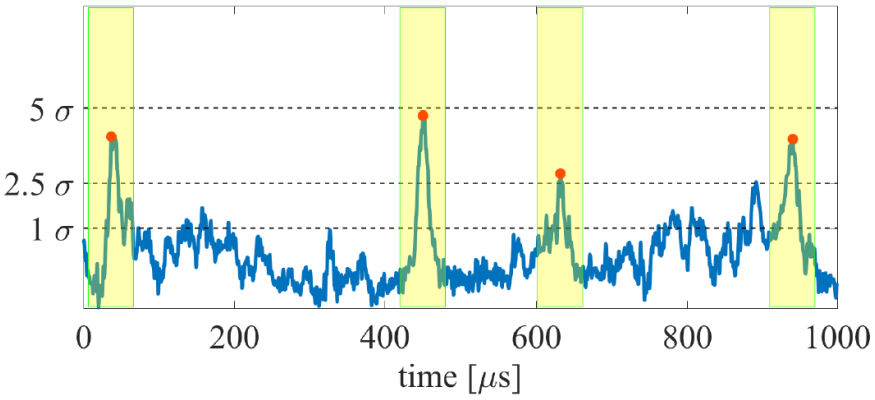

Figure 5.10: Illustration of the threshold method for blob detection. 1 ms time window of the high-pass filtered lithium light emission data measured by SOL APD channel 17 in COMPASS discharge #16090 is shown. It shows highlighted detected peaks above threshold of 2.5 σ and 60 μs time windows around the peaks used for conditional averaging.

is usually given as a multiple of the standard deviation σ [81]. The signal is scanned and all peaks above the prescribed threshold value are then considered to be part of individual blob events. This way it is possible to calculate the detection frequency of events, their amplitude distribution and their waiting time distribution. In the case of my analysis, threshold of 2.5 σ was used. Around the peak of each blob event, the signal was cut within a time window of ± 30 μs and stored for later conditional averaging.

Results of the analysis are shown in Figure 5.11. Figure 5.11a shows the conditionally averaged blob event, with exponential fits of the rise and fall times $\tau_r = 8.88$ μs and $\tau_f = 10.25$ μs. Figure 5.11b depicts the distribution of the blob waiting times. It was found that the distribution has two very distinct exponential dependences - in the region of short waiting times ($t < 30$ μs, $\tau_{w1} = 9.7$ μs) and for longer waiting times ($\tau_{w2} = 280$ μs). Figure 5.11c shows the exponential fit of the amplitude distribution ($\Delta A = 0.89$ σ) and also the amplitude distributions for the blobs with short and longer waiting times, which had practically identical slope but different number of events. The duration of the conditionally averaged blob event $\tau_d = 19.13$ μs is ~ 2 times longer than the calculated short waiting time and ~ 15 times shorter than the longer waiting time. These results suggest that the signal is composed of a mixture of 1) smaller quickly following or even overlapping events and 2) more frequently occurring larger events with longer waiting times. The real amplitude distribution of the measured SOL signal is expected to be a convolution of the Gamma distribution of the blobs (according to Equation 5.7) and Normal distribution of the noise:

$$f(\Phi|\mu,\sigma) = \frac{1}{\sigma\sqrt{2\pi}}\exp\left[-\frac{(\Phi-\mu)^2}{2\sigma^2}\right] \tag{5.8}$$

$$(f*g)(n) = \sum_m f(n-m)g(m) \tag{5.9}$$

where $f(\Phi|\mu,\sigma)$ is the Normal distribution with mean value μ and standard devi-

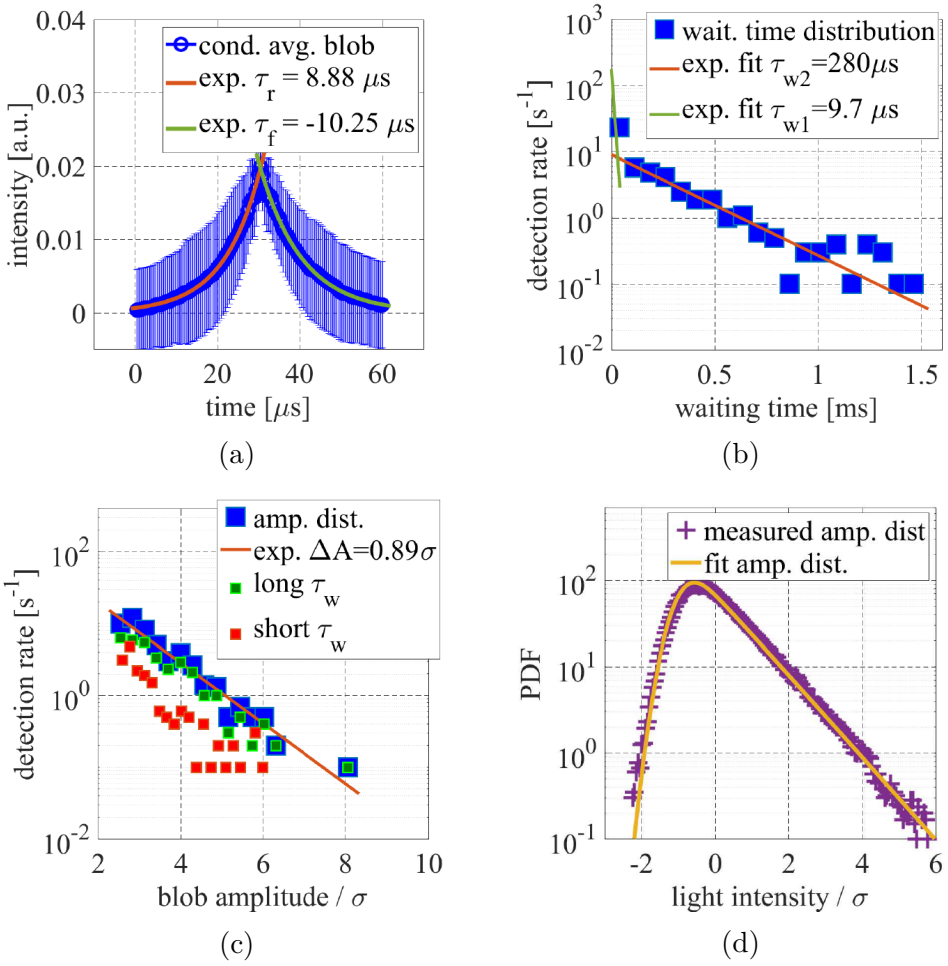

Figure 5.11: (a) Conditionally averaged blob calculated from 495 detected blob events with exponential fits determining the rise and fall times. (b) Waiting time distribution of the detected blob events with two exponential fits of the short ($t < 30$ μs) and longer waiting time regions (c) Amplitude distribution of the detected blob events (blue) with separate distributions for the blobs with short (red) and longer (green) waiting times (d) Amplitude distribution of the measured APD light signal fitted by a convolution of Normal and Gamma distribution.

ation σ and $f * g$ is the discrete convolution of functions f and g. The measured amplitude distribution was fitted by the convolution of the two distributions (see Figure 5.11d) and found to follow the convolved distribution nicely. The fitted shape parameter $\gamma = \tau_d/\tau_w$ of the Gamma distribution was found to be ~ 0.95, which gives a waiting time of $\tau_w \approx 20$ μs.

5.5 Poloidal rotation velocity

Shear of the poloidal plasma rotation velocity $\partial v_\theta/\partial r$ is one of the important factors responsible for the suppression of turbulence and thus reduction of transport in tokamaks by tearing of the turbulent structures. This sheared flow is tightly linked to the radial electric field E_r, as it consists of the equilibrium $E \times B$ flow velocity and intrinsic phase velocity of the turbulence [83]. E_r in the edge region of tokamak plasmas shows strong variation. In the confined region E_r is negative, determined by the radial pressure gradient $\partial p/\partial r$, while in SOL it changes sign and follows the plasma potential gradient $\partial \Phi/\partial r$, which is proportional to the temperature gradient $\partial T_e/\partial r$ [69]:

$$E_r^{edge} \approx \frac{1}{nq_e}\frac{\partial p}{\partial r} \tag{5.10}$$

$$E_r^{SOL} = -\frac{\partial \Phi}{\partial r} \propto -\frac{\partial T_e}{\partial r} \tag{5.11}$$

where n is plasma density and q_e is the elementary charge.

Using the COMPASS Li-BES system it is possible to gain information about both the poloidal flow velocity profile and its fluctuations using one and two point measurements. As the beam can be periodically deflected in poloidal direction with a high frequency up to 250 kHz, the time delay estimation (TDE) method can be applied for the determination of the poloidal component of the flow velocity assuming that the turbulent fluctuations in the range of $20 - 100$ kHz are coherent enough that their de-correlation time is much longer than the time needed for the average structure to travel past the detection volume. Other possibility is a one point measurement technique without beam deflection - autocorrelation width technique (described thoroughly by Bencze [84]), which provides information about the frequency characteristics of the poloidal velocity fluctuations.

5.5.1 TDE method

Time delay estimation method is a two-point method for determination of the poloidal velocity profile. It requires the beam to be periodically deflected in the poloidal direction, typically by $2 - 3$ cm. For each radial APD channel, the detected light signal is divided into two virtual beam signals at separate poloidal positions. The temporal resolution of virtual beam signals is defined by the period of beam deflection. Two approaches are used to calculate the time-delay needed for turbulent structures to travel between the 2 poloidal positions:

(1) The straightforward approach is to choose an appropriate time window and cross-correlate the virtual beam signals of corresponding APD channels. The

normalized cross-correlation function P_{xy} between two signals $x(t)$ and $y(t)$ is defined as:

$$P_{XY}(\tau) = \frac{1}{\sigma_x \sigma_y} \int \tilde{x}(t)\tilde{y}(t+\tau)dt \tag{5.12}$$

where τ is the time lag, σ_x and σ_y are the standard deviations of the signals and tilde signifies the difference from the mean value of signals $x(t)$ and $y(t)$. If the signals are discrete functions, then the integration is replaced by a sum over consecutive time steps. The maximum of cross-correlation function (CCF) for each pair of virtual beam channels is shifted from zero position by Δt :

$$\Delta t = \frac{\Delta z}{v_{pol}} \tag{5.13}$$

where Δz is the poloidal separation of virtual beams and v_{pol} is the poloidal flow velocity at given radial position of the APD channel. By fitting of the CCF by a model function, the time delay and therefore the poloidal velocity for each channel in the given time window can be determined. However, the best achievable temporal resolution of the virtual beam signals is limited by fast deflection electronics to 4 μs. Considering typical poloidal velocities of several km/s to several tens of km/s observed on tokamaks [85, 86, 87] and few cm poloidal separation of the virtual beams, the fitted time delay can be comparable to a single time lag in the CCF and the fit is subject to considerable error.

(2) More sophisticated approach, described in [88], requires calculating the coherence $C_{xy}(\omega)$ and the cross-phase $\theta(\omega)$ of the virtual beam channels:

$$S_{xy}(\omega) = \lim_{T\to\infty} \mathbf{E}\left[\hat{x}(\omega)^* \hat{y}(\omega)\right] \tag{5.14}$$

$$C_{xy}(\omega) = \frac{|S_{xy}(\omega)|^2}{S_{xx}(\omega) S_{yy}(\omega)} \tag{5.15}$$

$$\theta(\omega) = Arg(S_{xy}) \tag{5.16}$$

where $S_{xy}(\omega)$ is the complex cross spectral density of signals $x(t)$ and $y(t)$, $\hat{x}(\omega)^*$ denotes the complex conjugate of the finite Fourier transform of signal $x(t)$ (as defined by Equation 5.3) and $\mathbf{E}$ is the expected value operator. Coherence $0 \leq C_{xy}(\omega) \leq 1$ is a measure of causality between two signals as a function of frequency. If the studied turbulent density fluctuations are not de-correlated between the 2 virtual beams, the coherence of the signals should be high for the relevant frequency range. Firstly, an appropriate time window is chosen in a plasma discharge with high coherence of the virtual beam signals. Then, the cross-phase and the phase velocity of fluctuations v_{phase} is calculated as:

$$\theta(\omega) = \frac{\Delta z}{v_{phase}} \cdot \omega \tag{5.17}$$

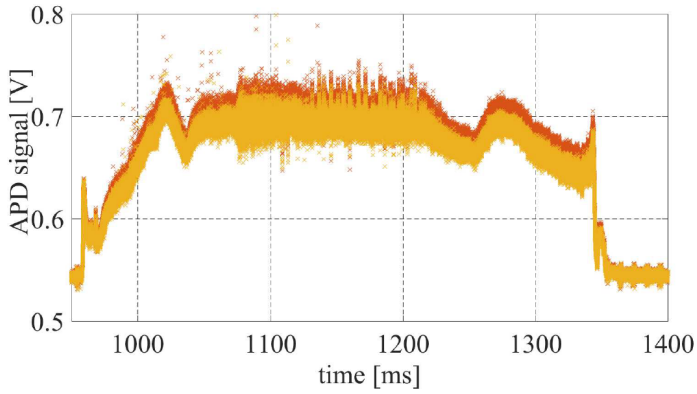

Figure 5.12: Separated virtual beam signals measured by APD channel 12 for a deflected lithium beam measurement in COMPASS discharge #12936.

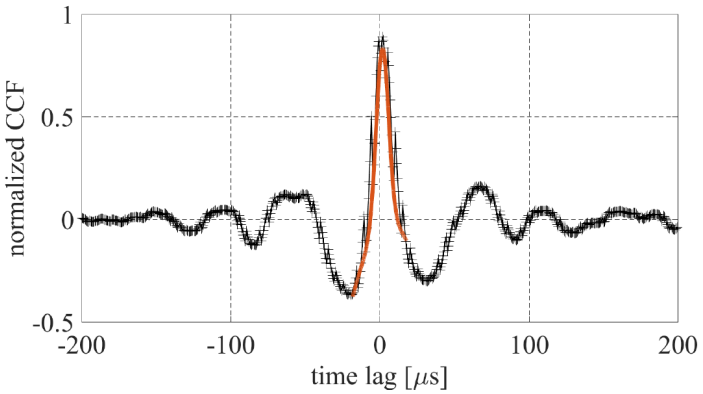

Figure 5.13: Gaussian fit of the CCF function of virtual beam signals measured by APD channel 16 in COMPASS discharge #12936.

where $\omega = 2\pi f$ is the angular frequency. If the dependence of the cross-phase on frequency is close to linear for the highly-coherent frequencies, this means that the phase velocity is approximately constant across that frequency range. One can then assume that the plasma poloidally rotates as a solid body with $v_{pol} = \langle v_{phase} \rangle$ [88].

I calculated the poloidal velocity profile in COMPASS discharge #12936 for a time window $t = 1300 - 1310$ ms using both of the above mentioned TDE methods. 60 keV lithium beam was deflected between 2 poloidal positions, separated by ~ 2 cm (calculated from the used deflection voltage of ± 200 V), with a frequency of 200 kHz. Figure 5.12 shows the raw light signal measured by APD channel 12 with different colors depicting the separated points belonging to the two poloidal beam positions. For each APD channel, the separated virtual beam signals were filtered by a Butterworth bandpass filter. The relevant frequency range of the turbulent structures was chosen as $0.2 - 250$ kHz. For fitting of the CCF functions, several model functions were tried and the best outcome in terms

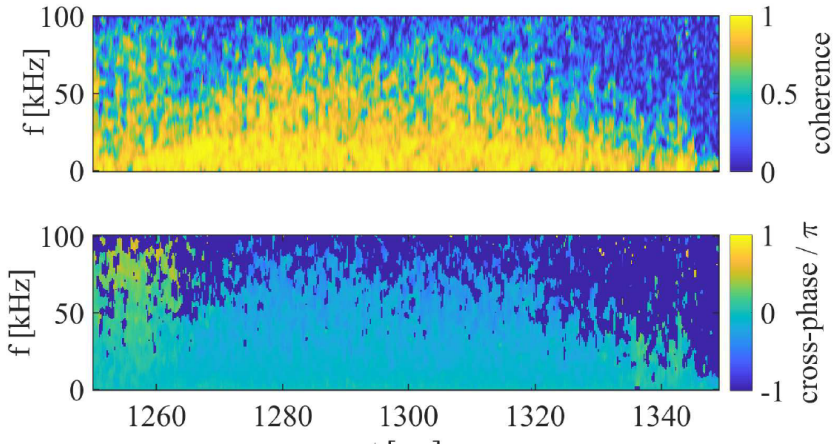

Figure 5.14: Temporal evolution of coherence and cross-phase spectra of the virtual beam signals measured by APD channel 16. 100 ms time window during COMPASS discharge #12936 is shown.

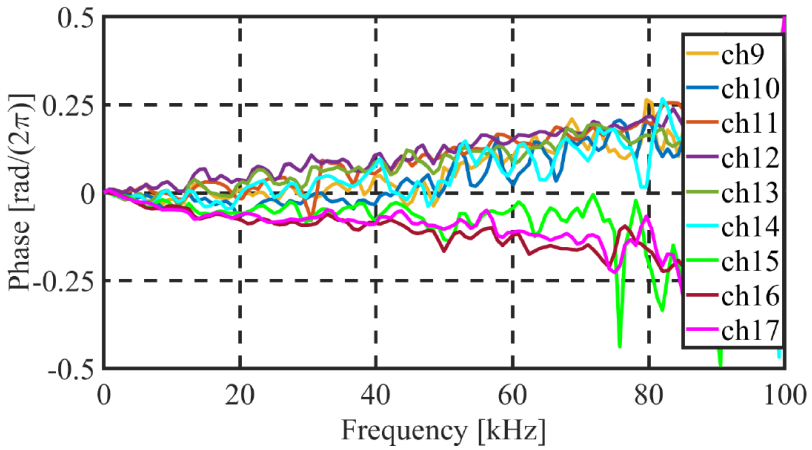

Figure 5.15: Cross-phase spectra of all virtual beam channels calculated for chosen 10 ms time–window in #12936.

of precision of the fit was achieved with modified gaussian fit (see Figure 5.13):

$$f(x) = A_1 e^{-\frac{z^2}{2}} + A_4 + A_5 x + A_6 x^2 \quad ; \quad z = \frac{x - A_2}{A_3} \tag{5.18}$$

The temporal evolution of the coherence and cross-phase of virtual beams measured by APD channel 16 for the relevant time window of the discharge can be seen on Figure 5.14. It shows that high coherence above 0.5 is seen for frequencies up to $\sim$ 80 kHz. Figure 5.15 shows the cross-phase of the virtual beam signals in the chosen 10 ms time window and for the high-coherency frequency range of $0-100$ kHz. It can be seen that the cross-phase dependence on frequency is close to linear for individual APD channels. The slope of a linear fit of the cross-phase signal then determines the respective time delay for each channel. Comparison of the calculated time delay profiles by both methods can be seen on Figure 5.16a. In comparison, the calculated time delay profiles by the two methods have a sim-

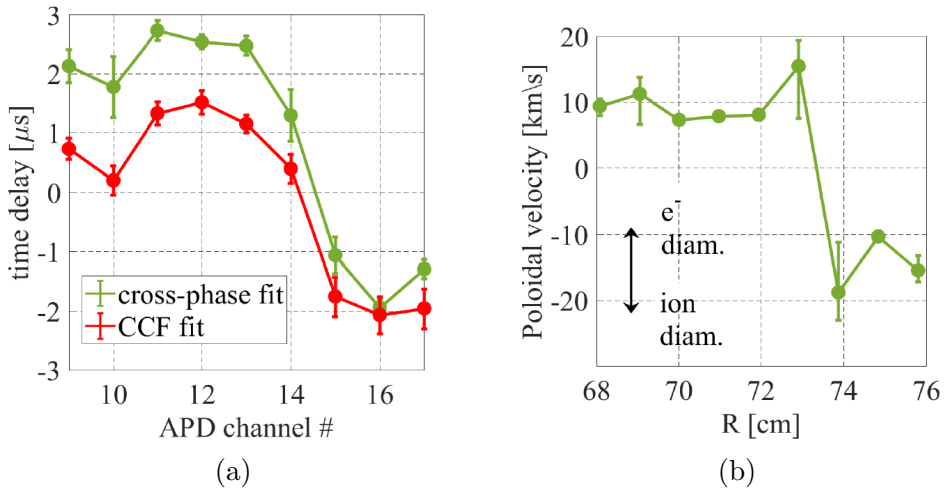

Figure 5.16: (a) Comparison of time-delay of virtual beam channels calculated by both methods for 10 ms time–window in #12936. (b) Radial profile of the poloidal flow velocity calculated by the cross-phase fit method. Here, positive velocity denotes the electron diamagnetic drift direction.

ilar shape but substantially differ in the amplitude. We consider the cross-phase fit method as the more reliable one, because the fit error is considerably smaller. Figure 5.16b shows the poloidal velocity profile calculated from the time delays of the cross-phase fit method, given the virtual beam separation of 2 cm. The negative (downward) velocity direction corresponds to the ion diamagnetic drift direction. The poloidal velocity shear is the highest in a narrow region near the separatrix, where the flow direction is reversed and its amplitude is in the order of 10 km/s. An integrated measurement of the poloidal rotation velocity done by spectroscopic measurements of the CIII triplet [17] on COMPASS specified the range of velocities as -10 to 2 km/s. It is important to note, that the Li-BES measurement suffers from a considerable error induced by the large diameter of the beam of $2-2.5$ cm which can lead to a large overestimation of the calculated velocities. From this reason, the measurement is suitable only for the determination of the velocity shear profile, not for the assessment of its absolute value.

5.6 Fast H-mode density observations

This section presents observations of the fast density changes by Li-BES APD system during ELMy H-mode discharges on COMPASS. Part of the observations was already published in [9, 53].

ELMs are categorized to several types, the most common being type I (large amplitude, less frequent, carrying $10-15$ % of the energy stored in plasma) and type III (smaller amplitude, more frequent, carrying $1-5$ % of energy) [89]. ELMs observed on COMPASS have a typical timescale of ~ 100 μs for the pedestal crash phase and ones to tens of ms for the pedestal relaxation phase, depending on the amplitude and frequency of the ELM event [2, 53]. Most of the ELMs observed on COMPASS are considered to be type III ELMs, while the observation of type I ELMs is disputed.

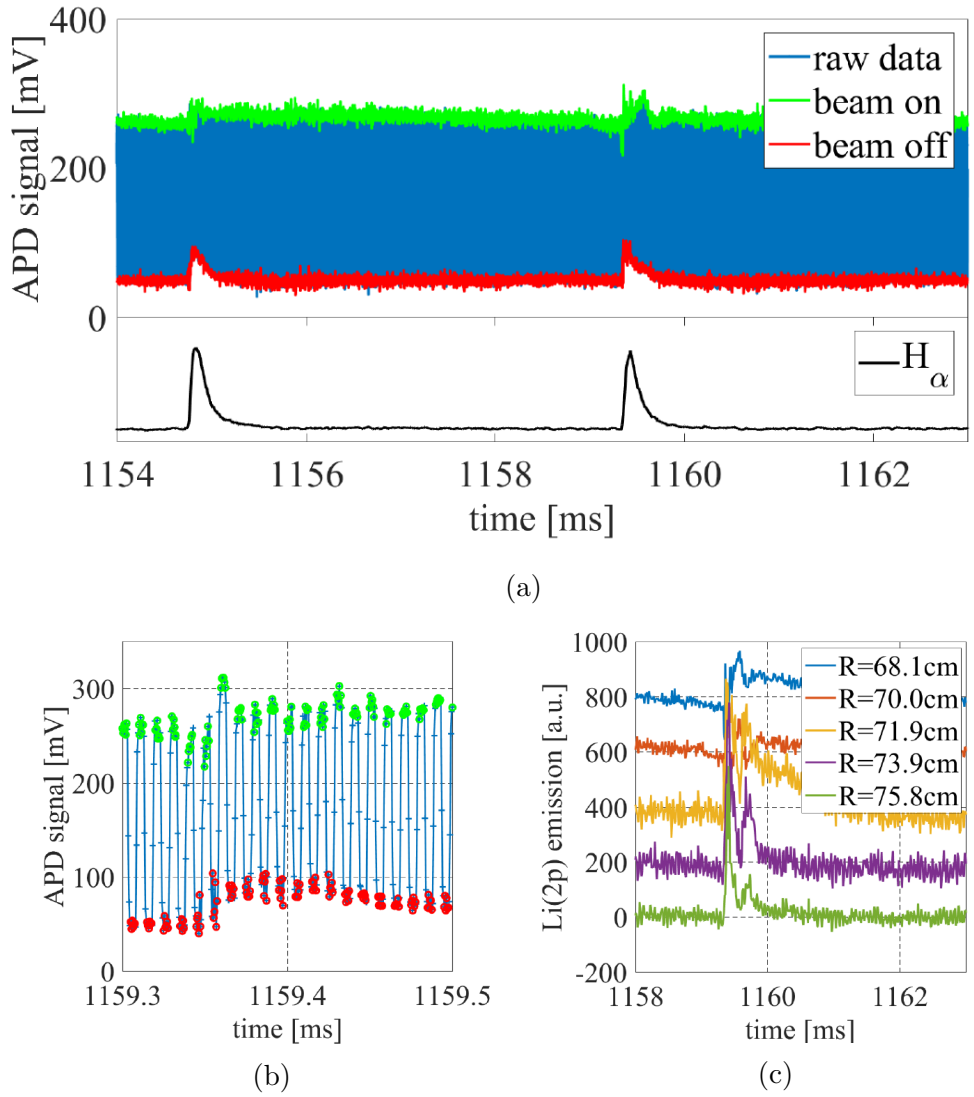

Figure 5.17: (a) 9 ms evolution of raw light signal (blue) measured by APD channel 11 during ELMy H-mode COMPASS discharge #14160. 60 keV lithium beam was injected with fast chopping period 10 μs. Separated beam-on (green) and beam-off (red) times are shown. The bottom plot shows H_α signal with the characteristic ELM peaks. (b) Detail of the fast chopped APD signal. (c) Background corrected lithium light emission signals for 5 chosen APD channels.

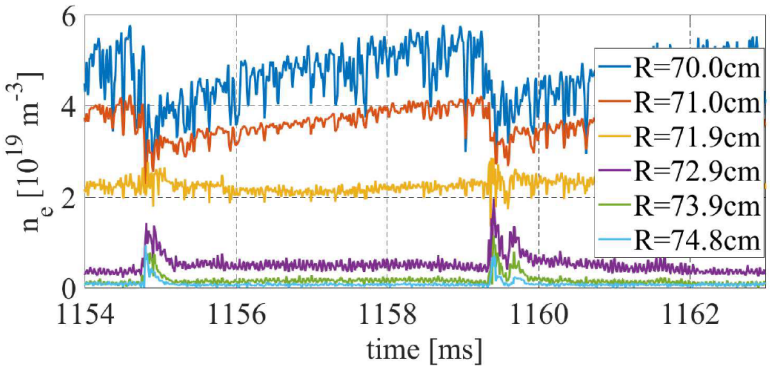

(a)

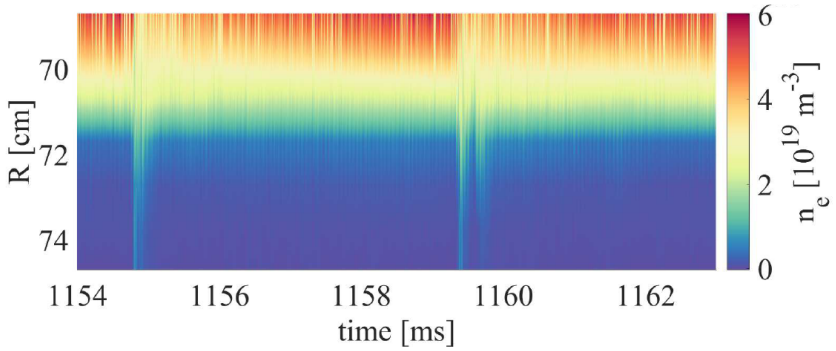

(b)

Figure 5.18: Evolution of reconstructed density from 6 APD channels during 9 ms time window of the ELMy part of the H-mode discharge #14160 illustrated by (a) series of line plots and (b) a surface plot.

Li-BES diagnostic on COMPASS contributes to the diagnostic mix capable of observing the fast ELM phenomena in density (Thomson scattering, microwave reflectometer, reciprocating probes) and its advantage is in the superior temporal resolution, while the disadvantage is moderate spatial resolution and moderate penetration depth of the beam. Lithium beam attenuates faster in the steep H-mode edge density gradient and this results in fewer reconstructed points in the density profile. Typically, Li-BES density reconstruction is not possible beyond pedestal densities of $5 \cdot 10^{19}$ m^{-3} due to insufficient lithium emission and large reconstruction error.

In the H-mode discharges, especially during the ELM crash event, background light signal measured by the APD system is greatly increased and rapidly changing. Therefore to properly evaluate the plasma density, it is necessary to use the fast beam chopping method for background correction. In Figure 5.17, one can see the signal of one APD channel during ELMy H-mode discharge #14160. 60 keV lithium beam was injected into plasma with 10 μs chopping period. The time window of 9 ms is chosen during the ELMy phase. Effect of 2 ELM events (their onset is illustrated by H_α signal) can be seen. Figure 5.17b depicts a detail of 200 μs time evolution of the APD signal during the ELM crash illustrating the fast chopping and separation of lithium emission signal and background. Figure 5.17c then shows the background corrected light signals of 5 chosen APD signals

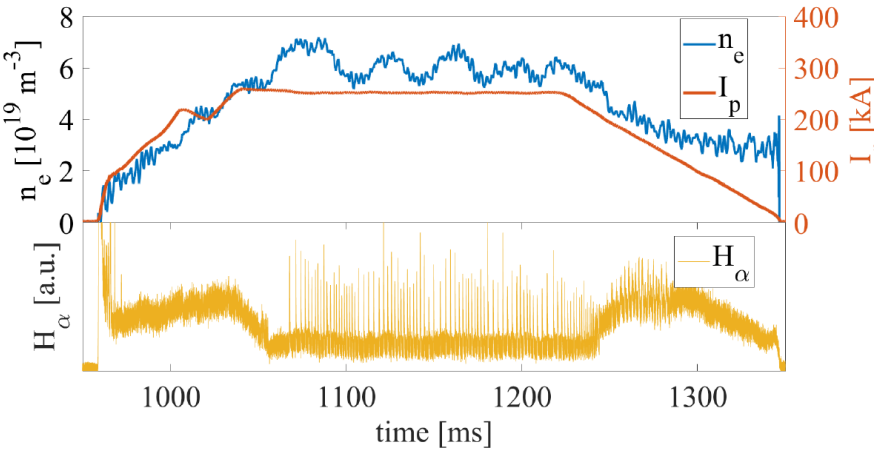

Figure 5.19: Plasma current (red), line averaged plasma density (blue) and H_α emission (yellow) during COMPASS discharge #11290 with long stable ELMy H-mode phase.

during the ELM crash. A fine structure of the ELM can be seen with 2 distinct filament structures. Density reconstructed for the same discharge can be seen in Figure 5.18. It clearly shows that the density is pumped out during the ELM crash. The plasma density on more inner radial positions quickly decreases, while the outer edge and SOL channels mark an increase. This fast ~ 200 μs phase is followed by a much longer density relaxation phase.

In order to reduce the noise of the fast reconstructed profiles and observe the evolution of an average ELM density, conditional averaging of ELM density profiles reconstructed by Li-BES was done for discharge #11290 (main parameters are shown in Figure 5.19). This particular discharge featured a long flat-top phase in ELMy H-mode with relatively stable plasma density and very periodic ELMs with similar amplitudes. 60 keV lithium beam was injected with chopping period of 4 μs. For the conditional averaging analysis, 65 ELMs were chosen in a time window $t = 1070 - 1210$ ms. ELM peak times were detected by the threshold method from the H_α signal, in a similar way as in the SOL blobs analysis in Section 5.4.2. For each ELM, the evolution of density profiles was stored for a normalized time window starting with the onset of the ELM and ending with the onset of the next ELM, thus covering the whole ELM cycle. The stored temporal evolutions of the density profile for 65 ELM events were then averaged and the results of the analysis are shown in Figure 5.20. In Figure 5.20a, the propagation of the density perturbation towards the outer channels can be clearly observed. The innermost reconstructed channel (normalized radius $\rho = 0.78$), which is beyond the top of the density pedestal, shows only minor perturbation, indicating that the core density levels beyond the pedestal are not much affected by the ELM. The evolution of the approximate top of the density pedestal ($\rho = 0.91$) can be seen in Figure 5.20b. It clearly shows the fast density pump out phase and longer relaxation phase. Also regarding Figure 5.20c, it can be seen that during the last ~ 20 % of the ELM cycle the density pedestal is practically fully rebuilt. This is the reason why pedestal scaling calculations on tokamaks are usually made only from measurements during the last 20% of the ELM cycle [53, 90].

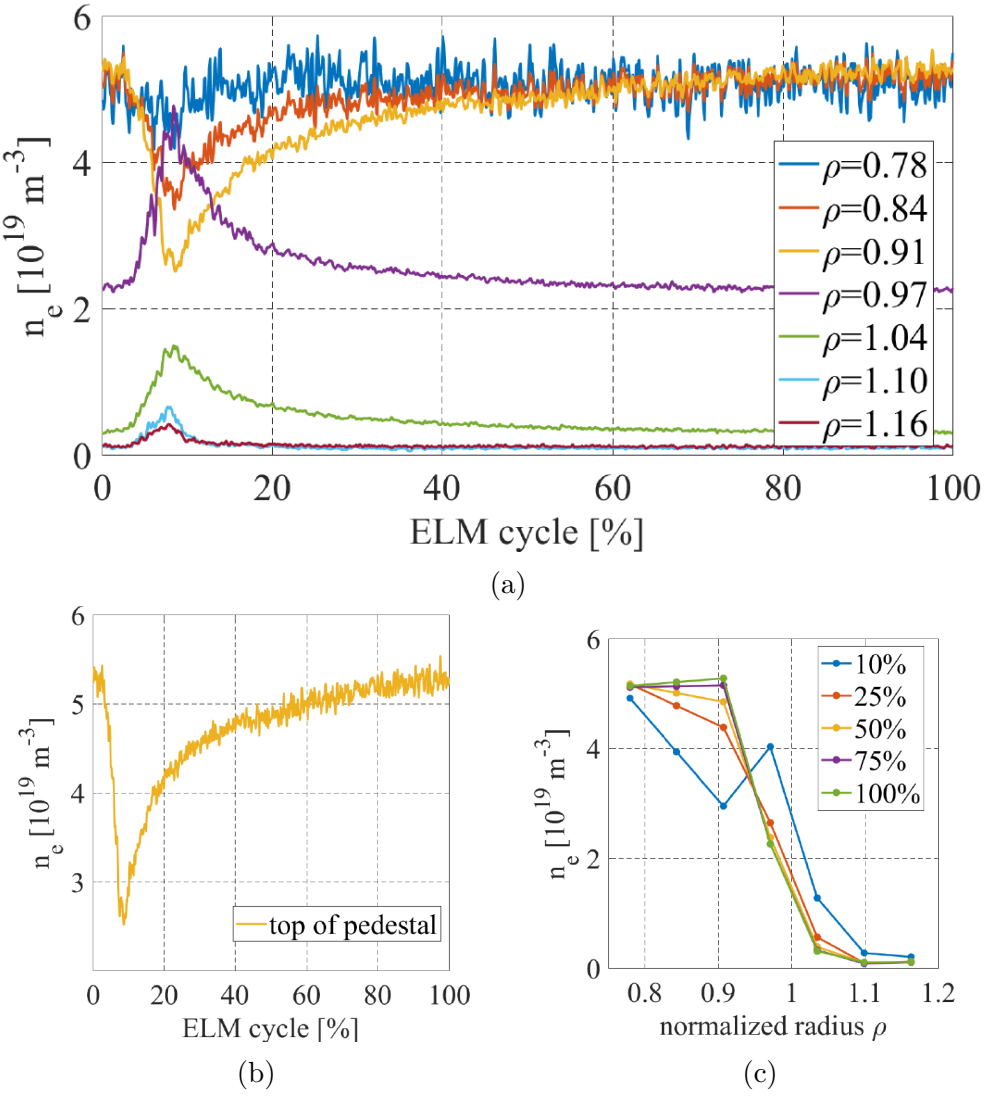

Figure 5.20: (a) Density evolution at different normalized radii for a conditionally averaged ELM from 65 ELM events in COMPASS discharge #11290. (b) Detail of the density evolution of APD channel at the top of density pedestal. (c) Radial density profiles at 5 different times of the ELM cycle.

6. Atomic Beam Probe

Atomic beam probe is a diagnostic method proposed as an extension of standard BES diagnostic using diagnostic neutral beams. It aims to (1) complement the edge electron density measurement by BES and (2) measure the fast changes of the edge plasma current density profile. Development of this new diagnostic method was one of the main goals of my thesis and consisted mostly of my independent work. The diagnostic development and measurement results are described in [A2] and also in [91, 92].

6.1 Motivation

Presently, the fusion research is in the stage of construction of the ITER tokamak and its main focus switched from physical to technological and operational tasks. However, there are still fundamental physical questions which need to be answered in order to ensure safe and successful operation of ITER. One of those open questions is the ELM instability. As was stated previously in Section 5.1.1, the widely accepted concept of ELM's formation in tokamaks is the theory of peeling-ballooning instability. To prove this theory, it is necessary to simultaneously measure the plasma pressure profile and the plasma current density profile with a good temporal and spatial resolution. The temporal resolution must be shorter than the characteristic time of the ELM cycle.

Multiple diagnostic techniques were developed on toroidal devices in order to address this issue. The main ones are described in the next few paragraphs:

(1) Zeeman effect is a quantum physics phenomenon, where the spectral line of an atom splits into several components in the presence of a magnetic field. The difference between the split energy levels is directly proportional to the local magnetic field: $\Delta E \propto \mu_B m_l B$, where μ_B is the Bohr magneton, m_l is the magnetic quantum number and B is the magnetic field strength. By measuring the spectral separation, polarization or intensity ratio of the split lines, it is possible to calculate the local magnetic field strength. If the poloidal component of the magnetic field can be distinguished from the much stronger toroidal field, then the current density in the observed area can be deduced. Such measurements were done on DIII-D [93, 94], JT-60U [95] and JET [96] measuring the split of the Lithium spectral line Li(2p-2s) from a diagnostic lithium beam into three ≈ 0.1 nm separated spectral lines. However, this diagnostic has limited temporal resolution.

(2) Heavy Ion Beam Probe (HIBP) [97, 98, 99] is a diagnostic injecting singly charged heavy ions (i.e. Cs^+) into the plasma with high enough energies (up to several MeV) to overcome the strong toroidal magnetic field. Secondary ionization of the beam occurs in plasma and the doubly ionized atoms follow a trajectory outside the vessel and are detected by an energy analyzer. HIBP primarily measures the plasma electric potential and plasma density fluctuations, but the toroidal shift of the detected ions can be used to deduce the poloidal magnetic flux (and thus the current density). Such measurement of the poloidal

magnetic flux was done on TEXT [100]. HIBP uses beam sweeping technique to change the place of secondary ionization (sample volume) and so to measure the whole poloidal magnetic flux profile. Again, this limits the temporal resolution of the diagnostic.

(3) Faraday effect is the rotation of polarization of a linearly polarized electromagnetic wave propagating along a magnetic field in plasma. It arises from the fact that left-hand (L-wave) and right-hand (R-wave) circularly polarized waves propagate with slightly different velocities. By measurement of the angle of Faraday rotation of a laser beam wave traveling through plasma, it is possible to deduce poloidal magnetic field (and so current density) fluctuations [101]. However, the effect is line-averaged along the laser beam path and thus limits the spatial diagnostic resolution.

(4) Recently, a similar method to HIBP, Laser-driven Ion-beam Trace Probe (LITB) was proposed to measure the current density profile in tokamaks [102].

The above mentioned diagnostic methods are complex and technically challenging and there are fundamental limitations of their temporal and spatial resolution. From these reasons, there has not yet been a measurement of the fast edge plasma current density changes in an individual ELM. The novel concept of the ABP diagnostic aims to fill this gap.

6.2 Principle of the diagnostic

The ABP diagnostic is a novel concept for determining the edge plasma current density with appropriate temporal and spatial resolution [91]. The main idea is derived from the concept of HIBP. Instead of detecting doubly ionized heavy ions moving across the plasma, ABP aims to detect once ionized light ions stemming from a diagnostic neutral beam. Also contrary to HIBP, the idea is to detect the ions leaving the plasma, but still inside the vacuum vessel, as HIBP needs to guide the ions well outside the tokamak magnetic field in order to allow measurement in the energy analyzer. Advantage of the ABP concept over HIBP is in the easier way to guide neutrals across the stray magnetic field of the tokamak to reach the confined plasma region and also in the presence of the ion-accelerator of the existing BES system. The disadvantage of this approach is that the use of light ion species in the BES system limits the method's applicability to small and medium-sized tokamaks [91, 103].

The injected neutral diagnostic beam atoms are excited and ionized by interaction with plasma particles. The excitation and ionization rate of the beam is determined by the plasma density and temperature along the beam path and can be calculated from the collisional radiative model described in Section 4.2. Excited atoms emit characteristic radiation and are collected by standard BES diagnostic. Trajectory of the beam ions is curved by the Lorentz force:

$$\mathbf{F} = q\left(\mathbf{E} + \mathbf{v} \times \mathbf{B}\right) \tag{6.1}$$

where q is the electric charge of the ion, $\mathbf{E}$ is the local electric field, $\mathbf{v}$ is the ion velocity and $\mathbf{B}$ is the local magnetic field. The strong toroidal magnetic field of

a tokamak curves the ion trajectory poloidally and basically determines the ion path, while (roughly one order of magnitude) lower poloidal component of the magnetic field along the beam path slightly deflects the ion in toroidal direction. In Figure 6.1, one can see magnetic field in a COMPASS discharge #16058 along with modeled ion trajectories for a 85 keV lithium beam.

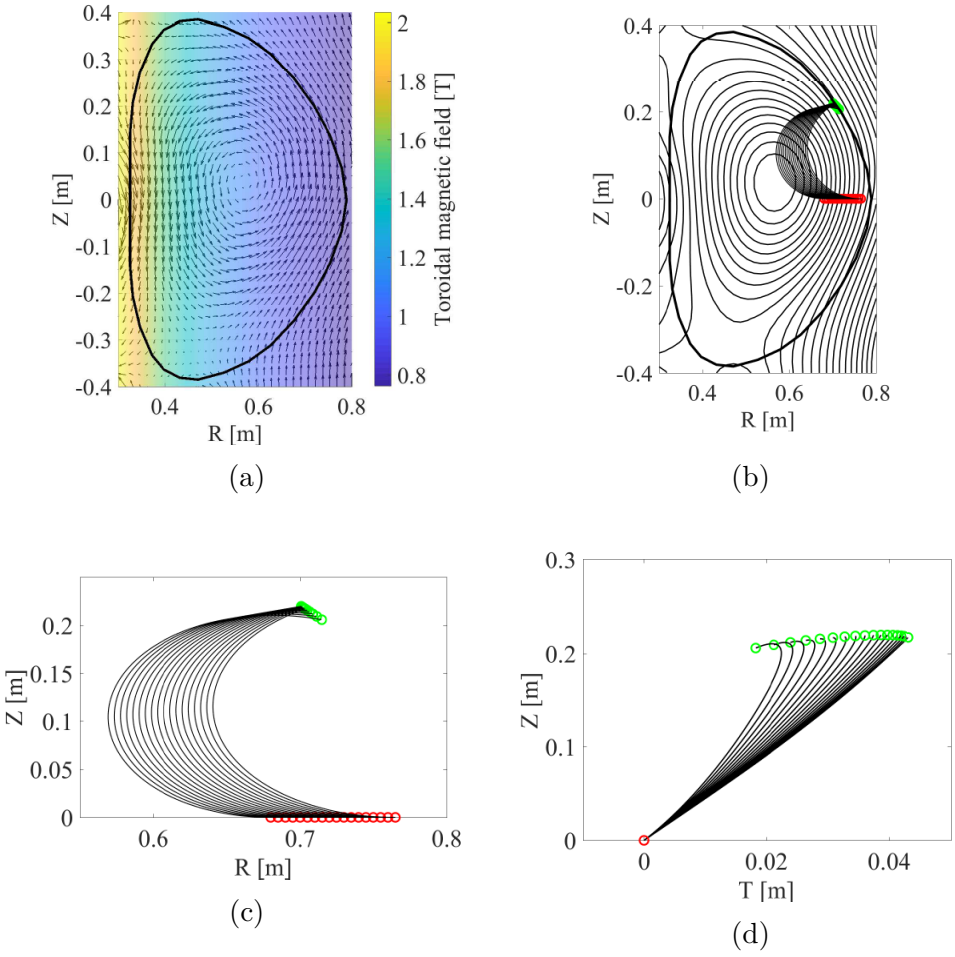

Figure 6.1: (a) Magnetic field in the flat-top phase of COMPASS discharge #16058. Surface plot shows the strength of the toroidal field while quiver plot shows the strength and direction of the poloidal field. (b) Modeled 85 keV lithium ion trajectories. (c) Detail of the modeled ion trajectories in radial-vertical plane. (d) Detail of the modeled ion trajectories in toroidal-vertical plane.

It is important to note that for diagnostic considerations, the effect of the plasma electric field in equation 6.1 on ion trajectories is considered negligible. Electric field in the tokamak plasma is highest in a several cm narrow band near the separatrix region, where (radial) electric field can reach few kV/m. The ions detected by ABP are born in that region. However, their path is influenced by that field and its variations only in the first few cm of their trajectory. As the ion reaches more core regions of plasma, the plasma potential changes are small and do not influence the ion path significantly. The changes of the ending ion position due to electric field were estimated in the order of hundredth of a millimeter [104]. That is one order of magnitude less than the best achievable

resolution of the diagnostic.

The modeled ion trajectories in Figure 6.1 well illustrate the diagnostic concept and the ability of the diagnostic to measure 1) plasma density profile and 2) changes in the edge plasma current density profile.

Density profile reconstruction

Beam ionization profile is determined by the plasma density and plasma temperature profiles along the beam path. Ions originating at different radial positions reach the place of detection at different toroidal-vertical positions. Measured spatial signal intensity distribution on the detector can thus be used to determine edge electron density profile.

Firstly, using ion trajectory modeling in the reconstructed magnetic field by EFIT [105], sample volumes have to be assigned to individual segments of the detector (see Figure 6.2). Equation 6.2 gives us the detected ion current from individual sample volume.

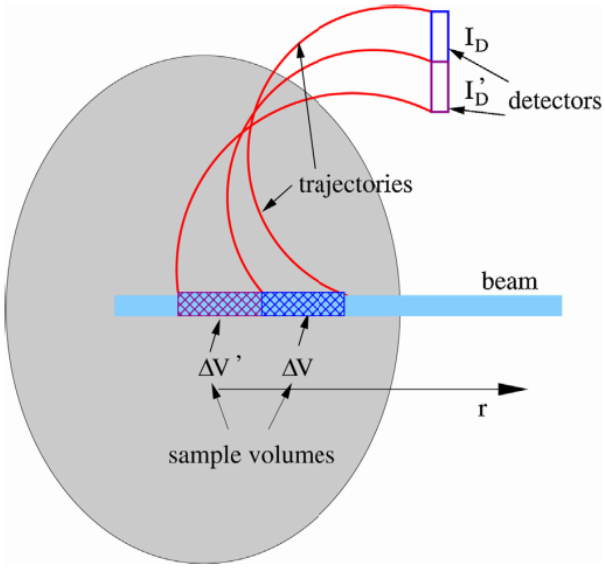

Figure 6.2: Principle of the edge plasma density measurement by the ABP diagnostic. Taken from [91]

$$I_D = n_0(r) \cdot q_e \cdot n_e(r) \cdot S(T_e, r) \cdot \Delta V(r) \tag{6.2}$$

where r is the radial position of the sample volume $\Delta V(r)$, I_D is the measured ion signal on the detector segment, $n_0(r)$ is density of neutral beam particles in the sample volume, q_e is the elementary charge and $S(T_e, r)$ is the beam ionization rate in the sample volume, which depends on local plasma temperature. Ionization rate S can be approximated by the following Equation 6.3 defined in [106] as:

$$S = 10^{-11} \frac{(T_e/E_{ion})^{1/2}}{E_{ion}^{3/2} \cdot (6.0 + T_e/E_{ion})} exp(-\frac{E_{ion}}{T_e}) \qquad [m^3 s^{-1}] \tag{6.3}$$

where T_e is plasma electron temperature in eV and E_{ion} is the first ionization potential. The ionization rate can be calculated using an independently measured plasma electron temperature profile by e.g. Thomson scattering diagnostic [13]. It is important to note that alkali atoms have generally high second ionization potential. The losses of signal due to the secondary ionization along the ion path were estimated by Berta [104] as < 0.5 % for lithium and ~ 1.5 % for sodium and we therefore consider them negligible for our measurement.

The determination of plasma density is complicated by the fact that n_0 in Equation 6.2 is attenuated by ionization along the beam path:

$$n_0(r) = n_0(0) \cdot exp[-\alpha(r)] \tag{6.4}$$

$$\alpha(r) = \frac{1}{v_b} \int_0^r n_e(r) S(T_e, r) dr \tag{6.5}$$

where $n_0(0)$ is the neutral beam particle density of the injected (non-attenuated) beam, $\alpha(r)$ is the attenuation factor and v_b is the beam velocity. A complex mathematical method for solving the above mentioned set of equations to reconstruct the plasma density is thoroughly described in the work of Fujisawa [107].

The most challenging task for the plasma density reconstruction by ABP is precise determination of the sample volumes. The numerical error of the ion trajectory calculation is determined by the systematic error of EFIT reconstruction of the tokamak magnetic field. The spatial resolution of the measurement could be as good as few millimeters, directly depending on the diameter of the injected beam and size of the detector segments. This would be a significant improvement of the standard edge plasma density profile measurement by Li-BES on COMPASS, which is 1 cm.

Edge current density measurement

The unique possibility of the ABP diagnostic is to follow the spatio-temporal changes of the edge plasma current density profile, which can be deduced from the toroidal shifts of ion trace on the detector.

Up to now, the only direct measurement of the edge current perturbations during the H-mode phase was done by Thomas [94]. It demonstrated that in a 1.5 MA discharge on the DIII-D tokamak, large current densities above 1 MA/m^2 build up before an ELM crash in a narrow, $2 - 3$ cm wide, edge plasma region near the separatrix. The total current in this narrow edge region equaled approximately 10 % of the total plasma current. If we scale this behavior down to COMPASS parameters, one can expect several tens of kA currents to build up in the edge plasma region during the ELM cycle. If the ABP diagnostic is able to resolve the effect of as high or smaller edge currents on ion trajectories, a measurement of current density evolution during a single ELM cycle is possible.

To assess this possibility, I modeled the ion trajectories (more about the modeling in the following Section 6.3) in a perturbed magnetic field on COMPASS. Local plasma current perturbation modifies the poloidal magnetic field, which in turn shifts the ion trace on the detector position toroidally with respect to its position calculated in non-perturbed magnetic field. In the first approximation, to simulate the effect of plasma current perturbation localized in the narrow

edge plasma region, I modeled this perturbation by a set of "elementary" toroidal currents placed equidistantly along the separatrix (see Figure 6.3).

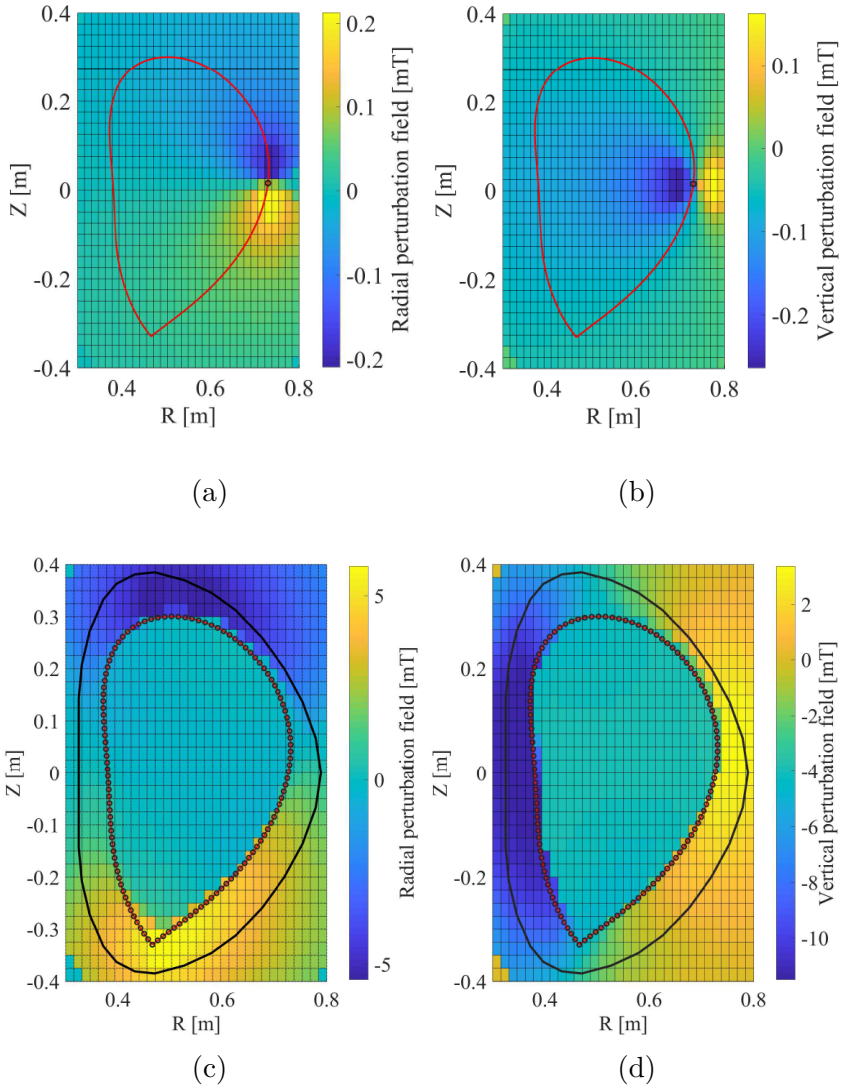

Figure 6.3: Calculated magnetic field components of elementary current loops in the geometry of COMPASS. Red separatrix line is taken from a COMPASS discharge #16058 at time $t = 1100$ ms. (a) Radial and (b) vertical magnetic field generated by a solitary current loop with current $I \approx 83$ A. (c) Radial and (d) vertical magnetic field generated by 120 current loops with total current $I = 10$ kA equidistantly distributed along the separatrix.

Magnetic field $\mathbf{B}(\mathbf{r})$ generated by a steady electric current I following a path C is defined by the Biot-Savart law as:

$$\mathbf{B}(\mathbf{r}) = \frac{\mu_0 \cdot I}{4\pi} \int_C \frac{d\mathbf{l} \times \mathbf{r}'}{|\mathbf{r}'|^3} \tag{6.6}$$

where μ_0 is the vacuum permeability and $\mathbf{r}' = \mathbf{r} - \mathbf{l}$ is the displacement vector from the wire element $d\mathbf{l}$ to the point at which the field is being computed ($\mathbf{r}$).

In our case, the "elementary" perturbation currents can be approximated by infinitely thin circular current loops. The evaluation of the radial and vertical magnetic field components created by these current loops at arbitrary spatial position is a rather complex mathematical problem. Relatively simple analytical expressions for the calculation of the magnetic field components of a horizontal circular current loop with radius a and the loop centre at the origin of cylindrical coordinate system $(r,z,\phi) = (0,0,0)$ are given by [108] as:

$$B_r = \frac{Cz}{2\alpha^2\beta r}[(a^2 + r^2 + z^2)E(k^2) - \alpha^2 K(k^2)] \tag{6.7}$$

$$B_z = \frac{C}{2\alpha^2\beta}[(a^2 - r^2 - z^2)E(k^2) - \alpha^2 K(k^2)] \tag{6.8}$$

while defining the following terms:

$$\alpha^2 \equiv a^2 + r^2 + z^2 - 2ar \tag{6.9}$$

$$\beta^2 \equiv a^2 + r^2 + z^2 + 2ar \tag{6.10}$$

$$k^2 \equiv 1 - \alpha^2/\beta^2 \tag{6.11}$$

$$C \equiv \mu_0 I/\pi \tag{6.12}$$

E and K are the complete elliptic integrals of the first and second kind, defined as:

$$K(m) = \int_0^1 [(1-t^2)\cdot(1-mt^2)]^{-\frac{1}{2}} dt \tag{6.13}$$

$$E(m) = \int_0^1 (1-t^2)^{-\frac{1}{2}} \cdot (1-mt^2)^{\frac{1}{2}} dt \tag{6.14}$$

The results of the edge perturbation currents simulation are illustrated in Figure 6.3. Figures 6.3c and 6.3d show radial and vertical perturbation magnetic field generated by 120 "elementary" currents with a total current of 10 kA localized along the separatrix of COMPASS discharge #16058 at time #1100 ms. Figures 6.3a and 6.3b illustrate the magnetic perturbation field of a solitary current loop located at the outer edge of separatrix.

I modeled 85 keV lithium ion trajectories for the particular COMPASS discharge and time, both in unperturbed magnetic field (reconstructed by EFIT) and in a field perturbed by edge currents of $2, 4, 6, 8$ and 10 kA localized along the separatrix. I calculated the beam ionization profile along its path using the collisional radiative model 4.2 for lithium - plasma interaction, which showed a peak at $R = 0.708$ m. Lithium ions in the model originated from a range of radii $R = 0.68 - 0.73$ m at the lithium beam axis on midplane. The results can be seen in Figure 6.4, which shows ending points of the ion trajectories in the toroidal-vertical ABP detector area. In Figure 6.4b, the points of expected maximum ion signal are shown, corresponding to ions originated at the point of maximum ionization. The toroidal (and slightly vertical) shift of the position of the expected maximum signal in the perturbed magnetic field is well visible, it is ~ 1.2 mm per 10 kA of the perturbation current.

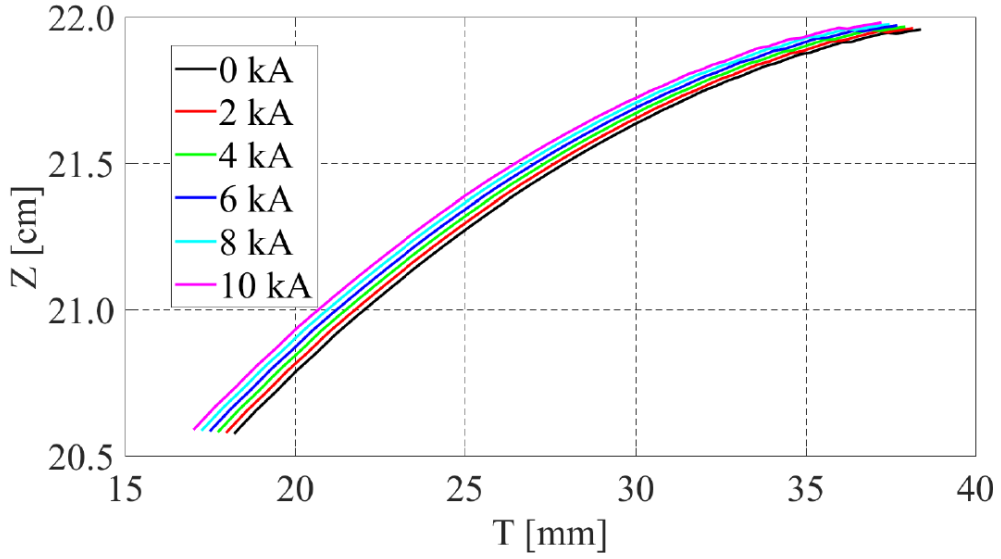

(a)

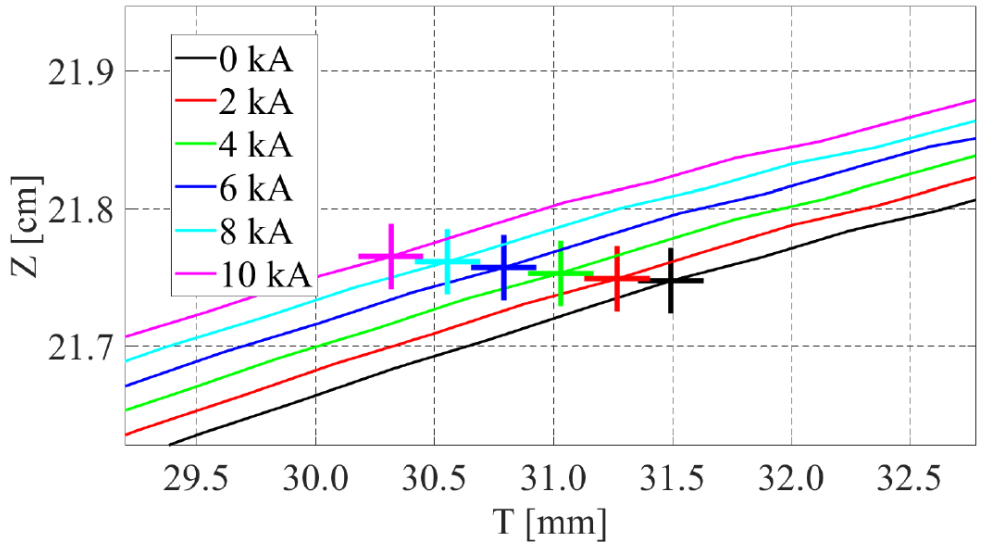

(b)

Figure 6.4: Modeled 85 keV lithium beam ion trace in the toroidal–vertical ABP detection area in COMPASS discharge #16058 at time $t = 1100$ ms with magnetic field perturbed by edge currents of $2, 4, 6, 8$ and 10 kA on the separatrix. On the zoomed Figure (b), cross markers depict the ending position of ions generated at the radius of maximum beam ionization.

The simulation showed that for the desired edge current density measurements during ELMs, the ABP detector has to be able to measure toroidal movements of the ion signal with a mm or even sub-millimeter resolution. This implied the necessity of reducing the injected beam diameter (standardly ~ 2.5 cm) and also limited the possible size of the detector segments. These requirements would in turn limit the level of detected ion signal which could be low compared to noise. Given these challenges, a test ABP detector [91, 109] was designed to prove the diagnostic concept experimentally in the COMPASS tokamak conditions (see Section 6.5).

6.3 Modeling of ion trajectories

From the beginning of the ABP development it was clear that the diagnostics needs to be supported by modeling of ion trajectories in order to:

1. explore the theoretical diagnostic possibilities (as was demonstrated in the previous Section 6.2),

2. support the ABP detector design,

3. support the ABP measurements and interpret the measured experimental data.

Therefore, I developed a sequential numerical code implemented in MATLAB. The code has 2 parts - 1) calculation of the ion source function and 2) calculation of the ion trajectories in given magnetic field.

The first part of the code solves the collisional-radiative model (described in 4.2) to calculate the ionization probability along the beam path and assigns appropriate starting positions to the desired ion population. As a first step, the relevant part of the beam path (usually the range of radii $65 - 75$ cm) is discretized (standardly to 0.1 mm steps) and the beam is thus segmented into small cylinders with the beam diameter. The inputs to the collisional-radiative model are plasma density and plasma temperature profiles along the beam path at a given time, which are provided by the Li-BES ($n_e(r)$) and/or Thomson scattering ($n_e(r), T_e(t)$) diagnostics. These profiles are fitted by a modified Gaussian function F [110] (see Figure 6.5):

$$F(r) = a_{height} \cdot e^{-(\frac{r}{a_{width}})^{a_{exp}}} \tag{6.15}$$

with r as the plasma minor radius and parameters a_{height}, a_{width} and a_{exp}.

Output of the collisional-radiative model is the ionization probability profile along the beam path (see Figure 6.6a). Ionization probabilities are then assigned to the individual beam segments and the number of ions originating from each segment is proportional to the local ionization probability. Starting ion positions in each segment are generated randomly.

Second part of the code solves numerically the equation of motion of ions in the inhomogeneous tokamak magnetic field using the classical fourth-order Runge–Kutta method (RK4) [111]:

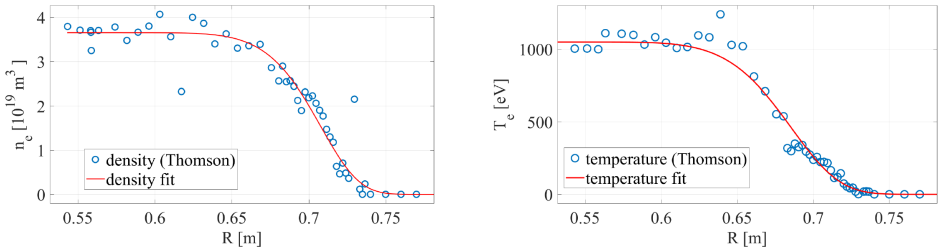

(a) (b)

Figure 6.5: Fit of (a) plasma density and (b) temperature profiles measured in COMPASS discharge #14069 at time $t = 1147$ ms by the Thomson scattering diagnostic

$$\dot{y} = f(t, y), \quad y(t_0) = y_0 \tag{6.16}$$

$$\begin{aligned} y_{n+1} &= y_n + \frac{1}{6}(k_1 + 2k_2 + 2k_3 + k_4) + O(h^5) \\ t_{n+1} &= t_n + h \end{aligned} \tag{6.17}$$

$$\begin{aligned} k_1 &= hf(t_n, y_n) \\ k_2 &= hf(t_n + \frac{h}{2}, y_n + \frac{k_1}{2}) \\ k_3 &= hf(t_n + \frac{h}{2}, y_n + \frac{k_2}{2}) \\ k_4 &= hf(t_n + h, y_n + k_3) \end{aligned} \tag{6.18}$$

Equation 6.16 is the initial value problem. y is an unknown function of time t. Time derivative of y is a function of time and of y itself. At the initial time t_0, the corresponding y value is y_0. Equation 6.17 describes the RK4 approximation of y function at incremental time steps h. Increment coefficients of the method are defined by Equations 6.18. In our case, the y functions to be approximated by RK4 method are the ion velocity vector $\mathbf{v}$ and the position vector $\mathbf{r}$:

$$\begin{aligned} \dot{\mathbf{r}} &= \mathbf{v} \\ \dot{\mathbf{v}} &= \frac{q_e}{m}\ (\mathbf{v} \times \mathbf{B}) \end{aligned} \tag{6.19}$$

where q_e is the elementary charge, m is the ion mass and $\mathbf{B}$ is the local vector of magnetic field. Components of the magnetic field used for the calculations are taken from the EFIT reconstruction data and interpolated to the ion position by bi-cubic spline functions in each time step of the iterative process. Time step of RK4 method is chosen in order to achieve precision of the ion trajectories (tested in homogeneous magnetic field) better than 0.1 mm. To illustrate the modeling code, trajectories of ions originating from 85 keV lithium beam with diameter

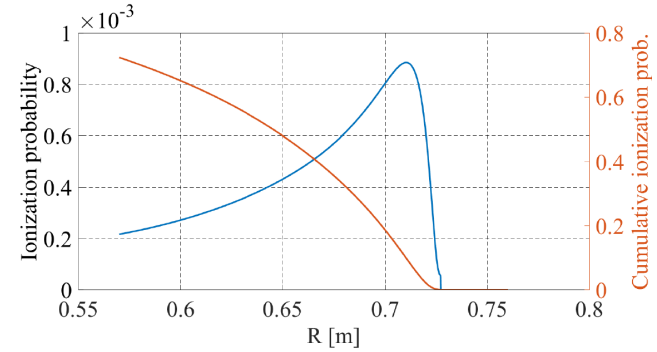

(a)

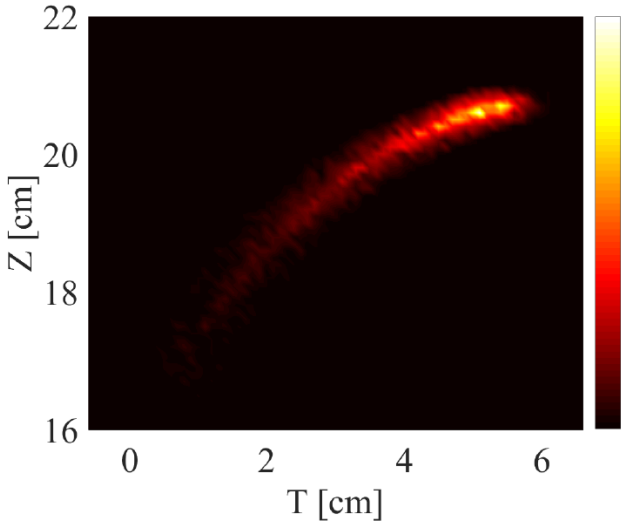

(b)

Figure 6.6: (a) Modeled ionization probability along 85 keV lithium beam path in COMPASS discharge #14069 at time $t = 1147$ ms. (b) Modeled lithium ion signal in the toroidal–vertical detector area for the same discharge and time. 10^4 particles were used in the simulation.

5 mm in COMPASS discharge #14069 at time $t = 1147$ ms were calculated and simulated ion signal at the ABP detector position is shown in Figure 6.6b.

During the development phase of the ABP diagnostic, I used the code for determining the theoretical diagnostic possibilities (more in Section 6.2), for supporting the performed plasma measurements and also to help with the design considerations of the final ABP detector solution. However, for interpretation of the edge current measurements by ABP, an iterative optimization approach is envisaged. From experiences with my code and older sequential code ABPIons [91] we concluded that sequential codes would not be fast enough for these calculations. Therefore, it was decided to adopt a parallel approach. Parallel code (TAIGA - **T**rajectory simulations of **A**BP **I**ons with **G**PU **A**cceleration), based on experience with the two previously mentioned sequential codes, was written by Aradi [112] in CUDA platform and can be run on different NVIDIA GPUs.

The TAIGA code uses also RK4 method to solve numerically the equation of motion of beam ions. The real beam is discretized into numerous parallel

virtual beams ($\sim 10^5$ pieces), and components of the tokamak magnetic field are interpolated using two-dimensional bi-cubic spline functions. Each thread of the given graphical processor is used to solve the equation of motion for particles in given virtual beam, thus virtual beams are processed in a parallel way (see Figure 6.7.). The ion source function in TAIGA is calculated from modeling of the beam ionization using the RENATE code [113].

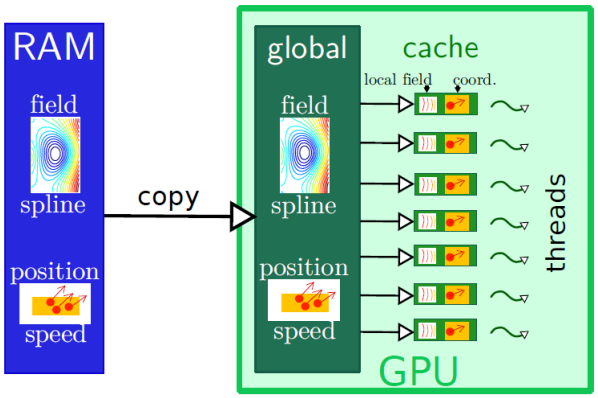

Figure 6.7: The scheme of the parallel calculation of ion trajectories on an NVIDIA type graphical processor. taken from [A2].

6.3.1 Trajectory modeling validation

For the experimental validation of both my code and the TAIGA code, we decided to model lithium ion trajectories for a simple setting of a gas shot on COMPASS without plasma discharge and only with the toroidal magnetic field present. The toroidal field was $B_t = 1.15$ T, energy of the lithium beam was $E_b = 40$ keV and the diameter of the beam was ~ 4 cm. The tokamak vessel was filled up with N_2 gas with pressure $4 \cdot 10^{-2}$ Pa. The ionization rate in such a low pressure gas is weak, the beam attenuation is almost negligible and therefore the ionization probability along the beam path can be considered constant. The lithium ion signal was measured by the test ABP detector (described in Section 6.5). After processing, we observed a very good agreement between the modeled data of both codes and the experimentally measured data.

The position of the maximum ion current intensity according to the TAIGA numerical code was $T_{nm1} = 0 \pm 0.01$ cm, $Z_{nm1} = 14 \pm 0.01$ cm (T denoting toroidal and Z vertical position, see Figure 6.8a). According to my code (see Figure 6.8b), $T_{nm2} = -0.5 \pm 0.5$ cm, $Z_{nm2} = 14 \pm 0.5$ cm. The errors are given by the size of pixels in the histogram, which was determined by the number of particles used in the particular simulation (TAIGA used 10^6 ions and my code used 10^5 ions). The experimentally observed maximum of ion trace on the ABP detector was found to be $T_{exp} = 0 \pm 0.1$ cm, $Z_{exp} = 14 \pm 0.5$ cm, where the error was determined by the size of the detector segments.

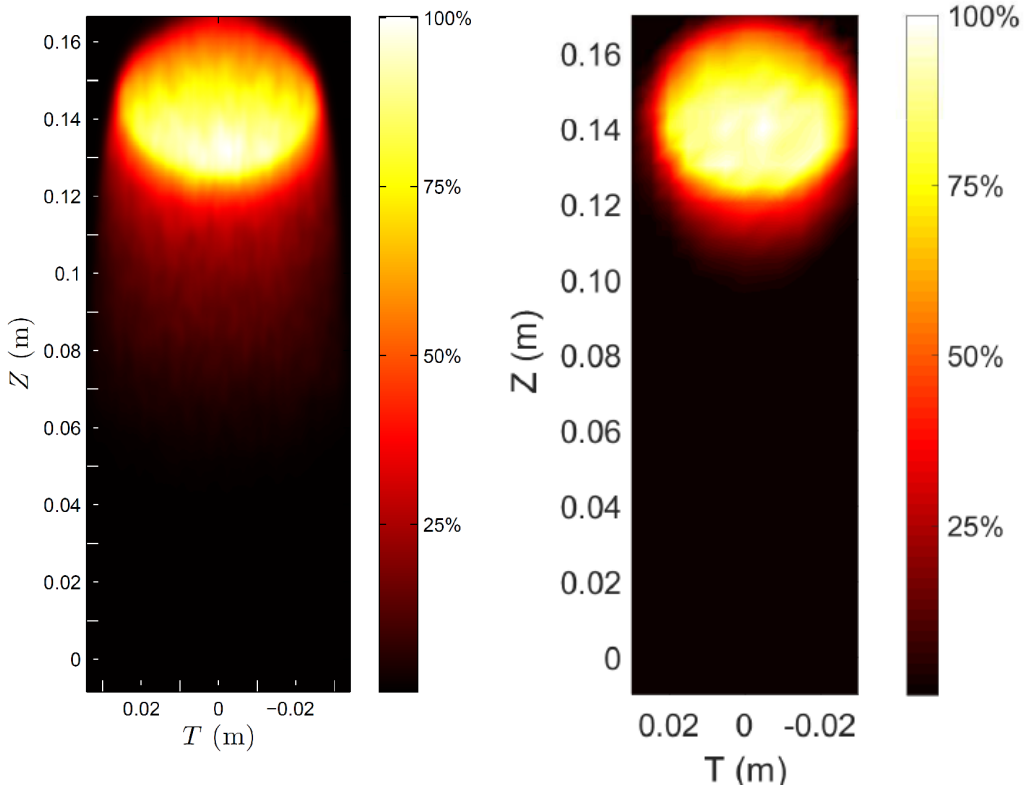

Figure 6.8: Modeled signal of ions in the ABP detector area by (left) TAIGA with 10^6 ions, (right) my MATLAB code with 10^5 ions. Ions originate from 40 keV lithium beam with diameter 4 cm in a gas shot with toroidal field 1.15 T on the COMPASS tokamak.

6.4 Improvements of the beam system

In order to measure with the novel ABP diagnostic technique, significant modifications of the diagnostic beam system were made.

1) Standard BES measurements for density profile reconstruction use $40-60$ keV beam. Higher beam energies would allow deeper beam penetration, but this effect is not significant, while neutralization efficiency decreases rapidly. However, to lead the beam ions out of COMPASS plasma towards the ABP detection area, their Larmor radius in the strong toroidal field needs to be sufficiently high. Larmor radius is the radius of circular motion of a charged particle in a magnetic field:

$$R_L = \frac{m \cdot v_\perp}{|q| \cdot B} \tag{6.20}$$

where m is the particle mass, q its charge and $v_\perp$ its velocity perpendicular to the magnetic field B. For standardly used lithium beam species, to reach the ABP detection area near the available port entrance at position $[R, z] \approx [0.71\text{ m}, 0.2\text{ m}]$ this means energies of $\sim 60-120$ keV for toroidal magnetic fields of $0.8-2.1$ T.

The beam HV parts as well as the HV power supplies were accommodated to achieve the quite ambitious goal of reaching 120 keV beam energy.

Another option for future consideration was investigated - the use of non-standard sodium emitter to create a sodium beam. In that case, beam energies roughly ~ 3.3 times lower (given by the inverse ratio of beam species masses) than for lithium are needed and the neutralization level is better, however significant changes would have to be made for standard BES beam operation (new optical system, new interference filters, inclusion of sodium cross sections in the density reconstruction algorithm).

2) Standard beam diameter in plasma for BES is ~ 2.5 cm depending on the focusing by ion optics. The beam diameter however defines the resolution of the ABP diagnostic (see Section 6.2). As very small toroidal shifts of the beam ion trace in the millimeter or even sub-millimeter order are to be observed by the ABP diagnostic, the beam diameter has to be reduced to a few mm size. For this purpose, a special rotational diaphragm structure was installed in the beam path, see Figure 6.9. The beam diameter can be changed from 1 mm to 20 mm in 5 steps $(1 - 3 - 5 - 10 - 25)$. The beam line is horizontal, the cylindrical structure of the beam reducer can rotate using a stepper motor (for accurate positioning).

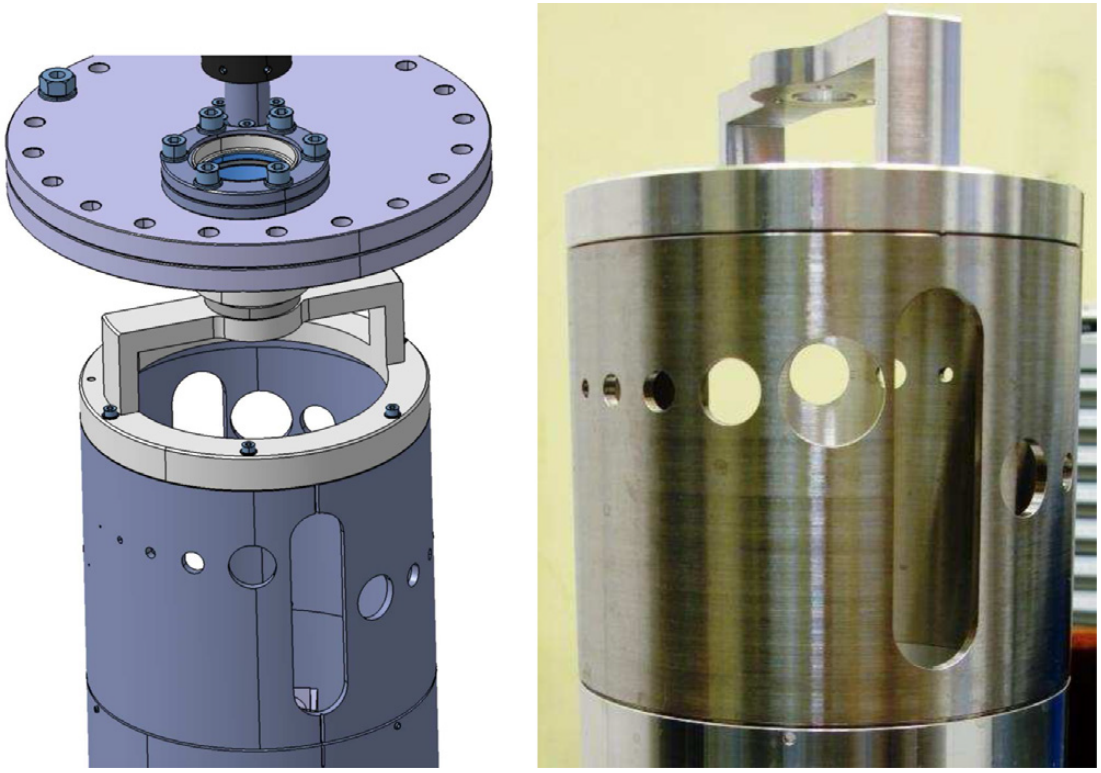

Figure 6.9: Catia model of the beam diameter reducer (left) and manufactured reducer (right). Taken from [91]

.

6.5 ABP test detector

This Section and following Sections 6.6, 6.7 and 6.8 are the extended form of the attached article [A2] Hacek et al.: *First measurements with atomic beam probe diagnostics on COMPASS*.

For detection of the beam ions by the ABP diagnostic on COMPASS, a detector with a matrix of conductive detection plates was designed, manufactured and installed [91, 92, 109]. There were two main aims of the COMPASS ABP test detector:

1. Prove the principle of the ABP diagnostic by detection of the beam ions in plasma and by assessment of the background noise.

2. Provide input for a design of the enhanced final detector solution.

The detector's purpose was to measure the incident ion current to a segmented copper plate. The test ABP detector consisted of a vertically movable aluminum holder structure, detector head with matrix of 20 gold-plated copper detector plates with different surface areas – 5×0.5 mm, 5×1 mm, 5×2 mm (vertical $\times$ toroidal), 4 Langmuir probes for estimation of the local plasma parameters and carbon limiters in order to protect the detector plates from direct plasma inflow (see Figure 6.10). As the detector plates had been placed in a strong toroidal magnetic field which was nearly parallel to their surface, the expectations were that most of the secondary electrons generated by UV/X-ray radiation and by the beam itself would not leave the plates and contribute to the signals.

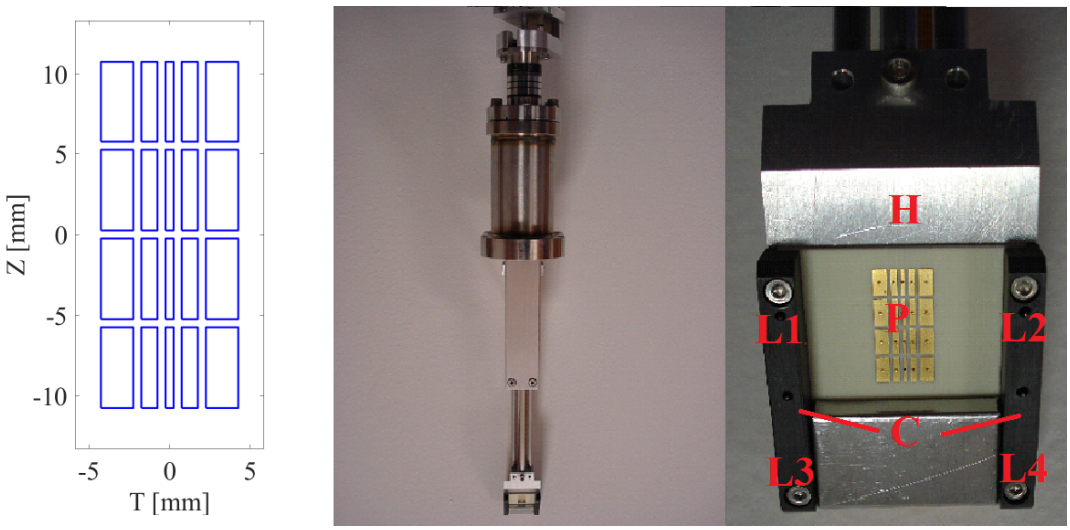

Figure 6.10: Test ABP detector. (left) Scheme of the spatial alignment of the detection plate segments. (middle) Photo of the test ABP detector before installation on COMPASS. (right) Detail photo of the test ABP detector head with copper detector plates of different size (H – Al holder, P – Cu plates, C – carbon limiters, L1, L2, L3, L4 – Langmuir probes).

The ion current level on the plates was expected in the order of μA [91]. To measure such low currents, current amplifiers were used to convert the currents to

voltage signals. The first stages of the amplifiers were connected to the detector plates and kept the input at ground potential [91]. The detector was inserted through a top vertical oval port at the same toroidal position as the lithium beam (see Figure 6.11). The vertical position of the detector head could be changed by approximately 10 cm - minimum insertion kept the detector well hidden in the port shadow while maximum insertion was located well inside the plasma for usual D-shaped COMPASS tokamak discharges. The test ABP detector head was grounded to the tokamak ground.

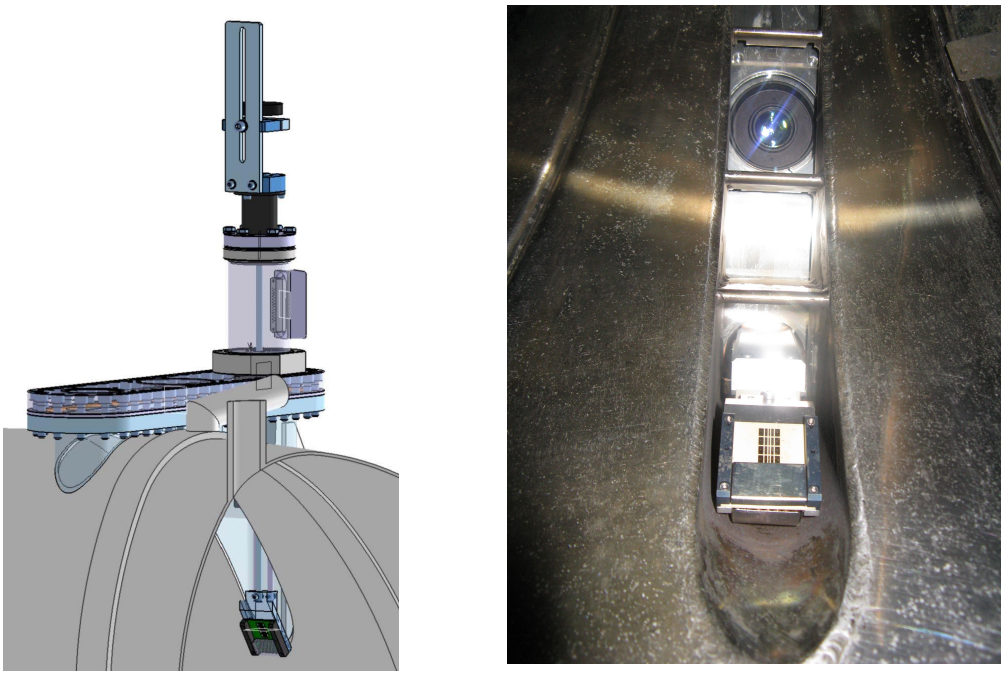

Figure 6.11: (left) CATIA model of the mounted ABP test detector through a top vertical oval port on the COMPASS tokamak. Taken from [91]. (right) Photo of the mounted test ABP detector on COMPASS

The fact that the test detector was not movable in the toroidal direction meant that while it was sufficient for the plasma noise determination, it could not detect the lithium beam ions in standard COMPASS plasmas with plasma currents exceeding certain threshold depending on the beam diameter and plasma shape. The ions were toroidally deflected by a few cm in the poloidal tokamak magnetic field and missed the detector plates (roughly 60 kV of plasma current deflects the center of ion trace toroidally by 1 cm). The way to observe the ions in a regular plasma discharge was either to shoot the beam under an angle of few degrees or detect the ions in the current ramp-up or ramp-down phase of a discharge. The ions could also be detected after the discharge, when the toroidal magnetic field was still present and the lithium beam was weakly ionized in the residual hydrogen/deuterium neutral gas. The test detector had been designed in this way to avoid mechanical difficulties, while delivering goals stated at the beginning of this Section. The results of the test detector were used to manufacture the proper final ABP detector head with the possibility of toroidal movement.

6.6 Laboratory measurements

In the first plasma measurements with the test ABP detector, several issues appeared. Firstly, the observed ion signal levels as well as the background noise levels were not proportional to the different detector plate sizes. Secondly, the observed ion signals were distorted. One can see the behavior in Figure 6.12 from COMPASS discharge #11344 with toroidal magnetic field 0.8 T and low plasma current of 95 kA. 60 keV Li-beam with $\sim$ 4 cm diameter was injected into the plasma. It was periodically chopped out of the plasma for background correction of the signal with period of 44 ms. The signal distortion appeared during the beam chopping times.

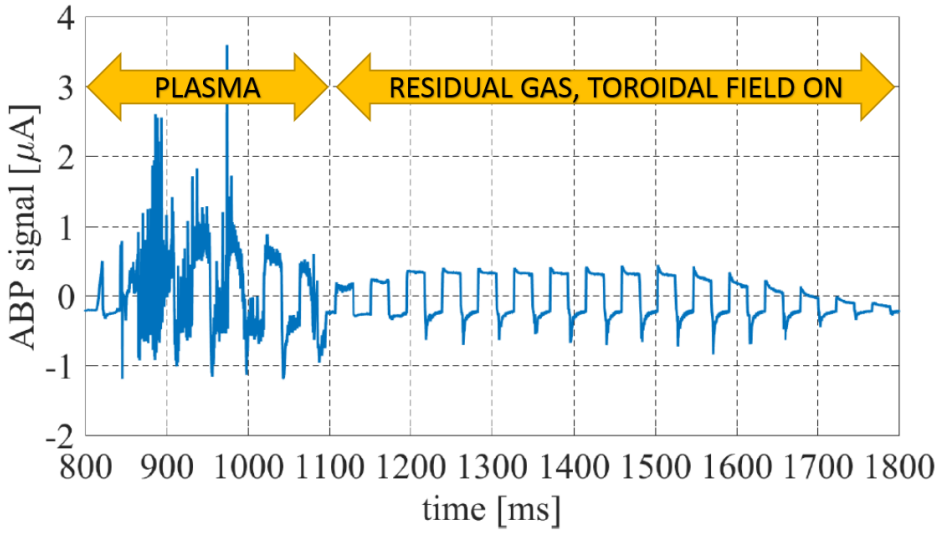

Figure 6.12: Distorted ion signal on 2 $\times$ 5 mm ABP plate in COMPASS plasma discharge #11344.

I found that the signal distortion is linked with a subsequent creation of a microscopic non-conductive layer of plasma-sprayed material on the unprotected detector head and plates. I also found that a significant charge accumulates on the insulation ceramic between individual plates and contributes to their signal in a complex way. To protect the ceramic and plates from these detrimental effects, I modified the detector head and put a copper mask with plate-sized holes 1 mm in front of the detector plates. The detector head was grounded to the tokamak vessel and the mask was isolated from the detector head in order to have a possibility to bias it.

6.6.1 Laboratory measurement setup

To properly understand the measured signals by the ABP detector, I decided to test it in simple laboratory conditions without the influence of plasma or tokamak energetics. I did tests with a laboratory alkali beam (lithium and sodium sources were used) in Wigner Research Centre for Physics in Budapest.

In order to understand the role of secondary electron emission on detector signals, beam ions were injected directly towards the detector. To simulate the tokamak magnetic field and its suppression effect on secondary electrons, neodymium magnets were used (scheme of the experiment is in Figure 6.13a) to create ~ 50 mT magnetic field parallel to the detector surface. To assess the role of the secondary electron emission due to ion impact, the mask was biased negatively and positively either to suppress or pull out the electrons from the plates. Subsequently, I employed a double mask design with a second mask added 2 mm in front of the detector (see scheme in Figure 6.13b). In this setup, the mask nearer to the plates was biased and the second one was grounded.

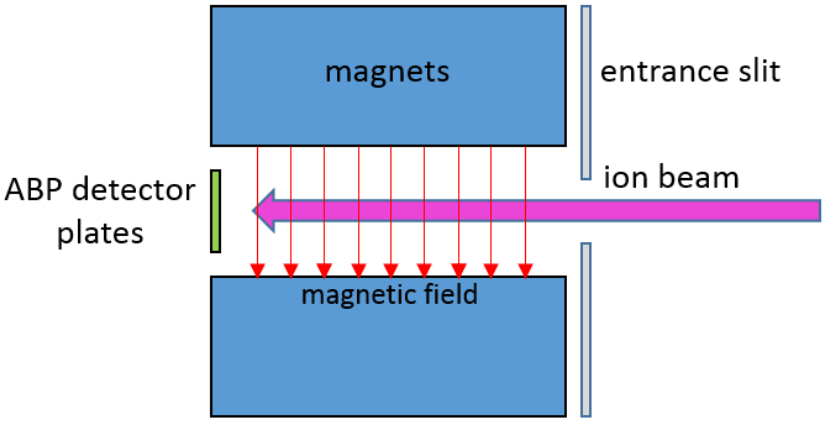

(a)

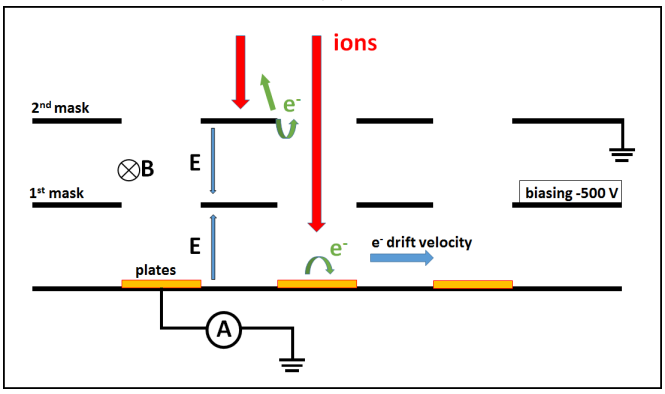

(b)

Figure 6.13: (a) Scheme of the laboratory measurement. (b) Scheme of the double-mask biasing experiment.

6.6.2 Role of secondary electrons

Secondary electrons (SE) are created both on the detection plates and other detector surfaces by ion impact and in plasma conditions also by photo-emission by plasma UV and X-ray radiation and by influx of fast plasma particles. Contribution is affected by the energy and angle of the impacting ions and by magnetic

field lines inclination to the plates.

It would seem the best to negatively bias the mask in front of the detector plates and to properly ground all other detector parts, so that SE emission is suppressed, similarly as in a Faraday cup measurement. The laboratory measurement with biased single and double mask setup can be seen in Figure 6.14. I observed that during positive biasing, voltages above 200 V are sufficient to

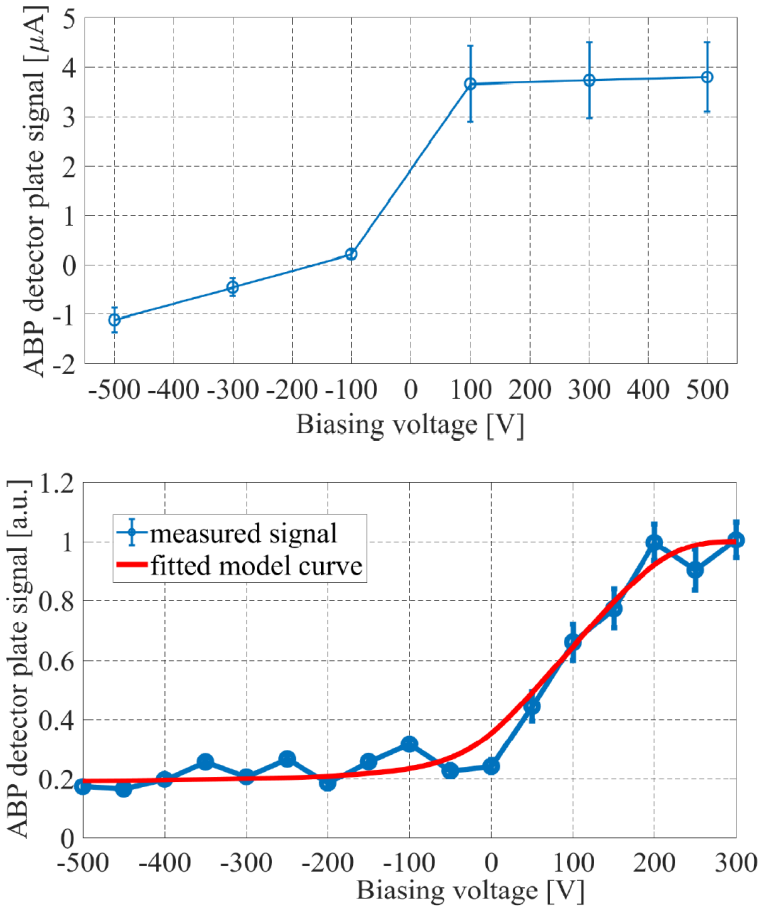

Figure 6.14: (top) Biasing experiment with a single detector mask. (bottom) Biasing experiment with double detector mask (first mask is biased, second one grounded). Experimental data are shown for ABP signals on 2×5 mm sized plates during 20 keV sodium beam laboratory measurement (blue). Red curve represents best fit of the ABP signal by a model, determining temperature of the SE.

stabilize the signal as all secondary electrons are carried away from the plates by $E \times B$ drift motion. During negative biasing, in a single mask setup, the plates' signal got negative and was not saturated for tested voltages up to -500 , V. I attributed this effect to SE originating on the edges of the mask holes, which are then repelled from the negatively biased mask and can reach the detector plates. The effect was not present or was severely limited for the double mask design, where the signals got clearly saturated even for low negative biasing voltages.

To qualitatively evaluate the measurement, I did a Monte Carlo modeling of the escaping SE in MATLAB and fitted the model to the measured data. Tem-

perature of the SE was the fitted parameter of the model. I assumed Maxwellian SE energy distribution and angular distribution of SE velocities determined by the cosine emission law [114]:

$$f(v) = \frac{m_e}{2\pi k_B T_e}^{3/2} \cdot 4\pi v^2 e^{-\frac{m_e v^2}{2k_B T_e}} \tag{6.21}$$

$$f(\theta) = cos(\theta) \tag{6.22}$$

where $f(v)$ is the probability density function of (absolute) electron velocity v, m_e is electron mass, k_B is the Boltzmann constant, T_e is electron temperature and $f(\theta)$ is the probability density function of the SE emission under angle θ to the emission surface normal. The starting electron positions on a detector plate are generated randomly with uniform distribution. The trajectories of individual electrons in the 3D geometry of crossed homogeneous electric and magnetic fields can be calculated analytically. Lets define the following geometry of the problem: Cartesian coordinate system with $\mathbf{E} = (E, 0, 0)$, $\mathbf{B} = (0, 0, B)$, initial electron velocities $\mathbf{v}(0) = (v_{0x}, v_{0y}, v_{0z})$ and positions $\mathbf{x}(0) = (0, 0, 0)$ at time $t = 0$. The electron follows a trochoid curve and its position at time t is [115]:

$$\begin{aligned} x(t) &= R_D - R_D \cdot cos(\omega_c t) \\ y(t) &= R_D \cdot sin(\omega_c t) - v_D t \\ z(t) &= v_{0z} \cdot t \end{aligned} \tag{6.23}$$

$$\omega_c \equiv \frac{q_e B}{m_e}; \quad v_D \equiv \frac{E}{B}; \quad R_D \equiv \frac{1}{\omega_c} \cdot \sqrt{v_{0x}^2 + (v_{0y} + v_D)^2} \tag{6.24}$$

In Figure 6.15a, one can see an illustration of the electron trajectory for different values of mask biasing. Figure 6.15b then shows simulated ratios of electrons escaping from a 2×5 mm plate depending on the biasing voltage of the detector mask and on the SE temperature. Iteratively, I was able to find a best fit of the experimental data (see Figure 6.14). The fit showed that SE induced by ion bombardment of the plates have a temperature $\sim$ 10.2 eV. SE yield was also deduced from the experimental data, as during sufficiently negative biasing, only ion signal is detected, while during sufficiently positive biasing, the measured signal is a sum of ion signal and the whole SE signal. SE yield was determined as $\sim$ 4.9 electrons per incident ion. Both values seem to be reasonable with regards to available literature [116].

Given these results, the contribution of SE on the ABP signal in COMPASS measurements could be estimated. Table 6.1 shows estimated ratios of SE which escape the ABP detection plates on COMPASS. The estimates are given for ABP measurement in a standard COMPASS magnetic field, which is $\sim$ 0.8 T in the place of the ABP detector (1.15 T on the magnetic axis) for different ABP plate sizes and taking into account a possible misalignment of magnetic field lines with respect to the detector plane. The effect of SE suppression by the use of negative biasing voltage -500 V of the first mask is given in brackets.

Given the calculated value of SE yield of $\sim$ 4.9 per incident ion and the tabulated values of the number of escaping SE, the contribution of SE to the

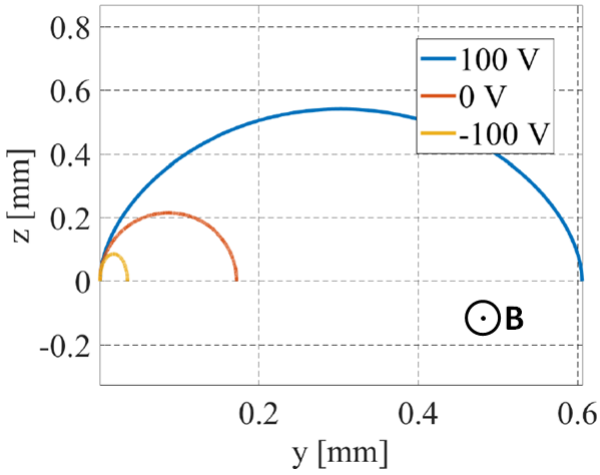

(a)

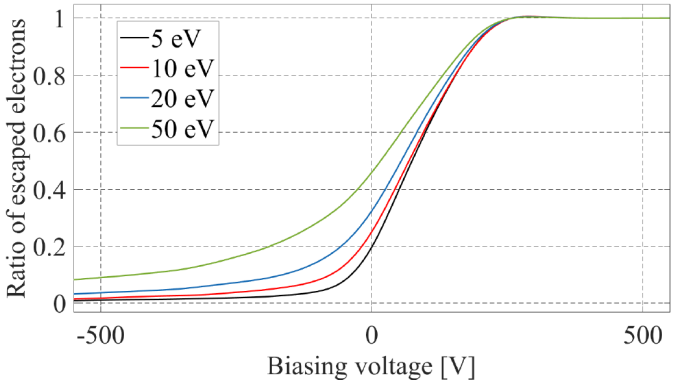

(b)

Figure 6.15: (a) Calculated single electron paths in the crossed electric and magnetic fields. Electron was generated with vertical velocity component only. Velocity was chosen as the mean velocity in 10 eV velocity distribution ($\sim 1.9{\cdot}10^6$ m/s). Electric field was in the z direction. (b) Ratios of escaping secondary electrons calculated for the laboratory biasing experiment with double detector mask for 4 different values of SE temperature.

Plate size [mm]	magnetic field misalignment		
	0°	2.5°	5°
0.5 × 5	3.59 (2.73)	5.65 (3.64)	8.03 (4.88)
1 × 5	2.07 (1.45)	4.26 (2.48)	6.68 (3.77)
2 × 5	1.28 (0.90)	3.50 (2.01)	5.92 (3.27)

Table 6.1: Estimated ratio of escaping SE in % due to the impact of beam ions. Numbers are given for different plate sizes and possible magnetic field misalignments with respect to the detector plane. Effect of SE suppression by negatively biasing detector mask to −500 V is in brackets.

measured signal can be significant, from several % to tens of %, depending on the plate size and magnetic field misalignment. Suppression of SE by negative

biasing of the detector mask can be effective, decreasing the number of escaping SE by tens of %.

An important observation was also that with the double mask setup and when suppressing SE by sufficient negative biasing voltage, the detected signal levels were perfectly proportional to the different plate sizes.

The outcome of the laboratory measurements was the decision to use the double-mask detector head design to 1) protect the insulation ceramic from direct ion impact and to protect the detector plates from being covered by a non-conductive layer during plasma experiments and 2) to use mask biasing as a method of SE suppression.

6.7 Plasma measurements

Measurements in COMPASS plasma discharges aimed to achieve the following goals:

1. assess the background plasma signal and identify background noise sources,
2. demonstrate the ability to reduce beam diameter to several mm,
3. demonstrate the ability of the detector to detect fast chopped beam signals with sub-millisecond time resolution in plasma conditions.

6.7.1 Background plasma signal

The aim of the background measurements was to identify the main noise sources and estimate the signal to background ratio of ABP measurements in regular plasma discharges on COMPASS. I did the measurements with the double-mask, the mask closer to the plates was biased to -270 V, the external one was grounded. ABP signals from 52 L-mode discharges and 17 H-mode discharges were used for the analysis having a wide range of plasma parameters and varying ABP detector insertion depth. The results of the analysis can be seen in Figure 6.16. The data points are mean signal levels of individual ABP plates (aggregate of all plate sizes) calculated over 100 μs time windows from the stable flat-top phase of the plasma discharges.

In Figure 6.16a, data from L-mode discharges with varying ABP insertion levels show a strong dependence of the absolute signal level on the distance of detector from plasma (calculated from EFIT reconstruction). It is clear that to keep a reasonable background signal level, the detector has to be sufficiently distanced from plasma. Figure 6.16b shows data from both L-mode and H-mode discharges, where the distance of the detector from separatrix was equal or greater than 4 cm. The observed background signal there is generally in the range of several tenths of μA. Both negative and positive signals were systematically detected, based on the particular shot and time, with a visible weak dependence on plasma density. During the ELMy H-mode phase, the ABP signals show positive peaks during the ELM crash. These peaks in signal can reach up to few μA.

The strong dependence of ABP signal on distance from separatrix indicates that the background noise is dominated by the inflow of scrape-off layer plasma

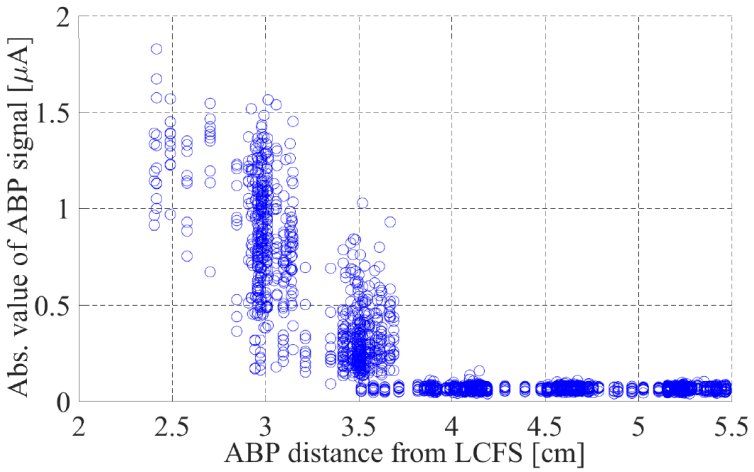

(a)

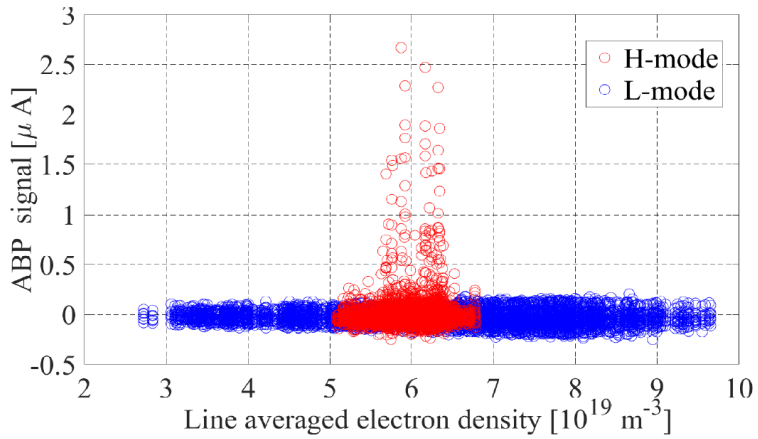

(b)

Figure 6.16: (a) Dependence of the absolute value of ABP background plasma signal on distance from the separatrix in L-mode COMPASS discharges. (b) Dependence of ABP background plasma signal on plasma density in L-mode and H-mode discharges with sufficient distance $d \geq 4$ cm of the detector from separatrix.

particles and not by photoemission by UV/X-ray radiation, which is likely well suppressed by the strong toroidal magnetic field. The electron inflow is more often higher than the ion one, even with the applied negative mask biasing, resulting in net negative signals.

As the measured Li-ion signal on the ABP detector is expected in the order of μA, the signal to background ratio in L-mode COMPASS shots is expected in the order of $10:1$ while in H-mode shots it can be as low as $1:1$. The use of sufficiently fast beam chopping technique will therefore be necessary to correct the signals for background.

6.7.2 Detection of Li-beam ions in COMPASS plasmas

Using the reducer to limit beam diameter does not allow beam injection under non-zero angle. Therefore, with the toroidally fixed test ABP detector, I was able to observe the beam ions only in the current ramp-down phase of plasma discharges. Main parameters of the reference discharge used for the ABP measurements are shown on Figure 6.17.

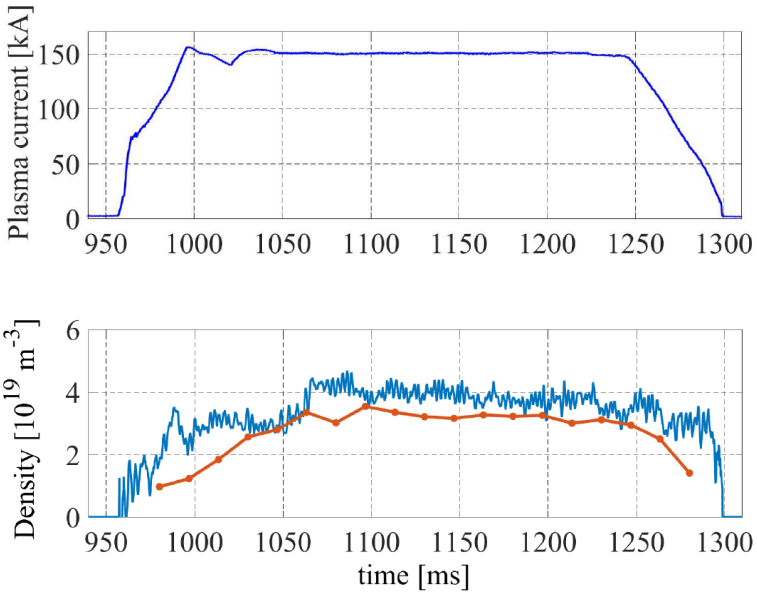

Figure 6.17: Main parameters of the plasma scenario used for Li-ion detection by the test ABP detector. (top) Plasma current, (bottom) Line averaged electron density measured by microwave interferometer (blue) and Thomson scattering diagnostic (red).

As can be seen in Figure 6.18, reduced beams with diameters of 10 mm, 5 mm and 3 mm and with the chopping time set to 1 ms are clearly detectable by the test ABP detector, both in the ramp-down phase of the discharge and after the plasma in residual gas. The ions stemming from the diagnostic beam arrive at detector position when the plasma current is sufficiently low and thus the toroidal deflection of beam ions is small enough. Increasing level of the detected ion current during the plasma current decrease was in agreement with the ion trajectory modeling.

It is important to note that for a proper modeling of beam ion trajectories and thus a successful interpretation of the measured signals, it is necessary to reliably reconstruct the edge plasma density profile along the beam path. That is in order to determine the profile of ionization rate of beam particles and thus starting ion positions. Therefore, a simultaneous measurement of the ABP and APD diagnostics is needed. Figure 6.19 shows the light emission of lithium atoms detected by an APD channel during the reduced beam discharges. Signals detected from 10 and 5 mm beams are sufficient for a density reconstruction while the light emission of 3 mm sized beam is at the detection limit of our BES observation system.

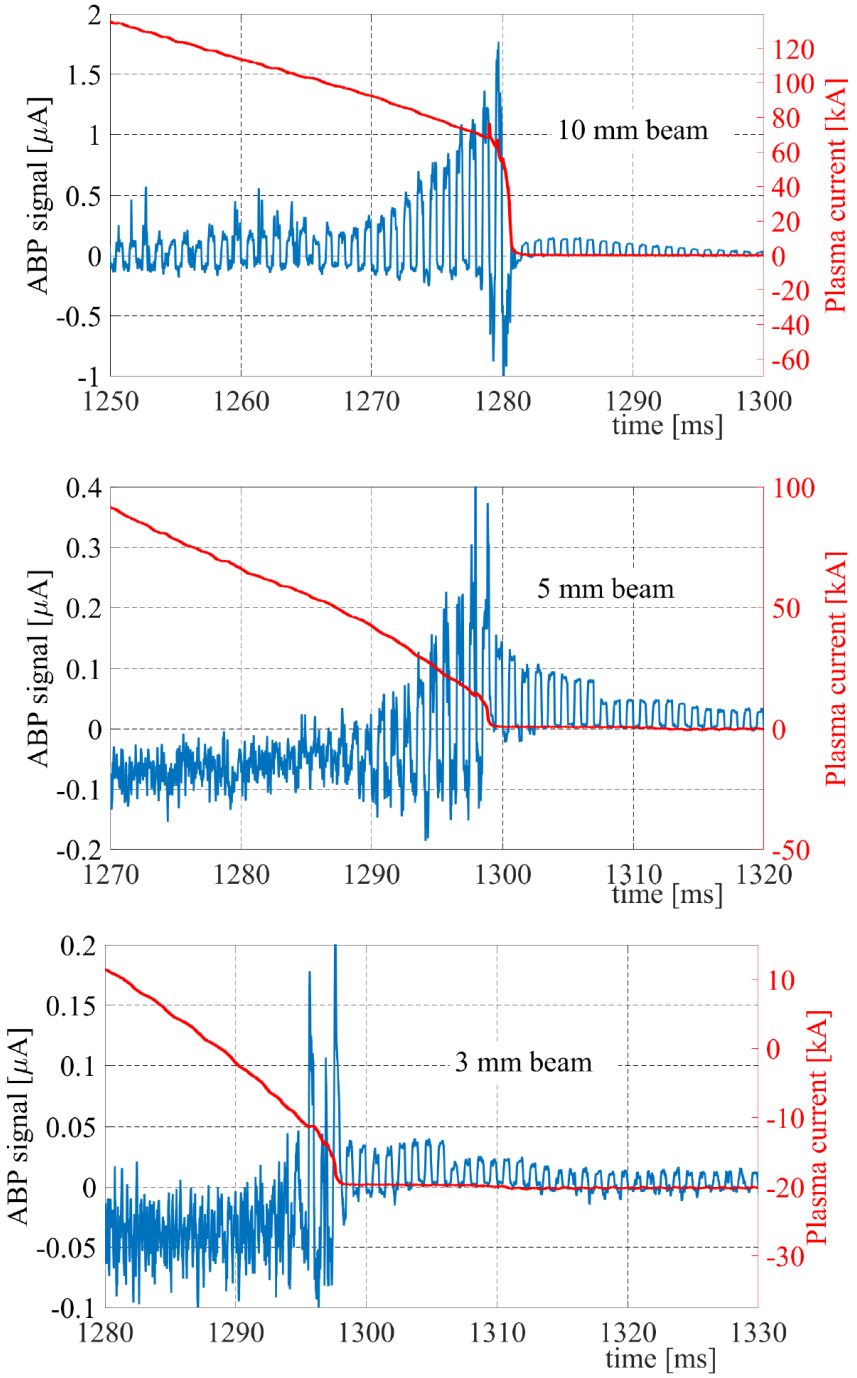

Figure 6.18: Li-ion signals of reduced beams in COMPASS plasma shots detected by 2×5 mm sized ABP plate. Plasma current signal in each discharge is also shown.

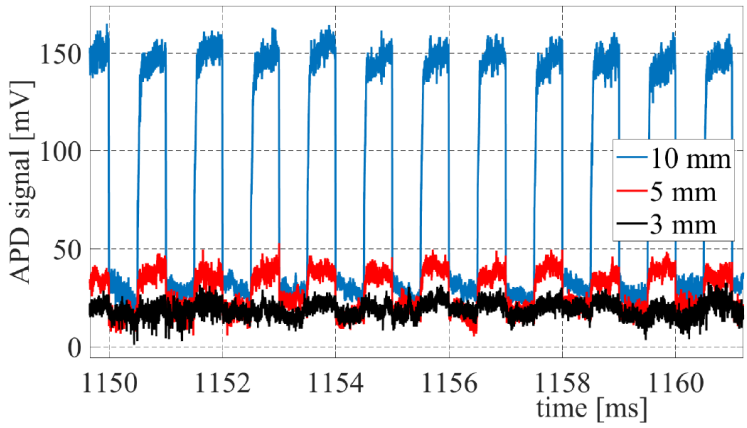

Figure 6.19: Li-beam emission signals detected by an avalanche photodiode detector channel during COMPASS plasma shots. Beams were injected with reduced diameters of 10, 5 and 3 mm. Li-beam was injected in each shot with 1 ms chopping period.

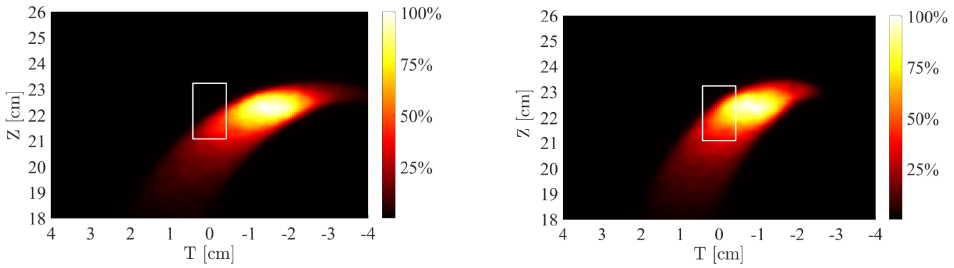

Figure 6.20: Modeled Li-ion trace on the ABP detector plane for 2 time slices of the COMPASS shot #14405 with 10 mm beam diameter.(left - $t = 1250$ ms, right - $t = 1275$ ms. White rectangular frame represents the sensitive area of the ABP test detector)

The ion trajectory modeling done by the TAIGA code for one of the discharges with 10 mm beam diameter is shown in Figure 6.20. It shows the lithium ion trace on the detector plane for 2 different times of COMPASS discharge #14405. The ion trace has a comet-shaped form where its curvature and its toroidal shift from zero position is determined by the edge plasma current. The ion signal intensity along the comet's curve is determined by the edge plasma electron density profile. The modeled pictures illustrate how the curved ion trace in the detector plane straightens and shifts towards less toroidally deflected position with decreasing plasma current, which is in good correspondence with the observed ABP signals.

In the dedicated experimental campaign, I studied also the effect of chopping time on the detection of Li-ions by the test ABP detector. For ABP measurements in H-mode discharges, to observe the signal behavior during fast ELM phenomena it is necessary to chop the beam out of plasma with a sub-millisecond period to correct the signal for background. The electronics on COMPASS allows a chopping frequency of up to 250 kHz. During the measurements we demonstrated the capability of the ABP detector to follow fast changes in ion signal during

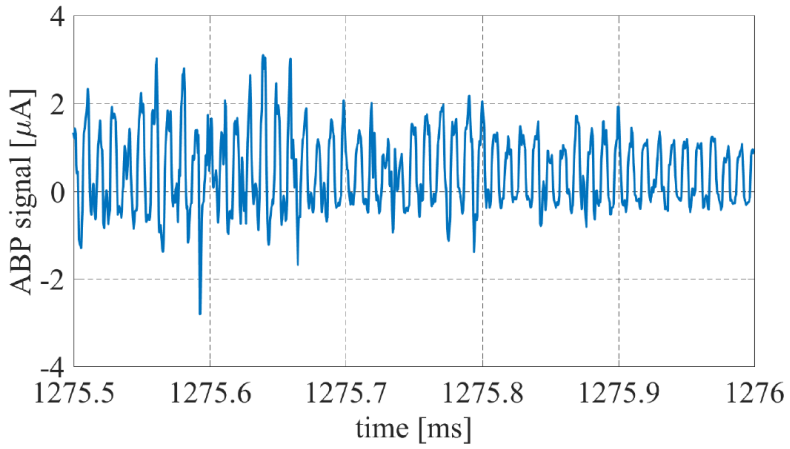

Figure 6.21: ABP signal on a 2×5 mm detection plate in COMPASS discharge #14412. Li beam was chopped with a period 10 μs.

chopping with frequencies up to 100 kHz. As an example, the detected ion signal from the measurement with the beam chopping period of 10 μs can be seen in Figure 6.21.

6.8 Final detector design

6.8.1 Specifications

As described in Section 6.5, the ABP test detector was designed as a detector with a fixed toroidal position, which limited its application in standard COMPASS discharges due to the toroidal ion shift. Therefore, for a relevant use as a plasma diagnostic, a detector with an adjustable toroidal position needed to be developed. By modeling of the toroidal ion shifts based on data from COMPASS H-mode plasma shots, I found that a new detector would need to reach toroidal positions of up to ~ 6 cm. Figure 6.22a shows modeled average toroidal shift values for 11 COMPASS H-mode discharges with a wide range of plasma currents and Figure 6.22b shows the toroidal-vertical ion spot areas for the same shots, coming from a 5 mm diameter beam.

The reduction of the beam size diameter to 3 mm is at the limit of the APD system (see Section 6.7.2). Therefore, a use of detection plates with smaller sizes does not bring any advantage. Our calculations imply that while using 5 mm diameter beam and 2×5 mm sized plates, depending on the level of noise, it is still possible to observe desired sub-millimeter shifts of the ion trace by calculating the movement of center-of-mass of the detected signals. Using a greater plate size also keeps advantages of a smaller SE effect and a higher signal-to-noise ratio.

To summarize, based on the experience from operation of the test ABP detector, I set the following requirements for a design of the final detector solution:

1. Detector head has to allow a measurement of ions toroidally shifted by up to 6 cm either solely by adjustable toroidal position or in combination with beam injection under a defined angle through a (modified) diameter reducer.

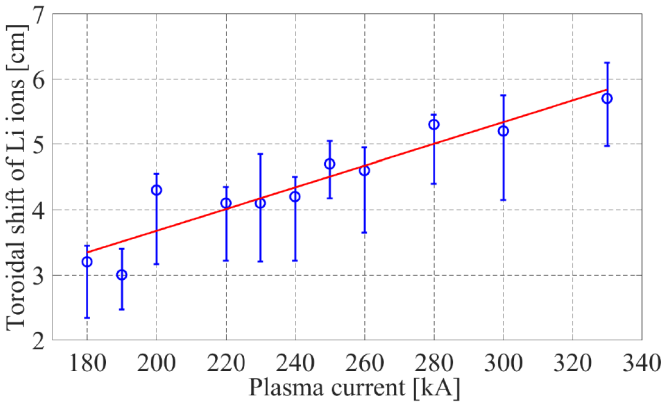

(a)

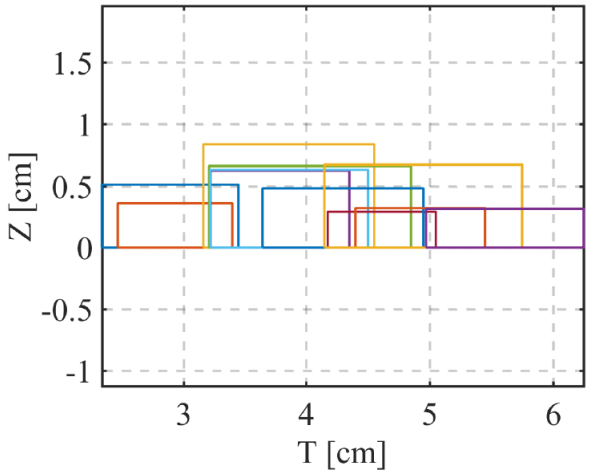

(b)

Figure 6.22: (a) Modeled toroidal ion shift values for COMPASS H-mode discharges with different plasma currents. Data points are points of maximum ion signal and error bars define the toroidal area of strong ion signal (FWHM). (b) Modeled toroidal-vertical ion spot size (FWHM in both dimensions) for the same shots. Modeled for 5 mm diameter, 85 keV lithium beam.

2. Two isolated masks in front of the detector plates will be used for protection of the sensitive detector area as well as for biasing to suppress SE.

3. Optimal detector plate size was chosen as 2×5 mm (toroidal $\times$ vertical). Based on available port space, new detector head will contain 50 plates in 5 rows of 10 plates covering an area of $\sim 2.2 \times 2.6$ cm.

6.8.2 Detector design and installation

Final detector head was manufactured in Wigner RCP based on the specifications above. Several additional ideas were implemented during the design process based on the experiences with the test ABP detector.

Detector head

The detector head consists of a 5×10 matrix of detector segments, a connector panel, two detector masks and compact graphite limiter structure. Test ABP measurements and associated calculations showed that SE contribution can play a significant role, especially if the magnetic field lines are not perfectly parallel to the detector surface (see Table 6.1). To further improve SE suppression, detector segments were manufactured as individual Faraday cups. The cups were electrically insulated from each other and all other surfaces were grounded. The dimensions of each Faraday cup are $1.8 \times 4.8 \times 0.8$ mm (toroidal $\times$ vertical $\times$ depth) and the distance between neighboring detectors is 0.4 mm in both directions [117]. Detector front and back side can be seen in Figure 6.23.

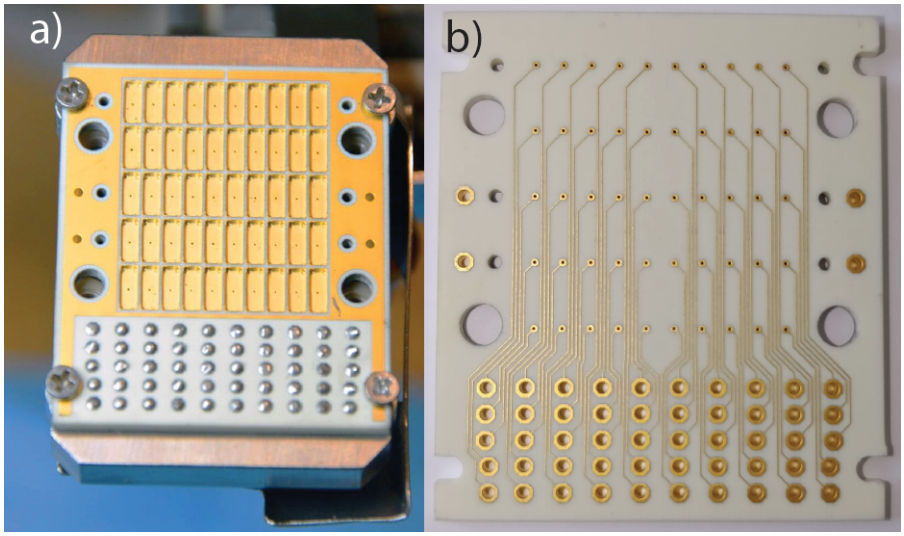

Figure 6.23: Photo of the (a) front and (b) back side of the detector Faraday cup matrix. Taken from [117].

Based on the assessment of the background plasma noise by the test ABP detector (see Section 6.7.1), it was decided to provide the final detector with robust graphite limiter to protect the sensitive detector area from influx of SOL plasma particles. The graphite limiter is grounded and the detector head is tilted by 38 ° with respect to the vertical axis to align it with COMPASS tokamak limiters. This is done in order to keep the detector head in the limiter shadow to protect it from direct contact with the plasma.

In front of the detectors, there are two masks, which are electrically separated from each other and also from the detector area. The spatial separation between both the two masks and also between the first mask and the detector area is 1 mm. The mask closer to the detector plates matrix can be either biased or grounded, while the outer one is grounded. All grounded parts of the detector head and the manipulator are grounded to the tokamak.

Manipulator

The main requirement on the manipulator was to allow both vertical and toroidal movement of the detector head. In the early design phase, it was found that in-

sufficient place in the vertical ABP port does not allow for toroidal sideways movement larger than 2.2 cm. This along with detector half-width of $\sim$ 1.1 cm gives us toroidal detector reach of maximally $\sim$ 3.3 cm, which would be suitable only for lower current plasmas up to $\sim$ 200 kA (according to calculations visualized in Figure 6.22a). Therefore, it was decided to solve the issue by manufacturing a modified beam diameter reducer, which would allow beam injection under a small toroidal angle to reduce the resultant toroidal ion shift. Extent of the vertical movement is 5 cm. At the upper position, ABP detector head is hidden in the port; at the lowermost position, the detector head limiter is aligned with the COMPASS LFS limiters. Assembled final ABP detector head and manipulator can be seen in Figure 6.24.

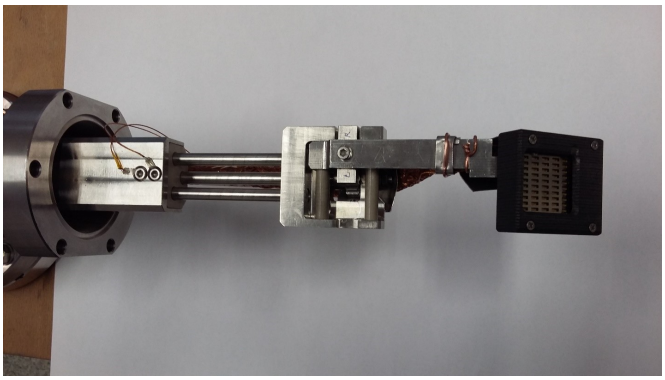

(a)

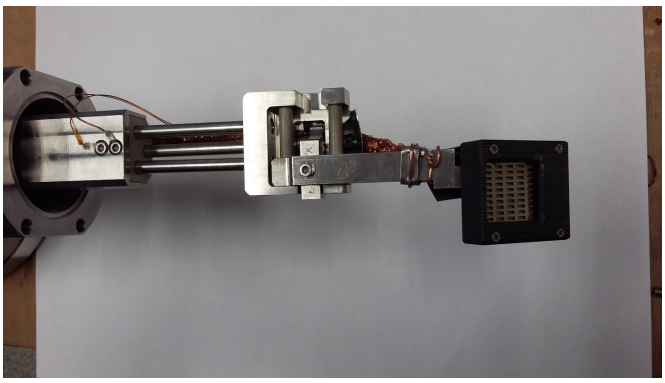

(b)

Figure 6.24: Final ABP detector. Photos demonstrate the extent of toroidal movement: (a) centre position and (b) the most toroidally shifted position.

Data acquisition system

Data acquisition system for the final ABP detector is an upgrade of the existing electronics used for the test detector. Each ABP detector plate is connected to a 2 kΩ resistor and the voltage on the resistor is amplified. The amplifier is a 2 stage, 20 channel differential amplifier with amplification factor of 100 and 500 kHz analogue bandwidth. The output voltage is digitized with a 32-channel analogue digital converter unit (ADC), the data are converted to UPD packages and sent to PC through an optically separated Gigabit Ethernet line [117].

Final ABP detector was installed on COMPASS in February 2018 (see Figure 6.25b).

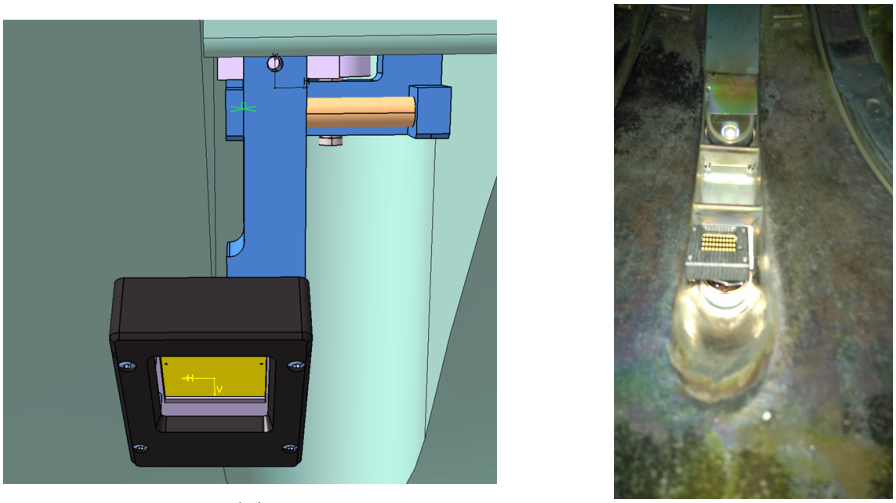

(a) (b)

Figure 6.25: (a) CATIA model of final ABP detector head in COMPASS tokamak port. (b) Photo of installed final ABP detector on COMPASS.

6.9 First measurements with the final ABP detector on COMPASS

In June 2018, first experimental campaign with the final ABP detector was performed. The reference discharge of the scenario was ohmic ELMy H-mode COMPASS discharge #17178 with long plasma current ramp-down. Main parameters of the discharge were: toroidal field $B_T = 1$ T, plasma current $I_p = 150$ kA and line averaged electron density $n_e \approx 4 - 6 \cdot 10^{19}$ m^{-3} (see Figure 6.26).

Lithium beam was operated at energies $80 - 90$ keV with high extracted beam currents $I_b \sim 2 - 4$ mA and with diameters 5 and 25 mm. Beam was injected radially, without any angle, as the expected toroidal shift for given I_p around 3 cm was within the achievable toroidal reach of the ABP detector. Beam was periodically chopped out of plasma for background correction with chopping frequencies $10 - 100$ kHz. First ABP detector mask was biased to -200 V during the measurements. At the time of the campaign, electronics only for 20 channels was available, therefore only 2 detector plate rows were connected (the top and bottom ones);

6.9.1 Observations

We were able to detect both 25 and 5 mm diameter beams in the whole plasma discharge, including the H-mode phase. Highest detected ion signals were ~ 3 μA for 25 mm beam and ~ 300 nA for 5 mm beam. As the ion signal in the spot centre should be roughly the same for both 25 and 5 mm beam diameters (detector plate size is 1.8×5 mm), it seems that during the 5 mm beam measurements,

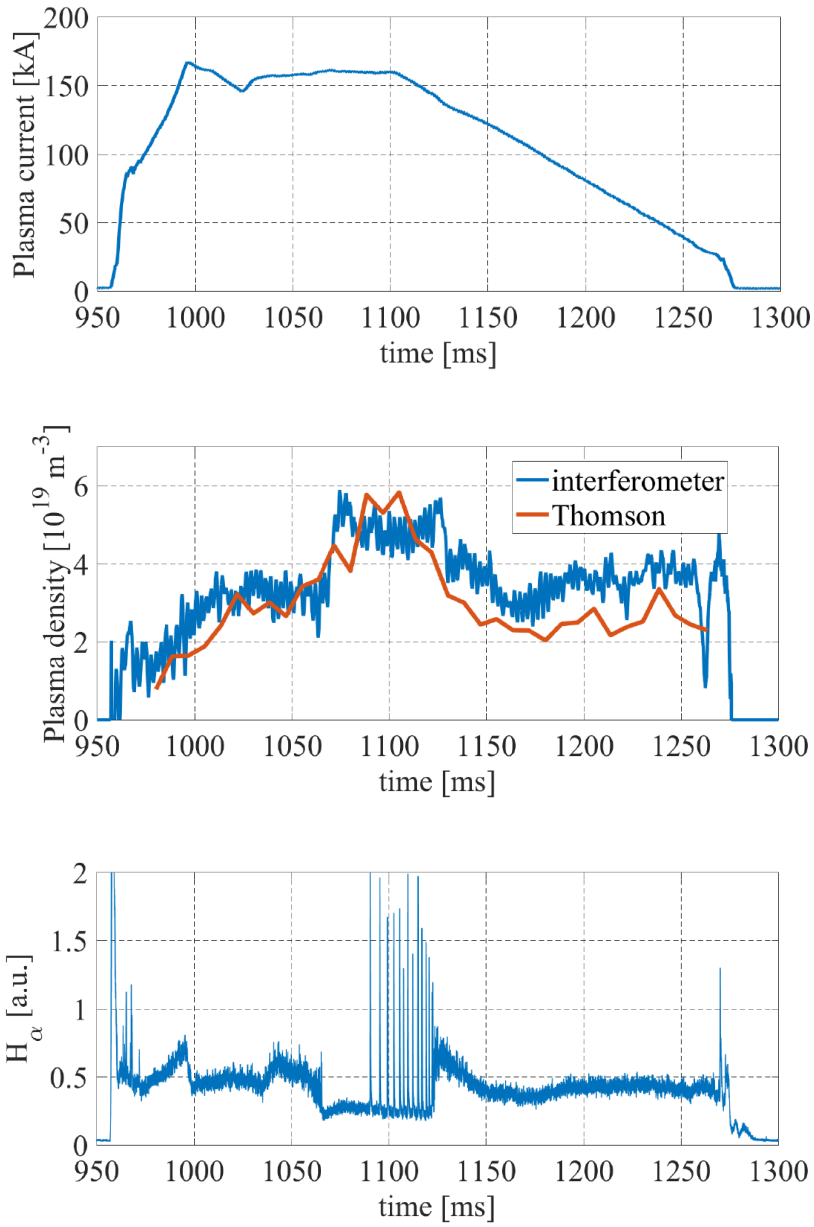

Figure 6.26: Main parameters of the COMPASS discharge #17178: (top) Plasma current, (middle) line-averaged plasma density measured by Thomson scattering and microwave interferometer, (bottom) H_α radiation signal. On H_α, the ELMy H-mode phase can be clearly identified.

the detector position was not set correctly and we observed only a fringe part of the beam ion spot.

To toroidally move the ABP detector head, it is necessary to push it vertically out of the port, therefore quite near to the plasma. This is a concern for the measurement, as the background plasma noise on ABP is strongly dependent on the detector distance from plasma (as observed by the test ABP detector, see Figure 6.16a). Calculated distance of the detector from the separatrix in the discharges was ~ 3.5 cm and increasing during the plasma current ramp-down phase. The observed plasma background level and background noise were however even higher than expected, equaling to ~ 2 μA and $\sim 0.5 - 1$ μA, respectively.

The detected ion signal to background ratio was therefore 1 : 1 with the full beam width and 1 : 10 with 5 mm reduced beam. The fast chopping technique allowed easily the background correction of the 25 mm signal (see Figure 6.27), while for 5 mm beam it was practically impossible and in this case the beam movement across the plates could be evaluated only through the analysis of the signal frequency spectra and presence of the frequency peak from the fast beam chopping.

Due to the very high level of noise, the resolution of nuanced beam spot movement on the ABP detector plates was reduced. To observe the toroidal shifts on the detector, time averaging of the background corrected signal had to be done in order to reduce the noise. In Figure 6.28, results from COMPASS discharges #17176 and #17178 are presented. In discharge #17176, 100 kHz beam chopping was applied while in the discharge #17178, slower beam chopping of 10 kHz was used. For both discharges, the temporal evolution of the ion beam signal on one toroidal row of 10 ABP detector channels is shown. In both cases, the signal was smoothed over 20 points, resulting in 200 μs and 2 ms resolutions, respectively.

In Figure 6.28a from discharge #17178, the reduced temporal resolution of 2 ms allows the observation of large-scale ion spot movements (depicted by the black line) during the shaping phase ($t = 1030 - 1070$ ms) as well as the ramp-down phase ($t = 1100 - 1250$ ms) of the discharge. Figure 6.28b from discharge #17176 with 10 times increased temporal resolution allows to observe even the small-scale movements in the inter-ELM period.

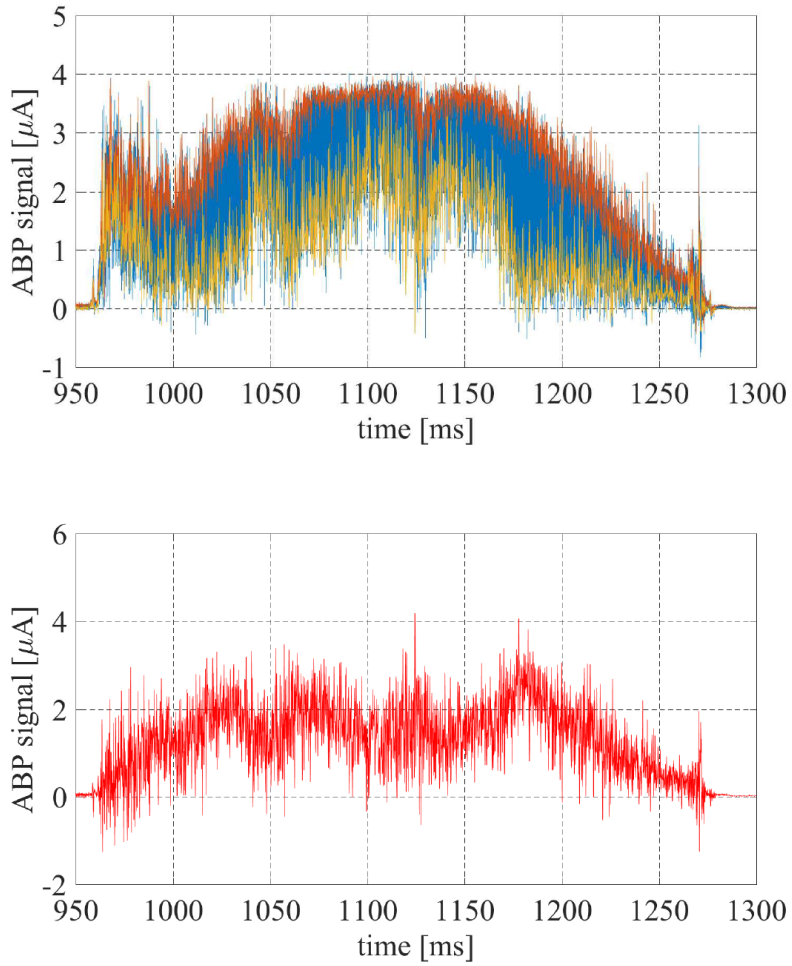

Figure 6.27: Background correction of the fast chopped beam signal measured by one ABP channel during the COMPASS discharge #17178. In the discharge, 80 keV lithium beam was injected with 25 mm diameter and 100 μs chopping period. Picture (a) shows the separated on (red) and off (yellow) beam signals as well as the raw signal (blue). Picture (b) then shows the background corrected signal.

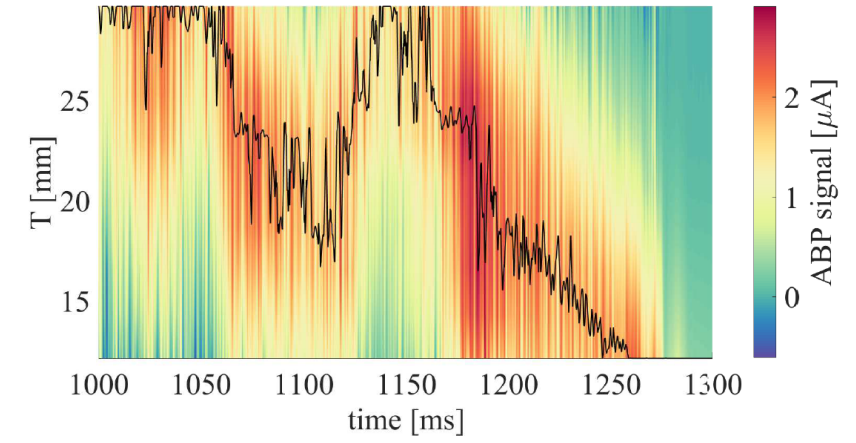

(a)

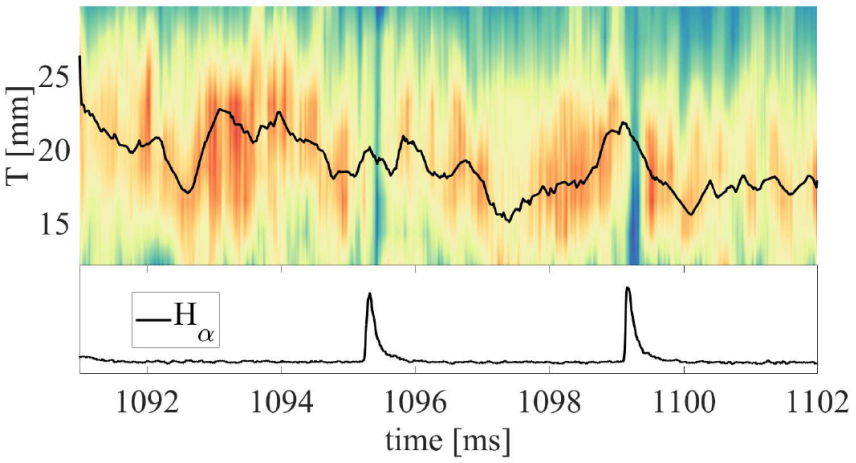

(b)

Figure 6.28: Temporal evolution of the background corrected lithium ion beam signals on one row of 10 ABP detector segments during the COMPASS discharges #17178 (a) and #17176 (b). 80 keV beam was injected into the plasma with 25 mm diameter. ABP detector head was moved to the most toroidally shifted position, thus the detector plates covered toroidal range $T \approx 11 - 33$ mm. The movement of the maximum of ion spot is shown by the black lines. 200 μs temporal resolution in the discharge #17176 allowed the observation of small-scale inter-ELM ion spot movements.

6.9.2 Outlook

Further data analyses from the first measurement campaign with the final ABP detector are ongoing. However, it is clear that to achieve the goal of the diagnostic, it is still needed to reduce the noise level on the detector plates. The most important factor is the distance of the detector from plasma. There are two possible ways to increase this distance to achieve reasonable noise levels: 1) measure in smaller plasmas radially more distanced from the outer tokamak wall, 2) measure with more retracted ABP detector head. The latter option would mean that the detector cannot be moved toroidally and so the beam has to be injected into the plasma under an angle. Both options can be reasonably achieved and will be done in the following experimental campaign planned in Autumn of 2018.

7. Conclusions

The thesis summarizes part of my technical and physical work done during my doctoral studies on the COMPASS tokamak. As the responsible person of the lithium beam group on COMPASS, I was tasked with the development, commissioning and operation of the lithium beam and related diagnostics, such as the Beam Emission Spectroscopy (LI-BES) and the Atomic Beam Probe (ABP). The following paragraphs go through the individual parts of the thesis and recount the results I achieved, both in my own independent work and as a member of the lithium beam group.

At first, the neutral lithium beam injection system on the COMPASS tokamak is described in sufficient details. It has to be noted that the COMPASS lithium beam system has several unique features, which distinguish it from similar devices. For purposes of Atomic Beam Probe measurements, it was designed as a high energy beam, capable of reaching energy 120 keV. Also, it uses a new advanced lithium ion source and a new design of a recirculating neutralizer developed by Wigner RCP, Budapest.

During the commissioning process, we had to learn and develop new processes for emitter and neutralizer operation as well as vacuum handling, which was crucial in order to avoid high voltage breaks and ensure safe beam operation. The commissioning process of the beam injector resulted in a routine and fully automated Li beam operation. Further, a detailed description of the diagnostic of beam emission spectroscopy using the neutral lithium beam is provided. This part of thesis gives a theoretical background of the collisional-radiative model of beam-plasma interaction and describes the density profile reconstruction from the measured spectroscopic data implemented for COMPASS.

This part also presents two installed detection systems for beam emission spectroscopy - CCD camera and avalanche photo-diode detector - and their capabilities. It shows the developed method of processing of the distorted CCD images and their background correction. It describes the performed spatial calibration of the avalanche photo-diode (APD) detector channels and spectroscopic measurements of the COMPASS plasma background leading to optimization of the interference filter design for the APD system. Lastly, comparisons with other COMPASS diagnostics are provided, showing a good agreement of the reconstructed density profiles and concluding the diagnostic commissioning.

The most important achievements are described in Chapters 5 and 6.

Beam Emission Spectroscopy

- Firstly, the motivation of the measurements and physics areas of interest are outlined. Li-BES measurement possibilities are also discussed and the quality of the data is assessed with respect to BES systems on devices worldwide.

- Then, a general assessment of the edge and scrape-off layer (SOL) plasma density fluctuations is presented. Significant change of fluctuation character

is observed on the boundary of confined plasma region. Relative fluctuation amplitude level rises from few % in plasma edge to $\sim 30-40$ % in SOL, in agreement with similar observations on other devices. Influence of H-mode operation is investigated and significant reduction ($\sim$ 4 times) of relative fluctuation level in the SOL region is observed. Also, the skewness of the fluctuation amplitude distribution is seen to change sign in the boundary region. Positive skewness in SOL is linked to blob-dominated turbulence in this region.

- A detailed analysis of blob structures in SOL was performed. Using a threshold method for blob detection, a conditionally averaged blob was calculated from 495 detected events. It followed well the theoretically predicted double-exponential shape, with faster rise time $\tau_r = 8.88$ μs and slower fall time $\tau_f = 10.25$ μs. It was found that blob amplitudes follow the theoretically predicted exponential distribution, while blob waiting times featured two distinct exponential dependences in the region of short and longer waiting times, $\tau_{w1} = 9.7$ μs and $\tau_{w2} = 280$ μs. These results suggest that signal consists of a mixture of smaller, quickly following and even overlapping blob events and more frequent larger events with longer waiting times. Measured positive tail of the amplitude distribution was found to follow well the theoretically predicted gamma distribution.

- Possibility of the Li-BES diagnostic to measure poloidal velocity rotation of plasma by fast beam sweeping was also investigated. Two methods using time delay estimation technique were used and compared. The measured poloidal velocity had the expected profile with a large shear in the boundary plasma region. The measured poloidal velocity values were in the range of 10 km/s, a factor of $2-3$ larger than expected. This was attributed to the large diameter of the swept beam causing probably significant overestimation of the calculation.

- Finally, measurements of fast density profile changes during ELMy H-mode plasmas are presented. Using the fast beam chopping technique for background correction, it was possible to reconstruct density profiles on a microsecond timescale ($\geq$ 2 μs) and observe fine ELM structure. A conditionally averaged ELM was calculated from 65 ELM events and showed the evolution of pedestal density during the ELM cycle.

Atomic beam probe

- At first, the thesis concentrates on the development process of this completely new and unique diagnostic method of for measurements of current density at the plasma edge. The idea of the diagnostic is presented, supported by modelling of ion trajectories in tokamak magnetic field. MATLAB code (and subsequently parallel CUDA code) was developed, solving the collisional radiative model for determination of beam ionization and calculating the trajectory of the ionized part of the beam.

- Test ABP detector was built in order to prove the diagnostic concept. Firstly, laboratory measurements were performed, explaining and quantifying

the role of secondary electron emission on detected signals. The measurements led to a decision to change the detector design and include a double-mask structure in front of the detector area to suppress secondary electron emission.

- Finally, test ABP detector measurements in COMPASS plasmas were done. Plasma background signal over a wide range of plasma parameters was determined. A special diameter reducer was used to cut the beam to several mm diameters necessary for the new diagnostic. Lithium beam ions coming from reduced 10, 5 and 3 mm beams were clearly detected by the detector proving the concept of the diagnostic. Based on the test ABP detector experience, final detector solution was specified. The detector was designed, manufactured and installed on COMPASS. In its first experimental campaign in June 2018, measurement was able to resolve fine toroidal movements of the ion trace on detector in the inter-ELM phase of H-mode COMPASS discharges.

On the following lines, I would like to formulate the main achieved results of the thesis.

Chapters 2–4 and the first part of chapter 5 may be summarized as the first part of the thesis, dealing with the commissioning of both the lithium beam injection system and the beam emission spectroscopy diagnostic. This work was done by the lithium beam group in collaboration with Wigner RCP, Budapest. The main results may be listed as follows: 1) New lithium beam emission spectroscopy (Li-BES) system was commissioned on COMPASS. It features high signal to background ($\sim 15:1$) and signal to noise ($\sim 50-100:1$) ratios, which is comparable to the best similar diagnostics worldwide. 2) Li-BES measurements with fast beam chopping technique allow fast density profile reconstructions with unparalleled temporal resolution of 2 μs. These results were described in the attached publications [A1] Berta, et al.: *Li-BES detection system for plasma turbulence measurements on the COMPASS tokamak* and [A3] Krbec, et al.: *Edge plasma density reconstruction by Li-BES on COMPASS* and also in [7, 18, 24, 36].

My independent work of analyzing the spectroscopic data provides these main physical results: 1) Characterization of the blob-dominated fluctuations in the SOL region and 2) Characterization of the fast pedestal density evolution during the ELM cycle. The results of chapter 5 were in part published in [A1], [9, 53] and publication of the results of SOL analysis is being prepared.

The main achieved results with the new unique diagnostics – Atomic Beam Probe may be summarized as: 1) The diagnostic concept was proven by successful reduction of the beam size to 5 mm and simultaneous detection of beam emission by BES system and lithium ions by the test ABP detector. 2) First measurements with the final ABP detector were able to resolve fine toroidal movements of the ion trace in the inter-ELM phase of H-mode COMPASS discharges. Development of the ABP detector is attached in [A2] Hacek, et al.: *First measurements with atomic beam probe diagnostics on COMPASS* and also in publications [91, 92, 109].

In the future scientific work, I would like to concentrate mainly on the measurements and interpretation of the ABP data with the goal of determining the edge current density evolution during the ELMy H-mode discharges and contributing to the understanding of this important tokamak physics phenomenon. Secondly, I would like to statistically analyze the density evolution during H-mode measured by the Li-BES system. The already large database of detailed H-mode measurements by Li-BES can provide insights into the ELM characteristics and can also help categorize the ELM events on COMPASS.

References

[1] Panek, R. et al. Reinstallation of the COMPASS-D tokamak in IPP ASCR. *Czechoslovak Journal of Physics*. **56**, 2006, B125. DOI: https://doi.org/10.1007/s10582-006-0188-1

[2] Panek, R. et al. Status of the COMPASS tokamak and characterization of the first H-mode. *Plasma Physics and Controlled Fusion*. **58**(1), 2015, 014015. DOI: https://doi.org/10.1088/0741-3335/58/1/014015

[3] Zajac, J. et. al. Power supply system for the COMPASS tokamak reinstalled at the IPP, Prague. *Fusion Engineering and Design*. **84**(7–11), 2009, 2020–2024. DOI: https://doi.org/10.1016/j.fusengdes.2008.11.092

[4] Hron, M. et. al. Overview of the COMPASS CODAC system. *Fusion Engineering and Design*. **89**(3), 2014, 177–185. DOI: https://doi.org/10.1016/j.fusengdes.2013.09.010

[5] Janky, F. et. al. Plasma density control in real-time on the COMPASS tokamak. *Fusion Engineering and Design*. **96-97**, 2015, 637–640. DOI: https://doi.org/10.1016/j.fusengdes.2015.04.065

[6] Urban, J. et. al NBI system for reinstalled COMPASS-D tokamak. *Czechoslovak Journal of Physics*. **56**, 2006, B176. DOI: https://doi.org/10.1007/s10582-006-0195-2

[7] Weinzettl, V. et al. Overview of the COMPASS diagnostics. *Fusion Engineering and Design*. **86**(6–8), 2011, 1227–1231. DOI: https://doi.org/10.1016/j.fusengdes.2010.12.024

[8] Krbec, J. *Measurement of edge plasma density by energetic beam of Li atoms on the COMPASS tokamak*. Prague, 2013. Diploma thesis. Czech Technical University in Prague. Faculty of Nuclear Science and Physical Engineering.

[9] Weinzettl, V. et al. Progress in diagnostics of the COMPASS tokamak. *Journal of Instrumentation*. **12**, 2017, C12015. DOI: https://doi.org/10.1088/1748-0221/12/12/C12015

[10] Havlicek, J. *Study of Equilibrium Magnetic Configuration in Tokamak Type Devices*. Prague, 2015. Doctoral thesis. Charles University in Prague. Faculty of Mathematics and Physics.

[11] Zajac, J. et. al. Upgrade of the COMPASS tokamak microwave reflectometry system with I/Q modulation and detection. *Fusion Engineering and Design*. **123**, 2017, 911–914. DOI: https://doi.org/10.1016/j.fusengdes.2017.03.088

[12] Zajac, J. et. al. EBE/ECE Radiometry on COMPASS Tokamak — Design and First Measurements. *AIP Conference Proceedings*. **1187**, 2009, 473. DOI: https://doi.org/10.1063/1.3273795

[13] Bilkova, P. et al. High resolution Thomson scattering on the COMPASS tokamak— extending edge plasma view and increasing repetition rate. *Journal of Instrumentation.* **13**, 2018, C01024. DOI: https://doi.org/10.1088/1748-0221/13/01/C01024

[14] Havranek, A. et al. Implementation of rapid imaging system on the COMPASS tokamak. *Fusion Engineering and Design.* **123**, 2017, 857–860. DOI: https://doi.org/10.1016/j.fusengdes.2017.03.129

[15] Vondracek, P. et al. Fast infrared thermography on the COMPASS tokamak. *Fusion Engineering and Design.* **123**, 2017, 764–767. DOI: https://doi.org/10.1016/j.fusengdes.2017.05.004

[16] Weinzettl, V. et al. Design of multi-range tomographic system for transport studies in tokamak plasmas. *Nuclear Instruments and Methods in Physics Research Section A.* **623**(2), 2010, 806–808. DOI: https://doi.org/10.1016/j.nima.2010.04.010

[17] Tomes, M. et al. Calculation of edge ion temperature and poloidal rotation velocity from carbon III triplet measurements on the COMPASS tokamak. *Nukleonika.* **61**(4), 2016, 443—451. DOI: https://doi.org/10.1515/nuka-2016-0073

[18] Anda, G. et al. Lithium beam diagnostic system on the COMPASS tokamak. *Fusion Engineering and Design.* **108**, 2016, 1–6. DOI: https://doi.org/10.1016/j.fusengdes.2016.04.022

[19] Adamek, J. et al. A novel approach to direct measurement of the plasma potential. *Czechoslovak Journal of Physics.* **54**, 2004, C95. DOI: https://doi.org/10.1007/BF03166386

[20] Adamek, J. et al. Profile measurements of the electron temperature on the ASDEX Upgrade, COMPASS, and ISTTOK tokamak using Thomson scattering, triple, and ball-pen probes. *Review of Scientific Instruments.* **87**, 2016, 043510. DOI: https://doi.org/10.1063/1.4945797

[21] Adamek, J. et al. Electron temperature and heat load measurements in the COMPASS divertor using the new system of probes. *Nuclear Fusion.* **57**(11), 2017, 116017. DOI: https://doi.org/10.1088/1741-4326/aa7e09

[22] Dimitrova, M. et al. Plasma Parameters in the COMPASS Divertor During Ohmic Plasmas. *10th International Workshop on Electric Probes in Magnetized Plasmas.* **54**(3), 2014, 255–260. DOI: https://doi.org/10.1002/ctpp.201410073

[23] Dimitrova, M. et al. Evaluation of the scrape-off-layer plasma parameters by a horizontal reciprocating Langmuir probe in the COMPASS tokamak. *Journal of Physics: Conference Series.* **514**, 2014, 012049. DOI: https://doi.org/10.1088/1742-6596/514/1/012049

[24] Hacek, P. et al. Diagnostic Lithium Beam System for COMPASS Tokamak. *WDS'11 Proceedings of Contributed Papers, Part II, 2011.* Prague: Matfyzpress, p.215—220. ISBN 978-80-7378-185-9

[25] Isler, R. C. An overview of charge-exchange spectroscopy as a plasma diagnostic. *Plasma Physics and Controlled Fusion*. **36**(2), 1994, 171. DOI: https://doi.org/10.1088/0741-3335/36/2/001

[26] Dullni, E. et al. Magnetic Field Measurements With a Lithium-Beam Using Zeeman- or Motional-Stark-Effect. *Physica Scripta*. **34**, 1986, 405–407. DOI: https://doi.org/10.1088/0031-8949/34/5/008

[27] Willensdorfer, M. et al. Characterization of the Li-BES at ASDEX Upgrade. *Plasma Physics and Controlled Fusion*. **56**, 2014, 025008. DOI: https://doi.org/10.1088/0741-3335/56/2/025008

[28] Brix, M. et al. Upgrade of the lithium beam diagnostic at JET. *Review of Scientific Instruments*. **81**, 2010, 10D733. DOI: https://doi.org/10.1063/1.3502320

[29] Stoschus, H. et al. Status and characterization of the lithium beam diagnostic on DIII-D. *Review of Scientific Instruments*. **84**(8), 2013, 083503. DOI: https://doi.org/10.1063/1.4816824

[30] Kojima, A. et al. Development of a high-brightness and low-divergence lithium neutral beam for a Zeeman polarimetry on JT-60U. *Review of Scientific Instruments*. **79**(9), 2008, 093502. DOI: https://doi.org/10.1063/1.2964225

[31] Lampert, M. et al. Combined hydrogen and lithium beam emission spectroscopy observation system for Korea Superconducting Tokamak Advanced Research. *Review of Scientific Instruments*. **86**, 2015, 073501. DOI: https://doi.org/10.1063/1.4923251

[32] Zoletnik, S. et al. Ultrafast two-dimensional lithium beam emission spectroscopy diagnostic on the EAST tokamak. *Review of Scientific Instruments*. **89**, 2018, 063503. DOI: https://doi.org/10.1063/1.5017224

[33] Zoletnik, S., S. Bato and G. Anda *Report on laboratory testing of enhanced Li ion emitter*. 2011. Not published.

[34] McCormick, K. *The charge-exchange cell for the neutral lithium beam probe on Pulsator, W7a and ASDEX*. IPP report III/82, March 1983. [cit. 15.7.2018]. online: https://tinyurl.com/yal2durc

[35] McCormick, K. et al. Edge density measurements with a fast Li beam probe in tokamak and stellarator experiments. *Fusion Engineering and Design*. **34-35**, 1997, 125–134. DOI: https://doi.org/10.1016/S0920-3796(96)00685-0

[36] Hacek, P. et al. New Detection System for Fast Density Measurements Using the Lithium Beam on the COMPASS Tokamak. *WDS'13 Proceedings of Contributed Papers, Part II, 2013*. Prague: Matfyzpress, p.86-–90. ISBN 978-80-7378-251-1

[37] McKee, G. R. et al. Turbulence imaging and applications using beam emission spectroscopy on DIII-D. *Review of Scientific Instruments*. **74**, 2003, 2014. DOI: https://doi.org/10.1063/1.1535248

[38] Field, A. R. et al. Beam emission spectroscopy for density turbulence measurements on the MAST spherical tokamak. *Review of Scientific Instruments*. **80**, 2009, 073503. DOI: 10.1063/1.3170034

[39] Wang, H. J. et al. Development of beam emission spectroscopy diagnostic on EAST. *Review of Scientific Instruments*. **88**, 2017, 083505. DOI: https://doi.org/10.1063/1.4997074

[40] Ahn, J.-W. et al. Development of fast helium beam emission spectroscopy on MST. *Review of Scientific Instruments*. **77**, 2006, 10F114. DOI: https://doi.org/10.1063/1.2236279

[41] Schmitz, O. et al. Status of electron temperature and density measurement with beam emission spectroscopy on thermal helium at TEXTOR. *Plasma Physics and Controlled Fusion*. **50**(11), 2008, 115004. DOI: https://doi.org/10.1088/0741-3335/50/11/115004

[42] Schweer, B. et al. Application of atomic beams in combination with spectroscopic observation for plasma diagnostic. *Transactions of fusion science and technology*. **53**, 2008, 425. DOI: https://doi.org/10.13182/FST08-A1728

[43] Janev, R. K. et al. *Atomic collision database for Li beam interaction with fusion plasmas*. IAEA Report INDC(NDS)-267, 1993. [cit. 15.7.2018]. online: https://tinyurl.com/ybe8ynj7

[44] Wutte, D. et al. Cross sections for collision processes of Li atoms interacting with electrons, protons, multiply charged ions, and hydrogen molecules. *Atomic Data and Nuclear Data Tables*. **65**(1), 1997, 155–180. DOI: https://doi.org/10.1006/adnd.1997.0736

[45] Schweinzer, J. et al. Database for inelastic collisions of lithium atoms with electrons, protons and multiply charged ions. *Atomic Data and Nuclear Data Tables*. **72**, 1999, 239–273. DOI: https://doi.org/10.1006/adnd.1999.0815

[46] Brandenburg, R. et al. Modelling of fast neutral Li beams for fusion edge plasma diagnostics. *Plasma Physics and Controlled Fusion*. **41**(4), 1999, 471. DOI: https://doi.org/10.1088/0741-3335/41/4/002

[47] Wiese, W. L. and J. R. Fuhr Accurate Atomic Transition Probabilities for Hydrogen, Helium, and Lithium. *Journal of Physical and Chemical Reference Data*. **38**, 2009, 565. DOI: https://doi.org/10.1063/1.3077727

[48] Schweinzer, J. et al. Reconstruction of plasma edge density profiles from Li I (2s-2p) emission profiles. *Plasma Physics and Controlled Fusion*. **34**(7), 1992, 1173. DOI: https://doi.org/10.1088/0741-3335/34/7/001

[49] Devernay, F., Faugeras O. Straight lines have to be straight. *Machine Vision and Applications*. **13**, 2001, 14–24. DOI: https://doi.org/10.1007/PL00013269

[50] Dunai, D. et al. Avalanche photodiode based detector for beam emission spectroscopy. *Review of Scientific Instruments*. **81**, 2010, 103503. DOI: https://doi.org/10.1063/1.3488458

[51] Janky, F. et al. Determination of the plasma position for its real-time control in the COMPASS tokamak. *Fusion Engineering and Design*. **86**(6–8), 2011, 1120–1124. DOI: https://doi.org/10.1016/j.fusengdes.2011.01.143

[52] Adamek, J. et al. Direct plasma potential measurements by ball-pen probe and self-emitting probe on COMPASS and ASDEX Upgrade. *Contributions to Plasma Physics, Special Issue: 10th International Workshop on Electric Probes in Magnetized Plasmas*. **54**(3), 2014, 279–284. DOI: https://10.1002/ctpp.201410072

[53] Komm, M. et al. Contribution to the multi-machine pedestal scaling from the COMPASS tokamak. *Nuclear Fusion*. **57**(5), 2017, 056041. DOI: https://doi.org/10.1088/1741-4326/aa6659

[54] Wagner, F. et al. Regime of Improved Confinement and High Beta in Neutral-Beam-Heated Divertor Discharges of the ASDEX Tokamak. *Physical Review Letters*. **49**, 1982, 1408–1412. DOI: https://doi.org/10.1103/PhysRevLett.49.1408

[55] Zohm, H. et al. Edge localized modes (ELMs). *Plasma Physics and Controlled Fusion*. **38**(2), 1996, 105–128. DOI: https://doi.org/10.1088/0741-3335/38/2/001

[56] Connor, J. W. et al. Edge-localized modes - physics and theory. *Plasma Physics and Controlled Fusion*. **40**, 1998, 531–542. DOI: https://doi.org/10.1088/0741-3335/40/5/002

[57] Kirk, A. et al. Spatial and Temporal Structure of Edge-Localized Modes. *Physical Review Letters*. **92**, 2004, 245002. DOI: https://doi.org/10.1103/PhysRevLett.92.245002

[58] Dejarnac, R. et al. Numerical evaluation of heat flux and surface temperature on a misaligned JET divertor W lamella during ELMs. *Nuclear Fusion*. **54**(12), 2014, 123011. DOI: https://10.1088/0029-5515/54/12/123011

[59] Matthews, G. F. et al. Melt damage to the JET ITER-like Wall and divertor. *Physica Scripta*. **2016**(T167), 2016, 014070. DOI: 10.1088/0031-8949/T167/1/014070

[60] de la Luna, E. et al. Understanding the physics of ELM pacing via vertical kicks in JET in view of ITER. *Nuclear Fusion*. **56**(2), 2015, 026001. DOI: 10.1088/0029-5515/56/2/026001

[61] Markovic, T. et al. Measurements and modelling of plasma response field to RMP on the COMPASS tokamak. *Nuclear Fusion*. **56**, 2016, 092010. DOI: 10.1088/0029-5515/56/9/092010

[62] Nie, L. et al. Comparison of ELM–Filament Mitigation Between Supersonic Molecular Beam Injection and Pellet Injection on HL–2A. *Plasma Science and Technology*. **18**(2), 2016, 120. DOI: 10.1088/1009-0630/18/2/04

[63] Shaing, K. C., and E. C. Crume, Jr. Bifurcation theory of poloidal rotation in tokamaks: A model for L-H transition. *Physical Review Letters.* **63**, 1989, 2369. DOI: https://doi.org/10.1063/1.859473

[64] Connor, J. W., and H. R. Wilson A review of theories of the L-H transition. *Plasma Physics and Controlled Fusion.* **42**(1), 2000, R1. DOI: https://doi.org/10.1088/0741-3335/42/1/201

[65] Aydemir, A. Y. Shear flows at the tokamak edge and their interaction with edge-localized modes. *Physics of Plasmas.* **14**, 2007, 056118. DOI: https://doi.org/10.1063/1.2727330

[66] Snyder, P. B. et al. Edge localized modes and the pedestal: A model based on coupled peeling–ballooning modes. Physics of Plasmas. **9**, 2002, 2037. DOI: https://doi.org/10.1063/1.1449463

[67] Horton, W. Drift waves and transport. *Review of Modern Physics.* **71**(3), 1999, 735–778. DOI: https://10.1103/RevModPhys.71.735

[68] La Haye, R. J. Neoclassical tearing modes and their control. *Physics of Plasmas.* **13**(5), 2006, 055501. DOI: https://10.1063/1.2180747

[69] Simon, P. *Investigation of geodesic acoustic mode flow oscillations using Doppler reflectometry in ASDEX Upgrade.* Stuttgart, 2017. Doctoral thesis. University of Stuttgart, Faculty of Energy-, Process- and Bio-Engineering.

[70] Seidl, J. et al. Electromagnetic characteristics of geodesic acoustic mode in the COMPASS tokamak. *Nuclear Fusion.* **57**(12), 2017, 126048. DOI: https://doi.org/10.1088/1741-4326/aa897e

[71] Scott, B. D. Tokamak edge turbulence: background theory and computation. *Plasma Physics and Controlled Fusion.* **49**(7), 2007, S25. DOI: https://doi.org/10.1088/0741-3335/49/7/S02

[72] Zoletnik, S. et al. Two-dimensional density and density fluctuation diagnostic for the edge plasma in fusion devices. *Review of Scientific Instruments.* **76**, 2005, 073504. DOI: https://doi.org/10.1063/1.1947727

[73] Asztalos, O. et al. Fluctuation response analysis of plasma turbulence with BES diagnostics. *44th EPS Conference on Plasma Physics, Belfast, 2017.* EPS Conference Proceedings. P4.109

[74] Nam, Y. U. et al. Edge electron density profiles and fluctuations measured by two-dimensional beam emission spectroscopy in the KSTAR. *Review of Scientific Instruments.* **85**, 2014, 11E434. DOI: https://doi.org/10.1063/1.4894839

[75] Crowley, T. P. et al. Heavy ion beam probe wavenumber measurements from the TEXT Tokamak edge. *Nuclear Fusion.* **32**(8), 1992, 1295. DOI: https://doi.org/10.1088/0029-5515/32/8/I01

[76] Hanson, T. P. et al. Density fluctuation measurements in ATF using correlation reflectometry. *Nuclear Fusion.* **32**(9), 1992, 1593. DOI: https://doi.org/10.1088/0029-5515/32/9/I07

[77] Zoletnik, S. et al. Density fluctuation phenomena in the scrape-off layer and edge plasma of the Wendelstein 7-AS stellarator. *Physics of Plasmas.* **6**, 1999, 4239. DOI: https://10.1063/1.873691

[78] D'ippolito, D. A., J. R. Myra, S. J. Zweben Convective transport by intermittent blob-filaments: Comparison of theory and experiment. *Physics of Plasmas.* **18**(6), 2011, 060501. DOI: https://10.1063/1.3594609

[79] Jirakova, K. *Charakterizace fluktuací okrajového plazmatu tokamaku COMPASS.*Prague, 2016. Bachelor thesis. Czech Technical University in Prague, Faculty of Nuclear Science and Physical Engineering.

[80] Garcia, O. E. et al. Fluctuations and transport in the TCV scrape-off layer. *Nuclear Fusion.* **47**(7), 2007, 667. DOI: https://doi.org/10.1088/0029-5515/47/7/017

[81] Garcia, O. E. et al. Stochastic Modeling of Intermittent Scrape-Off Layer Plasma Fluctuations. *Physical Review Letters* **108**(26), 2012, 265001. DOI: https://10.1103/PhysRevLett.108.265001

[82] Theodorsen, A. et al. Scrape-off layer turbulence in TCV: evidence in support of stochastic modelling. *Plasma Physics and Controlled Fusion.* **58**, 2016, 044006. DOI: https://doi.org/10.1088/0741-3335/58/4/044006

[83] Lee, W. et al. E × B flow velocity deduced from the poloidal motion of fluctuation patterns in neutral beam injected L-mode plasmas on KSTAR. *Physics of Plasmas.* **23**, 2016, 052510. DOI: https://doi.org/10.1063/1.4949350

[84] Bencze, A. et al. Observation of zonal flow-like structures using the autocorrelation-width technique. *Plasma Physics and Controlled Fusion* **48**, 2006, S137. DOI: https://doi.org/10.1088/0741-3335/48/4/S10

[85] Meister, H. et al. Measurement of poloidal flow, radial electric field and E × B shearing rates at ASDEX Upgrade. *Nuclear Fusion* **41**(11), 2001, 1633. DOI: https://doi.org/10.1088/0029-5515/41/11/313

[86] Field, A. R. et al. Comparison of measured poloidal rotation in MAST spherical tokamak plasmas with neo-classical predictions. *Plasma Physics and Controlled Fusion.* **51**(10), 2009, 105002. DOI: https://doi.org/10.1088/0741-3335/51/10/105002

[87] Chrystal, Colin *Experimental Tests of the Theory of Poloidal Rotation in the DIII-D Tokamak.* San Diego, 2014. Doctoral thesis. University of California, San Diego.

[88] Eliseev, L. et al. Two Point Correlation Technique for the Measurements of Poloidal Plasma Rotation by Heavy Ion Beam Probe. *Plasma and Fusion Research.* **7**, 2012, 2402064. DOI: https://10.1585/pfr.7.2402064

[89] Connor, J. W., A. Kirk and H. R. Wilson Edge Localised Modes (ELMs): Experiments and Theory. *AIP Conference Proceedings*. **1013**(174), 2008. DOI: https://doi.org/10.1063/1.2939030

[90] Beurskens, M. N. A. et al. H-mode pedestal scaling in DIII-D, ASDEX Upgrade, and JET. *Physics of Plasmas*. **18**, 2011, 056120. DOI: https://doi.org/10.1063/1.3593008

[91] Berta, M. et al. Development of atomic beam probe for tokamaks. *Fusion Engineering and Design*. **88**, 2013, 2875–2880. DOI: https://doi.org/10.1016/j.fusengdes.2013.05.064

[92] Hacek, P. et al. Measurements with Atomic Beam Probe Diagnostic on the COMPASS Tokamak. *WDS'15 Proceedings of Contributed Papers — Physics, 2015*. Prague: Matfyzpress, p.264—268. ISBN 978-80-7378-311-2

[93] Thomas, D. M. et al. Poloidal magnetic field measurements and analysis with the DIII-D LIBEAM system (invited). *Review of Scientific Instruments*. **61**, 2003, 1541. DOI: https://doi.org/10.1063/1.1526928

[94] Thomas, D. M. et al. Measurement of Pressure-Gradient-Driven Currents in Tokamak Edge Plasmas. *Physical Review Letters*. **93**, 2004, 065003. DOI: https://doi.org/10.1103/PhysRevLett.93.065003

[95] Kamiya, K. et al. Zeeman polarimetry measurement for edge current density determination using Li-beam probe on JT-60U. *Review of Scientific Instruments*. **81**, 2010, 033502. DOI: https://10.1063/1.3309793

[96] Korotkov, A. A. et al. Line ratio method for measurement of magnetic field vector using Li-multiplet (2^2S – 2^2P) emission. *Review of Scientific Instruments*. **75**, 2004, 2590. DOI: https://doi.org/10.1063/1.1763250

[97] Crowley, T. P. Magnetic field measurement techniques with heavy ion beam probes. *Review of Scientific Instruments*. **59**, 1988, 1638. DOI: https://doi.org/10.1063/1.1140170

[98] Shimizu, A. et al. Consideration of magnetic field fluctuation measurements in torus plasma with a heavy ion beam probe. *Review of Scientific Instruments*. **76**, 2005, 043504. DOI: https://doi.org/10.1063/1.1889230

[99] Melnikov, A. V. et al. Heavy ion beam probing—diagnostics to study potential and turbulence in toroidal plasmas. *Nuclear Fusion* **57**, 2017, 072004. DOI: https://doi.org/10.1088/1741-4326/aa5382

[100] Schwelberger, J. G. et al. Current density profile measurement on the Texas Experimental Tokamak using a heavy ion beam probe. *Review of Scientific Instruments*. **69**, 1998, 3828. DOI: https://doi.org/10.1063/1.1149185

[101] Ding, W.X. et al. Laser Faraday rotation measurement of current density fluctuations and electromagnetic torque. *Review of Scientific Instruments*. **75** (2004) 3387. DOI: https://doi.org/10.1063/1.1785275

[102] Yang, X. et al. 2D profile of poloidal magnetic field diagnosed by a laser-driven ion-beam trace probe (LITP). *Review of Scientific Instruments.* **87**, 2016, 11D608. DOI: https://doi.org/10.1063/1.4960761

[103] Galdon-Quiroga, J. et al. Conceptual design of a scintillator based Imaging Heavy Ion Beam Probe for the ASDEX Upgrade tokamak. *Jurnal of Instrumentation.* **12**, 2017, C08023. DOI: https://doi.org/10.1088/1748-0221/12/08/C08023

[104] Berta, M. *Zajdiagnosztikai eljárások a nukleáris energetikában (Noise methods in nuclear energetics).* Gyor, 2011. Doctoral thesis. Széchenyi István University.

[105] Havlicek, J., J. Urban A Magnetic Equilibrium Reconstruction in Tokamak. *WDS'07 Proceedings of Contributed Papers: Part II - Physics of Plasmas and Ionized Media, 2007.* Prague: Matfyzpress, p.234-239. ISBN 978-80-7378-024-1

[106] Huba, J. D. *NRL Plasma Formulary.* Naval Research Laboratory, Washington, DC, 1998. [cit. 15.7.2018]. online: https://tinyurl.com/y8rs89q9

[107] Fujisawa, A. et al. Prescription for density profile reconstruction using a heavy ion beam probe. *Review of Scientific Instruments.* **74**(7), 2003, 3335–3340. DOI: https://doi.org/10.1063/1.1581360

[108] Simpson, J. C. et al. Simple Analytic Expressions for the Magnetic Field of a Circular Current Loop. *Transactions on Magnetics.* 2001. [cit. 15.7.2018]. online: https://tinyurl.com/yc5vhtyk

[109] Hacek, P. et al. Atomic Beam Probe Diagnostic for COMPASS Tokamak. *WDS'10 Proceedings of Contributed Papers, Part II, 2010.* Prague: Matfyzpress, p.7-11. ISBN 978-80-7378-140-8

[110] Stefanikova, E. et al. Fitting of the Thomson scattering density and temperature profiles on the COMPASS tokamak. *Review of Scientific Instruments.* **87**, 2016, 11E536. DOI: https://doi.org/10.1063/1.4961554

[111] Press, W. H. et al. *Numerical Recipes 3rd Edition: The Art of Scientific Computing.* New York: Cambridge University Press, 2007. ISBN 978-0521880688

[112] Aradi, M. *Parallel computation of ion trajectories in tokamak magnetic fields based on graphical processors.* Gyor, 2016. Master thesis. Eotvos Lorand University.

[113] Guszejnov, D. et al. Three-dimensional modeling of beam emission spectroscopy measurements in fusion plasmas. *Review of Scientific Instruments.* **83**, 2012, 113501. DOI: https://doi.org/10.1063/1.4764564

[114] Endo, A., Ino S. Energy and angular distribution of secondary electrons emitted from Si(111)-7×7, $\sqrt{3}\times\sqrt{3}$-Ag and 5×2-Au surfaces. *Surface Science* **346**, 1996, 40–48. DOI: https://doi.org/10.1016/0039-6028(95)00922-1

[115] Kulhanek, P. *Úvod do teorie plazmatu*. Praha: AGA, 2011. ISBN 978-80-904582-2-2

[116] Bethge, K. and K. Lexa Secondary electron emission from metal surfaces by impact of charged and neutral lithium particles. *British Journal of Applied Physics* **17**(2), 1966, 181–186. DOI: https://doi.org/10.1088/0508-3443/17/2/304

[117] Refy, D. et al. Micro-Faraday cup matrix detector for ion beam measurements in fusion plasmas. *Review of Scientific Instruments*. To be published.

List of Figures

List of Tables

List of Abbreviations

ABP	Atomic beam probe
ADC	Analog-to-digital converter
APDCAM	Avalanche photo-diode detector camera
BES	Beam emission spectroscopy
CASTOR	Czech Academy of Sciences Torus
CCF	Cross-correlation function
COMPASS	Compact Assembly
CX	Charge exchange
CXRS	Charge exchange recombination spectroscopy
DW	Drift wave
EFIT	Equilibrium fitter
ELM	Edge localized mode
FC	Faraday cup
FWHM	Full width at half maximum
GAM	Geodesic acoustic mode
GPU	Graphics processing unit
H-mode	High confinement mode
HFS	High field side
HIBP	Heavy ion beam probe
ITER	International Thermonuclear Experimental Reactor
JET	Joint European Torus
L-mode	Low confinement mode
LCFS	Last closed flux surface
LED	Light emitting diode
LFS	Low field side
LITB	Laser-driven ion-beam trace probe
LOS	Line of sight
Li-BES	Lithium beam-based beam emission spectroscopy
MHD	Magnetohydrodynamics
MSE	Motional Stark effect
NBI	Neutral beam injection
NTM	Neoclassical tearing mode
Nd:YAG	Neodymium-doped yttrium aluminum garnet laser
PMT	Photomultiplier tube
PPD	Photoconductive photodiode
PSD	Power spectral density
RK4	Fourth order Runge Kutta method
SE	Secondary electron
SND	Single-null divertor
SNR	Signal-to-noise ratio
SNT	Single-null divertor with higher triangularity
SOL	Scrape-off layer
TAIGA	Trajectory simulations of ABP ions with GPU acceleration
TDE	Time delay estimation
UPD	User datagram protocol
UV	Ultraviolet radiation
ZF	Zonal flow

Attached publications

[A1] Berta, M. et al. Li-BES detection system for plasma turbulence measurements on the COMPASS tokamak. *Fusion Engineering and Design*. **96-97**, 2015, 795–798. DOI: https://doi.org/10.1016/j.fusengdes.2015.06.030

(Author of the thesis is the corresponding author of the article and presented it on 28th Symposium on Fusion Technology, Spain, 2014.)

[A2] Hacek, P. et al. First measurements with atomic beam probe diagnostics on COMPASS. *Review of Scientific Instruments*. Submitted for publication. June 2018.

[A3] Krbec, J. et al. Edge plasma density reconstruction by Li-BES on COMPASS. *Review of Scientific Instruments*. Submitted for publication. July 2018.

(Author of the thesis is the second author of the article.)

Li-BES detection system for plasma turbulence measurements on the COMPASS tokamak

M. Berta[a,b], G. Anda[c], A. Bencze[c], D. Dunai[c], P. Háček[a,d], M. Hron[a], A. Kovácsik[c,e], J. Krbec[a,f], R. Pánek[a], D. Réfy[c], G. Veres[c], V. Weinzettl[a], S. Zoletnik[c]

[a] *Institute of Plasma Physics AS CR, Prague, Czech Republic,*
[b] *Széchenyi István University, Győr, Hungary*
[c] *Wigner - RCP, HAS, Budapest, Hungary*
[d] *Faculty of Mathematics and Physics, Charles University in Prague, Prague, Czech Republic*
[e] *Department of Nuclear Techniques, Budapest University of Technology and Economics, Budapest, Hungary*
[f] *Faculty of Nuclear Sciences and Physical Engineering, Czech Technical University in Prague, Prague, Czech Republic*

Abstract

A new Li beam emission spectroscopy (Li-BES) diagnostic system with a ~ cm spatial resolution, and with beam energy ranging from 10 keV up to 120 keV and a 18 channel Avalanche Photo Diode (APD) detector system sampled at 2 MHz has been recently installed and tested on the COMPASS tokamak. This diagnostic allows to reconstruct density profile based on directly measured light profiles, and to follow turbulent behaviour of the edge plasma. The paper reports technical capabilities of this new system designed for fine spatio-temporal measurements of plasma electron density. Focusing on turbulence-induced fluctuation measurements, we demonstrate how physically relevant informations can be extracted using the COMPASS Li-BES system.

Keywords: BES, plasma diagnostics, COMPASS tokamak, density fluctuations, plasma density profile

1. Introduction

In modern fusion research non-perturbative plasma diagnostic methods have gained increasing importance as the detector technologies develop and the spatio-temporal resolution can be increased up to microsecond scales. From plasma operation point of view, the electron density is one of the important discharge parameters to be determined. Well known standard methods of electron density measurements are the Thomson scattering (TS) [1] and the microwave interferometry (MI) [2], both of them having their advantages and their drawbacks. While TS provides good spatial resolution, its time resolution is very much limited by the laser repetition rate. On the other hand, MI has good temporal resolution but the measurement is line integrated. An interesting diagnostic to be mentioned for density fluctuation measurements is the microwave imaging reflectometry [3].

Li-beam based Beam Emission Spectroscopy (Li-BES) can be considered as a powerful non-perturbative active diagnostic for detailed measurements of the electron density profile and its fluctuations with cm spatial and microsecond temporal resolution across the 70-80% of the plasma minor radius in smaller tokamaks [4, 5], and the edge region for larger machines.

Li-BES systems are used in tokamaks, like JET, ASDEX, DIII-D, JT-60U [6, 7, 8, 9] and are under commissioning at KSTAR and EAST. In 2010 a newly designed high energy (up to 120 keV/5 mA) Li-beam started to operate on the COMPASS tokamak.

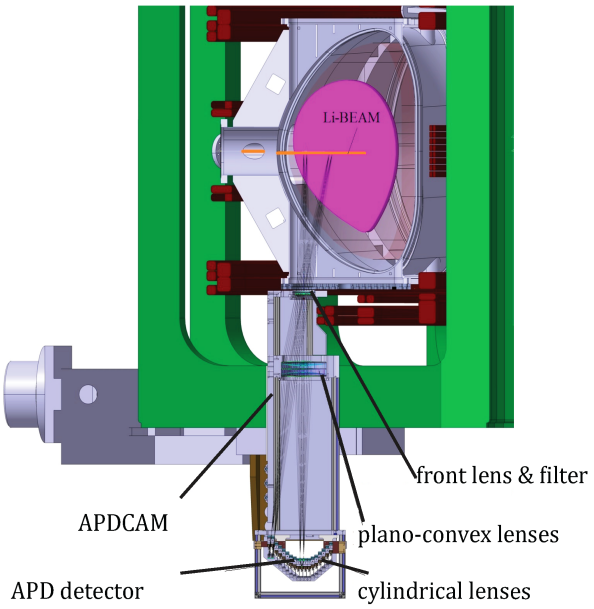

Figure 1: Scheme of installed APDCAM system on COMPASS

Lithium ions are extracted from a thermionic ion source and accelerated in an ion optic. The ions are neutralized in Sodium vapor and the neutral beam reaches the plasma without any significant energy loss. During the plasma-beam interaction Li-atoms are excited to the 2p state by the plasma electrons. The

Email address: hacek@ipp.cas.cz (P. Háček[a,d])

excited state decays by the emission of a photon of characteristic wavelength (λ = 670.8 nm). These photons can be observed using an appropriate interference filter and various detector systems (CCD camera, Photomultiplier, Photodiode or Avalanche Photodiode (APD)). The detected light intensity is–in the first approximation–proportional to the local electron density, observing the intensity and the fluctuations of this Li resonance line along the beam, it is possible to reconstruct the density profile and the quasi-2D correlation functions of the electron density fluctuation.

Using a pair of deflection plates the beam can be either chopped or poloidally deflected (swept). Chopping the beam makes possible to correct for the background, while the poloidal deflection allows quasi-2D measurements. The switching frequency of the sweeping/deflection system can be increased up to a 400 kHz [4, 5]. The poloidal resolution is limited by the ~ 2.5 cm of beam diameter.

2. The fast fluctuation measurement system

A compact APD camera unit (APDCAM) containing the optics, the interference filter and an array of 18 APDs with integrated amplifiers is installed on the bottom vertical port of the vacuum vessel of the COMPASS tokamak. (See Fig. 1)

2.1. Optics

The first optical lens is approximately 40 cm below midplane just behind the port window and it leads the light through the 1 nm wide interference filter for given wavelength of 670.8 nm (LiI 2s2p line) with 56% maximum light transmission. (See Fig. 2) The design of the filter has taken into account the combined effect of Doppler-shift and varying angle of incidence.

The second focusing element is a pair of plano-convex lenses projecting 1:1 image of the beam on to the array of cylindrical field lenses. These are used to lead the light from the image plane (approx. 10x50 mm radial-toroidal area corresponding to one channel) to the individual sensors (5x5 mm).

2.2. APD detector system

An APD-based detector system for beam emission spectroscopy on a diagnostic lithium beam has been designed, built and recently put in operation on the COMPASS tokamak.

The APDs have been chosen due to their superior performance in terms of the signal to noise ratio (SNR) in the wide region of incident photon flux $5 \times 10^8 - 5 \times 10^{10}$ photons/second compared to other possibilities like photomultiplier tubes (PMT) and photoconductive photodiodes (PPD) [10]. The system is tailor-made for the COMPASS tokamak, its compact assembly and size allowing to place the collection optics and the detection system near to the plasma and therefore the photon flux on the APDs is high.

Estimation of the incident photon flux from the measured signals is in the range of $(1 - 5) \times 10^{10}$ photons/second, which surpasses similar experiments on other devices. The minimum level of detectable plasma fluctuations is limited by the statistical photon noise, which is given by Poisson distribution as

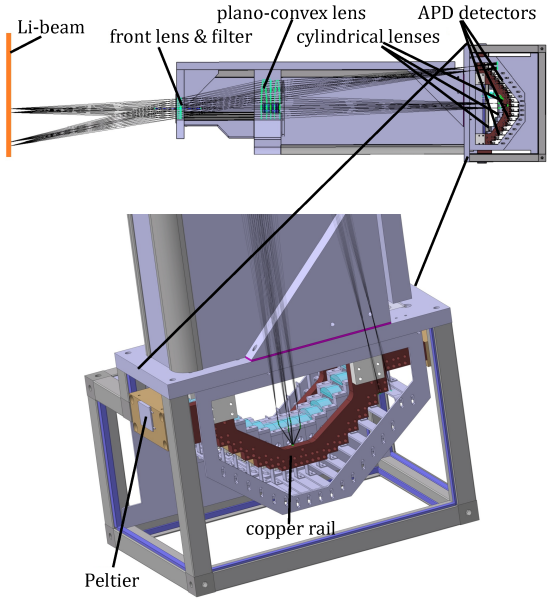

Figure 2: The optical setup of the APDCAM: the object (1 cm portion of the Li-BEAM) is seen on the left (upper image) at a distance of 400 mm from the 75 mm diameter front lens (focal length of f=500 mm). The object is 1:1 imaged into the APD detector. An interference filter is placed in front of the first lens, and cylindrical lenses are seen in front of the APD detectors.

$\delta n_e/n_e \approx 1/N^{1/2}$ where N is the number of photons detected during the integration period. For an incident light of 5×10^{10} photons/s, the photon noise level is ~ 0.6 % at 2 MHz bandwidth and so the sensitivity of the system to low level density fluctuations is high.

The APDs are solid state silicon Hamamatsu type S8664-55 detectors with 5x5 mm effective area sensitive to wavelengths 320-1000 nm. They feature high quantum efficiency (85 % at 650 nm) and intrinsic gain up to 100 for used reverse bias voltage in range 350-450 V. The APDs do not require cryogenic cooling, but in order to have the same sensitivity of sensors, they need to be stable in temperature. For this reason, they are mounted on a copper rail and cooled by two Peltier elements.

Each detector has its own special low noise operational amplifier developed in Wigner RCP, Hungary operated with 1 MHz bandwidth. The data acquisition system utilises four 8 channel, 2 MHz analogue-to-digital converters (ADCs) with 14 bit resolution [10].

2.3. Calibration

In order to calibrate the APD channels, a special calibration rod was developed. It was connected to the lithium beam system at the tokamak entrance port. The rod can be placed exactly into the lithium beam position on the tokamak midplane and moved radially along the whole tokamak's minor radius via electric stepper motor with submillimeter precision.

The rod carries a sheet with a light bulb for determination of the radial position (R) of individual channels from the sig-

nal maximum. As light bulb provides a stable light source, the difference of the maxima of detected signals on the individual sensors gives us also the difference in the sensors' sensitivities (S) (see Tab. 1).

R [m]	S	R [m]	S	R [m]	S
0.60	0.82	0.66	1.00	0.72	0.88
0.61	0.90	0.67	1.00	0.73	0.90
0.62	0.89	0.68	0.90	0.74	0.90
0.63	0.92	0.69	0.89	0.75	0.91
0.64	0.93	0.70	0.98	0.76	0.46
0.65	0.93	0.71	0.97		

Table 1: Relative sensitivities of APD detectors

3. Demonstration of capabilities

The above described fluctuation measurement system (FMS) has been tested and is routinely operated on the COMPASS tokamak. In this section we present some experimental data measured by the FMS in order to assess its capabilities.

3.1. Light and electron density profiles with high temporal resolution

An ELMy H-mode discharge (# 8175) was selected for demonstration of the fast profile detection. 40 keV, 2 mA Li-beam has been injected and chopped with 10 ms chopping period. Data were sampled at 2 MHz.

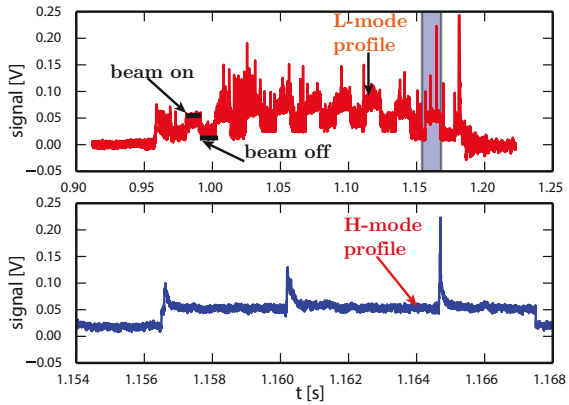

Figure 3: Raw signal of APDCAM channel 12 from ELMy H-mode shot #8175 on the COMPASS (top). Zoom of the period when Li-BEAM is in the plasma during H-mode (bottom).

The L-H transition starts at 1140 ms and the discharge ended by disruption. In this short H-mode almost two chopping periods (20 ms) are observed allowing both the background correction and the localization of few ELM events by the Li-beam (See Fig. 3).

Fig. 4 (top panel) shows two background corrected light profiles at different time instances comparing L-mode and H-mode.

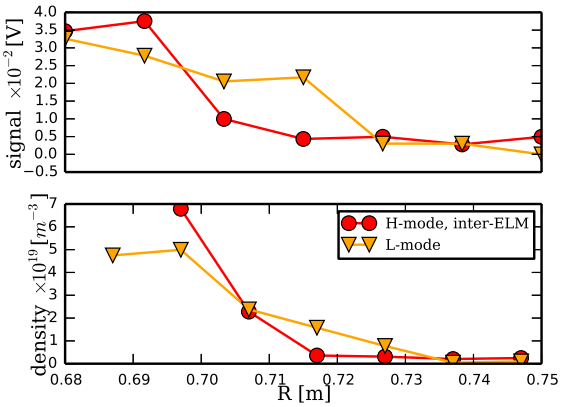

Figure 4: Top: background corrected light profiles measured by APDCAM system. (L-mode: at 1.121 s, H-mode: at 1.164 s). Bottom: Reconstructed density profiles in the scrape off layer region based on measured light profiles.

It is apparent from the figure that the L-mode profile is much broader than the relatively steep H-mode profile which is in agreement with the expected formation of a H-mode pedestal at the plasma edge.

Density profiles were reconstructed [11] from the previously discussed light profiles Fig. 4 (bottom panel), showing density steepening when the plasma undergoes L-H transition.

3.2. Light fluctuation characteristics

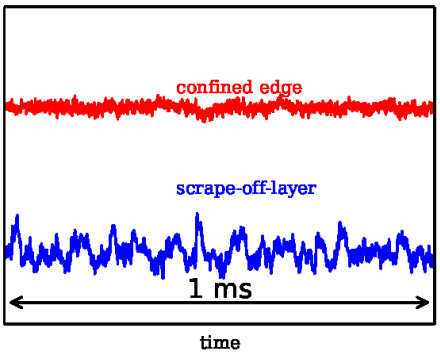

Figure 5: Time evolution of Li light fluctuations in the edge of the confined region (upper), and in the scrape-off-layer (lower).

In this section we present some typical examples of fluctuation measurements and the information one can extract, using standard data processing techniques. A well known fact in tokamak physics is the apparent difference of turbulence characteristics in scrape-off-layer and plasma edge [12]. The signals presented in the following analysis are taken from a standard D-shaped, diverted COMPASS ohmic discharge (# 7727) with $n_e = 6.6 \times 10^{19}$ m^{-3}, $I_p = 210$ kA. Fig. 5 shows two measured signals, the upper one showing small-scale fluctuations present in the confined edge plasma, while the bottom signal depicts blob dominated SOL turbulence.

Radial profiles of the relative fluctuation amplitudes and the radial distribution of skewness are shown in Fig. 6. The overall trend of the statistical moments is in good agreement with what was seen in the majority of fusion plasmas [12]. It is obvious that the statistics changes its character close to the separatrix. Around the last closed flux surface (channel # 13) the fluctuation amplitude grows fast from 5% to 30%. It is also interesting to note that the symmetry of the PDF changes its sign towards the SOL.

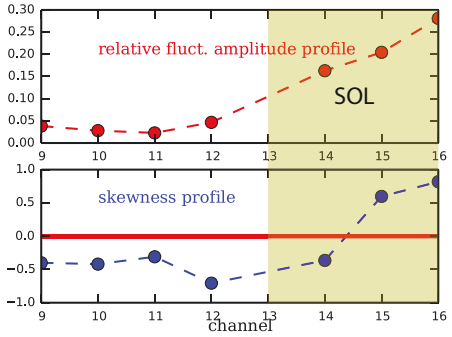

Figure 6: Radial profile of the relative fluctuation amplitude (upper panel), and radial profile of the skewness (lower panel). Integrated over a 40 ms long time window.

Calculating the auto-power spectral density (APSD) spectra for different radially distributed APD channels, one can observe the change in mode structure as we cross the last closed flux surface. The comparison in Fig. 7 indicates the presence of different features in the confined region, e.g. there is a sharp oscillatory peak at 29 kHz and a broadband quasi-coherent mode centred at 68 kHz. The identification of these modes is the subject of extensive ongoing research. On the other hand the turbulent spectra of the SOL plasma shows considerable increase in spectral power for the entire inertial range of fluctuations. In Fig. 8 the autocorrelation functions (ACFs) are shown for different radial positions. Data are filtered in such way that only the 35 – 250 kHz spectral range is retained where the relevant turbulent modes are located. The quasi coherent oscillation is seen in the confined region, while in the SOL decaying ACFs indicate different type of turbulence.

4. Conclusions

In this paper a new diagnostic system has been presented for fast detection of plasma density. This system is based on Beam Emission Spectroscopy performed on accelerated diagnostic Li-beam. The detector part consists of a carefully designed optical system which allows the 1:1 imaging of the beam into the high-quantum-efficiency Avalanche Photo Diode array. The photon flux entering the system through a narrow interference filter is sampled at 2 million samples/second. It has been demonstrated that the system can provide important data for edge physics research such as L-H transition, ELM dynamics and various facets of turbulent transport.

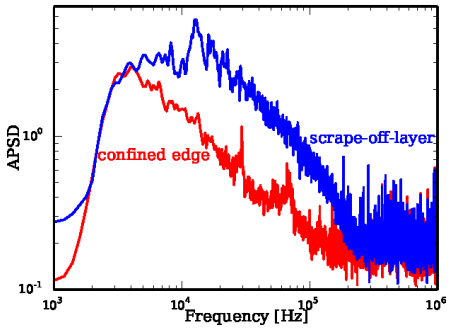

Figure 7: Auto-power spectral density from an L-mode COMPASS shot calculated from a 40 ms long time slice, showing the difference in spectral composition of data at different radial locations. A digital high-pass filter has been applied, with low cut frequency of 1 kHz.

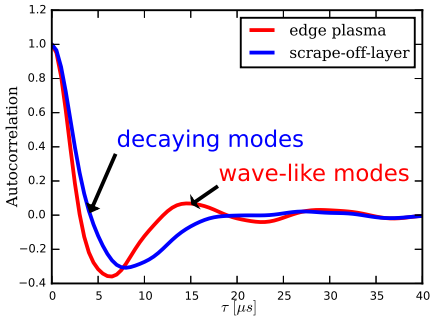

Figure 8: Autocorrelation function for Li-light fluctuations in different radial regions of the #7727 discharge. Data are band-pass filtered in the frequency range of 35 – 250 kHz.

5. Acknowledgements

This work has been carried out within the framework of the EUROfusion Consortium and has received funding from the European Union's Horizon 2020 Research and Innovation Programme under grant agreement number 633053. The views and opinions expressed herein do not necessarily reflect those of the European Commission.

This work was partly supported by MSMT Project # LM2011021.

6. References

[1] P. Bohm et al., Review of Scientific Instruments 85, 11E431 (2014)
[2] V. Weinzettl at al., Fusion Engineering and Design 86 (2011) 1227-1231
[3] T. Munsat at al., Rev. Sci. Instrum. 74, 1426 (2003)
[4] S. Zoletnik et al., Review of Scientific Instruments 76, 073504 (2005)
[5] M. Berta et al., Fusion Engineering and Design 88 (2013) 2875-2880
[6] Brix at al., 28th EPS Conference, ECA Vol. **25A** (2001) 389-392
[7] McCormick at al., Rev. Sci. Instrum. 56, 1063 (1985)
[8] D. M. Thomas, Rev. Sci. Instrum. 66, 806 (1995)
[9] A. Kojima at al., Plasma and Fusion Research, Vol. 5., (2010)
[10] D. Dunai et al., Review of Scientific Instruments 81, 103503 (2010)
[11] J. Schweinzer et al 1992 Plasma Phys. Control. Fusion 34 1173
[12] S. Zoletnik at al., Physics of Plasmas (1994-present) 6, 4239 (1999)

First measurements with atomic beam probe diagnostics on COMPASS

P. Hacek,[1,2,a)] M. Berta,[1,3] G. Anda,[4] M. Aradi,[5] A. Bencze,[4] D. Dunai,[4] J. Krbec,[1,6] R. Panek,[1] D. I. Refy,[4] J. Stockel,[1] V. Weinzettl,[1] and S. Zoletnik[4]

[1)] *Institute of Plasma Physics of the Czech Academy of Sciences, Prague, Czech Republic*

[2)] *Charles University in Prague, Faculty of Mathematics and Physics, Prague, Czech Republic*

[3)] *Szechenyi Istvan University, Gyor, Hungary*

[4)] *Wigner RCP, Budapest, Hungary*

[5)] *Graz University of Technology, Graz, Austria*

[6)] *Czech Technical University, Faculty of Nuclear Sciences and Physical Engineering, Prague, Czech Republic*

(Dated: 13 June 2018)

Atomic beam probe is a new diagnostic tool, using detection of ions coming from the ionized part of diagnostic neutral beams in tokamaks. The method aims to measure plasma density fluctuations and fast variations in the poloidal magnetic field, allowing to follow fast changes of the edge plasma current. Test detector has been installed on the COMPASS tokamak as an extension of the existing lithium beam diagnostic system. It employs a relatively simple concept of an array of conductive detection plates measuring the incident ion current, which is then amplified and converted to voltage signal. The aim of the test detector is to prove the concept of the diagnostic and provide background data for design and installation of a final detector. Also, a numerical code based on NVIDIA CUDA parallel computing platform has been developed for modeling lithium ion trajectories in the given COMPASS plasma shots. We present the developments of the test detector and proof-of-concept measurements of the diagnostic performed both in a laboratory beam system and on the COMPASS tokamak.

I. INTRODUCTION

With the construction of ITER, a new era of nuclear fusion has begun. Technological and operational aspects have come to the forefront. At the same time, we must not forget some fundamental issues of the underlying physics that have not yet been satisfactorily answered, but are extremely important for successful ITER's operation.

One such open and important question is the formation of Edge Localized Modes (ELMs)[1–3]. The widely accepted concept in the fusion community for ELM's formation in tokamaks is the theory of peeling-ballooning instability[4]. To prove this theory, it is important to observe experimentally the plasma pressure profile and the plasma current density profile simultaneously with a good temporal and spatial resolution. The temporal resolution must be better (shorter) than the characteristic time of ELM cycle duration (from $\sim$ hundreds of μs to 10 ms).

A well known phenomena of quantum physics is the so called Zeeman effect, where the degenerate quantum energy levels of an atom can split in the presence of a magnetic field due to the interaction of the electron magnetic momenta with the magnetic field. The change in the energy level is proportional to the local magnetic field: $\Delta E \propto \mu_B m_l B$, where μ_B is the Bohr magneton, m_l is the magnetic quantum number and B is the magnetic field strength. Observing the spectral separation of the Zeeman-split lines one can deduce the local magnetic field strength and if the poloidal component can be disentangled the current density can be calculated. This principle has been already used for plasma current density measurements on DIII-D[5], JT-60U[6], JET[7] and ASDEX[8] using the split of the Li(2p) state in three ≈ 0.1 nm separated spectral lines. The magnetic field measurement through the Zeeman split requires special technology and has limited time resolution.

Another diagnostic which can be used for measurements of plasma current density on toroidal devices is the Heavy Ion Beam Probe (HIBP).[9–11] Its concept is to inject into plasma singly charged heavy ions (i.e. Cs^+) with high energies of hundreds of keV or even MeV to overcome strong toroidal magnetic field. Secondary ionization of ions in plasma then curves their trajectory and allows them to be guided outside of the vessel into an energy analyzer. HIBP is primarily aimed at measuring plasma electric potential and density fluctuations, but can be used to deduce the poloidal magnetic flux (and therefore current density profile) from the toroidal displacement of detected ions. Such measurement was performed for example on TEXT.[12]

Recently, a new method of Laser-driven Ion-beam Trace Probe (LITB) was also proposed to diagnose the poloidal magnetic field profile in tokamaks.[13]

The Atomic Beam Probe (ABP) diagnostic is a novel concept for determining the edge plasma current density with the appropriate temporal and spatial resolution[14]. The main idea was inspired by the concept of HIBP, but instead of detecting two times ionized heavy ions moving across the plasma, ABP detects once ionized light ions stemming from a diagnostic neutral beam used primarily

[a)] hacek@ipp.cas.cz

for Beam Emission Spectroscopy (BES)[15,16]. ABP measures the ions leaving the plasma (see FIG. 1) but still inside the vessel. The toroidal displacement of ions on the detector is determined by the plasma current density profile. For ion detection at COMPASS a detector with a matrix of conductive detection plates was designed[14] which can be placed close to the plasma (see FIG. 1), while for ASDEX Upgrade a scintillator-based optical system[18] has been proposed which needs to be hidden in a port in order to protect it from X-ray and UV radiation. Advantage of this concept is in the easier way to guide neutrals across the stray magnetic field of the tokamak to reach the confined plasma, and also in the presence of the ion-accelerator of the existing BES system. The disadvantage of this approach is that the use of light ion species in the BES system limits the method's applicability to small and medium-sized tokamaks[14,18].

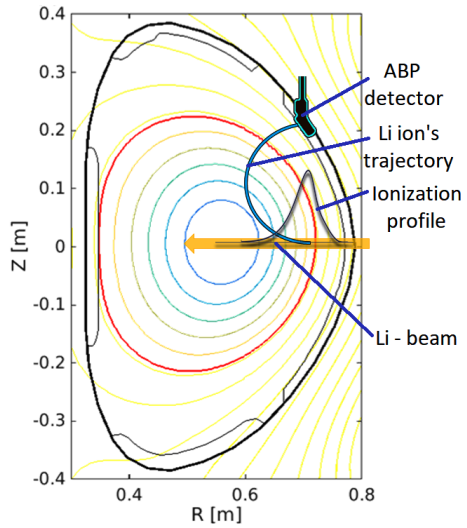

FIG. 1: The basic idea of ABP diagnostic. Toroidal movement of ion trace on the detector is determined by changes in the edge plasma current.

The COMPASS tokamak is the smallest device in operation with ITER-like plasmas (1:10 in a linear scale) with a good diagnostic coverage[19]. COMPASS is operated routinely in ELMy H-mode assisted by two Neutral Beam Injectors[20]. The BES diagnostic system with some modifications needed for ABP[14] was installed and commissioned successfully on COMPASS, thus the COMPASS tokamak is a good candidate for testing the concept of the ABP. The main mission of the BES system on COMPASS is routine measurement of the electron density profile. The fast observation system of the BES - 18 channels of avalanche photodiodes (APDs) in one row - allows us to reconstruct electron density profiles with high temporal (up to 2 μs) and with moderate spatial (1 cm) resolution[21,22].

For the proper interpretation of experimental results we need a precise modeling of the ion trajectory in the magnetic field of COMPASS. TAIGA, the parallel numerical code calculating trajectories of Li^+ ions in a magnetic field, is described in section II.

In section III. we describe briefly the test ABP detector installed on the COMPASS tokamak. In the very first measurements with ABP test detector during plasma discharges we have clearly detected deflected Li^+ ions from the Li-beam, but the character of signals from amplifiers showed some unexpected behavior. To understand this phenomenon we have conducted specifically prepared laboratory tests with the detector.

Results of laboratory tests are summarized in section IV. After laboratory tests we continued with test measurements on COMPASS. Section V. contains results from test experiments performed during plasma shots on COMPASS.

Consequences of the achieved experimental results of the ABP test detector for the final detector design are collected in the section VI.

In the last section we summarize experiences gained with ABP test detector on the COMPASS tokamak.

II. PARALLEL NUMERICAL CODE FOR ION TRAJECTORY CALCULATIONS

From the beginning of the ABP development it was clear that the diagnostics needs to be supported by modeling of ion trajectories in order to:

1. evaluate the effect of magnetic field on ions stemming from the neutral Li-beam, and also

2. interpret experimental data measured by the ABP detector.

For the first purpose we developed a sequential numerical code ABPIons[14] implemented in MATLAB. From experiences with ABPIons performance we concluded that sequential code will not be fast enough for a detailed interpretation of the experimental data. Therefore, we decided to adopt a parallel approach. This parallel code (TAIGA - **T**rajectory simulations for **ABPI**ons with **G**PU **A**cceleration) was written in CUDA and can be run on different NVIDIA GPUs.

A. Code Description

The TAIGA code solves numerically (using the Runge–Kutta method) the equation of motion for charged particles in inhomogeneous magnetic field.

As a first step the real beam is discretized into numerous parallel virtual beams ($\sim 10^5$ parts) on a regular grid and components of the tokamak's magnetic field are interpolated using two-dimensional bi-cubic spline functions. The ion source function is calculated from modeling beam ionization using the RENATE code[23].

Each thread of the given graphical processor is used to solve the equation of motion for particles in the given virtual beam, thus virtual beams are processed in parallel way (see FIG. 2.).

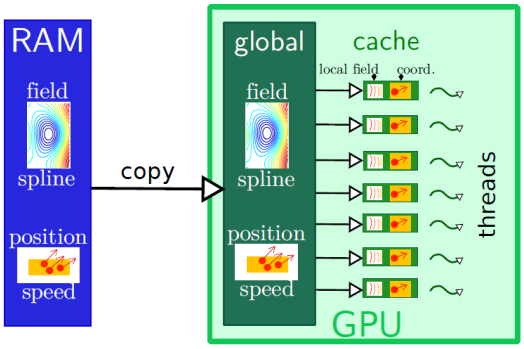

FIG. 2: The scheme of parallel calculation of the ion trajectories on an NVIDIA type graphical processor

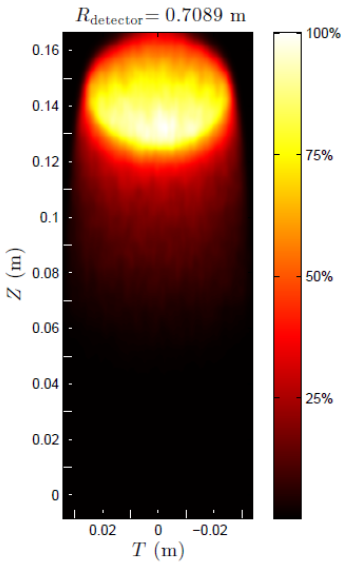

FIG. 3: Modeled spot of Li-ions on the ABP test detector in gas shot (#7955) on the COMPASS tokamak

B. Trajectory modeling validation

For the validation of the numerical code we have chosen the experimental approach. We decided to model ions' trajectories in a COMPASS gas shot (#7955) without plasma discharge and only with toroidal magnetic field present. The toroidal field was set to $B_t = 1.15\,\text{T}$, energy of the Li-beam was $E_b = 60\,\text{keV}$ and the diameter of the beam was $D_b = 4\,\text{cm}$. The tokamak vessel was filled up with N_2 gas with pressure $4 \cdot 10^{-2}\,\text{Pa}$, thus the ionization rate along the beam was constant. After processing, we observed very good agreement between experimental data and modeled trajectories. The position of the maximum ion current intensity according to the numerical model is $T_{nm} = 0 \pm 0.01\,\text{cm}$, $Z_{nm} = 14 \pm 0.01\,\text{cm}$ (T denoting toroidal and Z vertical position, see FIG. 3). The experimentally observed maximum of ion trace on the ABP detector was found to be $T_{exp} = 0 \pm 0.1\,\text{cm}$, $Z_{exp} = 14 \pm 0.5\,\text{cm}$, where the error is determined by the size of the plates.

III. TEST DETECTOR

The test ABP detector was installed on the COMPASS tokamak (see FIG. 4). It is using the COMPASS diagnostic Lithium beam[21,22] as an ion source. For purposes of the ABP measurements, the beam system was upgraded to be able to reach higher beam energies[14]. High voltage power supplies were upgraded to cover voltage range from 0 V to 120 kV. In a standard COMPASS magnetic field of 1.15 T, Li-beam energy of approximately 85 keV is needed to guide the Li-ions out of plasma to the ABP detector position. It is also possible to exchange the ion source to Sodium, which then requires $\sim$ 25 keV beam energy to reach the detector.

There are two main aims of the test detector:

1. prove the principle of the ABP diagnostic by detection of beam ions in plasma, and

2. provide input for a design of the enhanced final detector solution.

The detector purpose is to measure the incident ion current to a segmented copper plate. The test ABP detector consists of a vertically movable aluminum holder structure, detector head with matrix of 20 gold-plated copper detector plates with different surface areas (5 mm x 0.5 mm, 5 mm x 1 mm, 5 mm x 2 mm), 4 Langmuir probes for estimation of the local plasma parameters and carbon limiters in order to protect the detector plates from direct plasma inflow (see FIG. 5). As the detector plates are placed in a strong magnetic field which is nearly parallel to their surface, the expectations were that most of the secondary electrons generated by UV/X-ray radiation and by the beam would not leave the plate.

The ion current level on the plates is in the order of μA[14], therefore cannot be measured directly. Current amplifiers are used to convert the currents to voltage signals. The first stages of the amplifiers are connected to the detector plates and keep the input at ground potential[14]. The detector is inserted through a top vertical oval port at the same toroidal position as the lithium beam. The vertical position of the detector head can be changed by approximately 10 cm - minimum insertion keeps the detector well hidden in the port shadow while maximum insertion is located well inside the plasma for usual D-shaped COMPASS tokamak discharges.

The fact that the test detector is not movable in the toroidal direction means that while it is sufficient for the plasma noise determination, it cannot detect the Lithium beam ions in standard COMPASS plasmas with plasma currents exceeding certain threshold depending on the beam diameter and plasma shape. The ions are toroidally deflected by a few cm in the poloidal tokamak magnetic field and miss the detector plates (roughly 60 kV of

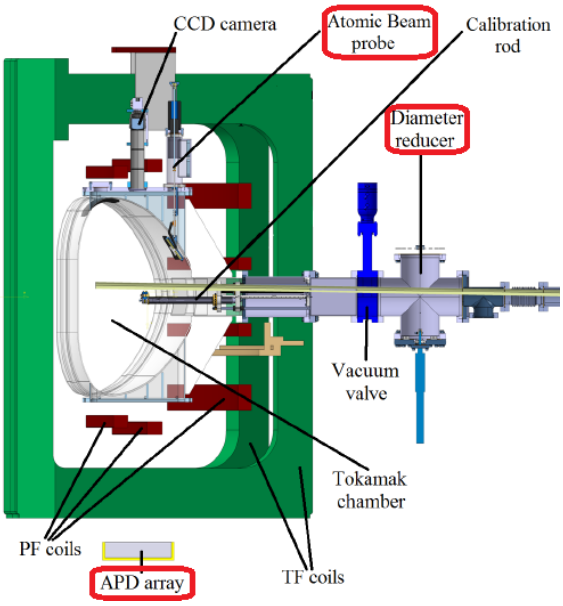

FIG. 4: The placement of test ABP detector, APD detector system and reducer on the COMPASS tokamak

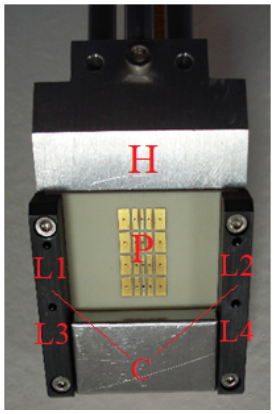

FIG. 5: The head of the test ABP detector with copper detector plates of different size (H – Al holder, P – Cu plates, C – carbon limiters, L1, L2, L3, L4 – Langmuir probes)

plasma current deflects the center of ion trace by 1 cm). The way to observe the ions in a regular plasma discharge is either to shoot the beam under an angle of few degrees or detect the ions in the current ramp-up or ramp-down phase of a discharge. The ions can also be detected after the discharge, when the toroidal magnetic field is still present and the lithium beam is weakly ionized in the residual hydrogen/deuterium neutral gas. The test detector was designed in this way to avoid mechanical difficulties, while delivering goals stated above. The results of this test detector will be used to manufacture a proper final ABP detector head with the possibility of toroidal movement.

IV. LABORATORY MEASUREMENTS

In the first plasma measurements with the test detector, several issues appeared. Firstly, the observed ion signal levels as well as the background noise levels were not proportional to the different detector plate sizes. Secondly, the observed ion signals were distorted. One can see the behavior on FIG. 6 from COMPASS discharge #11344 with toroidal magnetic field 0.8 T and low plasma current of 95 kA. 60 keV Li-beam with $\sim$ 4 cm diameter was injected into the plasma. It was periodically chopped out of plasma for background correction of the signal with period of 44 ms. The signal distortion appeared during beam chopping times.

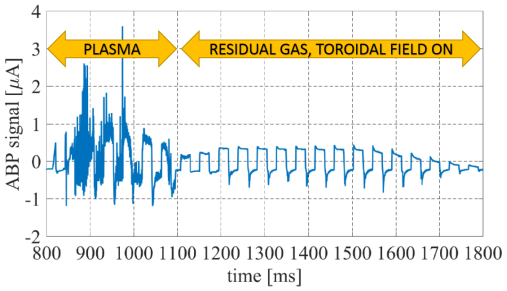

FIG. 6: Distorted ion signal on 2 mm ABP plate in COMPASS plasma discharge #11344.

It was found that the signal distortion is linked with a subsequent creation of a microscopic non-conductive layer of plasma-sprayed material on the unprotected detector head and plates. It was also found that a significant charge accumulates on the insulation ceramic between individual plates and contributes to their signal in a complex way. To protect the ceramic and plates from these detrimental effects, the detector head was modified and a copper mask with plate-sized holes was put 1 mm in front of the detector plates. The detector head was grounded to the tokamak vessel and the mask was isolated from the detector head in order to have a possibility to bias it.

A. Laboratory measurement setup

In order to properly understand the role of secondary electron (SE) emission on detector signals, tests were done with a laboratory alkali beam (Lithium and Sodium sources were used) in Wigner Research Centre for Physics. Accelerated ions were injected directly towards the detector. To simulate the tokamak magnetic field and its suppression effect on secondary electrons, neodymium

magnets were used (scheme of the experiment is on FIG. 7) to create 50 mT magnetic field parallel to the detector surface. To assess the role of secondary electron emission due to ion impact, the mask was biased negatively and positively either to suppress or pull out the electrons from the plates. Subsequently, a double mask design was also tested with a second mask added 2 mm in front of the detector. In this setup, the mask nearer to the plates was biased and the second one was grounded.

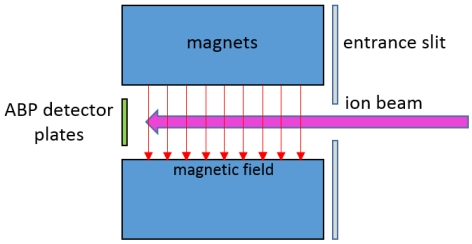

FIG. 7: Scheme of the laboratory measurement

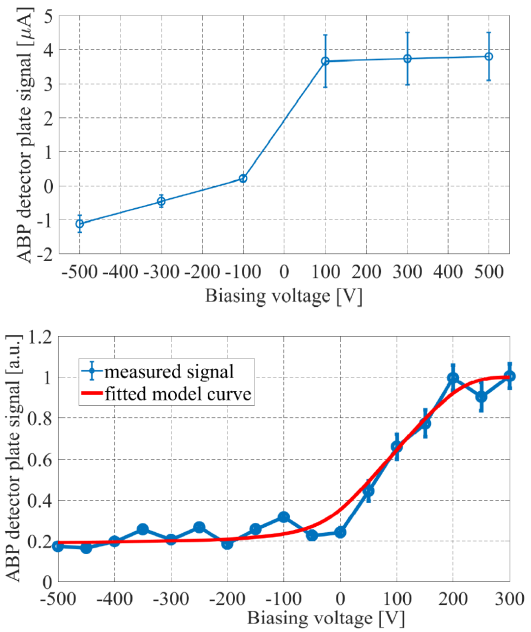

FIG. 8: (top) Biasing experiment with a single detector mask. (bottom) Biasing experiment with double detector mask (first mask is biased, second one grounded). Experimental data are shown for ABP signals on 2×5 mm sized plates during 20 keV Sodium beam laboratory measurement (blue). Red curve represents best fit of modeled ABP signal, determining the secondary electron temperature.

B. Role of secondary electrons

Secondary electrons are created both on the detection plates and other detector surfaces by ion impact and in plasma conditions also by photo-emission by plasma UV and X-ray radiation and by influx of fast plasma particles. Contribution is affected by the energy and angle of the impacting ions and by magnetic field lines inclination to the plates.

It would seem the best to negatively bias the mask in front of the detector plates and to ground all other detector parts, so that secondary electrons are suppressed, similarly as in a Faraday cup measurement. The laboratory measurement with biased single and double mask setup can be seen on FIG. 8. We observed that during a positive biasing, voltages above 200 V are sufficient to stabilize the signal as all secondary electrons are carried away from the plates by E×B drift motion. During a negative biasing, in a single mask setup, the plates' signal got negative and was not saturated for tested voltages up to -500 V. We attributed this effect to SE originating on the edges of the mask holes, which are then repelled from the negatively biased mask and can reach detector plates. The effect was not present or was severely limited for the double mask design, where the signals got clearly saturated even for low negative biasing voltages. An important observation was also that with the double mask setup and when suppressing SE by sufficient negative biasing voltage, the detected signal levels were perfectly proportional to the different plate sizes.

To qualitatively evaluate the measurement, a Monte Carlo modeling of the escaping SE was done in MATLAB and fitted to the measured data. Temperature of the SE was the fitted parameter of the model, assuming Maxwellian SE energy distribution and angular SE

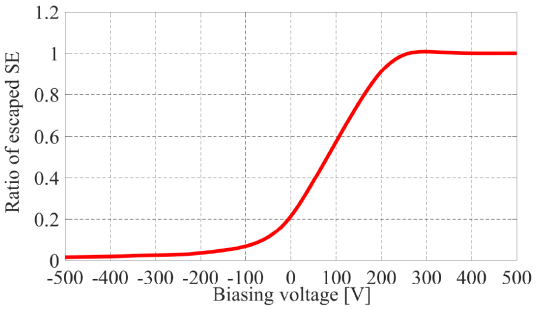

FIG. 9: Ratio of escaping secondary electrons calculated for the laboratory biasing experiment with double detector mask

distribution determined by the cosine emission law. The fit showed that SE induced by ion bombardment of the plates have temperature 10.2 eV and SE yield is 4.9 electrons per incident ion. Both values seem to be reasonable with regards to available literature[24], although experience from similar Faraday cup measurements of the COMPASS beam suggest presence of SE with higher energies of up to 100 eV.

Given these results, the contribution of SE on the ABP signal in COMPASS measurements could be estimated. Table I below shows estimated ratios of SE which escape the ABP detection plates. The estimates are given for ABP measurement in a standard COMPASS magnetic field, which is $\sim 0.8\,\mathrm{T}$ in the place of the ABP detector (1.15 T on the magnetic axis) for different ABP plate sizes and taking into account a possible misalignment of magnetic field lines with respect to the detector plane. The effect of SE suppression by the use of negative biasing voltage $-500\,\mathrm{V}$ of the first mask is given in brackets.

Plate size [mm]	magnetic field misalignment		
	0°	2.5°	5°
0.5×5	3.59 (2.73)	5.65 (3.64)	8.03 (4.88)
1×5	2.07 (1.45)	4.26 (2.48)	6.68 (3.77)
2×5	1.28 (0.90)	3.50 (2.01)	5.92 (3.27)

TABLE I: Estimated ratio of escaping SE in % due to the impact of beam ions. Numbers are given for different plate sizes and possible magnetic field misalignments with respect to the detector plane. Effect of SE suppression by negatively biasing detector mask to $-500\,\mathrm{V}$ is in brackets.

Given the calculated value of SE yield of ~ 4.9 per incident ion, the contribution of SE to the measured signal can be significant, from several % to tens of %, depending on the plate size and magnetic field misalignment. Suppression of SE by negative biasing of the detector mask can be effective, decreasing the number of escaping SE by tens of %.

The outcome of the laboratory measurements was therefore the decision to use the double-mask detector head design to (1) protect the insulation ceramic from direct ion impact and to protect the detector plates from being covered by a non-conductive layer during plasma experiments and (2) to use mask biasing as a method of SE suppression.

V. PLASMA MEASUREMENTS

Measurements in COMPASS plasma discharges aimed to achieve several goals: (1) assess the background plasma signal and identify background noise sources, (2) demonstrate the ability to reduce beam diameter to several mm, (3) demonstrate the detector ability to measure with microsecond temporal resolution.

A. Background plasma signal

The aim of the background measurements was to identify the main noise sources and estimate the signal to background ratio of ABP measurements in regular plasma discharges on COMPASS. We measured with the double-mask, the mask closer to the plates was biased to $-270\,\mathrm{V}$, the external one was grounded. ABP signals from 52 L-mode discharges and 17 H-mode discharges were used for the analysis having a wide range of plasma parameters and varying ABP detector insertion depth. The results of the analysis can be seen on FIG.10. The data points are mean signal levels of individual ABP plates (aggregate of all plate sizes) calculated over $100\,\mu\mathrm{s}$ time windows from the stable flat-top phase of the plasma discharges.

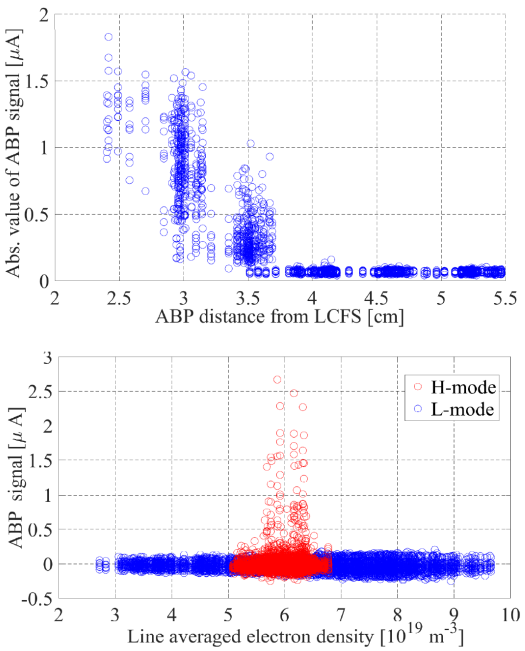

FIG. 10: (top) Dependence of the absolute value of ABP background plasma signal on distance from the separatrix in L-mode COMPASS discharges. (bottom) Dependence of ABP background plasma signal on plasma density in L-mode and H-mode discharges with sufficient distance of the detector from separatrix.

On the top figure of FIG. 10, data from L-mode discharges with varying ABP insertion levels show a strong dependence of the absolute signal level on the distance of detector from plasma (calculated from EFIT reconstruction). It is clear that to keep a reasonable background signal level, the detector has to be sufficiently distanced from plasma. The bottom figure shows data from both L-mode and H-mode discharges, where the distance of the detector from separatrix was equal or greater than 4 cm. The observed background signal there is generally in the range of several tenths of μA. Both negative and positive signals were systematically detected, based on the particular shot and time, with a visible weak dependence on plasma density. During the ELMy H-mode phase, the ABP signals show positive peaks during the ELM crash. These peaks in signal can reach up to few μA.

The strong dependence of ABP signal on distance from separatrix indicates that the background noise is dominated by the inflow of scrape-off layer (SOL) plasma particles and not by photoemission by UV/X-ray radiation, which is likely well suppressed by the strong toroidal

magnetic field. The electron inflow is more often higher than the ion one, even with the applied negative mask biasing, resulting in net negative signals.

As the measured Li-ion signal on the ABP detector is expected in the order of μA, the signal to background ratio in L-mode COMPASS shots is expected in the order of 10 : 1 while in H-mode shots it can be as low as 1 : 1. The use of sufficiently fast beam chopping technique will therefore be necessary to correct the signals for background.

B. Detection of Lithium ions in COMPASS plasmas

Beam reduction

The spatial resolution of ABP diagnostic is determined by the Li-beam diameter[14]. The standard Li-BES is using focused diagnostic beam with a diameter $\sim$ 2.5 cm. For the ABP diagnostic, such a large diameter is not acceptable, therefore, we decided to build a rotational beam reducer in the Li-beam system. It allows us to inject beams with different diameters for ABP purposes (2 mm, 3 mm, 5 mm, 10 mm), and can also be set for standard Li-BES measurements (see FIG. 11.)

FIG. 11: The photo of the beam reducer with different apertures to define the diameter of the diagnostic beam

Plasma measurements

Using the reducer to limit beam diameter does not allow beam injection under non-zero angle. Therefore, with the toroidally fixed test ABP detector, we were able to observe the beam ions only in the current ramp-down phase of plasma discharges. Main parameters of the reference discharge used for the ABP measurements are shown on FIG. 12. Dedicated measurements conducted in the above mentioned plasmas had a dual target:

1. to study performance of the beam reducer, and
2. to learn about the effect of fast chopping on the measured signals.

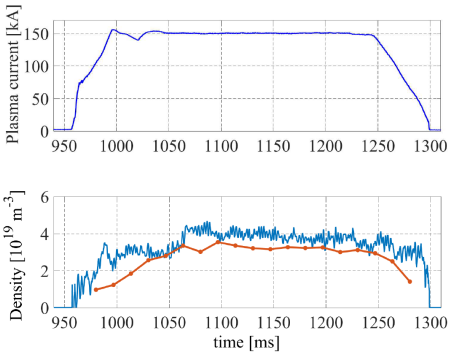

FIG. 12: Main parameters of the plasma scenario used for Li-ion detection by the test ABP detector. (top) Plasma current, (bottom) Line averaged electron density measured by microwave interferometer (blue) and Thomson scattering diagnostic (red).

As can be seen on FIG. 13, reduced beams with diameters of 10 mm, 5 mm and 3 mm and with chopping time set to 1 ms are clearly detectable by ABP, both in the ramp-down phase of the discharge and after the plasma in residual gas. The ions stemming from the diagnostic beam arrive at detector position when the plasma current is sufficiently low and so the toroidal deflection of beam ions by the edge plasma current is small enough. Increasing level of the detected ion current as the plasma current is decreasing results from decreasing toroidal shift of Li-ion's spot center, in agreement with the ion trajectory modeling.

It is important to note that for a proper modeling of beam ion trajectories and thus a successful interpretation of the measured signals, it is necessary to reliably reconstruct the edge plasma density profile along the beam path. That is in order to determine the profile of ionization rate of beam particles and thus starting ion positions. Therefore, a simultaneous measurement of the ABP and APD diagnostics is needed. FIG. 14 shows light emission of Lithium atoms detected by an APD channel during the reduced beam discharges. Signals detected from 10 and 5 mm beams are sufficient for a density reconstruction while the light emission of 3 mm sized beam is at the detection limit of our BES observation system.

The ion trajectory modeling done for one of the discharges with 10 mm beam diameter is shown on FIG.15. It shows the lithium ion trace on the detector plane for 2 different times of COMPASS discharge #14405. The ion trace has a comet-shaped form where its curvature and its horizontal (= toroidal) shift from zero position is determined by the edge plasma current. The ion signal intensity along the comet's curve is determined by the edge plasma electron density profile. The modeled pictures illustrate how the curved ion trace in the detector plane straightens and shifts towards less toroidally deflected position with decreasing plasma current, which is

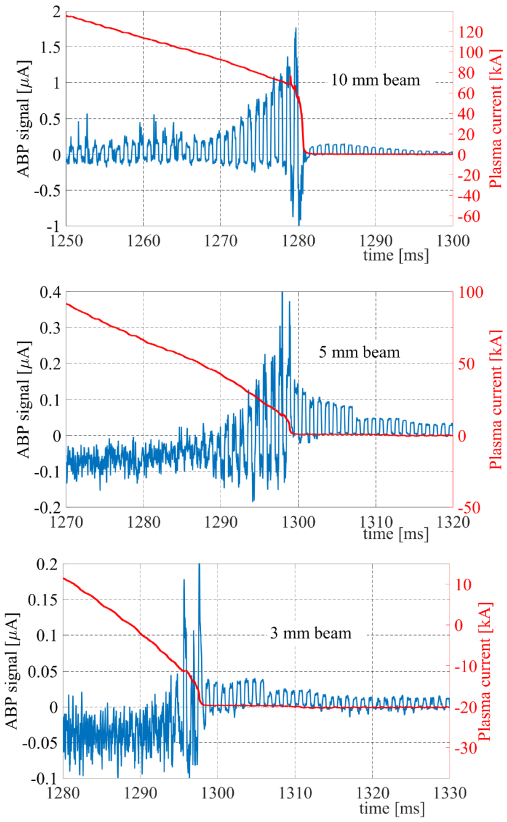

FIG. 13: Li-ion signals of reduced beams in COMPASS plasma shots detected by 2×5 mm sized ABP plate. Plasma current signal in each discharge is also shown.

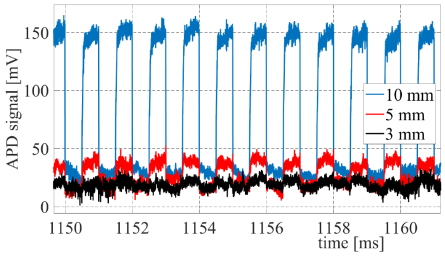

FIG. 14: Li-beam emission signals detected by an avalanche photodiode detector channel during COMPASS plasma shots. Beams were injected with reduced diameters of 10, 5 and 3 mm. Li-beam was injected in each shot with 1 ms chopping period.

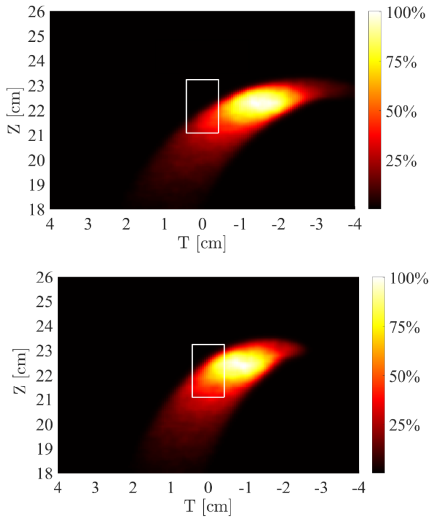

FIG. 15: Modeled Li-ion trace on the ABP detector plane for 2 time slices of the COMPASS shot #14405 with 10 mm beam diameter.(top - $t = 1250$ ms, bottom - $t = 1275$ ms. White rectangular frame represents the sensitive area of the ABP test detector)

in good correspondence with the observed ABP signals.

In the dedicated experimental campaign we studied also the effect of chopping time on the detection of Li-ions by the test ABP detector. For ABP measurements in H-mode discharges, to observe the signal behavior during fast ELM phenomena it is necessary to chop the beam out of plasma with a sub-millisecond period to correct the signal for background. The electronics on COMPASS allows a chopping frequency of up to 250 kHz. During the measurements we demonstrated the capability of the ABP detector to follow fast changes in ion signal during chopping with frequencies up to 100 kHz. As an example, the detected ion signal from the measurement with the beam chopping period of 100 μs can be seen on FIG. 16.

VI. FINAL DETECTOR DESIGN

The ABP test detector was designed as a detector with a fixed toroidal position, which limits its application in standard COMPASS discharges due to the toroidal ion shift. Therefore, for a relevant use as a plasma diagnostic, a detector with an adjustable toroidal position needs to be developed. By modeling of the toroidal ion shifts based on data from COMPASS H-mode plasma shots, it was found that a new detector needs to reach toroidal positions of up to $\sim$ 6 cm. FIG. 17 shows modeled toroidal shift values for COMPASS H-mode discharges in the whole achievable range of COMPASS plasma currents.

As stated in section V., the reduction of the beam size diameter to 3 mm is at the limit of the APD system. Therefore, a use of detection plates with significantly smaller sizes does not bring any advantage. Our calculations imply that while using 5 mm diameter beam and 2×5 mm sized plates, it is still possible to observe desired sub-millimeter shifts of the ion trace by calculating the movement of center-of-mass of the detected signals. Using a greater plate size also keeps advantages of a smaller

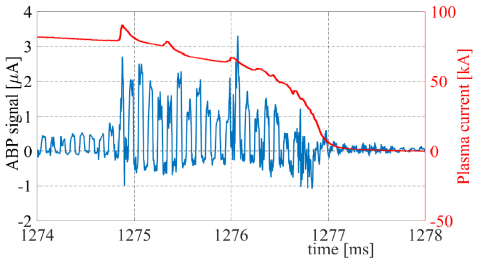

FIG. 16: ABP signal on a 2 mm detection plate in COMPASS discharge #14411. Li beam was chopped with period 100μs

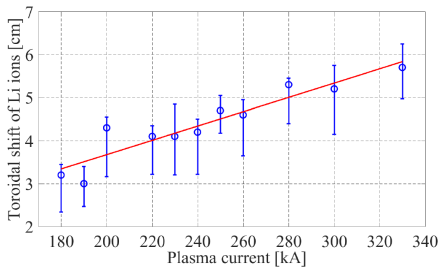

FIG. 17: Modeled toroidal shift values for COMPASS H-mode discharges with different plasma currents. Data points are points of maximum ion signal and error bars define the toroidal area of strong ion signal (above half of maximum ion signal)

SE effect and a higher signal-to-noise ratio.

To summarize, based on the experience from operation of the test ABP detector, following requirements for a design of the final detector solution were set:

1. Detector head has to allow a measurement of ions toroidally shifted by up to 6 cm either solely by adjustable toroidal position or in combination with beam injection under a defined angle through a (modified) diameter reducer.

2. Two isolated masks in front of the detector plates will be used for protection of the sensitive detector area as well as for biasing to suppress SE.

3. Optimal detector plate size was chosen as 2×5 mm (toroidal $\times$ vertical). Based on available port space, new detector head will contain 50 plates in 5 rows of 10 plates covering an area of $\sim 2.2 \times 2.6$ cm.

VII. CONCLUSIONS

A test detector was installed on the COMPASS tokamak to investigate the concept of atomic beam probe diagnostic as a tool to measure spatio-temporal variations of the edge plasma current profile. For the proper interpretation of experimental results, parallel numerical code TAIGA for fast calculation of ion trajectories was developed and validated. Laboratory measurements were conducted to understand the detected signals and led to improvements in the detector design in order to protect the sensitive detector area and successfully suppress the effect of SE. In COMPASS plasma measurements, we (1) analyzed the background noise levels, (2) demonstrated the possibility of reduction of the beam diameter up to 3 mm, (3) successfully detected Li-beam ions and (4) demonstrated the possibility of fast beam chopping as a method to correct for the background noise. Results of the test detector thus successfully proved the diagnostic concept and provided us with comprehensive design requirements for the final detector solution.

VIII. ACKNOWLEDGEMENT

This work received funding from the Czech Science Foundation project GA16-25074S and MEYS project LM2015045.

IX. REFERENCES

[1] H. Zohm, Plasma Phys. Control. Fusion **38** (1996) 105–128
[2] J. W. Connor, Plasma Phys. Control. Fusion **40** (1998) 531–542
[3] A. Kirk et al., Phys. Rev. Lett. **92** (2004) 245002
[4] P. B. Snyder at al., Phys. Plasmas **9** (2002) 2037
[5] D.M. Thomas et al., Rev. Sci. Instrum. **61** (2003) 1541
[6] K. Kamiya et al., Rev. Sci. Instrum. **81** (2010) 033502
[7] A.A. Korotkov et al., Rev. Sci. Instrum. **75** (2004) 2590
[8] D. M. Thomas et al., Phys. Rev. Lett. **93** (2004) 065003
[9] T. P. Crowley, Rev. Sci. Instrum. **59** (1988) 1638
[10] A. Shimizu et al., Rev. Sci. Instrum. **76** (2005) 043504
[11] A. V. Melnikov et al., Nuclear Fusion **57** (2017) 072004
[12] J. G. Schwelberger et al., Rev. Sci. Instrum. **69** (1998) 3828
[13] X. Yang et al., Rev. Sci. Instrum. **87** (2016) 11D608
[14] M. Berta et al., Fusion Engineering and Design **88** (2013) 2875-2880
[15] K. McCormick et al., Fusion Engineering and Design **34–35** (1997) 125–134
[16] S. Zoletnik et al., Rev. Sci. Instrum. **76** (2005) 073504
[17] S. Zoletnik et al., accepted for publication in Rev. Sci. Instrum. HTPD Conference Proceedings (2018)
[18] J. Galdon-Quiroga et al., Jurnal of Instrumentation **12** (2017) C08023
[19] V. Weinzettl et al., Journal of Instrumentation **12** (2017) C12015
[20] R. Pánek et al., Plasma Phys. Control. Fusion **58** (2015) 014015
[21] G. Anda et al., Fusion Engineering and Design **108** (2016) 1–6
[22] M. Berta et al., Fusion Engineering and Design **96–97** (2015) 795–798
[23] D. Guszejnov et al., Rev. Sci. Instrum. **83** (2012) 113501
[24] K. Bethge and K. Lexa, Brit. J. Appl. Phys. **17** (1966) 181-186

Fast density reconstruction of Li-BES signal on the COMPASS tokamak

J. Krbec,[1, a)] P. Háček,[1, b)] M. Berta,[2] J. Seidl,[1] M. Hron,[1] and R. Pánek[1]
[1)] *Institute of Plasma Physics of the CAS, Prague, Czech Republic*
[2)] *Department of Physics and Chemistry, Széchenyi István University, Győr, Hungary*

(Dated: 25 June 2018)

This article deals with the fast and automatic reconstruction of edge plasma electron density from radiation of energetic Li atoms of the diagnostic beam on the COMPASS tokamak. Radiation is detected by a CCD camera and an Avalanche Photo-Diode system with a temporal resolution 20 ms and 2 μs, respectively. Both systems are equipped with an optical filter 670,8 nm which corresponds to lithium $1s^2 2s^1$-$1s^2 2p^1$ transition. A theoretical model and a procedure of data processing from raw signal to density profile are described. The reconstruction algorithm providing absolutely calibrated electron density profiles with measurement error from relative light profiles is implemented in Python. Time consuming parts of a code were optimized to provide reconstruction of one profile in less than 10 ms which makes the code useful for processing of a large amount of data. Thanks to this calculation speed it is possible to reconstruct electron density profiles between two consecutive shots on the COMPASS tokamak with few μs time resolution.

Keywords: density, reconstruction, BES, Li-beam, COMPASS

I. INTRODUCTION

Understanding of edge plasma density behavior plays a crucial role in edge particle transport and ELMs physics. Edge plasma physics is one of the key research topics of the COMPASS tokamak [Panek *et al.* (2015)]. Studying of plasma behavior on the machine which has ITER-like geometry with a single-null-divertor and clear high confinement mode (H-mode) in ohmic regime helps understand plasma behavior on big machines like ITER. The COMPASS is well equipped with diagnostics, especially with a comprehensive set of diagnostics focused on the edge plasma. One of these diagnostic is a Li-beam injector used for Beam Emission Spectroscopy (BES) measurements.

Li-BES is an active spectroscopic method suitable for edge electron density measurement using line radiation detection of injected lithium atoms. The technique was used for radial density profile measurement at the TEXTOR [Pusztai *et al.* (2009); Wolfrum *et al.* (1993)] and and DIII-D [Thomas (1995)] tokamaks and it is used at the ASDEX [Willensdorfer *et al.* (2014)], JET [Réfy *et al.* (2018)], KSTAR [Lampert *et al.* (2015)] and EAST [Anda *et al.* (2018); Zoletnik *et al.* (2018)] tokamaks at present. The method was also successfully used for a 2D plasma density fluctuations measurement at the Wendelstein 7-AS stellarator [Zoletnik *et al.* (2005)].

Light radiation is detected by the CCD camera and the Avalanche Photo-Diode (APD) system with an excellent temporal resolution of 2 μs on the COMPASS tokamak [Anda *et al.* (2016); Berta *et al.* (2015)]. The reconstruction of electron density profile is based on a collisional-radiative (CR) model which is extended by the absolute calibration method described by Schweinzer [Schweinzer *et al.* (1992)].

A brief overview of BES and the experimental setup of Li-BES diagnostics on the COMPASS tokamak is listed in sections I A and I B. Information about the CR model, equation for density reconstruction and error estimation is summarized in the theoretical part of this article (section II). The reconstruction algorithm implemented in Python is described in section III. At the end of the article, experimental results from the APD system and execution time of the code is shown. It is important to mention and emphasize, the target of this work was to work out automatic and fast density reconstruction algorithm for the edge region of the COMPASS tokamak.

A. Description of BES

In general, BES is an active spectroscopic method based on an injection of neutral atoms into a plasma. These atoms undergo collisional processes due to an interaction with plasma particles. A subsequent spontaneous emission of excited atoms produces photons which are detected by an observation system. Plasma parameters can be estimated from the detected light spectrum. The interaction of the beam with plasma can be described by the CR model.

The light signal at a different position along the beam path is correlated which is a drawback of BES is that. Finite decay time of spontaneous emission and motion of beam atoms smears density information in a light profile. Beam attenuation along the path also causes propagation of information about density along the path which results in anti-correlation of the light signal on the rising and decreasing part of the light profile.

These artificial phenomena are removed from the light signal by a deconvolution process which results in reconstructed density [Pietrzyk, Breger, and Summers (1993)].

[a)] Also at Faculty of Nuclear Sciences and Physical Engineering, Czech Technical University in Prague, Prague, Czech Republic; Electronic mail: krbec@ipp.cas.cz
[b)] Also at Faculty of Mathematics and Physics, Charles University, Prague, Czech Republic

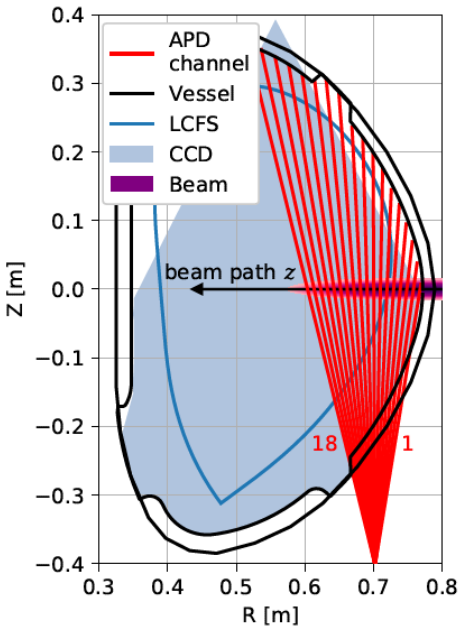

FIG. 1. Poloidal cross section of the COMPASS tokamak vessel with observation system's (18 APDs in one raw) lines of sight and typical diverted plasma shape.

A method used on the COMPASS tokamak which is based on Schweinzer algorithm [Schweinzer *et al.* (1992)] is described in a section III. Benefit of the method is the fact that the reconstruction does not need the absolutely calibrated light profile. It means, the knowledge about transmittance of optical elements, étendue and beam current in plasma is not required. Compared to the RENATE code [Guszejnov *et al.* (2012)] which is written in IDL and does forward calculation of light profile, the reconstruction code in Python was developed to make a forward calculation and a reconstruction fast enough and without using time consuming optimization methods.

B. Experimental setup

An experimental setup is shown in FIG. 1. The detection system is located at the same poloidal cross section as Li-beam and is observing the beam injected in the midplane as can be seen in FIG. 1. Lithium atoms accelerated up to 120 keV are used for BES on the COMPASS tokamak [Anda *et al.* (2016)].

The detection system consists of the CCD camera (640x480 @ 50 frames/s) located on the top of the tokamak vessel and the APD system (1x18 @ 2 MS/s) suitable for density fluctuation measurement [Berta *et al.* (2015)] located on the bottom of the vessel. The both systems are equipped with optical filter with central wavelength equal to 670,8 nm which corresponds to a lithium $1s^2 2p^1 \rightarrow 1s^2 2s^1$ transition.

A transition decay time given by spontaneous decay time (27 ns) and collisional de-excitation processes produce smearing of information about density to ≈ 2 cm for a 60 keV beam and plasma density $n_e = 3{\cdot}10^{19}$ m^{-3}. The article will focus on processing the signal from APD system because of low temporal resolution of CCD camera therefore temporal resolution is given by a beam chopping frequency (on/off modulation of the beam). The maximal chopping frequency is 250 kHz and the light profile can be obtained on the both raising and decreasing edge of the signal (FIG. 4) thus the maximal temporal resolution is 2 μs.

II. THEORETICAL MODEL

A. Collisional-radiative model

CR model describes population of excitation states of lithium atoms during an interaction with plasma. Equation for i-th excitation state N_i is given by equation (1)

where n_e, n_p are electron and proton density, $\langle \sigma_{e,ij} v \rangle$ stands for the rate coefficients (RC) for the electron impact processes from i-th to j-th state, $\sigma_{p,ij}$ express cross-section (CS) for proton impact processes from i-th to j-th state and $\sigma_{pEL,i}$ is proton impact electron loss, A_{ij} are the transition probabilities of spontaneous emission from i-th to j-th state, $\langle \sigma_{eion,i} v \rangle$ is rate coefficients for the electron impact ionization and v_b is beam velocity.

$$\begin{aligned}\frac{\mathrm{d}N_i}{\mathrm{d}z} = &\sum_{j,j\neq i} \frac{\langle \sigma_{e,ji} v \rangle}{v_b} n_e N_j - \sum_{j,j\neq i} \frac{\langle \sigma_{e,ij} v \rangle}{v_b} n_e N_i + \sum_{j,j\neq i} \sigma_{p,ji} n_p N_j - \sum_{j,j\neq i} \sigma_{p,ij} n_p N_i \\ &+ \sum_{j,j>i} \frac{A_{ji}}{v_b} N_j - \sum_{j,j<i} \frac{A_{ij}}{v_b} N_i - \frac{\langle \sigma_{eion,i} v \rangle}{v_b} n_e N_i - \sigma_{pEL,i} n_p N_i \end{aligned} \quad (1)$$

An approximate rate coefficients $\langle \sigma v \rangle$ were used in (1)

because of the fact the $v_\mathrm{p} \ll v_b \ll v_\mathrm{e}$ [1], relative velocities are $|v_\mathrm{p} - v_b| \approx v_b$ and $|v_\mathrm{e} - v_b| \approx v_\mathrm{e}$ and rate coefficients are

$$\langle \sigma_\mathrm{p} v \rangle = \sigma(v_\mathrm{p}) v_b, \ \langle \sigma_\mathrm{e} v \rangle = \int \sigma(v_\mathrm{e}) v_\mathrm{e} f(v_\mathrm{e}) \mathrm{d}v_\mathrm{e}$$

where $f(v_\mathrm{e})$ is electron velocity distribution functions.

Rate coefficient formula for Maxwell-Boltzmann velocity distribution function of electrons can be found in [Bell *et al.* (1983)]

$$\langle \sigma_\mathrm{e} v \rangle = \left(\frac{8kT}{\pi m_\mathrm{e}} \right)^{\frac{1}{2}} \int_{\frac{E_{Th}}{kT}}^{\infty} \sigma(E) \frac{E}{kT} e^{\frac{-E}{kT}} \mathrm{d} \left(\frac{E}{kT} \right) \qquad (2)$$

where m_e is the electron mass, E_{Th} is a threshold energy for the corresponding process and kT is a temperature of the plasma in eV.

The cross section for inelastic collisions of lithium atoms with electrons and protons was taken from databases [Janev and Smith (1993); Wutte *et al.* (1997); Schweinzer *et al.* (1999)]. Cross sections for downward transition processes are obtained from detailed balance condition.

B. Density equation

The implemented reconstruction method was described by Schweinzer [Schweinzer *et al.* (1992)]. The method is based on the algebraic rearrangement of the differential equation (1) for the 2p level obtaining the explicit equation for the density n_e as a function of the beam coordinate z and all occupation densities N_i

$$n_\mathrm{e}(z) = \frac{num}{den} \approx \frac{\alpha(Li_{2\mathrm{p}}(z+h) - Li_{2\mathrm{p}}(z)) - \alpha A_{22} \int_z^{z+h} Li_{2\mathrm{p}}(s)\mathrm{d}s - hA_{2k}N_k(z)}{\alpha \int_z^{z+h} \sigma_{22}(s) Li_{2\mathrm{p}}(s)\mathrm{d}s + \int_z^{z+h} \sigma_{2l}(s)\mathrm{d}s N_l(z)}, \ k \equiv j \neq 2, \ l \equiv j > 2 \qquad (3)$$

where $\sigma_{2j} = \sigma_{\mathrm{e},2j} + \sigma_{\mathrm{p},2j}$, h is an integration step,

$$\alpha Li_{2\mathrm{p}}(z) = N_2(z),$$

and α is a calibration constant which is unknown at the beginning of the reconstruction and it's initial value can be set arbitrarily. Estimation of the n_e comprises simultaneous calculation of (3) together with integration of the system of five ordinary differential equation (1) for 2s, 2p, 3s, 3p and 3d level. Inclusion of more bound Li(nl) states $n \geq 4$ into the calculations has been found unnecessary [Schweinzer *et al.* (1992)].

C. Error estimation theory

A measurement of radiation along the beam path is done in M points with a step Δz given by a spatial resolution of the detection system. Detected light in the j-th channel depends on densities in all previous channels because of the reasons mentioned in section I A, thus

$$Li_{2\mathrm{p}}(z_j) = f(n_\mathrm{e}(z_1), ..., n_\mathrm{e}(z_j)), \ j \in M \qquad (4)$$

where $Li_{2\mathrm{p}}(z_j)$ is the detected light intensity in j-th channel, $n_\mathrm{e}(z_i)$ is the electron density in i-th channel where $i \leq j$ and f represents the CR model.

A dependence of light signal amplitude on plasma temperature is negligible in comparison with the density dependence [Pietrzyk, Breger, and Summers (1993)]. It also means the reconstructed density profile will only slightly depend on the temperature profile. A comparison between density profiles reconstructed for same light profile but for different temperature profiles (measured by Thomson scattering diagnostics [Stefanikova *et al.* (2016)] and parabolic with the same central temperature) is shown in FIG. 2. The relative change in reconstructed density profile is ≈ 10 times lower than relative change in temperature profile therefore the region with 50% change in temperature profile produces only 5% change in density profile.

Lets denote the variables at position z_i with superscript ^{i} i.e. the $Li_{2\mathrm{p}}(z_j)$ as $Li^j_{2\mathrm{p}}$ and $n_e(z_i)$ as n^i_e

Let us suppose, from the measurement we are able to determine the uncertainty of a light profile in all channels σ^j_{Li}. Gauss' law of error propagation will hold, thus the uncertainty of light in j-th channel can be written as follows:

$$(\sigma^j_{Li})^2 = \sum_{i=1}^{j} \left| \frac{\partial Li^j_{2\mathrm{p}}}{\partial n^i_\mathrm{e}} \right|^2 (\sigma^i_{n_\mathrm{e}})^2, \qquad (5)$$

which can be rewritten into the vector form

$$\boldsymbol{\sigma^2_{Li}} = \mathbb{F} \, \boldsymbol{\sigma^2_{n_e}}, \qquad (6)$$

[1] For edge plasma $v_\mathrm{p}(75 - 150 \text{ eV}) = 1.2 - 1.7 \cdot 10^5$ m/s, $v_b(40 - 60 \text{ keV}) = 1.1 - 1.3 \cdot 10^6$ m/s and $v_\mathrm{e}(150 - 300 \text{ eV}) = 0.7 - 1.0 \cdot 10^7$ m/s

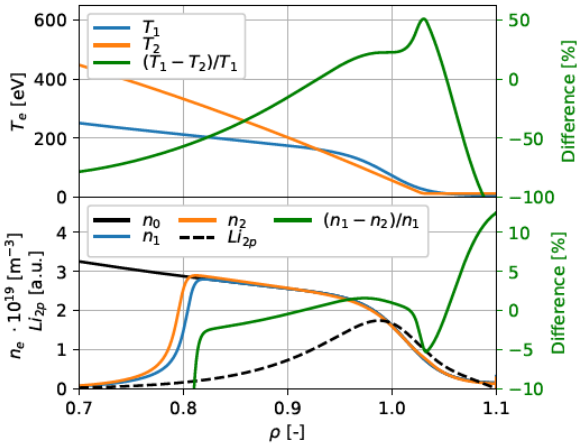

FIG. 2. Sensitivity of reconstruction algorithm on the temperature profile. COMPASS [Stefanikova *et al.* (2016)] T_1 and parabolic T_2 profiles (top graph) were used for reconstruction of light profile Li_{2p} obtained from profiles n_0 and T_1 using CR model. Density profiles n_1 and n_2 correspond to reconstruction with temperature profiles T_1 and T_2 respectively.

where error propagation matrix $\mathbb{F}$ is given by

$$\mathbb{F}_{ji} = \left| \frac{\partial Li^j_{2p}}{\partial n^i_e} \right|^2 \approx \left| \frac{Li^j_{2p}(n^i_e + \delta n^i_e) - Li_{2p}(n^i_e)}{\delta n^i_e} \right|^2 \quad (7)$$
$$\delta n^i \ll n^i.$$

The $\sigma^i_{n_e}$ can be obtained by solving system of equations (6). There are several issues when constructing the $\mathbb{F}$ matrix resulting from discrete measurement points. Firstly, the density profile is interpolated to numerical grid secondly, the Gaussian perturbation is added lastly, the profile is averaged to measurement points and δn^i_e is estimated. Gaussian perturbation must follow these requirements:

1. perturbation is small enough to fulfill linearization in (7)
2. perturbation is local i.e. only one density channel is influenced
3. biggest light perturbation is on the same channel as density perturbation

Otherwise the solution (6) will contain negative values for errors.

III. RECONSTRUCTION ALGORITHM

The aim of the reconstruction is to obtain a density profile from a $1s^22s^1$-$1s^22p^1$ transition radiation profile.

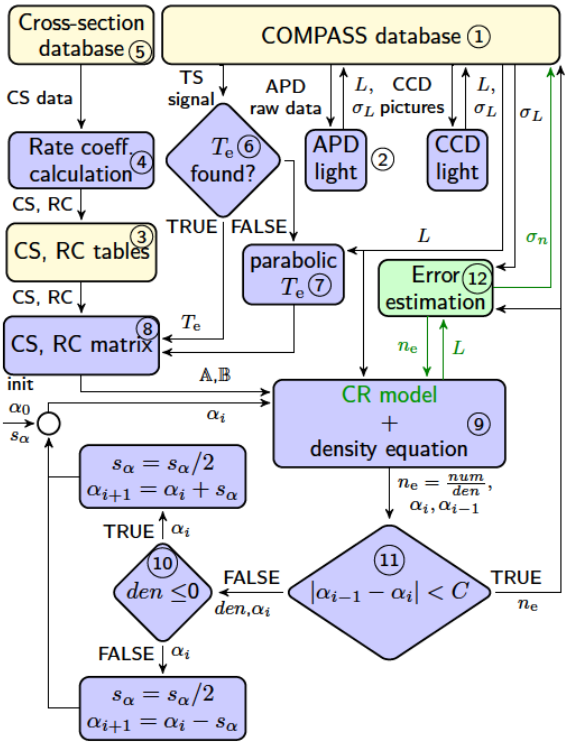

FIG. 3. Automated density reconstruction process. Numbers in the circles serve for referring from the text.

The overall reconstruction process which can run automatically is shown in FIG. 3.

The reconstruction process can be separated into 4 main phases:

- light profile generation (section III A)
- CS and RC calculation (section III B)
- density reconstruction (section III C)
- error estimation (section III D)

A. Light profile generation

Raw signals from APD and CCD camera are stored in the COMPASS database (CDB) (① in FIG. 3). This article will focus on processing of an APD signal because this detector is the only relevant for fast density measurement. A CCD camera signal processing is described elsewhere [Anda *et al.* (2016)].

Code "APD light" (② in FIG.3) reads a raw signal and generates light profile. A raw signal from APD channel 11 is show in FIG. 4. At first, the signal with S_{on} and without the beam S_{off} are separated with respect to

chopping frequency. Each time slice is given by the edge in the signal. It results in 2x higher sampling frequency than chopping frequency. As can be seen in FIG. 4 the lowest temporal resolution is 2 μs which comprises only 1 measurement point in each half-period[2].

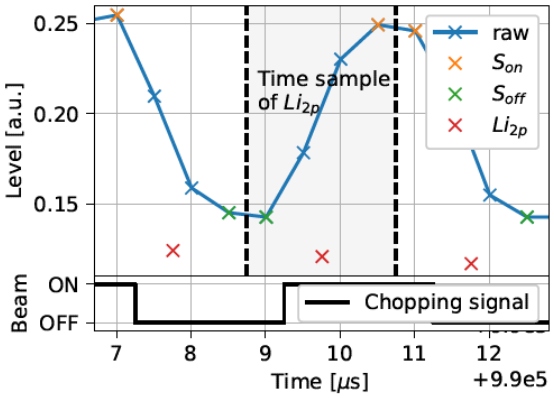

FIG. 4. Time evolution detail of signal from APD channel 11 in shot #13691 with 250kHz chopping signal.

A relative calibration of the APD channels and background subtraction is done on separated signals. In FIG. 5 is shown APD signal in neutral gas and plasma discharge. The APD signal contains electronic signal S_{el}, background signal S_{bg} and beam signal S_b.

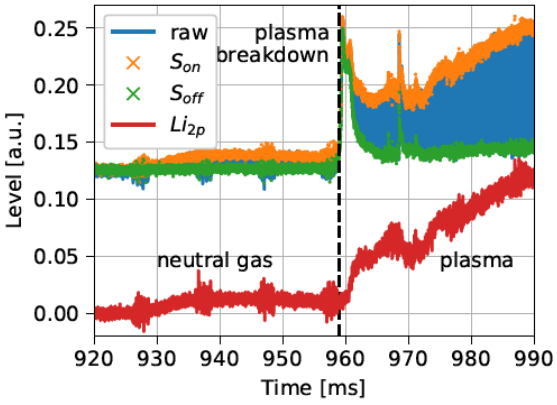

FIG. 5. Time evolution of signal from APD channel 11 in shot #13691 with 250kHz chopping signal.

[2] A 500 kHz bandwidth of an analog amplifier smears the 2 points on the edge

Part of the discharge with neutral gas is used for relative calibration. Due to low ionization rate in neutral gas and balance of excitation and de-excitation processes along the beam path, it is expected constant signal on all channels. Then a normalized calibration coefficient a_j for channel j is given by

$$a_j = \frac{S^j_{g,on} - S^j_{g,off}}{S^{ref}_{g,on} - S^{ref}_{g,off}},\ j \in M,\ j \neq ref$$
$$a_j = 1,\ j = ref \tag{8}$$

where $S^j_{g,on} = S^j_{el} + S^j_b$ and $S^j_{g,off} = S^j_{el}$ are signals in gas when the beam is on and off respectively and ref denotes reference channel (typically with the largest signal). The a_j include filter transmission, amplification of the channel and signal attenuation caused by geometrical reasons.

After calibration, the light profiles Li^j_{2p} are generated from APD signal during plasma discharge

$$Li^j_{2p} = \frac{S_{p,on} - S_{p,off}}{a_j} \tag{9}$$

where $S^j_{p,on} = S^j_{el} + S^j_{bg} + S^j_b$ and $S^j_{p,off} = S^j_{el} + S^j_{bg}$ are signals during plasma discharge when the beam is on and off respectively.

Calibration coefficients are dominant source of error which propagates to light signal since photon rates are $\approx 10^{4-5}$ ph/μs on the COMPASS tokamak [Berta *et al.* (2015)].

B. Cross-section and Rate coefficients

CS and RC tables (③ in FIG. 3) were pre-calculated (④ in FIG. 3) for wide range of energies and electron temperatures based on CS fitting coefficients from literature [Janev and Smith (1993); Wutte *et al.* (1997); Schweinzer *et al.* (1999)] (⑤ in FIG. 3). Before the reconstruction, CS and RC are interpolated from these tables according to temperature profile and beam energy in each shot.

Temperature profile is obtained from Thomson scattering (TS) diagnostics (⑥ in FIG. 3). In the case the TS profile is not available, a parabolic profile is used instead of it (⑦ in FIG. 3). The error in temperature profile is negligible because of low dependence of reconstructed density on the temperature profile see FIG. 2.

Collisional matrix $\mathbb{A}$ (3D i.e. path dependent) and spontaneous transition matrix $\mathbb{B}$ (2D - constant along the beam path) are used in reconstruction algorithm (⑧ in FIG. 3).

C. Reconstruction algorithm

The system of differential equations (1) can be rewritten into the matrix notation

$$\frac{\mathrm{d}\boldsymbol{N}}{\mathrm{d}z} = (\mathbb{A}(z)n_\mathrm{e}(z) + \mathbb{B})\boldsymbol{N} \tag{10}$$

and solved by four-step Adams-Bashforth method [Butcher (2016)]. Integration in (3) is done by Boole's rule method. Both equations (10),(3) are solved simultaneously (⑨ in FIG. 3) with initial condition $\boldsymbol{N} = \begin{bmatrix}1 & 0 & 0 & 0 & 0\end{bmatrix}^T$, $n_\mathrm{e}(z=0) = 0$ where $z = 0$ is a position of a tokamak vessel. After each run the α constant is changed by step s_α to fulfill a requirement that *num* and *den* of (3) change sign at the same z coordinate (⑩ in FIG. 3). A bisection method is used to find correct α therefore the initial estimate of α_0 and s_α must cover the expected value of α. The reconstruction stops when relative change of α is smaller then given constant C (⑪ in FIG. 3).

An integration step h has to be much smaller then a distance between measurement points to provide convergence of reconstruction scheme. Measurement points are interpolated to numerical grid using cubic splines. A reconstructed density profile is then averaged to measurement grid. FIG. 6 depicts one reconstruction profile with reconstruction error.

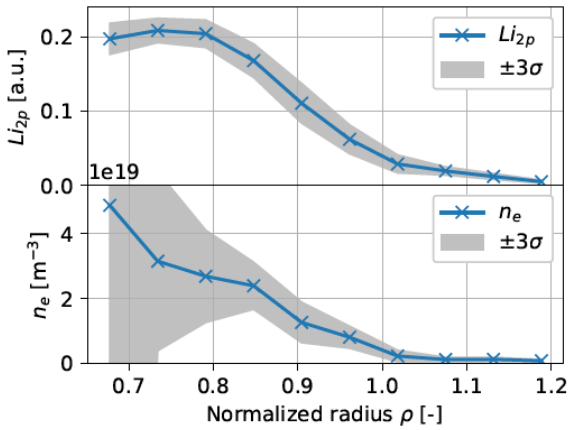

FIG. 6. Light and density profile with measurement uncertainty from the shot #13691 @ 1009 ms.

D. Error estimation

The error estimation code (⑫ in FIG. 3) reads measurement uncertainty of light profile from CDB (① in FIG. 3) and gets the density profile from the reconstruction code. Small density perturbations δn_e^i are applied channel by channel to the density profile and the profile is interpolated to numerical grid. The CR model is used for forward calculation of the perturbed light profile. The average value of light signal is calculated for each channel. A difference between perturbed light profile and measured light profiles gives information about light perturbation $\delta Li_{2\mathrm{p}}^j$. Error propagation matrix $\mathbb{F}$ is calculated using equation (7). Measurement uncertainty of density profile σ_{n_e} is obtained from equation (6). Light and density profiles with measurement uncertainty is shown in FIG. 6.

The error of density profile cumulates towards the center of the plasma because information about density propagates along the beam path. The maximal value is reached just behind the maximum of light profile at the position where the light profile is insensitive to density change. The response of the light profile to the small positive change of the density is positive on rising part of the light profile and negative in the decreasing part of the light profile. Somewhere between must be the point where the light signal is insensitive to density perturbation.

IV. RESULTS

A. Reconstructed density

Temporal evolution of electron density profile during Edge Localized Mode (ELM) event measured with 2 μs temporal resolution is shown in FIG. 7.

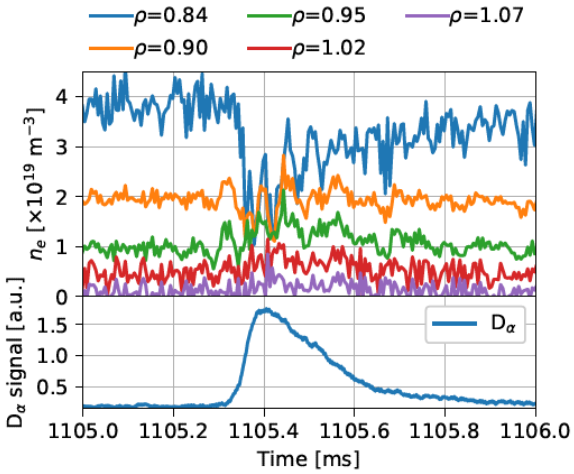

FIG. 7. A time evolution of the density profile during ELM event with a temporal resolution 2 μs (shot #17271). APD channel position is mapped to normalized radius ρ.

One can see decrease of density on the inner channel ($\rho = 0.84$) and increase of density on the outer channels ($\rho = 0.90$ and 0.95) together with density oscillations (D_α signal has been added to FIG. 7 as a reference for density reconstruction during an ELM period).

B. Reconstruction execution time

The reconstruction algorithm was originally written in MATLAB then it was rewritten in Python for the purpose to reduce execution time and of easier implementation into CDB post-processing routines (CDB is also implemented in Python [Urban *et al.* (2014)]).

Since the APD detector produces up to 10^6 light profiles during each plasma discharge, there is a need for fast reconstruction algorithm. Different implementations of a core section of reconstruction algorithm was compared from execution time point of view, see Table I. It can be seen Python code with Numba compiler gives quite a good results but after several modifications which comprises vectorization (vect.) and parallelization to 3 processor cores (par.) the whole reconstruction procedure was able to get below 10 ms for one profile thus it takes about 16 minutes to process 10^6 light profiles and this fact gives us a possibility to reconstruct density profiles with time resolution equal to 2 μs on shot to shot basis.

TABLE I. Execution time of one reconstruction for different code implementations at Intel Core i5-4460 CPU @ 3.20GHz with 88 GFLOPs[a]

Language	Execution Time [s]	%
MATLAB	0.672 ± 0.002	100
Python	1.888 ± 0.017	280
Python + Numba	0.104 ± 0.002	15
Python + vect.	0.018	
Python + vect. + par.	0.009	

[a] Benchmarked by LINPACK

C. Automation of the reconstruction

The light profiles are calculated immediately after the shot within several seconds. When the light profile is stored in the CDB the density reconstruction can start. A 300 ms long shot can be reconstructed with 2μs time resolution within 16 minutes or with 150 μs resolution within few seconds i.e. before the next shot (pause between shots on the COMPASS tokamak is at least 15 minutes). Density uncertainty estimation is calculated when density profiles for whole shot are ready.

V. CONCLUSION

This article describes in detail fast automatic density reconstruction process from Li-BES signal with a 2 μs temporal resolution on the COMPASS tokamak. It is shown that the presented reconstruction process is suitable for routine measurements producing a large amount of data e.g. diagnostics with high temporal resolution. This is also the case of the COMPASS tokamak where the Li-BES diagnostics focuses on density fluctuations and transition events as is successfully reconstructed by algorithm in FIG. 7. The implementation in Python language together with compilation of core parts with Numba decrease a requirements for computational time by one order of magnitude compared to MATLAB code. We were able to get under 10 ms execution time for one reconstruction with further optimization of code. There is still space for improvements by using Nvidia's CUDA parallel computation.

ACKNOWLEDGMENTS

This work was supported by grants of the Czech Science Foundation GA16-25074S, and co-funded by MEYS projects number 8D15001 and LM2015045. This work was also supported by the Grant Agency of the Czech Technical University in Prague, grant No. SGS17/138/OHK4/2T/14.

REFERENCES

Anda, G., Bencze, A., Berta, M., Dunai, D., Hacek, P., Krbec, J., Réfy, D., Krizsanóczi, T., Bató, S., Ilkei, T., *et al.*, Fusion Engineering and Design **108**, 1 (2016).

Anda, G., Dunai, D., Lampert, M., Krizsanóczi, T., Németh, J., Bató, S., Nam, Y., Hu, G., and Zoletnik, S., Review of Scientific Instruments **89**, 013503 (2018).

Bell, K., Gilbody, H., Hughes, J., Kingston, A., and Smith, F., Journal of physical and chemical reference data **12**, 891 (1983).

Berta, M., Anda, G., Bencze, A., Dunai, D., Háček, P., Hron, M., Kovácsik, A., Krbec, J., Pánek, R., Réfy, D., *et al.*, Fusion Engineering and Design **96**, 795 (2015).

Butcher, J. C., *Numerical methods for ordinary differential equations* (John Wiley & Sons, 2016).

Guszejnov, D., Pokol, G., Pusztai, I., Refy, D., Zoletnik, S., Lampert, M., and Nam, Y., Review of Scientific Instruments **83**, 113501 (2012).

Janev, R. K. and Smith, J., in *Atomic and plasma-material interaction data for fusion. V. 4* (1993).

Lampert, M., Anda, G., Czopf, A., Erdei, G., Guszejnov, D., Kovácsik, Á., Pokol, G., Réfy, D., Nam, Y., and Zoletnik, S., Review of Scientific Instruments **86**, 073501 (2015).

Panek, R., Adámek, J., Aftanas, M., Bílková, P., Böhm, P., Brochard, F., Cahyna, P., Cavalier, J., Dejarnac, R., Dimitrova, M., *et al.*, Plasma Physics and Controlled Fusion **58**, 014015 (2015).

Pietrzyk, Z., Breger, P., and Summers, D., Plasma physics and controlled fusion **35**, 1725 (1993).

Pusztai, I., Pokol, G., Dunai, D., Réfy, D., Pór, G., Anda, G., Zoletnik, S., and Schweinzer, J., Review of Scientific Instruments **80**, 083502 (2009).

Réfy, D., Brix, M., Gomes, R., Tál, B., Zoletnik, S., Dunai, D., Kocsis, G., Kálvin, S., Szabolics, T., and Contributors, J., Review of Scientific Instruments **89**, 043509 (2018).

Schweinzer, J., Brandenburg, R., Bray, I., Hoekstra, R., Aumayr, F., Janev, R., and Winter, H., Atomic Data and Nuclear Data Tables **72**, 239 (1999).

Schweinzer, J., Wolfrum, E., Aumayr, F., Pockl, M., Winter, H., Schorn, R., Hintz, E., and Unterreiter, A., Plasma physics and controlled fusion **34**, 1173 (1992).

Stefanikova, E., Peterka, M., Bohm, P., Bilkova, P., Aftanas, M., Sos, M., Urban, J., Hron, M., and Panek, R., Review of Scientific Instruments **87**, 11E536 (2016).

Thomas, D., Review of scientific instruments **66**, 806 (1995).
Urban, J., Pipek, J., Hron, M., Janky, F., Papřok, R., Peterka, M., and Duarte, A., Fusion Engineering and Design **89**, 712 (2014).
Willensdorfer, M., Birkenmeier, G., Fischer, R., Laggner, F., Wolfrum, E., Veres, G., Aumayr, F., Carralero, D., Guimarãis, L., Kurzan, B., *et al.*, Plasma Physics and Controlled Fusion **56**, 025008 (2014).
Wolfrum, E., Aumayr, F., Wutte, D., Winter, H., Hintz, E., Rusbüldt, D., and Schorn, R., Review of scientific instruments **64**, 2285 (1993).
Wutte, D., Janev, R., Aumayr, F., Schneider, M., Schweinzer, J., Smith, J., and Winter, H., Atomic Data and Nuclear Data Tables **65**, 155 (1997).
Zoletnik, S., Hu, G., Tál, B., Dunai, D., Anda, G., Asztalos, O., Pokol, G., Kálvin, S., Németh, J., and Krizsanóczi, T., Review of Scientific Instruments **89**, 063503 (2018).
Zoletnik, S., Petravich, G., Bencze, A., Berta, M., Fiedler, S., McCormick, K., and Schweinzer, J., Review of scientific instruments **76**, 073504 (2005).